Departament d'Enginyeria Mecànica

UNIVERSITAT POLITÈCNICA DE CATALUNYA

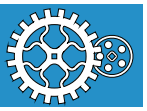

Advanced 2.5D meshless methodologies for soil-structure interaction problems in elastodynamics

by

Hassan Liravi

Thesis submitted to obtain the title of
Doctor in Mechanical, Fluids and Aerospace Engineering
by the
Universitat Politècnica de Catalunya (UPC)

June 28, 2022

Examining Committee Membership

The following experts served on the Examining Committee for this thesis.

External Examiners:	Mohammed Farouk Mohammed Hussein Professor Department of Civil and Architectural Engineering Qatar University
	Luís Godinho Professor Department of Civil Engineering University of Coimbra
Internal Examiner:	Andreu Balastegui Manso Associate Professor Department of Mechanical Engineering Universitat Politècnica de Catalunya (UPC)
Supervisors:	Robert Arcos Villamarín Associate Professor Department of Mechanical Engineering Universitat Politècnica de Catalunya (UPC)
	Arnau Clot Razquin Assistant Professor Department of Mechanical Engineering Universitat Politècnica de Catalunya (UPC)

Abstract

This thesis is concerned with the development of efficient and practical numerical methodologies to deal with longitudinally invariant soil-structure interaction problems in elastodynamics. All the approaches appearing in this thesis are formulated in the frequency-wavenumber domain. Moreover, the formulations can deal with full-space and half-space models of the soil. The novel proposed methods are mainly based on meshless approaches, which provide three main benefits: simplicity on the formulation and implementation, to avoid meshing requirements and to increase the computational efficiency of the evaluation of the soil-structure system response. Generally, these approaches are employed to model the wave propagation in unbounded mediums. Thus, in this thesis, meshless methods are used to model the soil, while the finite element method is mainly used to deal with the structure modelling. However, this thesis also demonstrates that meshless methods can also be used to model homogeneous structures. The performances of the novel approaches presented have been assessed in the context of railway tunnels embedded in the soil, especially for the case studies of circular and cut-and-cover tunnels. The studies are carried out for different elastodynamic models of the soil, including homogeneous full-space, homogeneous half-space and horizontally layered half-space.

Four new methodologies are presented in this thesis. Firstly, a two-and-a-half-dimensional finite element-boundary element methodology coupled with the method of fundamental solutions is developed. This approach uses the method of fundamental solutions to model the wave propagation in the soil once the soil-tunnel interaction has been determined, reducing the computational needs of computing the soil response. Afterwards, the second methodology further enhances the computational efficiency, the robustness and the simplicity of the approach, by modelling the soil response using the singular boundary method. To reach even higher computational benefits, a hybrid method that combines the singular boundary method and the method of fundamental solutions is proposed. This hybrid approach is found to be inheriting the computational efficiency of the method of fundamental solutions while keeping the robustness and accuracy presented by the singular boundary method. The hybrid methodology is finally extended to model both the structure and wave propagation in the soil, which leads to a fully meshless and efficient approach to deal with the soil-structure interaction problems.

Acknowledgements

The realization of this research work would have not been possible without the help and support of several people, to whom I wish to express my gratitude.

I would like to express my deepest gratitude to my supervisors, Prof. Robert Arcos and Prof. Arnau Clot, for their guidance, caring, and patience through the completion of the work. I am mostly grateful for their friendship and persistent help during my graduate studies at the Universitat Politècnica de Catalunya (UPC).

I hereby acknowledge the director of my thesis project, Prof. Jordi Romeu, for the continuous support of my doctoral study.

My sincere gratitude also goes to Prof. Luís Godinho and Prof. Paulo Amado-Mendes, who provided me with the opportunity to join their team as a visiting researcher at University of Coimbra, and who provided me with new insights in my research and helped me broaden my research horizons. I would also like to express my gratitude to their research group members for making me feel at home in Coimbra. Without their precious support and feedback, it would not have been possible to conduct a major part of my thesis.

I am grateful to Acoustical and Mechanical Engineering Laboratory (LEAM) of the Universitat Politècnica de Catalunya UPC and the project VIBWAY: Fast computational tool for railway-induced vibrations and re-radiated noise assessment, with reference RTI2018-096819-B-I00, supported by the Ministerio de Ciencia e Innovación, Retos de Investigación 2018.

I am also very grateful to all my colleagues at LEAM for their friendship and assistance.

Finally and most importantly, I would like to thank my wife and family for their endless support and encouragement.

Dedication

To my family.

Contents

List of Tables

List of Figures

List of abbreviations

Notation	Description
2.5D	Two-and-a-half-dimensional
2D	Two-dimensional
3D	Three-dimensional
BE	Boundary element
BEM	Boundary element method
EDT	Elastodynamics toolbox
FEM	Finite element method
HH	Half-half
MFS	Method of fundamental solutions
NpW	Nodes per wavelength
OIB	One-in-between
OIF	Origin intensity factor
PiP	Pipe-in-Pipe
PML	Perfectly matched layer
RMSE	Root mean square error
SBM	Singular boundary method
SSI	Soil-structure interaction
TTF	Traction transfer functions

List of symbols

Notation	Description
d	Distance between the collocation points and virtual sources boundaries
$\bar{\boldsymbol{F}}$	Vector that collects applied external forces for all the degrees of freedom along the mesh of the structure
$\bar{\mathbf{H}}_{bb}$	Matrix associated with the displacement Green's functions that relates the response on the boundary due to forces on it
$\bar{\mathbf{H}}^{\tau}_{bb}$	Matrix associated with the traction Green's functions that relates the response on the boundary due to forces on it
$\bar{\mathbf{H}}_{fb}$	Matrix of displacement Green's functions on the medium due to forces on the boundary
$\bar{\mathbf{H}}^{\tau}_{fb}$	Matrix of traction Green's functions on the medium due to forces on the boundary
$\bar{\mathbf{H}}_{cs}$	Matrix of displacement Green's functions on the collocation points due to the virtual sources
$\bar{\mathbf{H}}_{fs}$	Source-evaluation points Green's functions for displacements
$\bar{\mathbf{H}}^{\tau}_{fs}$	Source-evaluation points Green's functions for tractions
$\bar{\mathbf{H}}_{mm}$	Origin intensity factors in the SBM (Dirichlet)
$\bar{\mathbf{H}}^{\tau}_{mm}$	Origin intensity factors in the SBM (Neumann)
$\bar{\mathbf{H}}_{b_i b_j}$	Matrix that contains the displacement Green's functions associated to the collocation points defined on boundary b_i due to the set of virtual sources associated to the boundary b_j
$\bar{\mathbf{H}}^{\tau}_{b_i b_j}$	Matrix that contains the traction Green's functions associated to the collocation points defined on boundary b_i due to the set of virtual sources associated to the boundary b_j
$\mathbf{I}$	Identity matrix

$\mathbf{K}_0$	Stiffness matrix associated with FEM
$\mathbf{K}_1$	Stiffness matrix associated with FEM
$\mathbf{K}_2$	Stiffness matrix associated with FEM
$\bar{\mathbf{K}}_s$	Dynamic stiffness matrix of the soil
k_x	Wavenumber
L_i	Half length of the curve between the source points $\boldsymbol{x}^{i-1}$ and $\boldsymbol{x}^{i+1}$
$\mathbf{M}$	Mass matrix associated with FEM
$\mathbf{N}_b$	Matrix of the global shape functions
N_M	Number of MFS sources points
N_S	Number of SBM sources points
N_E	Number of evaluation points
R_c	Radius of a circumference where collocation points are located
R_s	Radius of a circumferences where source points are located
$\bar{\boldsymbol{S}}_n$	Vector of unknown strengths of the nth virtual source
$\bar{\boldsymbol{S}}_{M,n}$	Vector that collects the three components of the strength of the nth virtual source associated with the MFS
$\bar{\boldsymbol{S}}_{S,n}$	Vector that collects the three components of the strength of the nth virtual source associated with the SBM
$\bar{\boldsymbol{S}}_v$	Vector that collects all virtual source strengths in the three Cartesian coordinates
$\boldsymbol{S}^m_{S,1}$	Source strengths corresponding to mth SBM virtual source associated to the inner boundary of the structure
$\boldsymbol{S}^m_{M,1}$	Source strengths corresponding to mth MFS virtual source associated to the inner boundary of the structure
$\bar{\boldsymbol{T}}^{\Omega_2}_{b_2}$	Vector that collects the tractions at all the collocation points on the soil boundary
$\bar{\boldsymbol{T}}_b$	Vector of tractions on the boundary
$\bar{\boldsymbol{T}}_f$	Tractions at the field points
$\bar{\boldsymbol{U}}$	Vector that collects displacements for all the degrees of freedom along the mesh of the structure
$\bar{\boldsymbol{U}}_{b_1}$	Vector that collects the displacements at all the collocation points defined on the inner boundary of the structure
$\bar{\boldsymbol{U}}^{\Omega_1}_{b_2}$	Vector that collects the displacements at all the collocation points defined on the outer boundary of the structure

$\bar{\boldsymbol{U}}_{b2}^{\Omega_2}$	Vector that collects the displacements at all the collocation points on the soil boundary
$\bar{\boldsymbol{U}}_b$	Vector of displacements on the boundary
$\bar{\boldsymbol{U}}_c$	Vector that contains the displacements at all the collocation points and for the three Cartesian directions
$\bar{\boldsymbol{U}}_f$	Displacements at the field points
$\boldsymbol{x}_M^n$	Location of the mth MFS source point
$\boldsymbol{x}_S^n$	Location of the mth SBM source point
$\boldsymbol{x}_{S,1}^m$	Location of the mth SBM virtual source associated to the inner boundary of the structure
$\boldsymbol{x}_{M,1}^m$	Location of the mth MFS virtual source associated to the inner boundary of the structure
$\boldsymbol{y}_1^m$	Position of the mth collocation point located on the inner boundary
$\boldsymbol{y}_2^m$	Position of the mth collocation point located on the outer boundary
$\boldsymbol{y}_{S,1}^m$	The mth collocation point coincident with virtual source points, located on the inner boundary
$\boldsymbol{y}_{M,1}^m$	The mth collocation point not coincident with virtual source points, located on the inner boundary
$\boldsymbol{y}_{S,2}^m$	The mth collocation point coincident with virtual source points, located on the outer boundary
$\boldsymbol{y}_{M,2}^m$	The mth collocation point not coincident with virtual source points, located on the outer boundary
$\boldsymbol{y}_S^m$	Location of the mth collocation point coincident with virtual source points
Γ	Physical boundary of the structure or soil-structure interface
Γ_{m}	Segment of the boundary with length L_m
$\tilde{\Gamma}$	Virtual boundary
ε_r	Relative error
λ_s	Wavelength of the S-waves
$\boldsymbol{\Phi}$	Transformation matrix that converts the unknown nodal tractions on the boundary to nodal forces
Ω_{s}	Structure domain
Ω	Soil Domain
ω	Angular frequency

Chapter 1

Introduction

This chapter serves as an introduction of the present thesis. It begins with a brief introduction to the soil-structure interaction problems. Afterwards, a justification of the interest on introducing more practical numerical methodologies to deal with soil-structure interaction problems is presented. The justification is followed by the main objectives of the thesis. Finally, the chapter concludes with a brief outline of the contents of each of the chapters in the thesis.

1.1 Overview

Dynamic soil-structure interaction (SSI) refers to the engineering field devoted to the study of the dynamic response of structures resting or embedded in the soil. This field is an interdisciplinary subject that can be a prominent issue in the dynamic analysis of different types of structural engineering problems, for instance, the seismic analysis of the structures, the design of offshore industries and the prediction of traffic-induced vibrations [1].

The simulation approaches to deal with dynamic SSI problems can be categorised into two general forms: analytical/semi-analytical solutions and numerical approaches. The analytical/semi-analytical solutions have a limited scope of application, as they can only be defined for quite simple geometries. However, these solutions are extremely efficient in terms of computational time and can be used as a reference for the verification of numerical strategies. Methods of this type have been used in previous investigations to address various SSI problems such as footings [2] and pile-soil interaction [3]. On the contrary, numerical methodologies need to be adopted to study complex structures embedded in the soil, despite their larger computational time compared to analytical/semi-analytical methods. These approaches are commonly based on domain discretisation and they are specially designed to deal with complex finite systems (structures) embedded in unbounded domains (soil).

This thesis is devoted to the study of the numerical strategies for SSI when the structure is (or can be considered to be) longitudinally invariant, meaning that the system has constant geometrical and mechanical parameters along the longitudinal direction. Engineering structures such as at-grade railway or highway systems, underground tunnels or pipelines can be modelled within this assumption. Although the results presented in this thesis are associated with railway tunnels, the methodologies developed can be used for arbitrary longitudinally-invariant structures embedded in the soil.

1.2 Motivation

A large variety of numerical methods are presented in the literature for the dynamic assessment of SSI problems. This area of research brings new challenges to study

SSI problems related to different types of engineering structures. As mentioned earlier, some of these structures can be considered to be longitudinally invariant systems, for example, the cases of railway tracks, tunnels, roads and pipelines. Approaches formulated in the wavenumber-frequency domain, usually referred as two-and-a-half-dimensional (2.5D) approaches, are particularly suitable to model these types of systems. It is well-established that 2.5D modelling approaches [4] are a better alternative than three-dimensional (3D) models [5], since they inherently account for the longitudinal infiniteness of the system. From a computational point of view, 2.5D modelling approaches are considered more efficient than 3D models.

Mesh-based approaches are widely used to study SSI problems. Among them, finite element method (FEM), boundary element method (BEM) [6] and perfectly matched layer (PML) [7] and, especially, combinations of them are largely predominant. BEM can also be mentioned as an integration-based numerical strategy, since numerical integration along the boundary is a key procedure of the method. Despite of the benefits provided by these approaches in terms of accuracy, robustness and versatility dealing with diverse problems, they inherit two important drawbacks. On the one hand, the main disadvantage of the mesh-based methods is that they usually involve expensive mesh generation processes for high precision computations which result in large system of linear equations, requiring large computational capabilities. On the other hand, their implementation in practical algorithms has severe technical challenges [8].

To address these shortcomings, research on meshless approaches as alternative methods with significantly higher computational efficiency has gained momentum from both academia and industry in the last few years. The main benefits that the meshless methods provide are:

- Simplicity in the numerical formulation and, subsequently, in the algorithm implementation.
- To avoid the constraints of mesh generation required in mesh-based approaches.
- Enhanced the computational efficiency with respect to the mesh-based approaches.
- Lower computer memory requirements.

- To provide higher accuracy for non-complex smooth boundary geometries.

Motivated by the research gap in this field, novel meshless methodologies to deal with SSI problems have been developed. In this context, two of the most well-known meshless approaches are employed: the method of fundamental solutions (MFS) [9–14] and the singular boundary method (SBM) [15–19]. Generally, these approaches are employed to model the wave propagation in unbounded mediums. In this thesis, they are used to model the soil, while the FEM is initially used to deal with structure modelling. However, this thesis also demonstrates that meshless methods can be also employed to model bounded homogeneous structures. The performances of the novel approaches presented have been assessed in the context of railway tunnels embedded in the soil, especially for the case studies of circular and cut-and-cover underground railway tunnels. The studies are performed for various elastodynamic models of the soil, including homogeneous full-spaces, homogeneous half-spaces and layered half-spaces.

1.3 Thesis Objectives

The objective of this thesis is the *development of more efficient and practical numerical methodologies to deal with longitudinally invariant SSI problems*. This goal has been achieved by taking advantage of the benefits presented by novel approaches based on meshless methods. To this end, the following tasks have been undertaken:

- To study the applicability of the 2.5D MFS approach as a post-processing tool with the 2.5D FEM-BEM method to determine the response in the field points.
- To develop a coupled 2.5D FEM-SBM method, reaching a more robust methodology than the 2.5D FEM-MFS.
- To investigate the performance of the proposed coupled 2.5D FEM-SBM method in the context of railway tunnels, particularly for the case studies of circular and cut-and-cover underground railway tunnels.
- To propose a novel 2.5D hybrid SBM-MFS approach for elastic propagation problems that may inherit the benefits of both SBM and MFS methods.

- Study the effect of fictitious eigenfrequencies on the performance of 2.5D MFS, 2.5D SBM and 2.5D hybrid SBM-MFS methods.
- Development of a fully meshless method for longitudinally invariant SSI problems.
- To study the performance of the proposed coupled 2.5D SBM-MFS approach in the framework of railway tunnels embedded in the soil, particularly for the case studies of circular and cut-and-cover underground railway tunnels.

1.4 Thesis Outline

This dissertation is divided into seven chapters. In the current chapter, an overview of the problems, the motivation to do this research, the objectives of the present thesis, and the contents of each chapter are outlined.

Chapter 2 is concerned with presenting a review of previous researches regarding prediction models for wave propagation problems. Moreover, different methods (mesh-based and meshless) to address SSI problems are discussed in this chapter. The recent investigations related to the MFS and SBM approaches are reviewed in detail.

Chapter 3 is concerned with a new prediction methodology for longitudinally invariant SSI problems. This method uses the FEM to model the structure, the BEM to model the local soil surrounding the structure and the MFS to model the wave propagation through the soil, all formulated in the 2.5D domain. The chapter begins with an introduction to the proposed methodology. Afterwards, the numerical formulation of the proposed approach is developed. The performance of the method is demonstrated in the framework of different examples: a solid cylinder and a thin circular shell, considering homogeneous full-space and half-space models for the soil. Moreover, the computational efficiency of the proposed approach is studied. Also, a control methodology that ensures the robustness of the approach is presented.

Chapter 4 presents a more efficient and robust numerical methodology to deal with longitudinally invariant SSI problems. The methodology uses the FEM to model the structure and the SBM to model the wave propagation in the soil, both

formulated also in the wavenumber-frequency domain. First of all, the numerical formulation of the method is developed in detail. Afterwards, the accuracy of the proposed method is assessed by comparing it against 2.5D FEM-MFS and 2.5D FEM-BEM approaches for two cases: a thin cylindrical shell and a star-like beam structure, both embedded in a full-space medium. Moreover, the computational efficiency of the proposed method is evaluated. In the final step, the applicability of the proposed method is studied through two examples of a railway tunnel embedded in a layered half-space.

The hybridisation of the SBM with the MFS to deal with elastic wave propagation problems is studied in Chapter 5. The chapter starts with the theoretical background of the method. Afterwards, the accuracy of the 2.5D SBM, the 2.5D MFS and the hybrid methods are evaluated in the context of three examples: longitudinally infinite cavities with a circular, partially circular and square cross-sections, all considered in a homogeneous full-space medium. The computational efficiency of the proposed method is also assessed in this chapter. Finally, the effects of the fictitious eigenfrequencies on the responses are studied for all the considered methods.

In Chapter 6, the proposed 2.5D hybrid SBM-MFS methodology is extended for two domains to model both the structure and wave propagation in the soil, resulting in a fully meshless approach for dealing with SSI problems. The chapter begins with the theoretical background of the methodology. In the next step, the method is validated in the context of a circular shell embedded in the the soil by comparing it against the corresponding semi-analytical solution. The performance of the novel methodology has been assessed in the context of circular and cut-and-cover underground railway tunnels embedded in soils modelled as homogeneous full-spaces.

The conclusions from this investigation are summed up in Chapter 7. Some guidelines for further research in the topic are also pointed out.

Chapter 2

Background and literature review

This chapter begins with a literature review of the mesh-based approaches. Then, an introduction to the meshless methods is given, reviewing the previous investigations about the method of fundamental solutions, the singular boundary method and other existing meshless methods.

2.1 Background

Dynamic SSI is an engineering discipline that arises at the intersection of soil and structural dynamics and it is related to other disciplines as earthquake engineering, geophysics and geomechanics, material science and computational mechanics, among others [1]. The interest of scientific and technical communities in the dynamic assessment of SSI problems has been increasing over the last decades [20]. At the same time, a large variety of modelling methodologies has been developed in recent years to deal with these engineering problems. For the specific case of SSI that could be assumed to be longitudinally invariant, 2.5D modelling approaches [4] are found to be a better alternative than 3D models [21]. The wavenumber-frequency domain has been adopted in models that study the dynamic SSI between the soil and different types of infrastructures, such as at-grade railway tracks [22, 23], underground tunnel systems [22, 24], roads [25] and pipelines [26], among others.

Analytical and semi-analytical methods formulated in the wavenumber-frequency domain are a faster alternative to 2.5D numerical approaches. One of the most well-known semi-analytical models that consider a 2.5D approach is the Pipe-in-Pipe (PiP) model [27, 28], a computationally efficient method for underground railway tunnels of circular cross-section, embedded in a full-space medium. The extension to a layered half-space using a fictitious force method was later proposed by Hussein et al. [29]. The method ensures accurate results when the distance between the tunnel and the free surface or near layer interfaces is large. More recently, a general semi-analytical solution for the case of a tunnel embedded in a multi-layered half-space has been presented by He et al. [30]. Nevertheless, these semi-analytical approaches are limited to very simple tunnel geometries and numerical alternatives, mesh-based or meshless, are usually necessary to deal with cases involving complex geometries. In sections 2.2 and 2.3, the existing mesh-based and meshless approaches in the field are reviewed, respectively.

2.2 Mesh-based approaches

The applicability of 2.5D modelling strategies to SSI problems was firstly investigated by Hwang et al. [31], who presented the first work on 2.5D FEM, along with an application of the proposed methodology for soil-structure systems. Later,

a 2.5D approach based on finite and infinite elements was developed by Yang and Hung [32] to model longitudinally invariant unbounded systems subjected to moving loads. In their approach, the infinite elements are used to account for the unbounded domain. Furthermore, a 2.5D FEM approach was presented by Gavríc to compute the dispersion curves associated with longitudinally invariant structures with thin-walled [33] and solid [34] cross sections. A well-established approach to deal with SSI problems is the coupled FEM-BEM, where the FEM is used to model the structure and the BEM is employed to account for the soil medium. Sheng et al. [6, 35] proposed a FEM-BEM approach in the context of the 2.5D domain. François et al. [23] proposed also a 2.5D FEM-BEM approach that uses the Green's functions of a layered half-space as fundamental solutions instead of the full-space ones, leading to a significant reduction on the number of boundaries to be meshed. The application of this method to the prediction of railway-induced vibrations is investigated in [22]. An alternative approach for obtaining the Green's functions required in 2.5D BEM in elastodynamics is the thin layer method [36]. Another method to deal with SSI problems is proposed by Lopes et al. [37], who studied the vibration induced in buildings due to the underground railway traffic using the 2.5D FEM-PML approach, where the FEM is used to model the structure and the PML is employed to account for the unbounded soil domain.

In 2.5D models, the structure and surrounding soil are assumed to be invariant in the longitudinal direction. However, due to the physical periodicity of the railway tracks, this assumption is not valid in all frequencies. Specifically, for typical railway tunnel structures, the periodicity of the system does not influence the transfer functions in frequencies below 80 Hz [38]. Alternatively, periodic modelling can be used to simulate the response of railway systems at higher frequencies. In this regard, Gupta et al. [39] compared the results obtained by a coupled FEM-BEM periodic model of the track-tunnel-soil system with the ones obtained with the PiP model, and they highlighted the benefits and drawbacks of both models. Furthermore, Gupta and Degrande [38] assessed the efficiency of continuous and discontinuous floating slab tracks using a periodic model of track-tunnel-soil system.

In order to avoid the limitations of mesh-based approaches and also to improve the computational efficiency of the integration-based numerical strategies, meshless methods have been proposed to model the wave propagation.

2.3 Meshless approaches

The meshless methods, as an alternative to the mesh-based approaches, started to capture the interest of a broader community of researchers over the last decades. In meshless methods, there is no inherent reliance on a particular mesh topology which is associated with simpler formulations and computational implementation procedures of the method. Over the last years, numerous studies have been carried out on novel meshless approaches. MFS and SBM are probably the most popular approaches in this category. In what follows, general conceptual description of these two methods as well as a review of the previous studies found in the literature are presented. Afterwards, a summary of alternative meshless methods is also presented.

2.3.1 Method of fundamental solutions (MFS)

The MFS is a meshless method that employs the fundamental solution of the governing equation of interest as the interpolation basis function. It is especially useful for dealing with wave propagation problems in unbounded or partially unbounded domains. This method provides two main benefits with respect to the BEM in terms of numerical efficiency: on the one hand, it does not require to discretise the boundary and it avoids the integration over the boundary and, on the other hand, the system of equations to solve is usually much smaller than the one required in BEM. The earliest works associated with the application of the MFS were presented by Shippy and Kondapalli for acoustic problems [40, 41]. Later, the application of the MFS to solve the Helmholtz eigenvalue problems was studied [42]. This method was proven to be effective also for elastodynamic problems, as shown in [43]. Its application is based on a distribution of collocation points, which evaluate the boundary conditions at discrete positions, and on a distribution of source points (or virtual forces, in elastodynamic problems), where those with strengths evaluated to comply with the boundary condition at the collocation points. In the MFS the collocation points are located on the boundary, while the source points are placed outside the domain. For many years, it has been a concern of researchers to define guidelines on the positioning of the source points, since the accuracy of MFS has been found largely dependent on their distribution, particularly in complicated shapes. An incorrect selection of this distribution may

lead to large errors in the numerical method [44]. Besides, it should be noted that the amount of source points also affects the numerical convergence and stability of the results [45]. Chen et al. [46] proposed to minimise the error of the MFS through two algorithms. They considered one algorithm that minimises the error on the boundary condition satisfaction and the leave-one-out cross-validation algorithm which minimises the distance between the physical and auxiliar boundaries to find the optimal position of the virtual source points. Furthermore, Wong et al. [47] showed that there is a strong relation between the optimal position and density of the virtual source points and the effective-condition-number, which thus can be used as an indicator to optimise the virtual sources distribution. The need for an optimal determination of the distribution of virtual sources belongs to the inherent numerical instability of the MFS. A non-proper distribution of the virtual sources may result in various numerical issues. Among them, the singularity of ill-conditioned matrices [48, 49] or ill-posed problems [50] are the most common numerical issues associated with the MFS application.

To extend the capabilities of the MFS, methodologies that combine it with mesh-based approaches to deal with SSI problems have been developed. Godinho et al. [51] presented a 2D FEM-MFS modelling approach for these types of problems. An extension of the method to the 2.5D domain was presented by Amado-Mendes et al. [52], where a methodology that models the structure using 2.5D FEM and the surrounding soil with 2.5D MFS is proposed. Godinho et al. [53] presented a fully meshless method to deal with SSI problems in the frequency domain where the MFS is used to model the soil while the meshless local Petrov–Galerkin method is used to model the structure. More recently, Liravi et al. [14] proposed a 2.5D FEM-BEM-MFS approach which uses the BEM to obtain the soil stiffness matrix at the SSI, while the MFS is employed to determine the radiated field in the soil induced by the system. This work also presents a control methodology to reduce the existing errors associated with the MFS predictions. However, both FEM-MFS and FEM-BEM-MFS methods exhibit complications dealing with complex boundary shapes, due to the difficulties arising in the selection of virtual sources distribution for these geometries.

2.3.2 Singular boundary method (SBM)

The SBM is a novel and emerging meshless boundary collocation method for the solution of boundary value problems that, in contrast to MFS, locates the virtual source points on the physical boundary. The SBM inherits some of the key advantages of the BEM and some of the MFS. On the one hand, the integration procedure that is computationally expensive in BEM-based methods is avoided. On the other hand, the SBM addresses the drawbacks of the MFS associated with the position of the virtual source points by relocating them on the physical boundary, overlapping the collocation points. Although this technique eliminates the difficulties with the distribution of the source points, it arises the singularities of the fundamental solutions on the boundary due to the overlap between collocation points and virtual forces. Thus, a regularisation technique should be adopted to overcome these singularities. In the SBM, this is performed by introducing the concept of origin intensity factor (OIF) [54]. In Dirichlet boundary conditions, the OIF can be derived directly as an average value of the fundamental solutions over a portion of the boundary [55]. In the original SBM, the inverse interpolation technique is also introduced in [56, 57] for the calculation of OIFs by using sample solutions of the governing equation of the problem. For Neumann boundary conditions, the OIFs can be derived by using a subtracting and adding-back technique [58, 59]. Chen and Gu [60] proposed a desingularisation procedure that uses this technique to obtain a numerical-analytical solution which allows to directly determine the OIFs without any sample solutions. Gu et al. [54] proposed a SBM formulation for the solution of orthotropic elastic problems. This technique has been followed by Sun et al. [61] to deal with wave propagation problems in poroelastic systems.

The original SBM has been reformulated in various works to be adapted to particular cases. Asymmetric formulation of the SBM has been proposed for problems with mixed boundary conditions [62]. This type of formulation not only improves the computational efficiency but also enhances the stability of the method. Fu et al. [15] developed a SBM formulation to study acoustic radiation which has been adapted to deal with periodic systems [63] and to longitudinally invariant systems [18]. More recently, these authors developed a 3D coupled FEM-SBM approach to address acoustic radiation problems for underwater acoustics [64]. Fakhraei et al. [65] presented a full assessment of the 2.5D SBM for both scattering and

radiation acoustic problems. They studied the accuracy and robustness of the method with respect to 2.5D MFS and 2.5D BEM by proposing different examples with complex geometries. A formulation for the 2.5D SBM for elastodynamics has been recently presented in [19]. In that work, the authors used the FEM to model the structure and SBM to model the wave propagation in the medium. Despite that the SBM presents multiple benefits, it also has a number of shortcomings. One of the drawbacks of the traditional 3D SBM is the difficulties of simulating large-scale problems. This shortcoming is addressed in various studies by presenting a novel algorithm based on the recursive skeletonisation factorisation [66] and by proposing a localised singular boundary method [67] that incorporates a local subdomain at every node of the domain in conjunction with the Chebyshev collocation scheme [68], resulting in the reduction of computational time and the data storage memory by the method.

2.3.3 Alternative meshless approaches

Many other alternative meshless methods have been proposed in the literature. For instance, the regularised meshless method is another modification scheme that was firstly introduced in [69] and later developed by using the double layer potential in the desingularisation procedure [70]. Another technique, named the boundary distributed source approach, has proposed to replace concentrated sources with circular distributed ones [71, 72], providing a method free of singularities. Other meshless methods introduced in the literature are the boundary collocation method [73], boundary knot method [74], localised boundary knot method [75], singular meshless method [76] and local Petrov–Galerkin method [77] which is coupled with the BEM in [78], for addressing the acoustic wave propagation problems [78].

Some studies have also considered the combination of different meshless methodologies in a single approach with the aim of inheriting the advantages of them. In this context, a hybrid meshless method that coupled the hybrid boundary node method with the dual reciprocity method was proposed for solving the Helmholtz-type equation [79]. More recently, a hybrid localised meshless method has been developed and formulated by mixing the generalised finite difference method and the Crank–Nicolson scheme for solving transient groundwater flow [80]. In this context, the hybridisation of SBM and MFS approaches is a novel methodology that will be studied in this work.

Chapter 3

A 2.5D coupled FEM-BEM-MFS methodology for longitudinally invariant soil-structure interaction problems

This chapter is concerned with a new prediction methodology for longitudinally invariant soil-structure interaction problems in elastodynamics. The method uses the finite-element method to model the structure, the boundary-element method to model the local soil surrounding the structure and the method of fundamental solutions to model the wave propagation through the soil, all of them formulated in the two-and-a-half dimensional domain. The proposed method firstly obtains the displacement field on the soil-structure interaction boundary making use of a two-and-a-half dimensional coupled finite element-boundary element method. The method of fundamental solutions is used then as a post-processing tool to compute the response of the soil, increasing the computational efficiency of the overall methodology with respect to a methodology that considers the boundary element method as a model of the wave propagation through the soil. The accuracy of the methodology is verified for four calculation examples: a solid cylinder and a circular thin shell embedded in a homogeneous full-space and also in a homogeneous half-space. This verification is performed comparing the results with available analytical or semi-analytical solutions and a conventional two-and-a-half dimensional coupled finite element-boundary element method. Furthermore, a control methodology to

increase the robustness of the method is presented.

In the current chapter, a 2.5D FEM-BEM-MFS approach formulated in Cartesian coordinates and in the frequency domain is presented. The method uses the MFS as a post-processing tool to obtain the displacement and traction fields on the soil from the displacement field on the SSI boundary. That displacement field on the boundary is proposed to be obtained by using a 2.5D FEM-BEM approach. The main novelty of the proposed method is, thus, the way MFS is applied, which leads to two global benefits. On the one hand, the application of this methodology results to an increase of the computational efficiency of the method with respect to traditional 2.5D FEM-BEM approaches [23], especially when many evaluation points are required to be analysed. On the other hand, a substantial difference between the work of Amado-Mendes et al. [52] and the method proposed here is related about how the dynamic stiffness matrix of the soil at the SSI boundary is obtained: Amado-Mendes work uses the MFS while the present method uses the BEM. Since the BEM discretises the boundary in elements instead on the discrete collocation points employed in the MFS, the methodology presented here ensures higher accuracy on the computation of the displacement and traction fields on the SSI boundary, which results in a significant reduction of the errors associated with the displacement and traction fields on the soil. As shown in this chapter, this is of special importance for the traction field on the soil, since it has a stronger dependency on the accuracy of the displacement and traction responses on the boundary. In terms of computational efficiency, the 2.5D FEM-MFS generally overcomes the proposed method since it avoids the integration along the boundary required in BEM. However, it is demonstrated in this chapter that the new proposed method is specially relevant for large amounts of evaluation points: in these cases, both 2.5D FEM-MFS and 2.5D FEM-BEM-MFS methods exhibit very similar levels of efficiency. Also, in this chapter, an interpolation-based technique that considerably increases the accuracy/efficiency of the method is studied. In this technique, the values on the boundary obtained by 2.5D FEM-BEM are interpolated to have more collocation points to be used in the MFS. All of these capabilities lead to a comprehensive method that encompasses the robustness of FEM-BEM approaches combined with the computational efficiency of the MFS. The methodology is tested and verified for homogeneous full-space and half-space cases for two structures: a solid and a cavity embedded in the soil. Finally, an error detection tool to control the error of the displacement and traction fields on the soil, ensuring the robustness of the methodology, is proposed

in this chapter. This control technique is based on control points in the field fully evaluated by the 2.5D FEM-BEM. These control points can be used to find the location of the virtual sources that optimises the MFS performance in terms of accuracy. This is a new feature as compared with the 2.5D FEM-MFS method.

3.1 Numerical method

A general description of the methodology developed in the current chapter is presented in Fig. 3.1. This methodology is devoted to deal with SSI problems in elastodynamics and it consists of two general steps. First of all, the displacements at the soil-structure interface Γ for a structure Ω_s embedded inside the medium Ω are calculated using a mesh-based method. Numerical approaches such as the coupled FEM-BEM and the FEM-PML are suitable of this task. In step two, the MFS is applied in order to compute the displacement and traction fields on the soil. The displacements on the boundary Γ obtained in the first step are used as the input boundary conditions for the MFS: the boundary nodes of the mesh-based approach where the boundary condition is evaluated are transformed to collocation points. Virtual sources are located inside the virtual boundary $\tilde{\Gamma}$ (which is in geometrical accordance to Γ), outside the Ω domain, and their strengths are obtained using the fundamental solutions or the Green's function of the soil, depending on whether a full-space or a half-space model of the soil is considered. In this method, the MFS is proposed to be applied considering the same number of virtual sources as number of collocation points. Finally, the MFS can be used to provide the desired displacement and traction fields on the soil.

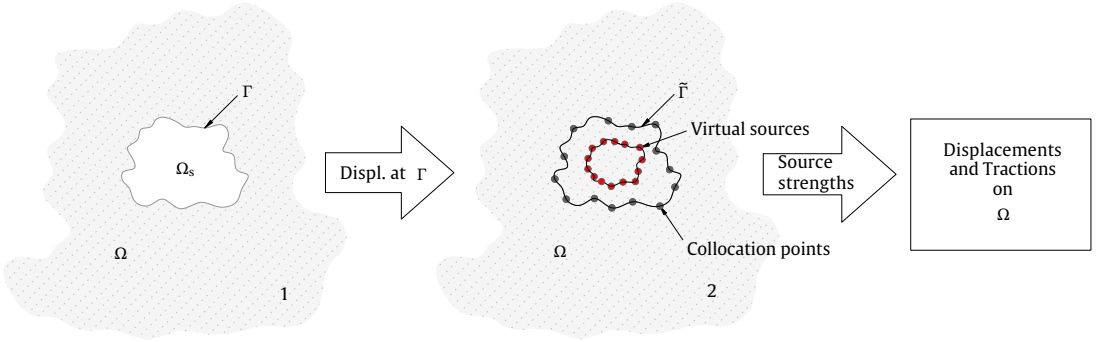

FIGURE 3.1: General description of the methodology. Collocation points are denoted by grey dots while virtual sources are denoted by red ones.

This methodology is described for the particular case of longitudinally invariant soil-structure problems, as shown in Fig. 3.2. To do so, all methods included in the methodology are formulated in the wavenumber-frequency domain (2.5D). Thus, the mesh-based method used to obtain the displacement response at the SSI boundary is based on a 2.5D FEM-BEM approach, which is detailed in Section 3.1.1. The 2.5D MFS approach for elastodynamics used for the computation of the response in the soil domain is presented in Section 3.1.2. The combination of these two approaches results in a global methodology called 2.5D FEM-BEM-MFS.

Although the method can be potentially applied to problems with arbitrary soil-structure interface geometries, the applications appearing in this chapter are restricted to circular boundaries, as also shown in Fig. 3.2. In this context, collocation points and virtual sources are located along two circumferences of radius R_c and R_s, respectively, with the same angular positions for both cases.

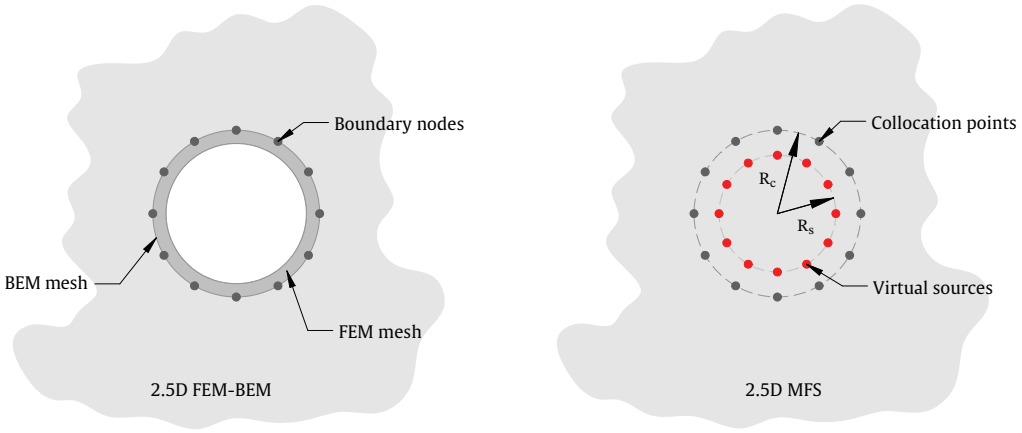

FIGURE 3.2: Visual description of the 2.5D FEM-BEM and the 2.5D MFS models considered in this chapter.

In this work, matrices and tensors are denoted by upright bold letters and vectors are denoted by bold italic letters. Also, the bar notation represents variables in the wavenumber domain, while the upper case notation is used to denote frequency domain variables.

3.1.1 2.5D FEM-BEM approach

In order to obtain the response at Γ using a 2.5D FEM-BEM approach, the soil-structure system is divided into two sub-domains, as shown in Fig. 3.2 (left) for the

case of a tunnel structure, the first one consisting of the structure and the second one consisting of the unbounded semi-infinite medium, as a model of the soil. The FEM is used to model the structure sub-domain and the BEM is used to model the soil. The considered formulation for the 2.5D FEM-BEM approach used in this chapter comes from [23] when half-space models of the soil are adopted, while the work of Ghangale et al. [81] is employed for full-space cases. These approaches are chosen for their computational efficiency, particularly significant in the case of [81], and because of the avoidance of using an explicit evaluation scheme of the required singular traction integrals and their capability of using half-space Green's functions, which simplifies the meshing effort. In both methods, the response of the soil-structure system can be obtained by

$$\left[\mathbf{K}_0 - \mathrm{i}k_x\mathbf{K}_1 + k_x^2\mathbf{K}_2 + \bar{\mathbf{K}}_s - \omega^2\mathbf{M}\right]\bar{\boldsymbol{U}} = \bar{\boldsymbol{F}}, \tag{3.1}$$

where $\mathbf{K}_0$, $\mathbf{K}_1$, $\mathbf{K}_2$ and $\mathbf{M}$ are the stiffness and mass matrices associated with the 2.5D FEM domain. The matrix $\mathbf{K}_0$ corresponds to a combination of the classical two-dimensional in-plane and out-of-plane FE stiffness matrix, while matrices $\mathbf{K}_1$ and $\mathbf{K}_2$ account for the 3D wave propagation in the structure, where the in-plane and out-of-plane degrees of freedom are coupled. $\bar{\mathbf{K}}_s$ is the dynamic stiffness matrix of the soil obtained from the 2.5D BEM model, k_x is the longitudinal wavenumber and ω is the angular frequency. The stiffness of the soil is frequency and wavenumber dependent, while the stiffness and mass matrices related to FEM domain are independent to them. Moreover, $\bar{\boldsymbol{U}}$ and $\bar{\boldsymbol{F}}$ are vectors that collect displacements and applied external forces, respectively, for all the degrees of freedom along the mesh of the structure. The dynamic stiffness matrix of the soil can be computed by

$$\bar{\mathbf{K}}_s = \boldsymbol{\Phi}\bar{\mathbf{H}}_{bb}^{-1}[\bar{\mathbf{H}}_{bb}^{\tau} + \mathbf{I}], \tag{3.2}$$

where $\bar{\mathbf{H}}_{bb}$ and $\bar{\mathbf{H}}_{bb}^{\tau}$ are square matrices associated with the displacement and traction Green's functions, respectively, that relate the response on the boundary due to forces on it. Furthermore, $\mathbf{I}$ represents the identity matrix and $\boldsymbol{\Phi}$ is the transformation matrix that converts the unknown nodal tractions on the boundary to nodal forces.

The response of the soil in terms of displacements, represented by $\bar{\boldsymbol{U}}_f$, can be then obtained by

$$\bar{\boldsymbol{U}}_f = \bar{\mathbf{H}}_{fb}\bar{\boldsymbol{T}}_b - \bar{\mathbf{H}}^{\tau}_{fb}\bar{\boldsymbol{U}}_b, \tag{3.3}$$

where $\bar{\boldsymbol{U}}_b$ and $\bar{\boldsymbol{T}}_b$ are vectors that collect displacement and traction of all the degrees of the nodes on Γ, respectively, and $\bar{\mathbf{H}}_{fb}$ and $\bar{\mathbf{H}}^{\tau}_{fb}$ are the matrices of displacement and traction Green's functions on the medium due to forces on the boundary, respectively. Eq. (3.3) represents the discretised form of the boundary integral equation in BEM [23]. The displacements on the boundary can be computed using Eq. (3.1).

Most of the computational time required in 2.5D FEM-BEM approaches relies on the computation of the displacement and traction Green's functions required to construct the matrices $\bar{\mathbf{H}}_{bb}$, $\bar{\mathbf{H}}^{\tau}_{bb}$, $\bar{\mathbf{H}}^{\tau}_{fb}$ and $\bar{\mathbf{H}}_{fb}$, especially for half-space cases, where the Green's functions are not analytical expressions. When full-space models of the soil are adopted, strategies to reduce the computational time associated with these matrices are explained in [81]. These strategies cannot be directly used in the half-space problems, since the Green's function are also depending on the source depth in comparison with full-space cases, where the only geometric information required from the source and the receiver is its relative distance. For half-space models of the soil, François et al. [23] proposed to obtain these matrices by interpolation over a 2D grid of fixed points. However, using a 2D fixed grid to account for the particular boundary of the problem could result on a significant amount of unnecessary evaluation points. Also, interpolation could result in a loss of accuracy of the system response due to improper sampling of source and evaluation locations. In the present methodology and the others to come in this thesis, however, it is proposed to construct a unique set of source-receiver combinations taking into account the relative source-receiver distance and also the source depth. The results on this unique set of source-receiver combinations are then mapped for the original configuration of source and receivers. Refer to [81] for more details on how to construct this unique set of source-receiver combinations and its mapping to the global set. Since for half-space cases this strategy is less efficient than in full-space ones due to the dependency on the source depth, it can be combined with one-dimensional interpolation along the boundary. All this strategy is found to be considerably more efficient in terms of computational time. In the present

scheme, the Green's function for 2.5D elastodynamic problems in a full-space are proposed to be obtained with the formulation presented by [82] and adapted by [83], while the Green's functions for homogeneous and layered half-space problems are proposed to be computed using the EDT toolbox [84] or the method proposed by Noori et al. [85], respectively. This also applies for all the other methods described in the present PhD thesis.

3.1.2 2.5D MFS approach

The MFS is a mesh-free and integration-free approach capable to deal with boundary value problems. In this method, a set of virtual sources located outside of the domain that produces the input response at the boundary are used to obtain an approximation to the response inside the domain, always by means of the fundamental solutions (or the Green's functions, depending on the problem) of the medium. In the present method, the displacements on the collocation points are obtained from the 2.5D FEM-BEM by computing the response on the boundary. The sources, as shown in Fig. 3.2 (right), are located outside the domain, i.e. outside the BEM domain from the 2.5D FEM-BEM approach. As previously mentioned, the displacement and traction Green's functions used in this method are the same ones that are proposed for the 2.5D FEM-BEM approach. Given the displacements at the collocation points, the source strengths can be calculated as

$$\bar{\boldsymbol{S}}_v = \bar{\mathbf{H}}_{cs}^{-1}\bar{\boldsymbol{U}}_c, \tag{3.4}$$

where $\bar{\boldsymbol{S}}_v$ is the vector that collects all virtual source strengths in the three Cartesian coordinates, $\bar{\mathbf{H}}_{cs}$ represents the matrix of displacement Green's functions on the collocation points due to the virtual sources and $\bar{\boldsymbol{U}}_c$ is the vector that contains the displacements at all the collocation points and for the three Cartesian directions. If the collocation points are considered to be directly the nodes of boundary mesh, $\bar{\boldsymbol{U}}_c$=$\bar{\boldsymbol{U}}_b$. If the configuration is different, the displacement in the collocation points $\bar{\boldsymbol{U}}_c$ should be obtained by interpolation along the boundary from $\bar{\boldsymbol{U}}_b$. Once the source strengths are computed, the displacement and traction responses on the medium, $\bar{\boldsymbol{U}}_f$ and $\bar{\boldsymbol{T}}_f$, can be computed by means of

$$\bar{\boldsymbol{U}}_f = \bar{\mathbf{H}}_{fs}\bar{\boldsymbol{S}}_v, \quad \bar{\boldsymbol{T}}_f = \bar{\mathbf{H}}_{fs}^{\tau}\bar{\boldsymbol{S}}_v, \tag{3.5}$$

where $\bar{\mathbf{H}}_{fs}$ and $\bar{\mathbf{H}}^{\tau}_{fs}$ represent the source-evaluation points Green's functions for displacements and tractions, respectively, and $\bar{\boldsymbol{U}}_f$ and $\bar{\boldsymbol{T}}_f$ stands for the displacement and traction of the field points, inside the domain.

3.2 Verification for the case of a structure embedded in a homogeneous full-space

In this section, the current methodology is verified for the case particular structure embedded in homogeneous full-space. For this verification, two calculation examples are considered: a solid cylinder and a thin circular shell, both embedded in a homogeneous full-space. The shell has a thickness of 0.1 m and the external radius for both cases is equal to 1 m. The geometrical description of these two case studies can be found in Figs. 3.3 and 3.9, respectively. In the example of the solid cylinder, the structure is assumed to be defined by the exact same mechanical parameters as the soil. Thus, for this case, the new methodology results can be compared with the ones obtained with the analytical solution for the 2.5D Green's functions in a homogeneous full-space [82]. Also, the results obtained using a 2.5D FEM-BEM approach [23] of the entire soil-structure system are included in the comparison only for the case of displacement Green's functions. In the case of the thin circular shell, the verification of the new methodology is made only comparing the results with a 2.5D FEM-BEM model of the entire soil-structure system. The mechanical parameters of the soil and the structures appearing in these two examples are presented in Table 3.1. The FEM meshes of all the structures considered in this verification are constructed using with linear triangular elements. For the solid cylinder, the density of the FEM mesh close to the boundary is selected to have at least 10 boundary elements (BE) per wavelength of the shear waves in the soil and assuming maximum frequencies interest of 100 Hz and 250 Hz, achieving BEM meshes of 36 and 104 BE, respectively. These two frequencies are selected in accordance to the frequency ranges of interest for ground-borne vibration and noise defined in the standards, which are 1-80 Hz and 16-250 Hz, respectively [86]. For the thin circular shell, meshes for 6 and 10 elements per wavelength are constructed, resulting in 24 and 36 BE, respectively (for a maximum frequency of 100 Hz), and 64 and 104, respectively (for a maximum frequency of 250 Hz). In both calculation cases, the MFS is applied considering the same number of virtual

sources as number of collocation points and a distance between them, defined by $d = R_c - R_s$, of 0.15 m. This value comes from the control scheme presented in Section 3.4. This verification is shown in terms of two different results: displacement and traction Green's functions in the wavenumber-frequency domain due to a vertical load, presented in dB based on references of 10^{-12} m/(N/m) and 1 (N/m^2)/(N/m), respectively; and also in terms of the receptances and the traction transfer functions obtained from those Green's functions, considering the evaluation point at the longitudinal position x_0 and the longitudinal distribution of the load as $\delta(x - x_0)$, presented in dB based on references of 10^{-12} m/N and 1 (N/m^2)/N, respectively. Stating the transformation of an arbitrary response $g(x, t)$ in the space-time domain to the wavenumber-frequency domain on the basis of a double Fourier transform defined by

$$\bar{G}(k_x, \omega) = \int_{-\infty}^{+\infty} \int_{-\infty}^{+\infty} g(x, t) \mathrm{e}^{\mathrm{i}(k_x x - \omega t)} \mathrm{d}x \mathrm{d}t, \tag{3.6}$$

the receptance and traction transfer functions at $x = 0$ can be obtained from the following inverse Fourier transforms

$$\boldsymbol{U}_f(\omega) = \frac{1}{2\pi} \int_{-\infty}^{+\infty} \bar{\boldsymbol{U}}_f(k_x, \omega)\, \mathrm{d}k_x, \qquad \boldsymbol{T}_f(\omega) = \frac{1}{2\pi} \int_{-\infty}^{+\infty} \bar{\boldsymbol{T}}_f(k_x, \omega)\, \mathrm{d}k_x. \tag{3.7}$$

Due to the symmetries of the displacements and tractions in the wavenumber-frequency domain due to a vertical load, the x components of the receptances and traction transfer functions for this direction are null at $x = 0$. In contrast, the other components can be computed by

$$U_f^i(\omega) = \frac{1}{\pi} \int_0^{\infty} \bar{U}_f^i(k_x, \omega)\, \mathrm{d}k_x, \qquad T_f^i(\omega) = \frac{1}{\pi} \int_0^{\infty} \bar{T}_f^i(k_x, \omega)\, \mathrm{d}k_x, \qquad \text{for } i = y, z \tag{3.8}$$

where i refers to the component of the receptance or the traction transfer function.

System	Young's modulus [MPa]	Density [kg/m^3]	Poisson's ratio	Damping
Soil	108	1800	0.33	0.05
Solid cylinder	108	1800	0.33	0.05
Thin circular shell	31000	2500	0.2	0.001

TABLE 3.1: Mechanical parameters of the soil and the structures considered in the case studies in this chapter.

3.2.1 Solid cylinder embedded in a full-space

In first instance, the verification study for the proposed 2.5D FEM-BEM-MFS method in the case of the solid cylinder is performed based on the displacement Green's functions results. The geometry of the structure, the location of the evaluation points A and B and the location of the force are indicated in Fig. 3.3. In this case, the mesh of system has a total number of 457 FEM nodes and 36 BEM nodes. The FEM mesh close to the load position is refined to approximately simulate the load considered in the analytical solution, defined in the y-z plane as $\delta(y)\delta(z)$. Points A and B are selected to represent near and far field responses on the soil with respect to the structure, respectively. The comparisons between the different methods are presented in two forms: displacement Green's function plotted against frequency for two fixed wavenumbers, presented in Fig. 3.4 and plotted against wavenumber for two fixed frequencies, illustrated in Fig. 3.5. The chosen fixed wavenumbers in Fig. 3.4 are 0.1 rad/m and 1 rad/m and the fixed frequencies considered in Fig. 3.5 are 10 Hz and 50 Hz. As can be seen, very good agreement of the results between the three methods compared is observed in all the plots. The 2.5D FEM-BEM and the analytical solution are matching perfectly in all cases, as expected due to the selection of 10 BE per wavelength. Only slight differences between the 2.5D FEM-BEM-MFS and the other two methods are observed in displacement Green's functions at near field evaluation point (point A) for frequencies higher than 80 Hz, mostly for the wavenumber of 0.1 rad/m.

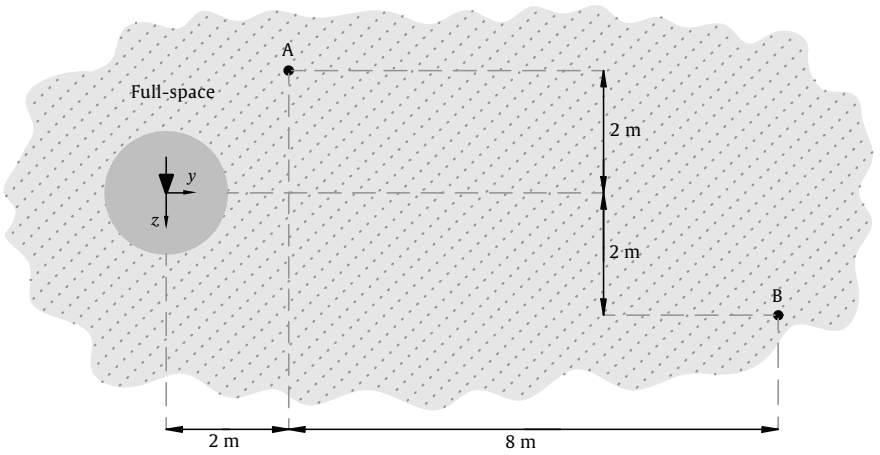

FIGURE 3.3: Geometry of the calculation example of a solid cylinder embedded in a full-space. Two evaluation points are considered: A and B. The input vertical force is represented by a big arrow.

Using the same model presented for the displacement Green's functions comparison, the traction Green's functions are compared with the analytical solution of the problem. It can be found that the proposed 2.5D FEM-BEM-MFS approach reaches high levels of accuracy associated with the traction Green's functions in the soil. Again, results at frequencies higher than 80 Hz are the only ones having slight disagreement with respect to the analytical solution. In the case of tractions, these inaccuracies can also be seen in the far field evaluation point, mostly in the case of the wavenumber 0.1 rad/m.

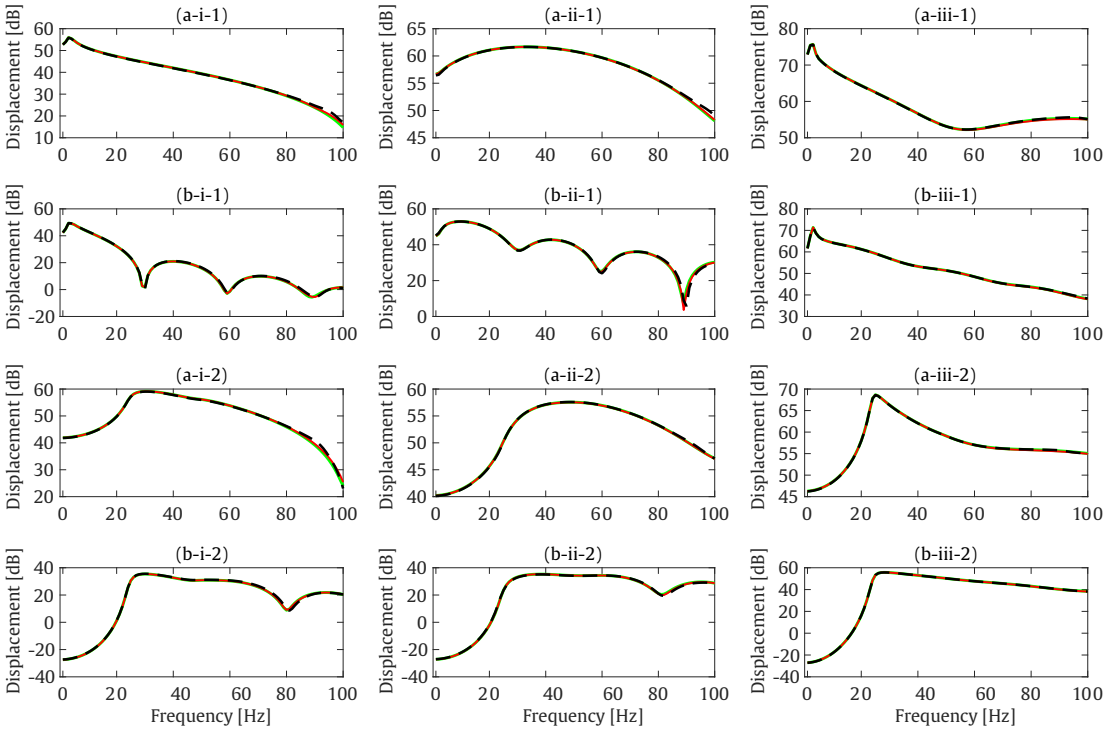

FIGURE 3.4: Displacement Green's functions. Methods: 2.5D FEM-BEM (solid red line), 2.5D FEM-BEM-MFS (dashed black line) and analytical solution (solid green line). The results are obtained at points A (a) and B (b) for x (i), y (ii) and z (iii) directions and for wavenumbers of 0.1 rad/m (1) and 1 rad/m (2).

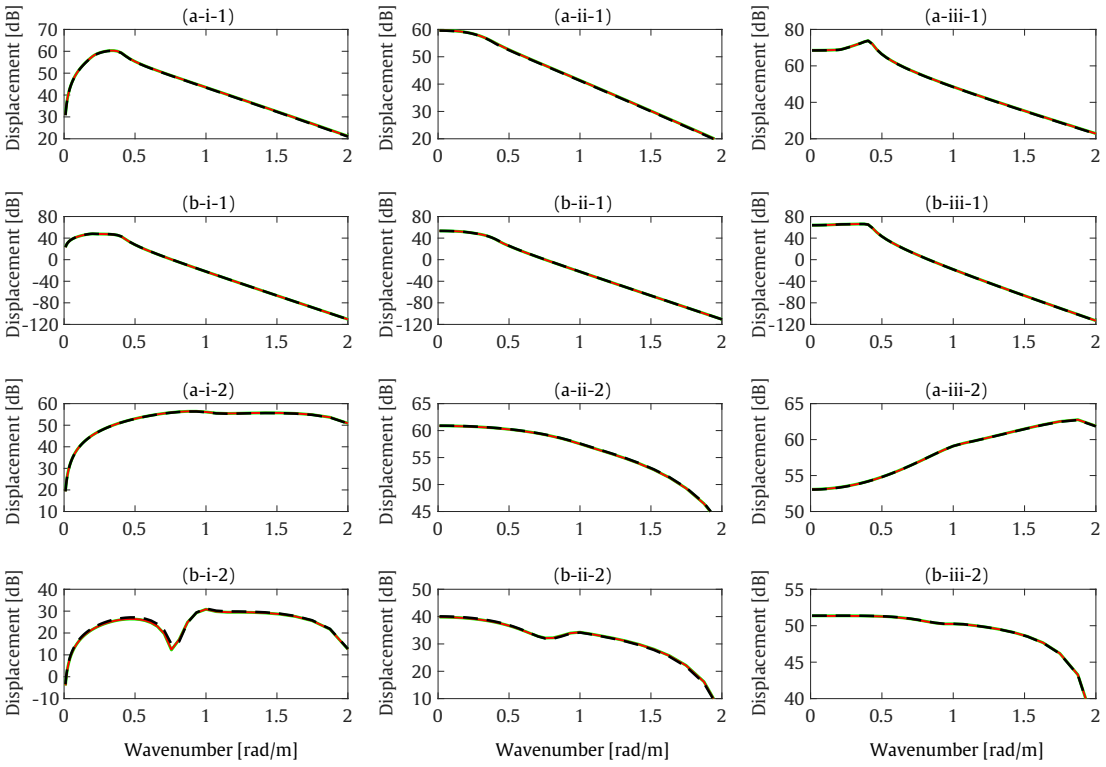

FIGURE 3.5: Displacement Green's functions. Methods: 2.5D FEM-BEM (solid red line), 2.5D FEM-BEM-MFS (dashed black line) and analytical solution (solid green line). The results are obtained at points A (a) and B (b) for x (i), y (ii) and z (iii) directions and for frequencies of 10 Hz (1) and 50 Hz (2).

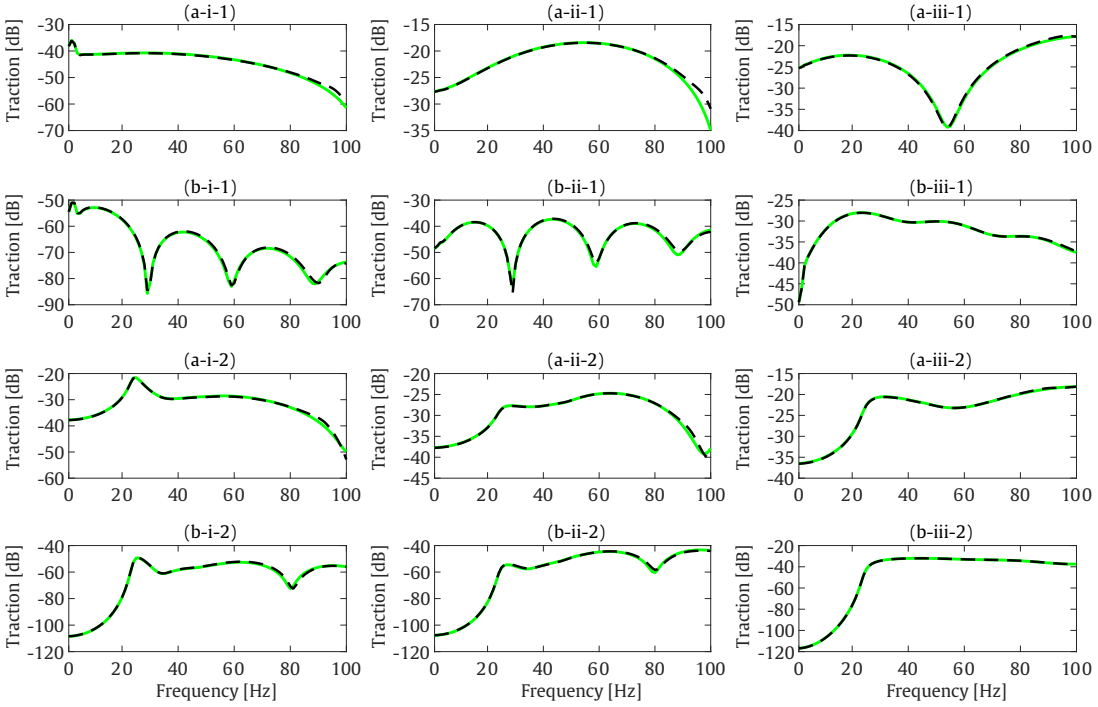

FIGURE 3.6: Traction Green's functions. Methods: 2.5D FEM-BEM-MFS (dashed black line) and analytical solution (solid green line). The results are obtained at points A (a) and B (b) for x (i), y (ii) and z (iii) directions and for wavenumbers of 0.1 rad/m (1) and 1 rad/m (2).

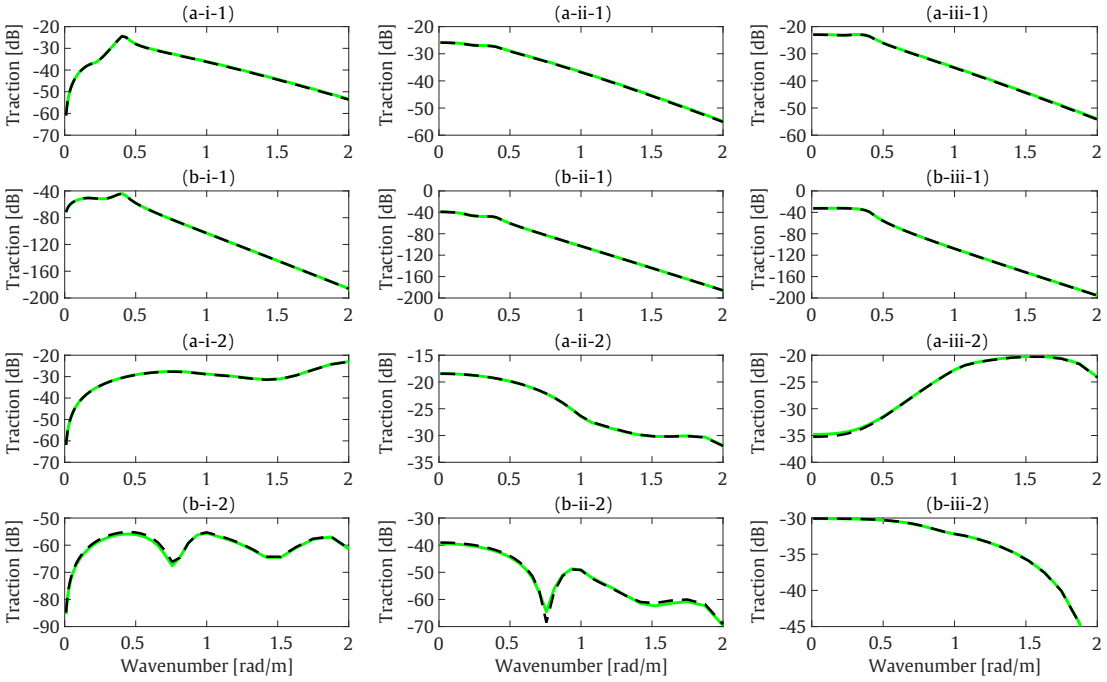

FIGURE 3.7: Traction Green's functions. Methods: 2.5D FEM-BEM-MFS (dashed black line) and analytical solution (solid green line). The results are obtained at points A (a), B (b) and C (c) for x (i), y (ii) and z (iii) directions and for frequencies of 10 Hz (1) and 50 Hz (2).

Receptances and traction transfer functions are also considered to verify the method in this case study. In Fig. 3.8, receptances and traction transfer functions obtained by the proposed methodology are compared with the ones obtained by the 2.5D FEM-BEM approach and the analytical solution of the problem up to 250 Hz. The meshes used here are done imposing 10 BE per wavelength, resulting in a total of 2335 FEM nodes and 104 BEM nodes. In the receptances comparisons presented in this figure, only slight discrepancies can be seen between the analytical solution and both numerical methods (which are in full agreement with each other) for frequencies above 200 Hz, for the y component of the response and specially for the near field evaluation point. These discrepancies are also appearing in the case of traction transfer functions.

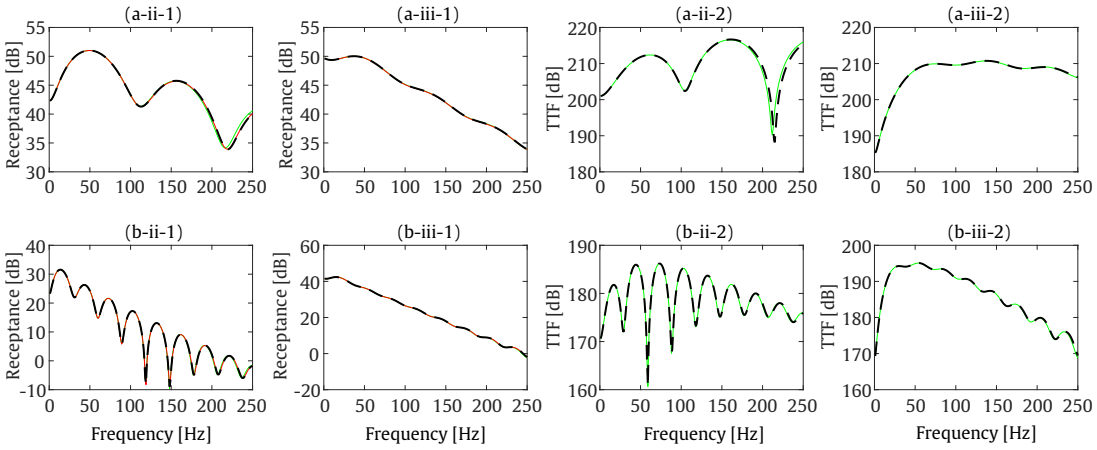

FIGURE 3.8: Receptances (1) and traction transfer functions (2). Methods: 2.5D FEM-BEM (solid red line), 2.5D FEM-BEM-MFS (dashed black line) and analytical solution (solid green line). The results are obtained at points A (a) and B (b) for y (ii) and z (iii) directions

.

3.2.2 Thin circular shell structure embedded in a full-space

In the second calculation example, a thin circular shell embedded in a homogeneous full-space is modelled. The geometrical description of the system, the position of the evaluation points considered and the location and direction of the input force are illustrated in Fig. 3.9. In this example, the new 2.5D FEM-BEM-MFS methodology is compared with a 2.5D FEM-BEM of the entire soil-structure system. In context of these two methods, eight different modelling options are taken into account in the comparison. They are listed and described in Table 3.2.

In this example, the comparison is done in terms of the receptances due to a vertical force applied in the bottom of the cavity. For the calculation of the receptances, the wavenumber in the x direction was logarithmically sampled from 0 rad/m to 55 rad/m with 1025 points. In first instance, modelling options associated with maximum frequency of 100 Hz are compared. For this case, the differences between the five proposed numerical models are negligible for frequencies below 80 Hz. Thus, receptances are plotted in Fig. 3.10 only in the frequency range from 80 Hz to 100 Hz, where the most significant discrepancies between methods can be seen. From the observation of these plots, the first insight that arises is that 2.5D FEM-BEM and 2.5D FEM-BEM-MFS methods show a strong agreement when the number of boundary nodes considered is the same, which verifies the new

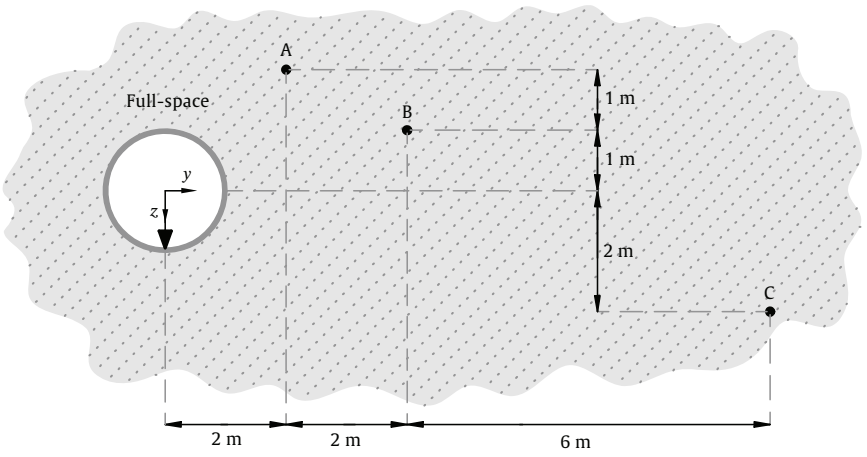

FIGURE 3.9: Geometry of the calculation example of a thin circular shell structure embedded in a full-space. Three evaluation points are considered: A, B and C. The input vertical force is represented by a big arrow.

Max. F	BE per λ_s	Modelling options	$N_{\text{BEM}}/N_{\text{CP}}$	N_{FEM}
100 Hz	6	2.5D FEM-BEM-24	24	241
		2.5D FEM-BEM-MFS-24-24	24/24	241
		2.5D FEM-BEM-MFS-24-36	24/36	241
	10	2.5D FEM-BEM-36	36	283
		2.5D FEM-BEM-MFS-36-36	36/36	283
250 Hz	6	2.5D FEM-BEM-MFS-64-64	64/64	563
	10	2.5D FEM-BEM-MFS-104	104	603
		2.5D FEM-BEM-MFS-104-104	104/104	603

TABLE 3.2: Specifications of the modelling options considered for the case of thin shell structure. In this table, λ_s represents the wavelength of the S-waves for the maximum frequency and N_{BEM}, N_{FEM} and N_{CP} represent the number of BEM nodes, FEM nodes and collocation points, respectively.

proposed approach for the present calculation example. The modelling option 2.5D FEM-BEM-MFS-24-36 is an enhanced version of the 2.5D FEM-BEM-MFS-24-24 one, where the displacements on the 24 boundary nodes are interpolated based on a third degree polynomial to a set of 36 collocation points. As can be observed in Fig. 3.10, this method generally increases the accuracy of the 2.5D FEM-BEM-MFS when it is compared with a 2.5D FEM-BEM with the same number of boundary nodes, providing enhanced accuracy results with respect to the 2.5D FEM-BEM-MFS-24-24 method. However, it should be noted that the interpolation-based methodology can only converge to the solution for the same

number of boundary nodes. Due to that, the accuracy level of the 2.5D FEM-BEM-MFS-24-36 results is similar to the one associated with the 2.5D FEM-BEM-24 method but lower than the 2.5D FEM-BEM-MFS-36-36 one.

Furthermore, the results obtained by the modelling options associated with a maximum frequency of 250 Hz are shown in Fig. 3.11. The accuracy of the proposed method, even for the 2.5D FEM-BEM-MFS-64-64 model (which is the method with the coarser mesh for this case), has been found to be high. The interpolation-based method is not considered in this comparison due to the high accuracy of that non-interpolated 2.5D FEM-BEM-MFS-64-64 method.

The computational efficiency of the current method is studied with respect to the 2.5D FEM-BEM solution in the context of the thin shell case study with 36 BEM nodes. Both methodologies have been implemented in MATLAB. The efficiency comparison is performed over a high performance cluster with 2 GHz Intel® Xeon® Gold 6138 CPU (with 40 cores). The computational efficiency of the methodology is investigated for two case scenarios. Firstly, a computation for 2048 wavenumber values, a frequency of 50 Hz and only one evaluation point is performed in only one core of the cluster and the computational costs are assessed. The results indicate that the 2.5D FEM-BEM methodology consumes 78 seconds to obtain the displacement response in the evaluation point, while the current methodology spends a total time of 69 seconds, divided in 63 seconds to get the response in the collocation points with the 2.5D FEM-BEM and 6 seconds to obtain the field point response using the 2.5D MFS (the latter computational time includes the source strengths computation). In the second example, the algorithms are run for one value of the wavenumber and the frequency, and for 5, 25, 100, 500, 1000 and 2500 evaluation points. The computational costs of both methods for this second example are indicated in Table 3.3. It is worth to be mentioned that the computational time to obtain the boundary conditions by 2.5D FEM-BEM in the context of the 2.5D FEM-BEM-MFS method is equal to 0.119 seconds and it is constant for all cases. According to the results, the time consumed by the 2.5D FEM-BEM method increases exponentially with respect to the number of evaluation points, while the computational cost of the current methodology increases in a linear trend. Thus, the computational efficiency of the current methodology with respect to the 2.5D FEM-BEM method is demonstrated to be very high for large amounts of evaluation points, while the improvement for few evaluation points is almost insignificant.

Number of evaluation points	5	25	100	500	1000	2500
Time: 2.5D FEM-BEM-MFS [s]	0.9	0.91	0.96	1.02	1.08	1.32
Time: 2.5D FEM-BEM [s]	2.46	2.49	2.82	5.3	11.8	48.1

TABLE 3.3: Computational costs of both methods depending of the number of evaluation points considered.

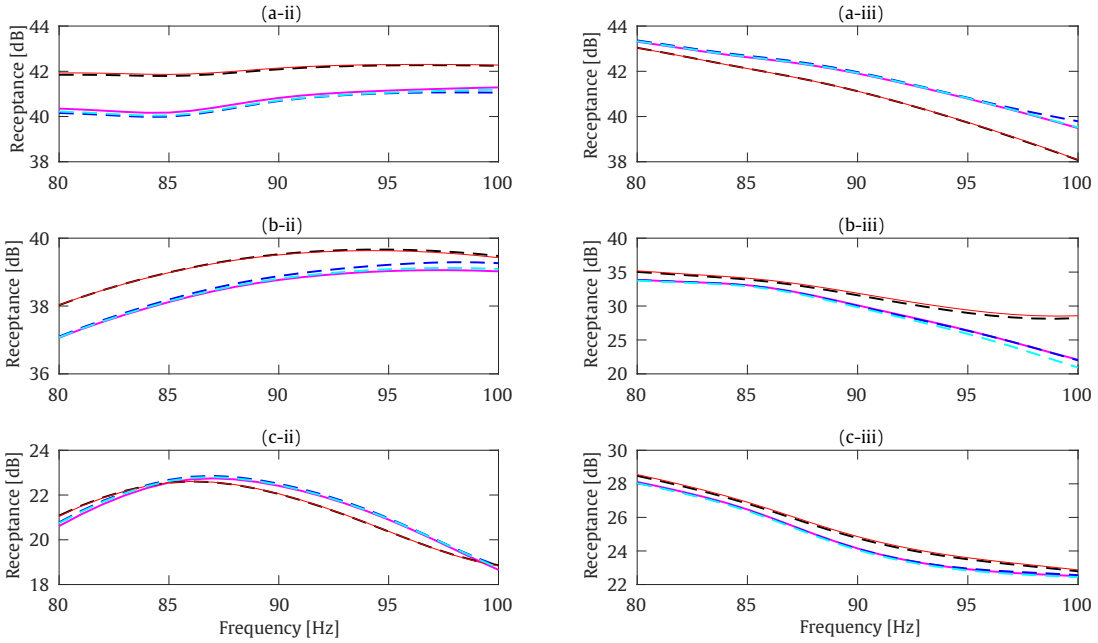

FIGURE 3.10: Receptances. Methods: 2.5D FEM-BEM-36 (solid red line), 2.5D FEM-BEM-24 (solid magenta line), 2.5D FEM-BEM-MFS-24-24 (dashed blue line), 2.5D FEM-BEM-MFS-24-36 (dashed cyan line) and 2.5D FEM-BEM-MFS-36-36 (dashed black line). The results are obtained at points A (a), B (b) and C (c) for y (ii) and z (iii) directions.

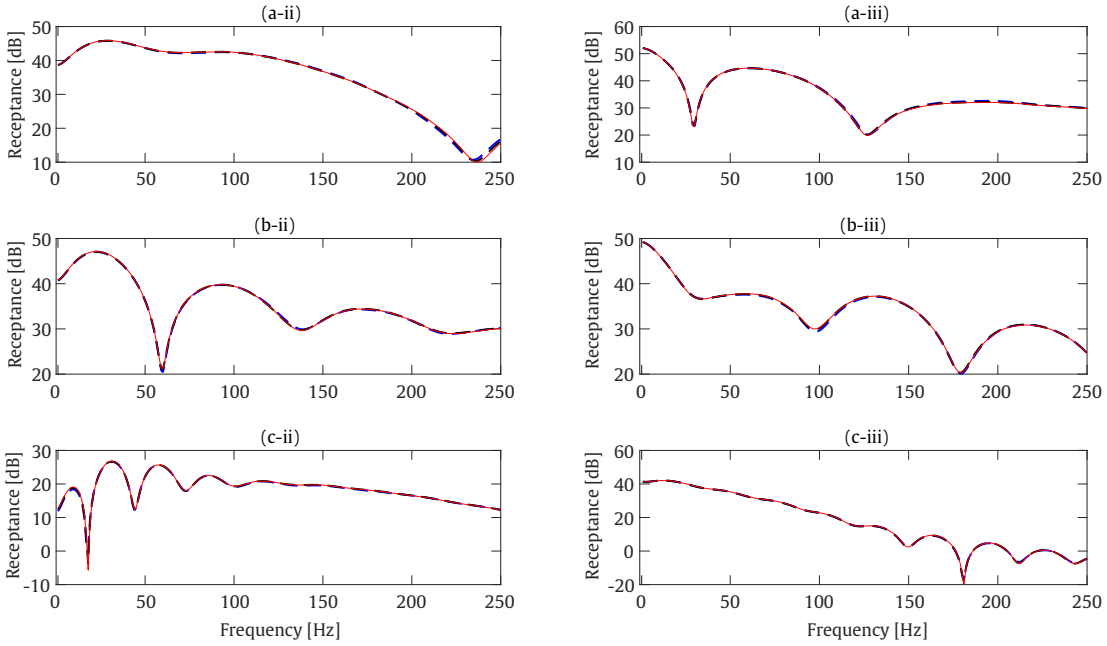

FIGURE 3.11: Receptances. Methods: 2.5D FEM-BEM-104 (solid red line), 2.5D FEM-BEM-MFS-64-64 (dashed blue line) and 2.5D FEM-BEM-MFS-104-104 (dashed black line). The results are obtained at points A (a), B (b) and C (c) for y (ii) and z (iii) directions.

3.3 Verification for the case of a structure embedded in a homogeneous half-space

In this section, the performance of the current method is verified for the case of particular structures embedded in homogeneous half-spaces. The verification is performed for two examples: a solid cylinder and a thin circular shell, both buried in a homogeneous half-space. The external radius for both structures is equal to 1 m and the shell thickness is equal to 0.1 m. The geometrical characteristics of these two calculation examples are indicated in Figs. 3.12 and 3.18, respectively. The material properties are described in Table 3.1. As assumed in the full-space case, the same material is used for the structure and medium for the solid cylinder case. Therefore, the results of this case can be directly compared with the semi-analytical solution for the 2.5D Green's functions of a homogeneous half-space. The semi-analytical solution is obtained in the basis of the direct stiffness method proposed by Kausel [87] using the EDT toolbox [84]. The 2.5D Green's functions required in 2.5D FEM-BEM-MFS and 2.5D FEM-BEM methods are also computed in this

way for both calculation examples. The FEM meshes for these cases are the same ones that have been created for the full-space case studies. The MFS is also applied for these calculation examples considering the same number of virtual sources as number of collocation points and a distance between them of 0.15 m. Results presented in this section are of the same form as the ones presented for the full-space cases.

3.3.1 Solid cylinder embedded in a half-space

As explained before, three types of results are compared in the verification of the new proposed approach for the displacement Green's functions in the case of the solid cylinder embedded in a half-space: the ones obtained by the 2.5D FEM-BEM-MFS, by the 2.5D FEM-BEM and by the semi-analytical solutions of a homogeneous half-space. The geometry of the structure, the location of the evaluation points A, B and C and the location of the force are indicated in Fig. 3.12. The evaluation point A is located on the ground surface and points B and C are located in the soil to investigate the near and far field responses, respectively. According to Figs. 3.13 and 3.14, the Green's function displacements for all calculation cases are consistent with those obtained by the semi-analytical method and 2.5D FEM-BEM approach. The only significant difference is observed in the displacement in the y component in point B for the wavenumber of 0.1 rad/m (Fig. 3.13 (b-ii-1)), where errors up to 16% difference at high frequencies (higher than 80 Hz) for both 2.5D FEM-BEM-MFS and 2.5D FEM-BEM approaches with respect to the semi-analytical solution are observed.

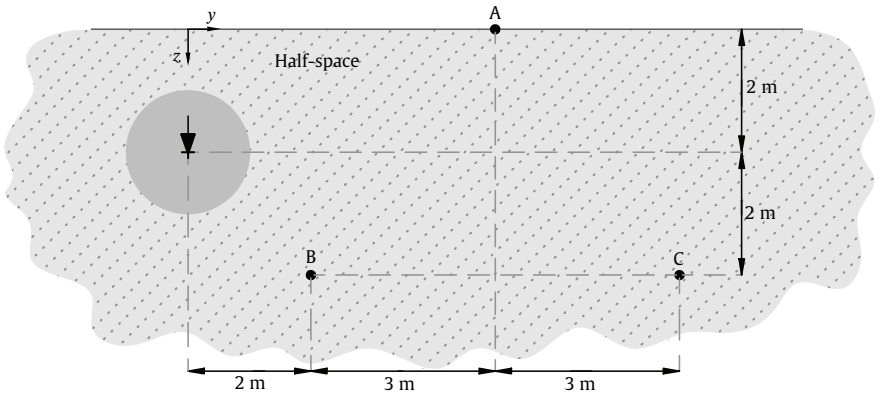

FIGURE 3.12: Geometry of the calculation example of a solid cylinder embedded in a half-space. Three evaluation points are considered: A, B and C. The input vertical force is represented by a big arrow.

In the case of traction Green's functions, the verification study only accounts for the 2.5D FEM-BEM-MFS method and the semi-analytical solution. The comparison of these two methods for the selected calculation parameters are illustrated in Figs. 3.15 and 3.16. As demonstrated in the presented plots, very good accuracy of the traction Green's functions is provided by the new method. Since the traction Green's functions in vertical direction are equal to zero for evaluation points at the ground surface, no plot is presented for the z component in the point A. Only slight differences at frequencies higher than 80 Hz can be observed, again, for the y component of the traction in point B and the wavenumber of 0.1 rad/m (Fig. 3.15 (b-ii-1)) and also for the wavenumber of 1 rad/m (Fig. 3.15 (b-ii-2)).

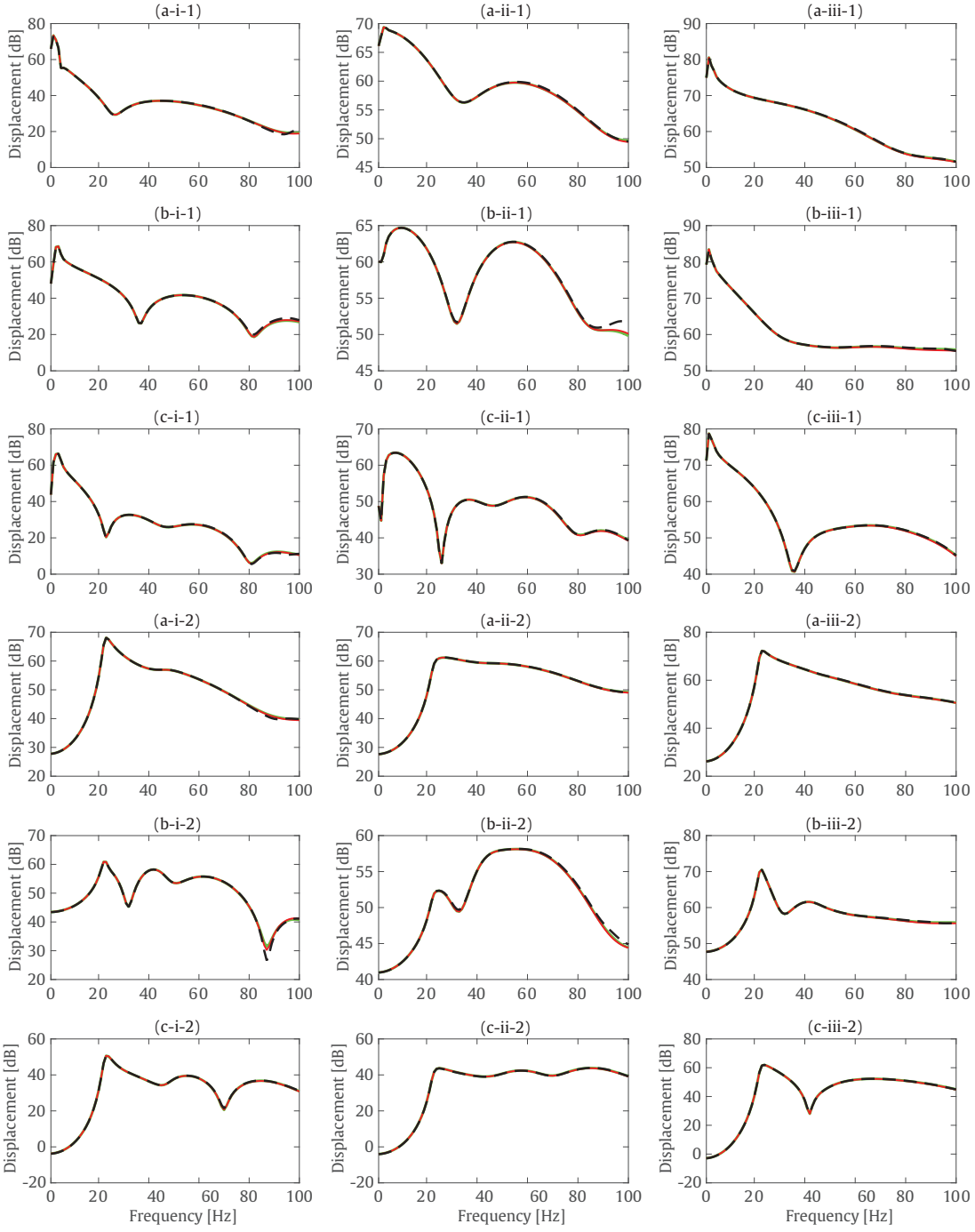

FIGURE 3.13: Displacement Green's functions. Methods: 2.5D FEM-BEM (solid red line), 2.5D FEM-BEM-MFS (dashed black line) and semi-analytical solution (solid green line). The results are obtained at points A (a), B (b) and C (c) for x (i), y (ii) and z (iii) directions and for wavenumbers of 0.1 rad/m (1) and 1 rad/m (2).

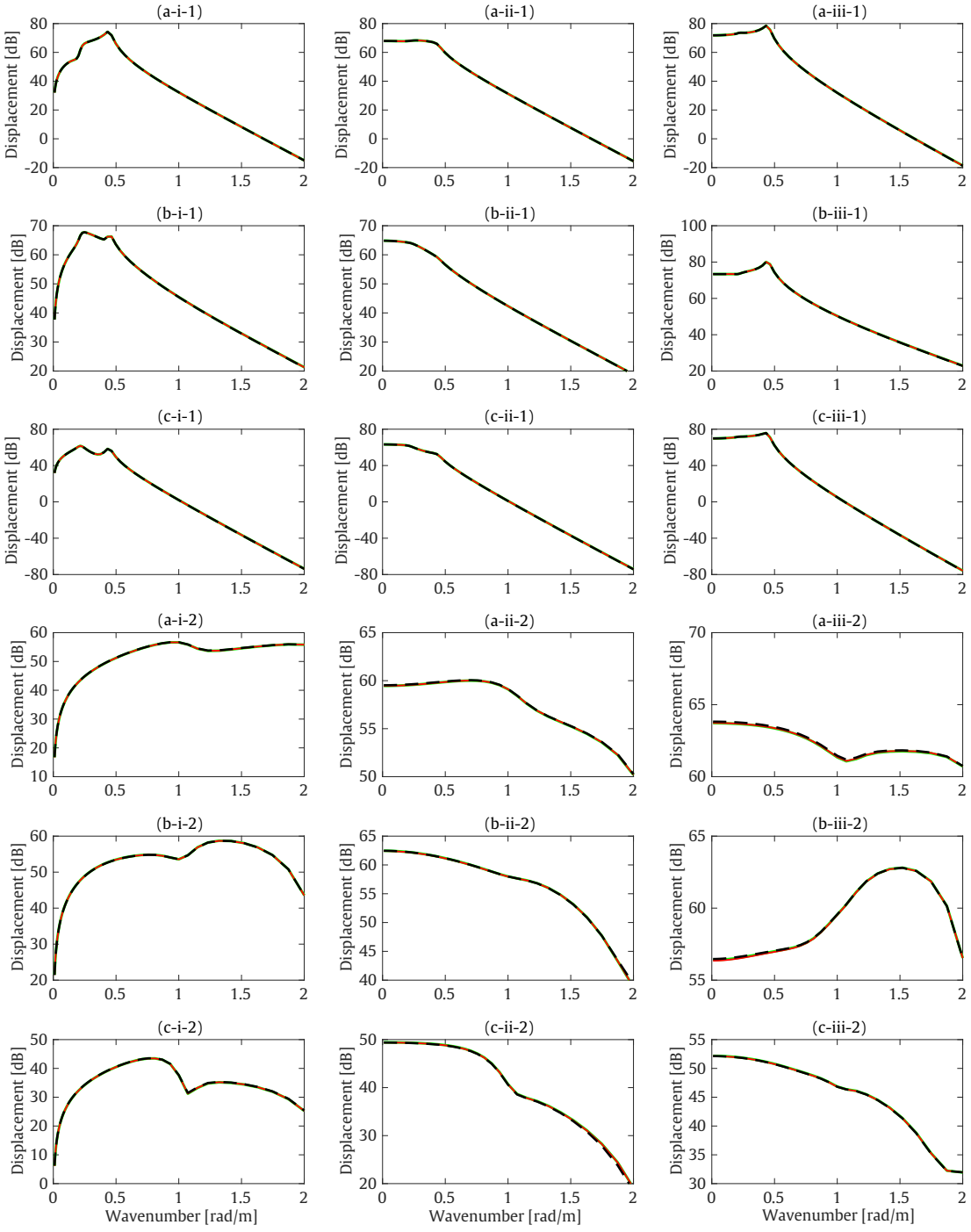

FIGURE 3.14: Displacement Green's functions. Methods: 2.5D FEM-BEM (solid red line), 2.5D FEM-BEM-MFS (dashed black line) and semi-analytical solution (solid green line). The results are obtained at points A (a), B (b) and C (c) for x (i), y (ii) and z (iii) directions and for frequencies of 10 Hz (1) and 50 Hz (2).

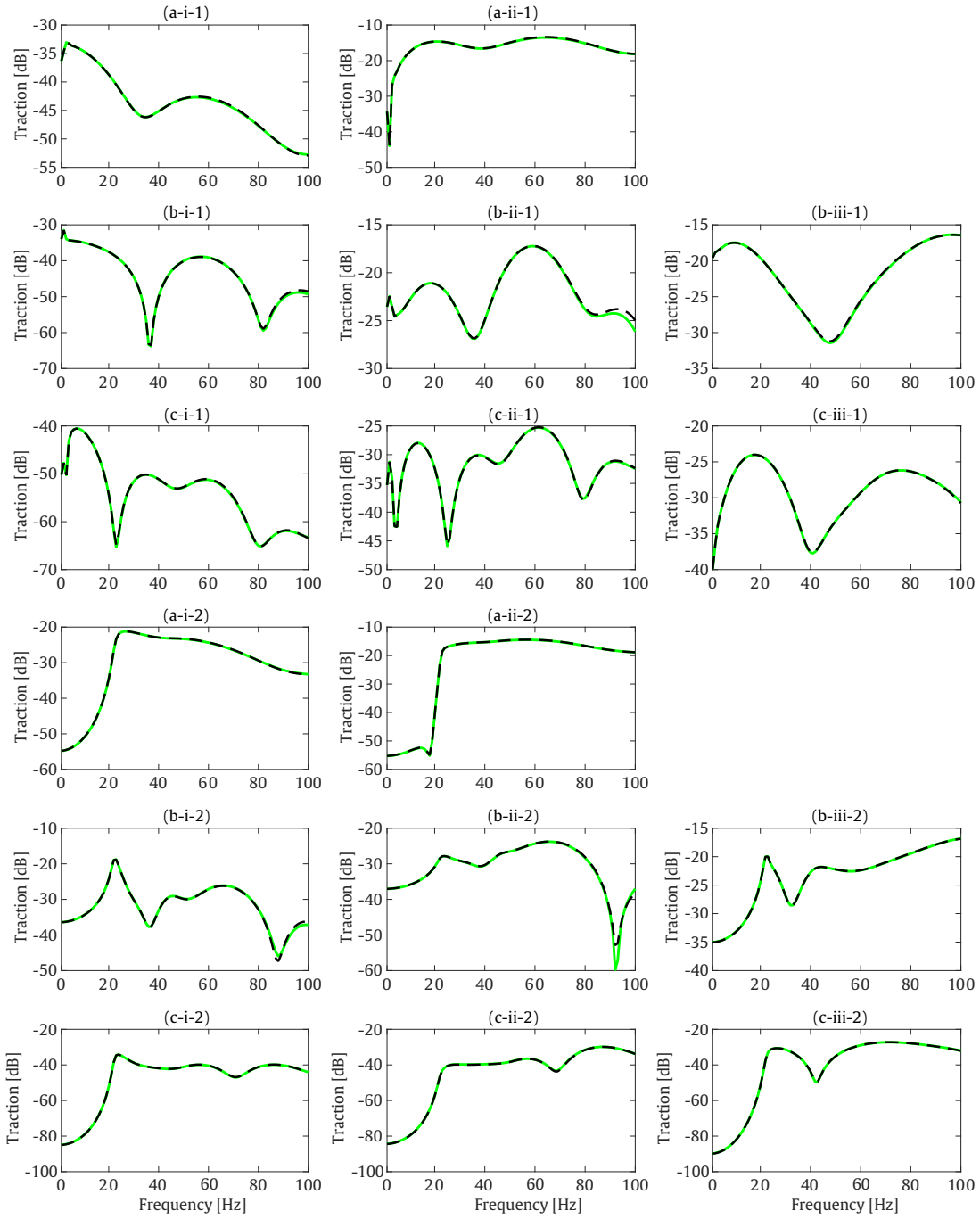

FIGURE 3.15: Traction Green's functions. Methods: 2.5D FEM-BEM-MFS (dashed black line) and semi-analytical solution (solid green line). The results are obtained at points A (a), B (b) and C (c) for x (i), y (ii) and z (iii) directions and for wavenumbers of 0.1 rad/m (1) and 1 rad/m (2).

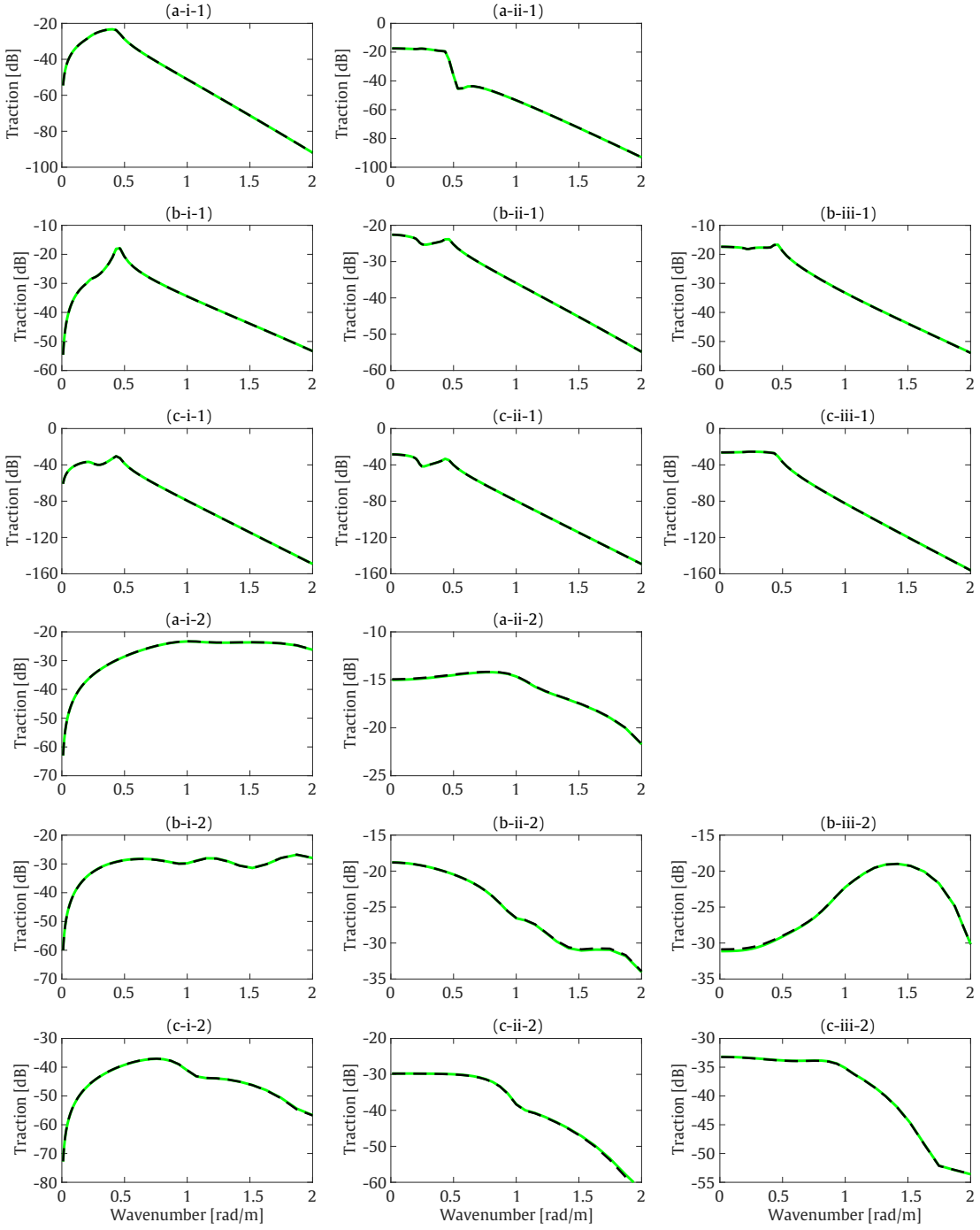

FIGURE 3.16: Traction Green's functions. Methods: 2.5D FEM-BEM-MFS (dashed black line) and semi-analytical solution (solid green line). The results are obtained at points A (a), B (b) and C (c) for x (i), y (ii) and z (iii) directions and for frequencies of 10 Hz (1) and 50 Hz (2).

Moreover, the accuracy of the proposed method is also studied in terms of receptances and traction transfer functions. The same mesh with 10 BE per wavelength and a maximum frequency of 250 Hz used in the full-space cases is adopted here.

Results of this study are presented in Fig. 3.17, where the proposed method is compared with the 2.5D FEM-BEM approach and the semi-analytical solution. To compute the desired transfer functions, the wavenumber in the longitudinal direction was logarithmically sampled from 0 rad/m to 55 rad/m with 257 points. Slight discrepancies are observed at frequencies above 200 Hz for the y and z components of the response in the field points B and C, for both receptances and traction transfer functions.

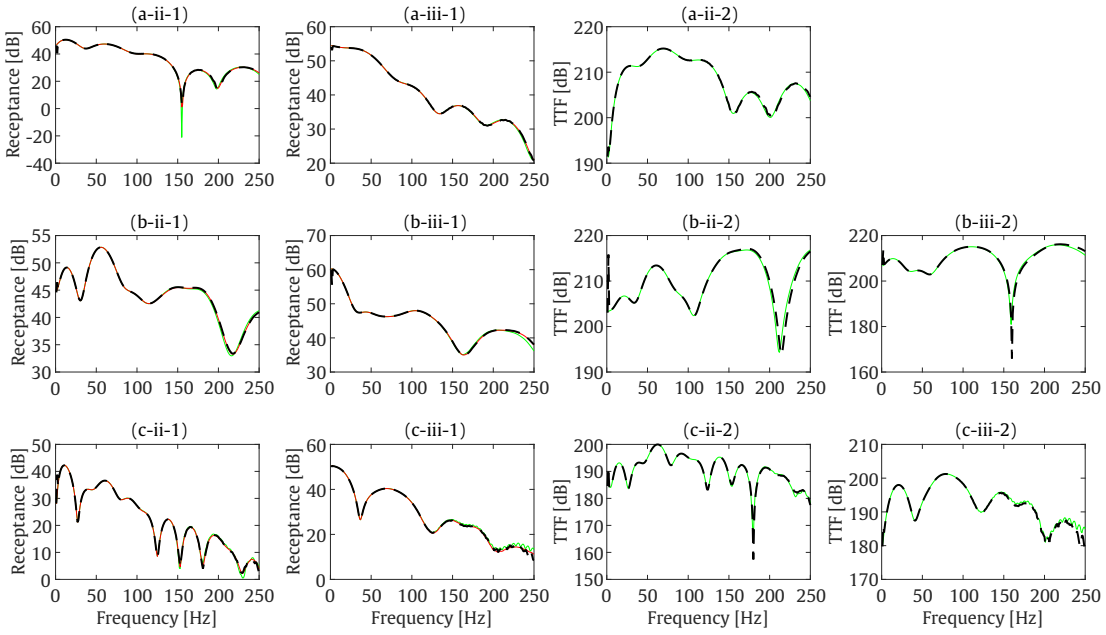

FIGURE 3.17: Receptances (1) and traction transfer functions (2). Methods: 2.5D FEM-BEM (solid red line), 2.5D FEM-BEM-MFS (dashed black line) and semi-analytical solution (solid green line). The results are obtained at points A (a), B (b) and C (c) for y (ii) and z (iii) directions

.

3.3.2 Thin circular shell structure embedded in a half-space

The last case study considered to verify the proposed 2.5D FEM-BEM-MFS approach consists of a thin circular shell embedded in a homogeneous half-space. The studied system is visually described in Fig. 3.18, where the evaluation points and the input force are defined. For this example, the same eight modelling options described in Section 3.2.2 are also taken into consideration here. For the methods comparison, results are shown in terms of the receptances. In this case, the wavenumber in the longitudinal direction was logarithmically sampled from 0

rad/m to 55 rad/m with 129 points. For the case of a maximum frequency of 100 Hz, this comparison is presented in Fig. 3.19 only for the frequency range of 80 Hz to 100 Hz. As shown for the case of a thin shell embedded in a full-space, significant differences between the different methods compared can only be seen above 80 Hz. Following the same trend as full-space case results, Fig. 3.19 shows that the receptances obtained by 2.5D FEM-BEM and 2.5D FEM-BEM-MFS methods are approximately matching when the number of boundary nodes is equal, confirming the accuracy of the new method. The interpolation-based method applied in the 2.5D FEM-BEM-MFS-24-36 modelling option is slightly improving the accuracy of the results, as also encountered in the full-space case study. Modelling options associated with a maximum frequency of 250 Hz are compared in Fig. 3.20. Similarly to the full-space case, very good agreement is observed between the three modelling options.

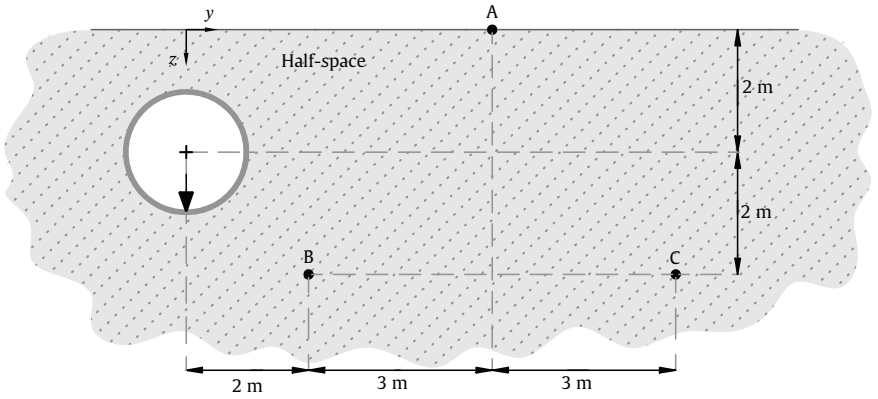

FIGURE 3.18: Geometry of the thin circular shell structure embedded in a half-space medium studied in this chapter for the verification of the 2.5D FEM-BEM-MFS. Three evaluation points are considered: A, B and C. The input vertical force is represented by a big arrow.

The computational efficiency of the current method is compared to the 2.5D FEM-BEM approach in the context of the thin shell case study considering 36 BEM nodes. Both methodologies have been implemented in MATLAB and they have been executed with the same desktop configuration described in the full-space scenarios. The computational cost of the methods is studied for two different cases. Firstly, the results are compared for one evaluation point, one frequency and 128 wavenumber values. The running times for the new method and for 2.5D FEM-BEM are 702 (divided in 431 seconds for the 2.5D FEM-BEM and 271 seconds for the 2.5D MFS) and 475 seconds, respectively. Due to EDT toolbox algorithm

design, the new method is even slower than the 2.5D FEM-BEM; however, it should be noted that the benefits of the method are arisen for large amounts of evaluation points. Secondly, a computational efficiency study is carried out taking one value of the wavenumber and the frequency and 5, 25, 60, 100, 160 and 200 evaluation points. The total computational costs consumed by the 2.5D FEM-BEM-MFS and 2.5D FEM-BEM methods are shown in Table 3.4. It should be noted that the computational time to obtain the boundary conditions in the 2.5D FEM-BEM-MFS by the 2.5D FEM-BEM is equal to 4.5 seconds regardless of the amount of evaluation points. It is found that the computational time spent by both methods raises with a quadratic trend with respect to the number of evaluation points, being the second-order coefficient associated with the curve obtained from the new method considerably smaller than the one associated with the 2.5D FEM-BEM approach. Although the computational efficiency of the current methodology for half-space problems has increased, the improvement does not reach the same levels of the method in full-space cases. That is due to the semi-analytical nature of the 2.5D elastodynamic Green's functions for a half-space and also because of the selected algorithm to calculate them, which in this case is the EDT toolbox.

Number of evaluation points	5	25	60	100	160	200
Computational time: 2.5D FEM-BEM-MFS [s]	7.5	10	15	20	30	45
Computational time: 2.5D FEM-BEM [s]	15	20	44	70	181	241

TABLE 3.4: Computational costs of both methods depending of the number of evaluation points considered.

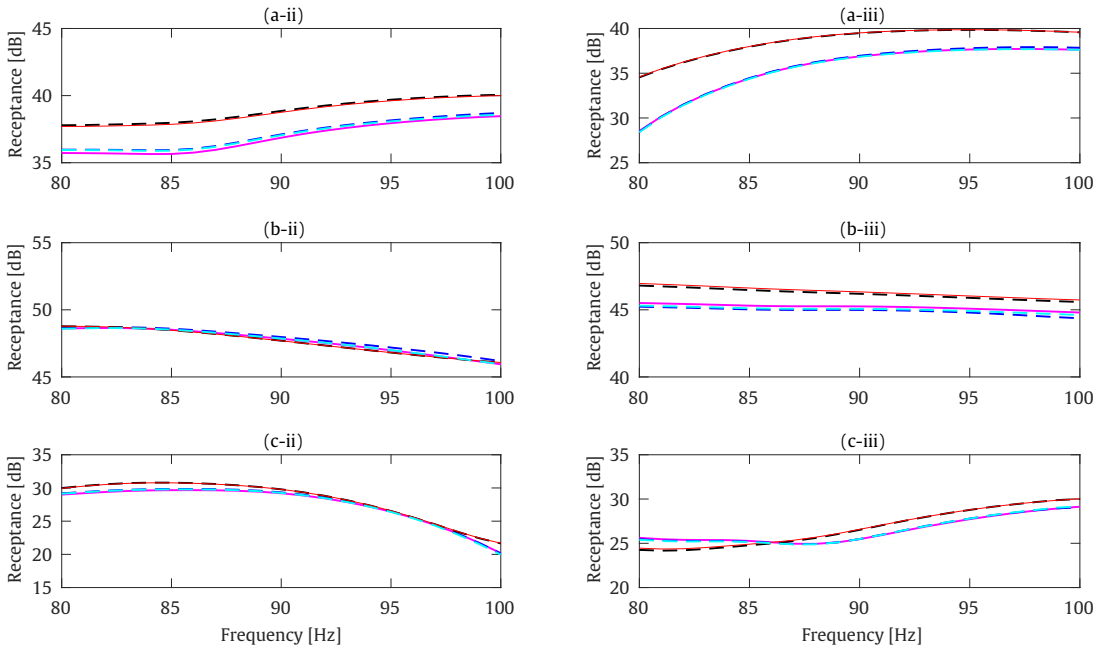

FIGURE 3.19: Receptances. Methods: 2.5D FEM-BEM-36 (solid red line), 2.5D FEM-BEM-24 (solid magenta line), 2.5D FEM-BEM-MFS-24-24 (dashed blue line), 2.5D FEM-BEM-MFS-24-36 (dashed cyan line) and 2.5D FEM-BEM-MFS-36-36 (dashed black line). The results are obtained at points A (a), B (b) and C (c) for y (ii) and z (iii) directions.

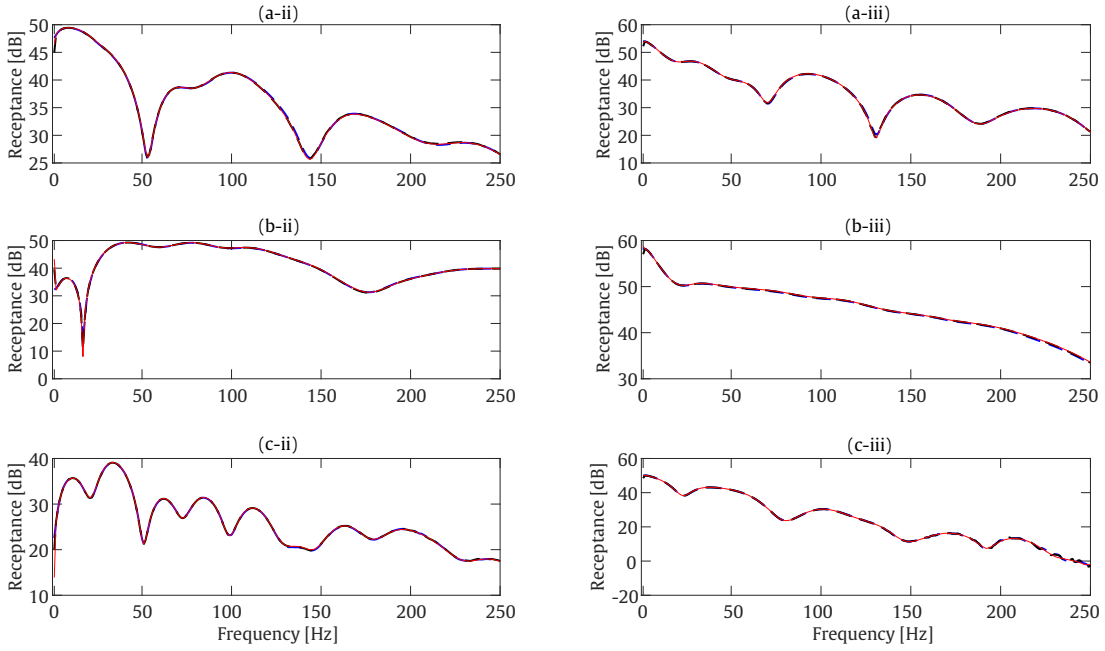

FIGURE 3.20: Receptances. Methods: 2.5D FEM-BEM-104 (solid red line), 2.5D FEM-BEM-MFS-64-64 (dashed blue line) and 2.5D FEM-BEM-MFS-104-104 (dashed black line). The results are obtained at points A (a), B (b) and C (c) for y (ii) and z (iii) directions.

3.4 Control methodology for MFS robustness

As mentioned in the introduction section, the distance between collocation and source points in the MFS should be properly selected to avoid large numerical errors of the method. In the present section, a control technique that finds the optimal distance between collocation and source points that minimises the error of the method is described. The error of the method is evaluated in a limited group of points in the medium, called control points, distributed in the area where the final results are required. Assuming a MFS application where the number of virtual forces is always the same as collocation points and BE nodes, where the auxiliary boundary is a scaled version of the physical boundary and where the sources are uniformly distributed along the boundary, as adopted in the present work, the distance between collocation points and virtual sources d is the only variable that should be selected and, thus, the only variable that controls the robustness of the method. In order to optimise d without losing computational efficiency, the control technique is carried out only considering three field points (near, not-so-near and far field locations), three frequencies (representing low, medium and high values of the total frequency range) and two wavenumbers (representing low and high values of the total wavenumber range). The relative error is calculated at these sampling points for various values of the distance d by comparing the results obtained by the 2.5D FEM-BEM-MFS method and those obtained from the 2.5D FEM-BEM approach. The optimal d is determined from the inspection of the obtained relative errors. Consequently, this control method is not affecting the overall computational efficiency of the methodology if the amount of sampling points (considering field points, frequency and wavenumber) are large, which is the common situation for SSI problems. Unless to the previous techniques [44, 46], the proposed control method is easier to be implemented. A relative error parameter ε_r is defined to determine the robustness of the method [88].

$$\varepsilon_r = \sqrt{\frac{1}{3N}\sum_{i=1}^{3}\sum_{j=1}^{N}\left|\frac{\bar{U}_{fn}^{ij} - \bar{U}_{fr}^{ij}}{\bar{U}_{fr}^{ij}}\right|^2} \tag{3.9}$$

where i and j are the indices associated with the three displacement components and the N control points, respectively. Moreover, $\bar{U}_{fn}^{ij}$ and $\bar{U}_{fr}^{ij}$ represent the displacements obtained by the new method and by a reference method, respectively,

in the control point j and in the direction i. For all the cases, the reference method is the 2.5D FEM-BEM approach.

In this investigation, this control methodology has been applied to the four calculation examples described in Sections 3.2 and 3.3. The control points considered are the evaluation points selected in each case. In Figs. 3.21 and 3.22, the relative error in full-space and half-space cases, respectively, is plotted for frequencies ranging 1 Hz to 100 Hz and for distances d ranging between 5 cm to 75 cm and for two wavenumbers: 0.1 rad/m and 1 rad/m. From the optimisation process for the calculation examples in full-space, it can be seen that only distances lower than 0.1 m are not recommended. The rest of the source-collocation points distances in the range considered are resulting in accurate results and very similar to each other. Only some slight errors appear as constant trends with respect to the distance for some specific frequencies. Particularly, errors at around 89 Hz in the case of the subplot (a-i) in Fig. 3.21 is related to the trough appearing at this frequency in the subplot (b-ii-1) in Fig. 3.4. On the other hand, results associated with half-space cases behave differently. For these cases, distances between sources and collocation points larger than 0.5 m results in high errors of the new methodology, as seen in the subplots denoted by (a) and (b) in Fig. 3.22, which represent the results obtained for the cases of a solid cylinder and a thin shell, respectively. These cases are developed, both for the new method and the 2.5D FEM-BEM, in the basis of a Green's function calculation with the EDT toolbox considering a slowness associated with the wavenumber in the y direction logarithmically sampled from 10^{-7} to 10^{3} with 919 points. This is the sampling used in all the half-space Green's functions computations required for the results in previous sections of the present work. However, subplot (c) of Fig. 3.22 is related to the case of the thin shell structure when the half-space Green's functions in the new methodology are computed using a sampling for the slowness ranging between 10^{-11} to 10^{7} with 13240 samples, while the 2.5D FEM-BEM is based on the previous sampling scheme. The results obtained in subplot (c) are more likely the ones presented in full-space case which leads to the conclusion that the new methodology is more sensitive to the accuracy of the Green's functions than the 2.5D FEM-BEM. This finding turns the control methodology presented even more essential to ensure the correctness and the computational efficiency of the method, since a proper selection of the distance d results on accurate results of the method, even if the half-space Green's functions are computed using the same

sampling scheme for the numerical integration.

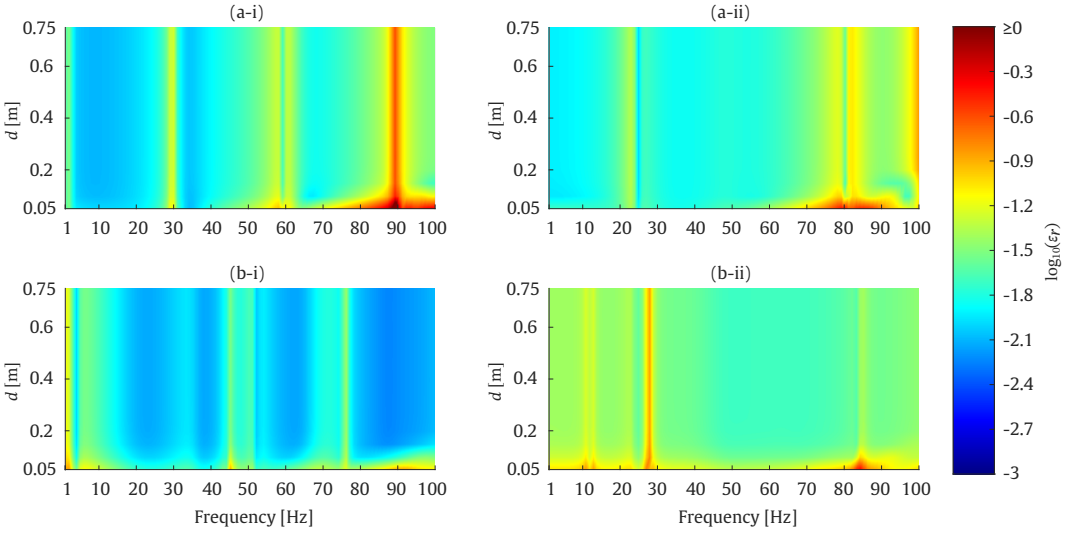

FIGURE 3.21: Relative error of the displacement Green's functions of the new methodology for the calculation examples in full-space, where (a) and (b) denote solid cylinder and thin shell structures, respectively, and (i) and (ii) represent the wavenumber of 0.1 rad/m and 1 rad/m, respectively.

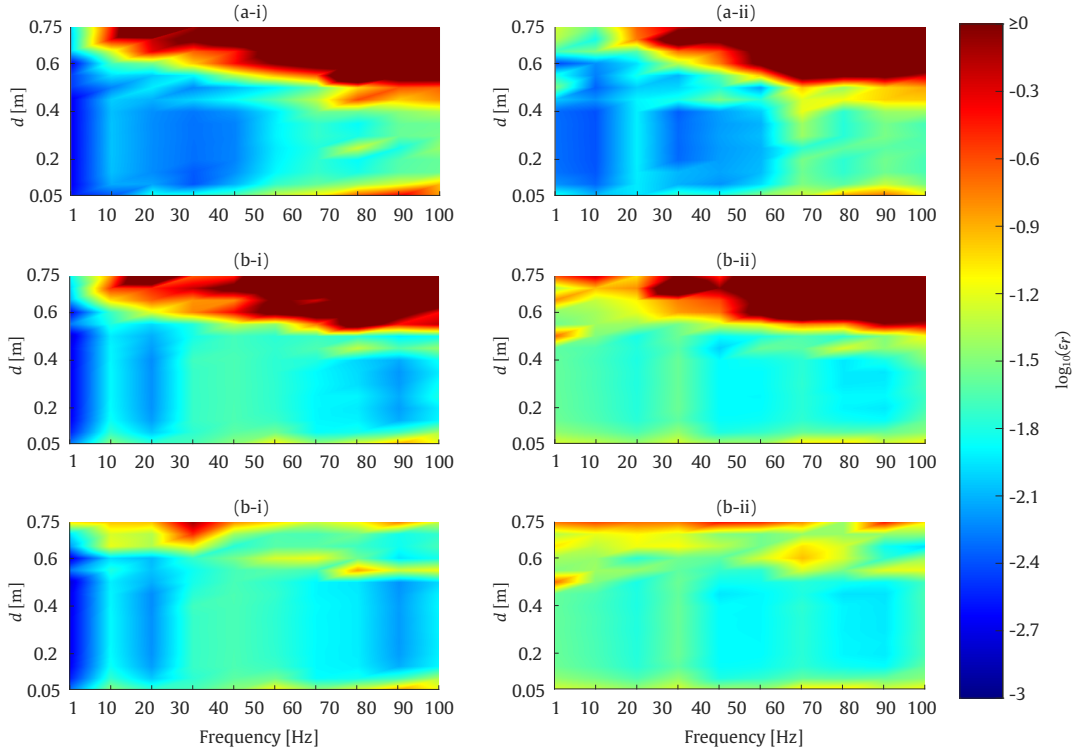

FIGURE 3.22: Relative error of the displacement Green's functions of the new methodology for the calculation examples in half-space, where (a), (b) solid cylinder and thin shell structures, respectively, and (i) and (ii) represent the wavenumber of 0.1 rad/m and 1 rad/m, respectively. The plots denoted by (c) are related to the case of the thin shell structure in which the used 2.5D Green's functions of the half-space are computed highly accurately.

3.5 Conclusions

This chapter presents a methodology to deal with longitudinally invariant SSI problems in elastodynamics. The method uses a 2.5D FEM-BEM approach to model structure and the locally surrounding soil and, then, uses a 2.5D MFS approach in elastodynamics to model the wave propagation through the soil. The new methodology is verified in terms of the displacement and traction Green's functions as well as the receptances and traction transfer functions up to frequencies of 100 Hz and 250 Hz. According to the results obtained, this method provides similar levels of accuracy than a full 2.5D FEM-BEM model of the soil-structure system but it spends a smaller amount computational time especially when the number of evaluation points is high. Furthermore, the simplicity of MFS formulation leads to a very simple implementation of the method as a post-processing tool

after the application of a numerical approach to accurately evaluate the response at the soil-structure interface. However, it is also found, as was expected, that the accuracy of the 2.5D FEM-BEM-MFS strongly depends on the accuracy of this soil-structure boundary response. Besides these general outcomes, this study has arisen other significant findings:

- A comparison between the new approach and the 2.5D FEM-BEM in terms of the computational efficiency has been carried out and the results indicate that, for the calculation examples where the soil is modelled as a full-space medium, the time consumed by the new method follows a linear trend with the number of evaluation points, while the computational time associated with the 2.5D FEM-BEM method increases exponentially. For the half-space calculation examples, the benefits of the proposed methodology in terms of computational time are also confirmed, although the improvement is not as high as in full-space problems. That is due to the numerical integration required for the evaluation of the 2.5D elastodynamic Green's functions in a half-space, in contrast to the analytical nature of the ones for full-space, and because of the particular computational performance of the algorithm used for their calculation.

- Cubic interpolation from the displacements on the boundary nodes to a larger set of collocation points has been found to be an interesting procedure, since it induces an enhancement of the results accuracy by adding no significant increment in the computational time of the full method. This improvement is shown by comparing the accuracy of the results obtained by taking 24 boundary nodes and 36 collocation points with respect to the case of 24 boundary nodes and 24 collocation points.

- A control technique that minimises the MFS error by optimising the distance between collocation points and virtual sources has been also presented. This control technique is demonstrated to be very useful in cases where the Green's functions have a semi-analytical nature, since the 2.5D MFS is found to be much more sensitive to the Green's functions accuracy than the 2.5D FEM-BEM when the response at field points is computed. This sensitiveness is observed in the application of the control technique in half-space cases,

where the 2.5D elastodynamic Green's functions computation requires a numerical integration. In contrast, it is not observed in the calculation examples considering a full-space, since the Green's functions for this case are analytical. From the results obtained, it is proposed a practical application of this control technique based only on few control points (located at the area where the final response is required) and some selected frequencies, in order to avoid compromising the computational efficiency of the whole method.

Despite all the mentioned capabilities of the proposed methodology, its accuracy is subjected to the distribution of virtual sources, particularly in terms of amount and location, especially in the case of complex boundary geometries. This is a major challenge associated with the MFS. A new step on developing a strongly robust and efficient method for 2.5D SSI dynamic computations is presented in the next chapter, where the BEM and MFS methods are substituted by the SBM, resulting in a 2.5D FEM-SBM approach, a method that avoids the problems induced by the source location in MFS and provides even larger computational benefits than 2.5D FEM-BEM-MFS.

It should be also mentioned that the proposed 2.5D FEM-BEM-MFS approach cannot overcome the problems associated with the fictitious eigenfrequencies, since the responses on the boundary are obtained using BEM, which is not capable of solving them. This issue is fully investigated later in Chapter 5.

Chapter 4

A 2.5D coupled FEM-SBM methodology for soil-structure dynamic interaction problems

In this chapter, a 2.5D FEM-SBM numerical method for longitudinally invariant soil-structure interaction problems is proposed. In this method, the structure is modelled using the 2.5D FEM and a 2.5D SBM approach is adopted to model the surrounding soil. Due to the previously discussed benefits of the SBM with respect to the BEM and the MFS to model unbounded domains, the proposed 2.5D FEM-SBM method exhibits advantages with respect to FEM-BEM and FEM-MFS approaches: modelling simplicity, numerical efficiency and robustness. These benefits are evaluated, analysed and described in this chapter. In the 2.5D SBM approach adopted in the present work, the singularities arisen in the method are avoided using the concept of origin intensity factor (OIF).

The chapter is organised as follows. In Section 4.1, the proposed formulation of the novel 2.5D FEM-SBM approach is presented in detail. Section 4.2 presents a verification study of the novel method, assessed in the context of two examples: a thin cylindrical shell and a solid beam with star-like cross section, both embedded in a homogeneous full-space. These two examples were selected in order to show the versatility of the method. In the first example, the accuracy of the 2.5D FEM-SBM in terms of the response of the system at the soil-structure boundary and in the soil medium is compared to the responses provided by 2.5D FEM-MFS [52] and 2.5D FEM-BEM [23] approaches. In the second example, the accuracy of the proposed

method is compared against the one of 2.5D FEM-BEM in terms of receptances of the system in the soil medium. Moreover, the computational efficiency of the proposed method is compared to the one of other numerical strategies in the context of the first calculation example. Finally, in Section 4.3, the applicability of the proposed method for railway-induced vibration assessment problems is discussed through two examples of a railway tunnel embedded in a half-space.

4.1 Numerical method formulation

The 2.5D FEM-SBM method is developed to address 2.5D dynamic SSI problems. The method considers that the whole system can be divided into two distinct domains, the structure and the soil, each one of them modelled using a different approach: as in Chapter 3, the structure is modelled using the FEM and in contrast to previous chapter, the unbounded domain representing the soil is modelled by the SBM. As before, the new approach is proposed for longitudinally invariant SSI problems (2.5D) and is formulated in the wavenumber-frequency domain. In Fig. 4.1, these sub-systems are denoted by the domains Ω_s (structure) and Ω (soil). The SBM method approximates the solution of the displacement and traction fields at Ω using a set of virtual sources collocated along the boundary Γ that comply with the boundary conditions evaluated at these same collocation points, which are also distributed along Γ. The coupling between the two sub-systems is done by assuming displacement compatibility and force equilibrium. In this work, the set of FEM nodes on the boundary, collocation points and virtual sources are geometrically coincident, as shown in Fig. 4.1, which strongly simplifies the coupling procedure. The detailed formulations for the 2.5D SBM and its coupling with the 2.5D FEM are presented in Sections 4.1.1 and 4.1.2, respectively.

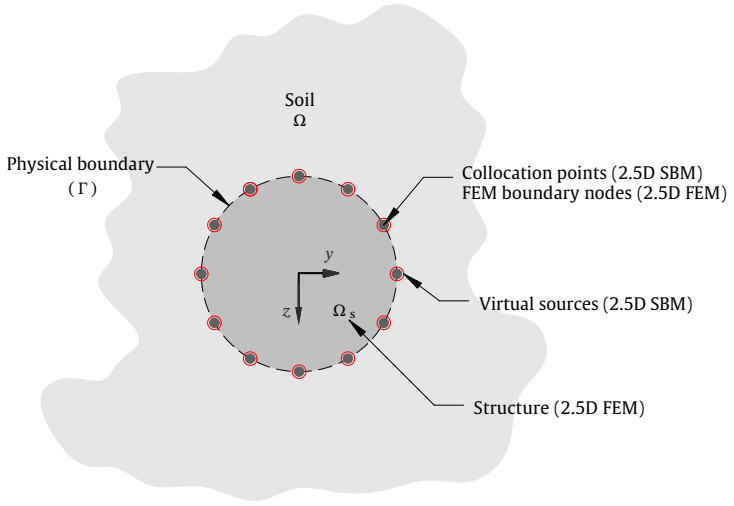

FIGURE 4.1: General description of the proposed 2.5D FEM-SBM methodology. Collocation points and FEM boundary nodes are denoted by grey solid points and virtual forces are denoted by red circles.

4.1.1 The 2.5D singular boundary method (2.5D SBM)

Using a radial basis function interpolation, the displacement and traction of the soil are approximated by the following linear combination of fundamental solutions with respect to N different source points:

$$\bar{\boldsymbol{U}}(\boldsymbol{y}, k_x, \omega) = \sum_{n=1}^{N} \bar{\mathbf{H}}(\boldsymbol{y}, \boldsymbol{x}^n, k_x, \omega)\bar{\boldsymbol{S}}_n(k_x, \omega), \tag{4.1}$$

$$\bar{\boldsymbol{T}}(\boldsymbol{y}, k_x, \omega) = \sum_{n=1}^{N} \bar{\mathbf{H}}^{\tau}(\boldsymbol{y}, \boldsymbol{x}^n, k_x, \omega)\bar{\boldsymbol{S}}_n(k_x, \omega) \tag{4.2}$$

where $\bar{\boldsymbol{U}}(\boldsymbol{y}, k_x, \omega)$ and $\bar{\boldsymbol{T}}(\boldsymbol{y}, k_x, \omega)$ are the displacements and tractions of the soil, respectively, at an arbitrary field point located at $\boldsymbol{y}$, $\bar{\boldsymbol{S}}_n(k_x, \omega)$ is the vector of unknown strengths of the nth virtual source located at $\boldsymbol{x}^n$ (being n the subscript/superscript used in Eqs. (4.1) and (4.2)), and where $\bar{\mathbf{H}}(\boldsymbol{y}, \boldsymbol{x}^n, k_x, \omega)$ and $\bar{\mathbf{H}}^{\tau}(\boldsymbol{y}, \boldsymbol{x}^n, k_x, \omega)$ are the displacement and traction dynamic Green's functions of the soil. For clarity, the wavenumber and frequency dependencies will be omitted in the remaining of the chapter. For longitudinally invariant structures, the solution of the 3D elastodynamic problem can be expressed in the 2.5D domain. This transformation is derived, for example, in [52], and it is not repeated here for the sake of brevity. Accounting for the 2.5D framework, $\boldsymbol{x}^n$ and $\boldsymbol{y}$ are vectors of two elements, while $\bar{\boldsymbol{U}}(\boldsymbol{y})$, $\bar{\boldsymbol{T}}(\boldsymbol{y})$ and $\bar{\boldsymbol{S}}_n$ have three elements, collecting the three components in space of the displacements, tractions and virtual forces, respectively. To evaluate the source strengths, the SBM, as other boundary-type collocation methods, considers the boundary conditions in a set of points, called collocation points, distributed along the boundary. Then, Eqs. (4.1) and (4.2) are used to relate the response at the collocation points with the strengths of all virtual sources. These strengths are finally determined solving the resulting system of equations.

In contrast to the assumptions considered in the MFS, the SBM method assumes that both the collocation and source points are all placed in the same physical boundary, and there is no need of defining a virtual boundary. To avoid the singularities that arise from this assumption when Eqs. (4.1) and (4.2) are employed to evaluate the solution on a set of collocation points geometrically coincident with the set of virtual sources, the SBM method assumes that these equations can be

rewritten as follows [54]

$$\bar{\boldsymbol{U}}(\boldsymbol{y}^m) = \sum_{n=1, n\neq m}^{N} \bar{\mathbf{H}}(\boldsymbol{y}^m, \boldsymbol{x}^n)\bar{\boldsymbol{S}}_n + \bar{\mathbf{H}}_{mm}\bar{\boldsymbol{S}}_m, \tag{4.3}$$

$$\bar{\boldsymbol{T}}(\boldsymbol{y}^m) = \sum_{n=1, n\neq m}^{N} \bar{\mathbf{H}}^{\tau}(\boldsymbol{y}^m, \boldsymbol{x}^n)\bar{\boldsymbol{S}}_n + \bar{\mathbf{H}}^{\tau}_{mm}\bar{\boldsymbol{S}}_m. \tag{4.4}$$

where $\boldsymbol{y}^m$ is the location of the mth collocation point and where $\bar{\mathbf{H}}_{mm}$ and $\bar{\mathbf{H}}^{\tau}_{mm}$ are defined as the origin (or source) intensity factors (OIFs) in the SBM literature. A considerable number of numerical and analytical methods have been used to compute the OIFs for different types of problems. In the following, the expression of the OIFs used in this work is derived.

The OIF associated with the Neumann boundary condition is obtained by applying a subtracting and adding-back technique [89] to Eq. (4.2). The resulting expression can be written as

$$\begin{aligned}
\bar{\boldsymbol{T}}(\boldsymbol{y}^m) = &\sum_{n=1}^{N} \bar{\mathbf{H}}^{\tau}(\boldsymbol{y}^m, \boldsymbol{x}^n)\left(\bar{\boldsymbol{S}}_n - \frac{L_n}{L_m}\bar{\boldsymbol{S}}_m\right) \\
&+ \left[\sum_{n=1}^{N} \frac{L_n}{L_m}\left(\bar{\mathbf{H}}^{\tau}(\boldsymbol{y}^m, \boldsymbol{x}^n) - \mathbf{H}^{\tau}(\boldsymbol{y}^m, \boldsymbol{x}^n)\right)\right]\bar{\boldsymbol{S}}_m \\
&+ \left[\sum_{n=1}^{N} \frac{L_n}{L_m}\left(\mathbf{H}^{\tau}(\boldsymbol{y}^m, \boldsymbol{x}^n) + \mathbf{H}^{\tau,I}(\boldsymbol{x}^n, \boldsymbol{y}^m)\right)\right]\bar{\boldsymbol{S}}_m - \\
&\qquad \left[\sum_{n=1}^{N} \frac{L_n}{L_m}\mathbf{H}^{\tau,I}(\boldsymbol{x}^n, \boldsymbol{y}^m)\right]\bar{\boldsymbol{S}}_m,
\end{aligned} \tag{4.5}$$

where L_i is the half length of the curve between the source points $\boldsymbol{x}^{i-1}$ and $\boldsymbol{x}^{i+1}$, which is approximated in this work as

$$L_i = \frac{d\left(\boldsymbol{x}^{i-1}, \boldsymbol{x}\right)}{2} + \frac{d\left(\boldsymbol{x}, \boldsymbol{x}^{i+1}\right)}{2}, \tag{4.6}$$

where $d(\boldsymbol{x}, \boldsymbol{y})$ refers to the Euclidean distance between points $\boldsymbol{x}$ and $\boldsymbol{y}$.

In Eq. (4.5), the terms $\mathbf{H}^{\tau}(\boldsymbol{y}^m, \boldsymbol{x}^n)$ and $\mathbf{H}^{\tau,I}(\boldsymbol{y}^m, \boldsymbol{x}^n)$ are the Green's functions for the traction of the plane strain elastostatic case in the exterior and interior domains, respectively. These two fundamental solutions are related as follows [61]

$$\begin{cases} \mathbf{H}^{\tau}(\boldsymbol{y}^m, \boldsymbol{x}^n) = -\mathbf{H}^{\tau,I}(\boldsymbol{y}^m, \boldsymbol{x}^n), & \text{if} \quad \boldsymbol{x}^n \neq \boldsymbol{y}^m, \\ \mathbf{H}^{\tau}(\boldsymbol{y}^m, \boldsymbol{x}^n) = \quad \mathbf{H}^{\tau,I}(\boldsymbol{y}^m, \boldsymbol{x}^n), & \text{if} \quad \boldsymbol{x}^n = \boldsymbol{y}^m. \end{cases} \tag{4.7}$$

Defining [54, 88]

$$\mathbf{A}_m = L_m \left[\mathbf{H}^{\tau}(\boldsymbol{y}^m, \boldsymbol{x}^m) + \mathbf{H}^{\tau}(\boldsymbol{x}^m, \boldsymbol{y}^m)\right] \approx \int_{\Gamma_m} \left[\mathbf{H}^{\tau}(\boldsymbol{y}^m, \boldsymbol{x}) + \mathbf{H}^{\tau}(\boldsymbol{x}, \boldsymbol{y}^m)\right] \mathrm{d}\Gamma_m(\boldsymbol{x}), \tag{4.8}$$

where Γ_m is the segment of the boundary with length L_m on which the mth collocation point is located, and where the integration is applied componentwise (i.e. the integration is performed for each component of the matrix) and using the relations given by Eqs. (4.7) and (4.8), Eq. (4.5) can be expressed as

$$\begin{aligned} \bar{\boldsymbol{T}}(\boldsymbol{y}^m) = \sum_{n=1, n\neq m}^{N} \bar{\mathbf{H}}^{\tau}(\boldsymbol{y}^m, \boldsymbol{x}^n)\bar{\boldsymbol{S}}_n - \left[\sum_{n=1, n\neq m}^{N} \frac{L_n}{L_m}\mathbf{H}^{\tau}(\boldsymbol{x}^n, \boldsymbol{y}^m)\right]\bar{\boldsymbol{S}}_m \\ + \frac{1}{L_m}\mathbf{A}_m\bar{\boldsymbol{S}}_m - \left[\sum_{n=1}^{N} \frac{L_n}{L_m}\mathbf{H}^{\tau,I}(\boldsymbol{x}^n, \boldsymbol{y}^m)\right]\bar{\boldsymbol{S}}_m. \end{aligned} \tag{4.9}$$

The previous expression can be further simplified using that

$$\sum_{n=1}^{N} \frac{L_n}{L_m}\mathbf{H}^{\tau,I}(\boldsymbol{x}^n, \boldsymbol{y}^m) = -\frac{1}{L_m}\mathbf{I}, \tag{4.10}$$

where $\mathbf{I}$ is the identity matrix. Eq. (4.10) can be derived following a procedure similar to the one presented, for example, in [88]. The following direct boundary integral equation for the elastostatic plane strain problem for an interior domain is initially considered [54]:

$$\boldsymbol{U}(\boldsymbol{y}) = \int_{\Gamma} \left[\mathbf{H}^{I}(\boldsymbol{x}, \boldsymbol{y})^T\boldsymbol{T}(\boldsymbol{x}) - \mathbf{H}^{\tau,I}(\boldsymbol{x}, \boldsymbol{y})^T\boldsymbol{U}(\boldsymbol{x})\right] \mathrm{d}\Gamma(\boldsymbol{x}), \quad \boldsymbol{y} \in \Omega^I, \tag{4.11}$$

where $\boldsymbol{y}$ is a field point located inside the domain. Substituting the elementary solutions corresponding to rigid-body displacements of the whole body in the direction of each one of the coordinate axes (i.e. $\boldsymbol{U}_1(\boldsymbol{x}) = [1 \quad 0 \quad 0]^T$, $\boldsymbol{U}_2(\boldsymbol{x}) = [0 \quad 1 \quad 0]^T$ and $\boldsymbol{U}_3(\boldsymbol{x}) = [0 \quad 0 \quad 1]^T$ with null tractions, the following expression

can be obtained [54]:

$$\int_{\Gamma} \mathbf{H}^{\tau,I}(\boldsymbol{x},\boldsymbol{y})\,\mathrm{d}\Gamma(\boldsymbol{x}) = -\mathbf{I}, \quad \boldsymbol{y}\in\Omega^I, \tag{4.12}$$

where it has been used that the transpose of the identity matrix is the identity matrix. When the field point $\boldsymbol{y}$ approaches the boundary collocation point $\boldsymbol{y}^m$, Eq. (4.12) can be discretised as follows

$$\int_{\Gamma} \mathbf{H}^{\tau,I}(\boldsymbol{x},\boldsymbol{y}^m)\,\mathrm{d}\Gamma(\boldsymbol{x}) = \sum_{n=1}^{N}\int_{\Gamma_n} \mathbf{H}^{\tau,I}(\boldsymbol{x},\boldsymbol{y}^m)\,\mathrm{d}\Gamma_n(\boldsymbol{x}) \approx \sum_{n=1}^{N} \mathbf{H}^{\tau,I}(\boldsymbol{x}^n,\boldsymbol{y}^m)L_n, \quad \boldsymbol{y}^m\in\Gamma, \tag{4.13}$$

where, as before, Γ_n is the segment of boundary on which the nth collocation point is located and L_n is its length. Therefore, it can be seen from Eqs. (4.12) and (4.13) that

$$\sum_{n=1}^{N} \mathbf{H}^{\tau,I}(\boldsymbol{x}^n,\boldsymbol{y}^m)L_n = -\mathbf{I} \tag{4.14}$$

and Eq. (4.10) can be finally obtained by dividing the previous equation by L_m. Using it Eq. (4.9) can be rewritten as

$$\bar{\boldsymbol{T}}(\boldsymbol{y}^m) = \sum_{n=1,n\neq m}^{N} \bar{\mathbf{H}}^{\tau}(\boldsymbol{y}^m,\boldsymbol{x}^n)\bar{\boldsymbol{S}}_n + \left[\frac{1}{L_m}\mathbf{I} + \frac{1}{L_m}\mathbf{A}_m - \sum_{n=1,n\neq m}^{N}\frac{L_n}{L_m}\mathbf{H}^{\tau}(\boldsymbol{x}^n,\boldsymbol{y}^m)\right]\bar{\boldsymbol{S}}_m. \tag{4.15}$$

The term in brackets can be identified as the OIF for the Neumann boundary conditions defined in Eq. (4.4), i.e.

$$\bar{\mathbf{H}}^{\tau}_{mm} = \frac{1}{L_m}\left[\mathbf{I} + \mathbf{A}_m - \sum_{n=1,n\neq m}^{N} L_n\mathbf{H}^{\tau}(\boldsymbol{x}^n,\boldsymbol{y}^m)\right]. \tag{4.16}$$

In the case of the OIF associated with the Dirichlet boundary condition, the singularity that arises is weak (its order being $\ln r$). Due to this, the OIF associated with the mth collocation point can be directly calculated as an average value of

the fundamental solution over Γ_{m}, i.e. the small portion of the boundary that contains the singular point [54]. In the results presented in this chapter, this portion of the boundary is approximated by the union of two straight segments, i.e. $\Gamma_{\mathrm{m}} \approx [(\boldsymbol{x}^{m-1} + \boldsymbol{x}^{m})/2, \boldsymbol{x}^{m}] \cup [\boldsymbol{x}^{m}, (\boldsymbol{x}^{m} + \boldsymbol{x}^{m+1})/2]$. The integral in Eq. (4.8), which allows to estimate the term $\mathbf{A}_m$, is computed using the same integration scheme.

4.1.2 Coupling between the structure and the soil

The displacements and tractions on the physical boundary Γ can be obtained by considering Eqs. (4.3) and (4.4) for each one of the N collocation points. The obtained systems of equations can be expressed in a matrix form as

$$\bar{\boldsymbol{U}}_b = \bar{\mathbf{H}}_{bb}\bar{\boldsymbol{S}}, \quad \bar{\boldsymbol{T}}_b = \bar{\mathbf{H}}^{\tau}_{bb}\bar{\boldsymbol{S}}, \tag{4.17}$$

where $\bar{\boldsymbol{U}}_b$ and $\bar{\boldsymbol{T}}_b$ are vectors that collect the displacements and tractions at the degrees of freedom of all collocation points, respectively, having a total size $3N$, $\bar{\boldsymbol{S}}$ collects the three components of all virtual forces and $\bar{\mathbf{H}}_{bb}$ and $\bar{\mathbf{H}}^{\tau}_{bb}$ are square matrices containing the displacement and traction dynamic Green's functions that relate all virtual forces with all collocation points degrees of freedom. Due to the procedure presented in the previous section, no singularities arise on the computation of the $\bar{\mathbf{H}}_{bb}$ and $\bar{\mathbf{H}}^{\tau}_{bb}$ matrices. Note that these matrices directly collect the Green's functions along the boundary, and they are different to the typical BEM square matrices, which are determined integrating the displacement and traction Green's functions on the boundary elements [23]. Thus, the global soil stiffness matrix seen by the structure at the FEM boundary nodes can be consequently written as

$$\bar{\mathbf{K}}_s = \boldsymbol{\Phi}\bar{\mathbf{H}}^{\tau}_{bb}\bar{\mathbf{H}}^{-1}_{bb}, \tag{4.18}$$

where $\boldsymbol{\Phi}$ is a matrix that transforms the unknown nodal tractions on the collocation points to nodal forces. This transformation matrix is defined by

$$\boldsymbol{\Phi} = \int_{\Gamma} \mathbf{N}_b^T \mathbf{N}_b \mathrm{d}\Gamma, \tag{4.19}$$

where $\mathbf{N}_b$ is the matrix of the global shape functions that discretises the displacements and the tractions on the boundary to the collocation points. Once the soil stiffness matrix is obtained, it can be introduced to the finite element equilibrium equation of the structure, resulting on [23]

$$\left[\mathbf{K}_0 - \mathrm{i}k_x\mathbf{K}_1 + k_x^2\mathbf{K}_2 + \bar{\mathbf{K}}_s - \omega^2\mathbf{M}\right]\bar{\boldsymbol{U}} = \bar{\boldsymbol{F}}, \tag{4.20}$$

where $\mathbf{K}_0$, $\mathbf{K}_1$, $\mathbf{K}_2$ and $\mathbf{M}$ are the stiffness and mass matrices associated with the 2.5D FEM model of the structure and $\bar{\mathbf{K}}_s$ is the dynamic stiffness matrix of the soil obtained from the 2.5D SBM model. The stiffness of the soil is frequency and wavenumber dependent, while the stiffness and mass matrices related to FEM domain are not. Vectors $\bar{\boldsymbol{U}}$ and $\bar{\boldsymbol{F}}$ collect nodal displacements and forces, respectively, in all the degrees of freedom of the FEM model. In contrast to the formulation of the 2.5D FEM-MFS approach presented in [52], the present method leads to a symmetric matrix of the coupled system.

The displacements on the collocation points $\bar{\boldsymbol{U}}_b$ due to external forces applied to the structure can be determined using Eq. (4.20). Then, the corresponding virtual forces to that displacement field on the boundary can be determined by

$$\bar{\boldsymbol{S}} = \bar{\mathbf{H}}_{bb}^{-1}\bar{\boldsymbol{U}}_b. \tag{4.21}$$

Once the source strengths are computed, the displacement and traction response at an arbitrary field point on the soil can be computed by means of

$$\bar{\boldsymbol{U}}_f = \bar{\mathbf{H}}_{fb}\bar{\boldsymbol{S}}, \quad \bar{\boldsymbol{T}}_f = \bar{\mathbf{H}}_{fb}^{\tau}\bar{\boldsymbol{S}}, \tag{4.22}$$

where $\bar{\mathbf{H}}_{fb}$ and $\bar{\mathbf{H}}_{fb}^{\tau}$ represent the matrices of source-receiver dynamic Green's functions for displacements and tractions, respectively, and $\bar{\boldsymbol{U}}_f$ and $\bar{\boldsymbol{T}}_f$ stand for the displacement and traction at the field point, respectively.

In the present approach, the 2.5D elastodynamic fundamental solutions for a homogeneous full-space can be calculated with the formulation presented by Tadeu and Kausel [82] and extended by [83], while the Green's functions for homogeneous and layered half-space problems can be computed through the EDT toolbox [84], the approach proposed by Noori et al. [85] or the thin-layer method [36], although other alternative method could also be perfectly adequate.

4.2 Verification and computational efficiency assessment

The accuracy of the proposed methodology is exhibited in this section for the two cases presented in Fig. 4.2 (a) and Fig. 4.2 (b). As illustrated, the structures of these two cases consist of a thin cylindrical shell and a solid beam with star-like cross section, respectively, both embedded in a full-space model of the soil. The results obtained using the proposed 2.5D FEM-SBM methodology are compared with those obtained using a 2.5D FEM-MFS [52] approach, only in the case of the thin cylindrical shell, and a 2.5D FEM-BEM [23] approach. In boundary methods, accuracy on the method strongly relies on the accuracy of the boundary condition. Thus, the responses are firstly compared on the physical boundary of the structure in the thin cylindrical shell example. For the sake of certainty, the responses at different field points in the soil have been also compared. The system's symmetry has been taken into account when presenting the boundary results. Therefore, results for only half of the boundary have been presented in the plots.

The comparison between the three numerical approaches is performed in terms of receptances and traction transfer functions (TTF) computed in the frequency domain. In both cases, a harmonic vertical point load is applied on the embedded structure at $x = 0$. The position of the loads within both cross section has been presented in Fig. 4.2 (a) and Fig. 4.2 (b) with a larger grey arrow. In both examples, the soil response has been calculated at three different locations, identified as point A ($x = 0$ m; $y = 2$ m; $z = -2$ m), B ($x = 0$ m; $y = 4$ m; $z = -1$ m) and C ($x = 0$ m; $y = 10$ m; $z = 2$ m). Eq. (3.8) is used to compute the receptances and TTF.

In all calculations carried out in this section, both integrals have been computed numerically with a total of 1025 sampling points consisting of $k_x = 0$ and a logarithmically spaced vector of wavenumbers ranging from 10^{-3} to 10^{2} rad/m. For the 2.5D FEM-BEM three Gaussian points are considered. Results for the receptances and the TTF are presented in dB based on references of 10^{-12} m/N and 1 $(\mathrm{N/m^2})/\mathrm{N}$, respectively.

The results have been obtained considering the following mechanical parameters for the soil: a Young's modulus of 108 MPa, a density of 1800 $\mathrm{kg/m^3}$, a Poisson's

ratio of 0.33 and material damping ratio of 0.05. The comparisons has been performed in the frequency range of 0 to 100 Hz.

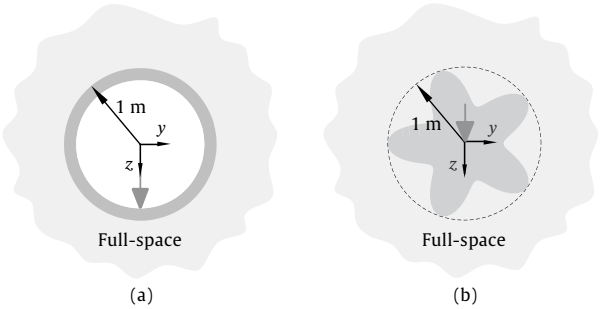

FIGURE 4.2: Geometry of the thin cylindrical shell (a) and the star-like shape (b) used for the comparison between the three methods.

4.2.1 Thin cylindrical shell

The case studied in this section is presented in Fig. 4.2 (a). The cylindrical shell is assumed to have a thickness of 0.1 m and material properties of a common concrete: a Young's modulus of 31000 MPa, a density of 2500 kg/m^3, a Poisson's ratio of 0.2 and a material damping ratio of 0.001. Two meshing strategies have been considered to model this system. In the first strategy, the density of the FEM mesh at the boundary has been selected to have at least 10 nodes per wavelength (NpW) of the soil shear waves at 100 Hz, which is the highest frequency of the range considered. Due to the coupling strategy between the FEM and SBM models adopted in the present methodology, 10 NpW at the boundary also implies 10 collocation points and 10 virtual sources per wavelength. In the second case, up to 24 NpW have been considered. For these two cases, the results on the boundary are compared with the ones obtained by the 2.5D FEM-BEM and 2.5D FEM-MFS approaches. In the 2.5D FEM-MFS approach, the virtual sources are located outside of the soil domain (i.e. inside the structure domain), uniformly distributed in a concentric circumference to the cylindrical shell. The radius of this auxiliary boundary for the virtual sources has been optimised using the method presented in [14], reaching a value of 85 cm. This optimisation is performed accounting for point B as the control point. In the same way as in the proposed SBM methodology, the FEM-MFS approach has been applied considering the same amount of virtual sources as collocation points.

Results for the cylindrical shell case study are presented in Figs. 4.3 and 4.4. Fig. 4.3 compares the receptances and tractions transfer functions along the soil-structure interface obtained using the three mentioned numerical approaches for the case of 10 NpW and considering two excitation frequencies: 10 Hz and 80 Hz. The results are only compared for y and z components since the displacements and tractions in the x direction are equal to zero. A very good match can be observed between the three methods in the receptance plots. However, for both excitation frequencies, some differences arise between the traction transfer functions obtained with the 2.5D FEM-MFS and the two other methods. It is found that these discrepancies are coming from the instability of the 2.5D MFS method at high wavenumbers. Also, the accuracy of the results is sensitive to the control points chosen in the control technique [14] and, consequently, the location of the virtual sources [12, 46]. Fig. 4.4 shows the comparison between the three numerical approaches for the case 24 NpW. The new results show a good agreement between the three methods in all the cases considered. The discrepancies previously observed for the 2.5D FEM-MFS method have been clearly reduced, a result that suggests that a larger number of NpW should be used in this method.

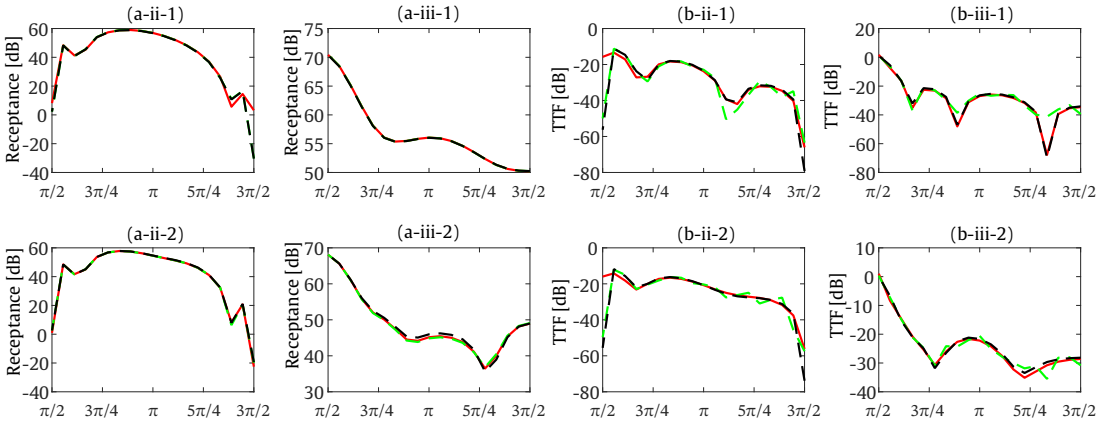

FIGURE 4.3: Receptances (a) and traction transfer functions (b) on the boundary for the case of 10 NpW. Methods: 2.5D FEM-BEM (solid red line), 2.5D FEM-SBM (dashed black line) and 2.5D FEM-MFS (dashed green line). The results are obtained for y (ii) and z (iii) directions at frequencies of 10 Hz (1) and 80 Hz (2).

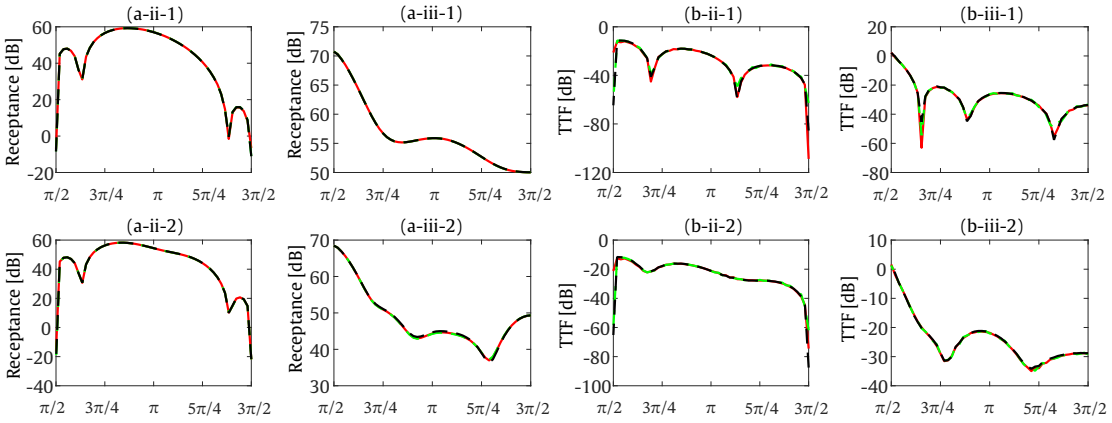

FIGURE 4.4: Receptances (a) and traction transfer functions (b) on the boundary for the case of 24 NpW. Methods: 2.5D FEM-BEM (solid red line), 2.5D FEM-SBM (dashed black line) and 2.5D FEM-MFS (dashed green line). The results are obtained for y (ii) and z (iii) directions at frequencies of 10 Hz (1) and 80 Hz (2).

The accuracy of the presented method is also studied in this section by comparing the soil response obtained using the three numerical approaches previously considered. In this case, the comparison between these methods has been performed computing the soil receptance and traction transfer functions for excitation frequencies ranging from 0 to 100 Hz. The results have been computed for the three field points previously detailed (A, B and C) and considering 10 NpW. The comparisons are presented in Fig. 4.5, which shows a very good agreement between the three methods for all the cases considered. The results presented in this section in terms of boundary and field displacements and tractions confirm that the proposed method can be used to deal with problems that have geometrically smooth soil-structure interfaces.

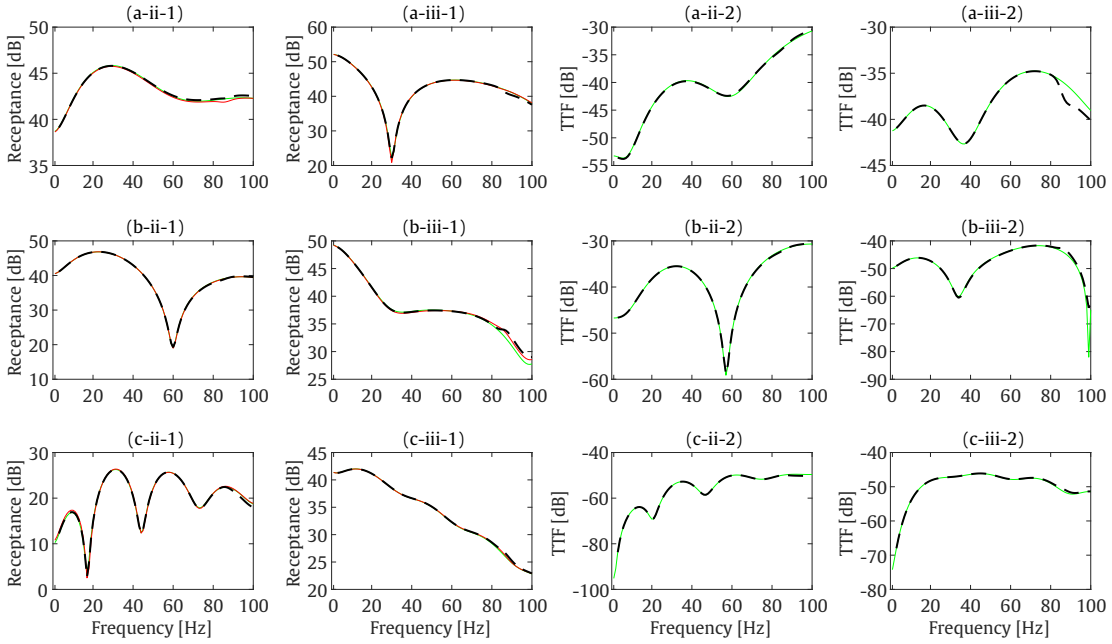

FIGURE 4.5: Receptances (1) and traction transfer functions (2) at the field points A (a), B (b) and C (c) for y (ii) and z (iii) directions and for the case of 10 NpW. Methods: 2.5D FEM-BEM (solid red line), 2.5D FEM-SBM (dashed black line) and 2.5D FEM-MFS (dashed green line).

The accuracy of the method has been also assessed by comparing the results with an analytical solution in terms of receptances and traction transfer function. In this regard, the calculation has been repeated replacing the concrete material by soil material, allowing to compare the proposed method with the cylindrical cavity solution. According to Fig. 4.6, good agreement can be observed between the proposed method and the other presented solutions.

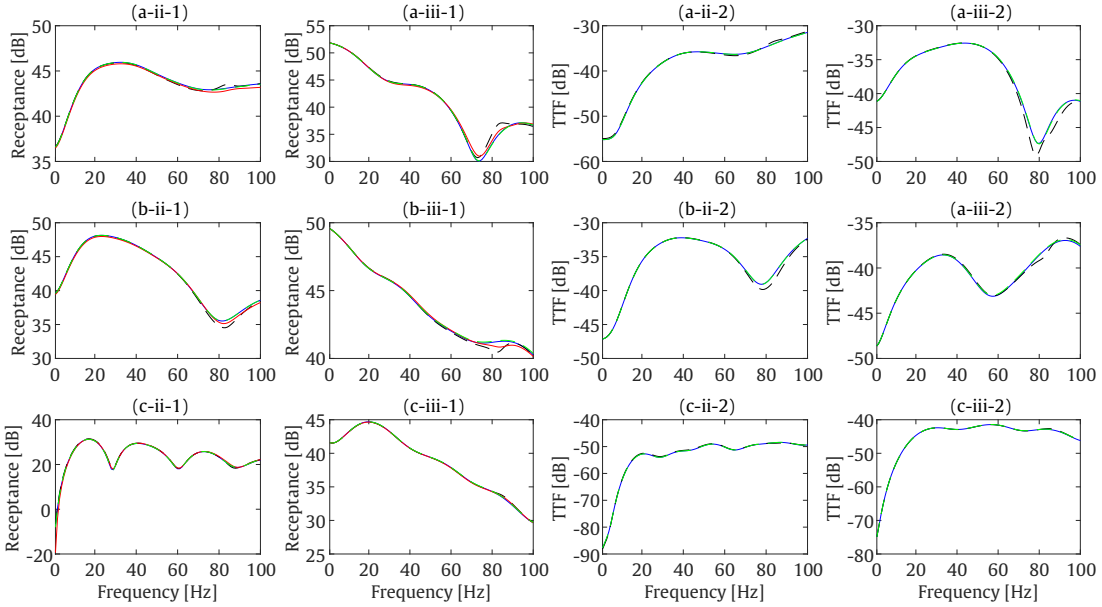

FIGURE 4.6: Receptances (1) and traction transfer functions (2) at the field points A (a), B (b) and C (c) for y (ii) and z (iii) directions and for the case of 10 NpW. Methods: 2.5D FEM-BEM (solid red line), 2.5D FEM-SBM (dashed black line), 2.5D FEM-MFS (dashed green line) and cylindrical cavity solution (solid blue line).

Furthermore, the performance of the 2.5D FEM-SBM approach is evaluated by analysing its convergence with respect to 2.5D FEM-BEM and 2.5D FEM-MFS methods. For this aim, the relative error of the methods is calculated for the case presented in Fig. 4.6 using the equation below:

$$\varepsilon_r = \sqrt{\frac{1}{N_E}\sum_{j=1}^{N_E}\left|\frac{\frac{1}{3}\sum_{i=1}^{3}U_f^{ij} - \frac{1}{3}\sum_{i=1}^{3}U_{fr}^{ij}}{\frac{1}{3}\sum_{i=1}^{3}U_{fr}^{ij}}\right|^2}, \tag{4.23}$$

where i is the index associated with the coordinate components (x, y and z), j is the index associated with the field points and N_E refers to the total number of evaluation points in the model. Moreover, U_f^{ij} and U_{fr}^{ij} represent the receptances on the field points obtained by the selected method and by a reference method, respectively, at the field point j and in the direction i.

The cylindrical cavity solution is adopted as the exact reference solution for the convergence analysis. The receptances at field points A, B and C are computed using the wavenumber sampling previously described. The analysis is carried out

based on a number of NpW ranging from 6 to 20 with unit intervals. As shown in Fig. 4.7, the 2.5D FEM-SBM has a better performance than 2.5D FEM-BEM for low frequency (10 Hz) but worsens for higher ones (80 Hz). 2.5D FEM-MFS has proven a potential to be more accurate than the other methods, but it requires a proper optimisation process [14] to determine the sources location, which is challenging (or even impossible) for complex geometries. In contrast, at high frequencies, more than 10 NpW is required by the 2.5D FEM-SBM approach to achieve approximately 10% error. However, errors achieved by all methods are more than acceptable for engineering applications.

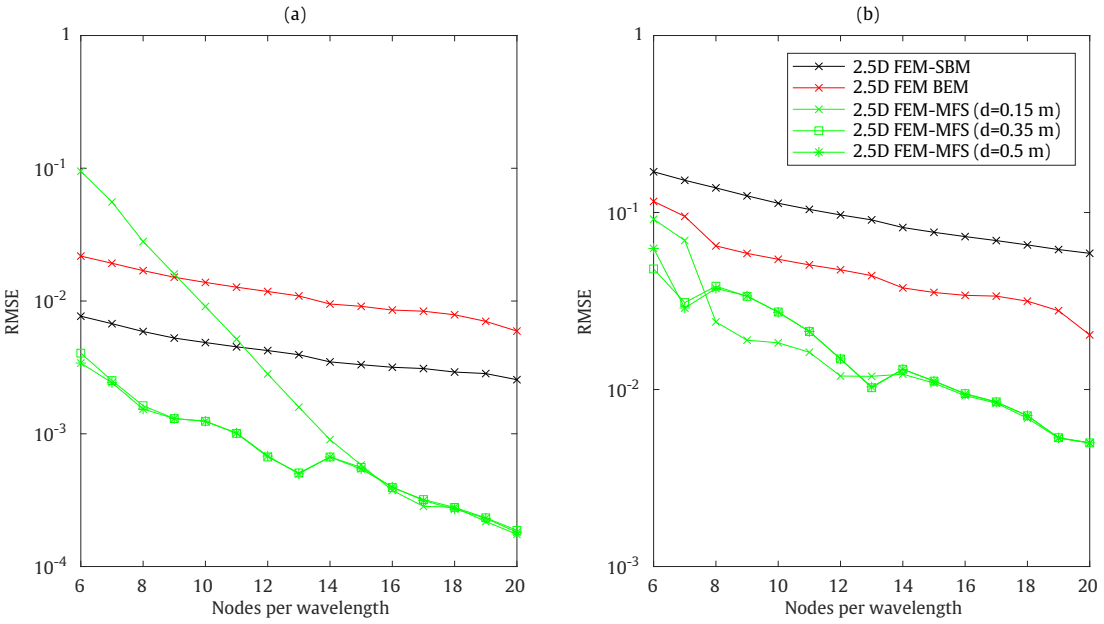

FIGURE 4.7: Convergence analysis for receptances averaged at the three fields points A, B and C and at 10 Hz (a) and 80 Hz (b).

4.2.2 Star-like shape structure

To demonstrate the generality of the proposed approach, the accuracy of the method is investigated in this section for the case of a solid beam with a star-like cross section embedded in a full-space, as illustrated in Fig. 4.2 (b). The parametric representation of the star-like shape boundary geometry is

$$y = \frac{1}{m^2}(m^2 + 2m + 2 - 2(m+1)\cos(m\phi))\cos(\phi), \tag{4.24}$$
$$z = \frac{1}{m^2}(m^2 + 2m + 2 - 2(m+1)\cos(m\phi))\sin(\phi),$$

where m represents the shape factor ($m = 5$ is considered in this study) and ϕ denotes the angular coordinate of the polar coordinate system. Two different materials have been considered for the structure in order to perform two comparisons between the proposed 2.5D FEM-SBM method and the 2.5D FEM-BEM method. While in the first comparison the star-like structure is considered to be solid concrete with the same properties of the cylindrical shell presented in the previous section, in the second comparison its mechanical properties are assumed to be the same as those considered for the surrounding soil. Since in this second calculation example both the structure and the soil have the same mechanical properties, the responses obtained by the proposed method can be also compared to the fundamental solution of a homogeneous full-space [82]. For both cases, the comparisons are presented at the same three field points that have been considered in the previous section (field points A, B and C). The results have been computed considering 10 NpW and these points are distributed uniformly along the perimeter of the boundary.

Fig. 4.8 presents a comparison between the results obtained by the novel 2.5D FEM-SBM and the 2.5D FEM-BEM approaches for the case of the concrete star-like structure. The results show that the receptances computed by the proposed method at points A, B and C agree reasonably well with those obtained by the 2.5D FEM-BEM approach. Discrepancies up to 0.3 dB are found at the near-field (see Fig. 4.8 (a-ii)).

Fig. 4.9 shows the results obtained using the 2.5D FEM-SBM approach for the case where both the structure and the soil have the same mechanical properties. In the case of the receptances, these results are compared with those obtained using the 2.5D FEM-BEM approach and using the elastodynamic fundamental solutions of a homogeneous full-space. For the traction transfer functions, the 2.5D FEM-SBM results are only compared to the fundamental solutions. Good agreements are observed between the 2.5D FEM-SBM results and the results obtained with the other approaches. Only small discrepancies are observed in traction transfer functions in the far-field (see Fig. 4.9 (c-ii-2)), especially at low frequencies. Therefore, from the results obtained in these two examples, it can be interpreted that the proposed method not only is practical for structures with simple geometries, but also provides good accuracy in cases where geometrically complicated structures are involved.

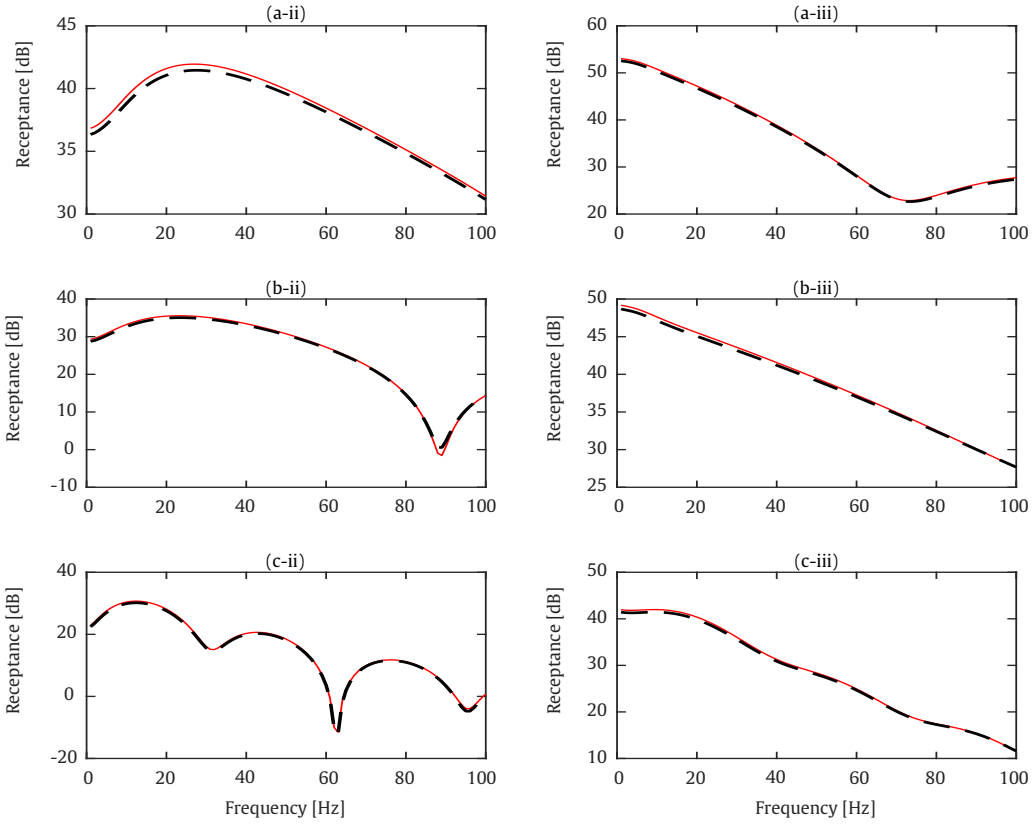

FIGURE 4.8: Receptances at the field points A (a), B (b) and C (c) for y (ii) and z (iii) directions. Methods: 2.5D FEM-BEM (solid red line), 2.5D FEM-SBM (dashed black line).

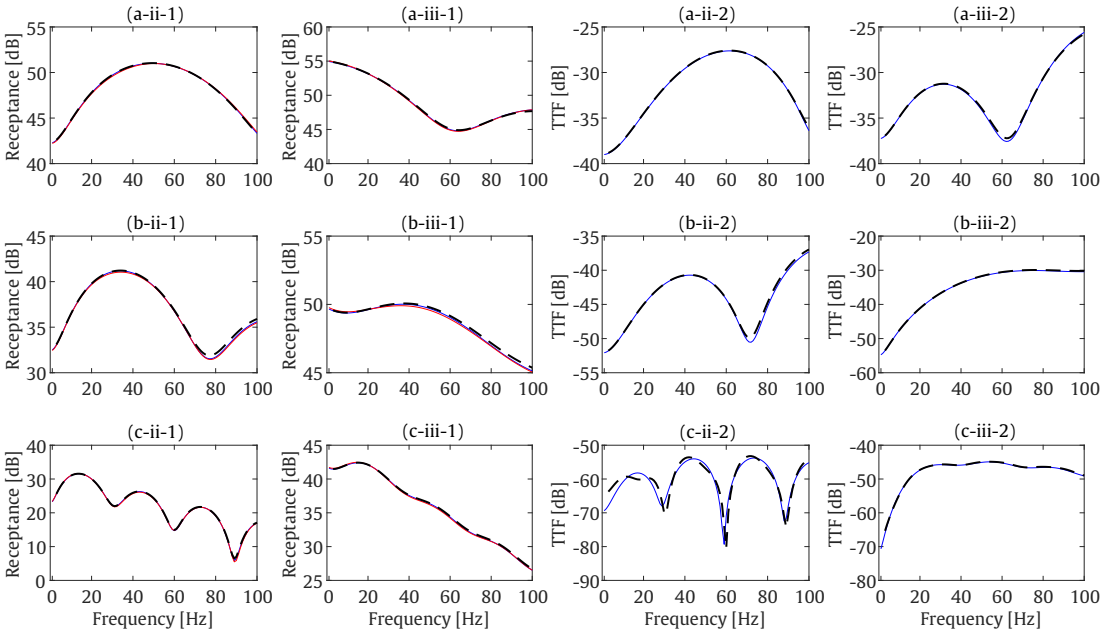

FIGURE 4.9: Receptances (1) and traction transfer functions (2) at the field points A (a), B (b) and C (c) for y (ii) and z (iii) directions. Methods: 2.5D FEM-BEM (solid red line), 2.5D FEM-SBM (dashed black line) and fundamental solution (solid blue line).

4.2.3 Comparison of the relative error between the methods

In the previous sections, the results obtained with the 2.5D FEM-SBM method have been compared to the ones obtained with the 2.5D FEM-BEM and the 2.5D FEM-MFS approaches for two different case studies. Even though the accuracy of the presented method could be inferred from these results, it is desirable to investigate it using more robust indicators. In this section, the accuracy of the new approach is assessed by evaluating the relative errors between all three numerical approaches with respect to the displacement and traction Green's functions on the boundary in the wavenumber-frequency domain. The comparison is performed considering the case of the thin cylindrical shell embedded in a full-space presented in Section 4.2.1, considering a vertical load at the bottom. It is worth mentioning that the term $\mathbf{A}$ presented in Eq. (4.8) has not been used in the calculations described in this section, since this term does not provide significant benefits in terms of accuracy of the results in the case of smooth geometries. The relative errors associated with the displacement and traction Green's functions along the

boundary are computed using the following expressions

$$\varepsilon_r = \sqrt{\frac{1}{N}\sum_{j=1}^{N}\left|\frac{\frac{1}{3}\sum_{i=1}^{3}\bar{U}_b^{ij} - \frac{1}{3}\sum_{i=1}^{3}\bar{U}_{br}^{ij}}{\frac{1}{3}\sum_{i=1}^{3}\bar{U}_{br}^{ij}}\right|^2}, \qquad \varepsilon_r^{\tau} = \sqrt{\frac{1}{N}\sum_{j=1}^{N}\left|\frac{\frac{1}{3}\sum_{i=1}^{3}\bar{T}_b^{ij} - \frac{1}{3}\sum_{i=1}^{3}\bar{T}_{br}^{ij}}{\frac{1}{3}\sum_{i=1}^{3}\bar{T}_{br}^{ij}}\right|^2}, \tag{4.25}$$

where i is the index associated with the coordinate components (x, y and z), j is the index associated with the collocation points and N refers to the total number of collocation points in the model. Moreover, $\bar{U}_b^{ij}$ and $\bar{U}_{br}^{ij}$ represent the displacement Green's functions in the wavenumber-frequency domain on the boundary obtained by the selected method and by a reference method, respectively, at the collocation point j and in the direction i. Analogously, $\bar{T}_b^{ij}$ and $\bar{T}_{br}^{ij}$ represent the traction Green's functions in the wavenumber-frequency domain on the boundary obtained by the selected method and by a reference method, respectively, at the collocation point j and in the direction i. Both errors have been computed for frequencies between 0 and 100 Hz, for wavenumber values from 0.1 rad/m to 10 rad/m, and considering 10 or 24 NpW.

The color map plots presented in Fig. 4.10 show the relative errors obtained when 10 NpW are considered. For clarity, the errors are presented on a logarithmic scale. Also, receptances and traction transfer functions corresponding to these color maps are also presented, where the relative errors between the methods have been computed using the same expressions as before but replacing the displacement and traction Green's functions with the corresponding transfer function. The results show that the displacement and traction Green's functions obtained by the proposed method converge well to those obtained using the 2.5D FEM-BEM approach. Color map plots show that the discrepancies between the 2.5D FEM-MFS and the 2.5D FEM-BEM methods at large wavenumbers are significant for almost all the range of frequencies, although these discrepancies have a small effect on the receptances and traction transfer functions. The relative errors between the 2.5D FEM-SBM and the 2.5D FEM-BEM approaches associated with the displacements are smaller than the errors between the 2.5D FEM-MFS and the 2.5D FEM-BEM approaches at frequencies between 20 Hz and 80 Hz. In contrast, the opposite trend is observed below 20 Hz and above 80 Hz. However, larger

discrepancies are observed in the relative error associated with the traction Green's functions. In this case, the relative errors between the 2.5D FEM-SBM and the 2.5D FEM-BEM approaches are considerably smaller than those found between the 2.5D FEM-MFS and the 2.5D FEM-BEM.

The results previously presented in Section 4.2.1 showed that the accuracy of the 2.5D FEM-SBM and 2.5D FEM-MFS can be significantly improved by considering a larger number of NpW. Therefore, it is expected that an increase in the number of collocation points should result in a decrease of the relative error between the presented meshless methods and the 2.5D FEM-BEM approach. This hypothesis is confirmed by the results presented in Fig. 4.11, in which the relative errors between the methods have been calculated considering 24 NpW instead of 10. It can be observed that displacement results exhibit lower discrepancies between the methods, although the accuracy enhancement provided by the use of 24 NpW is not high enough to justify a mesh refinement such as this. The same tendency can be observed for the traction results, for which such a refinement is found to be more important to ensure the 2.5D FEM-MFS proper performance.

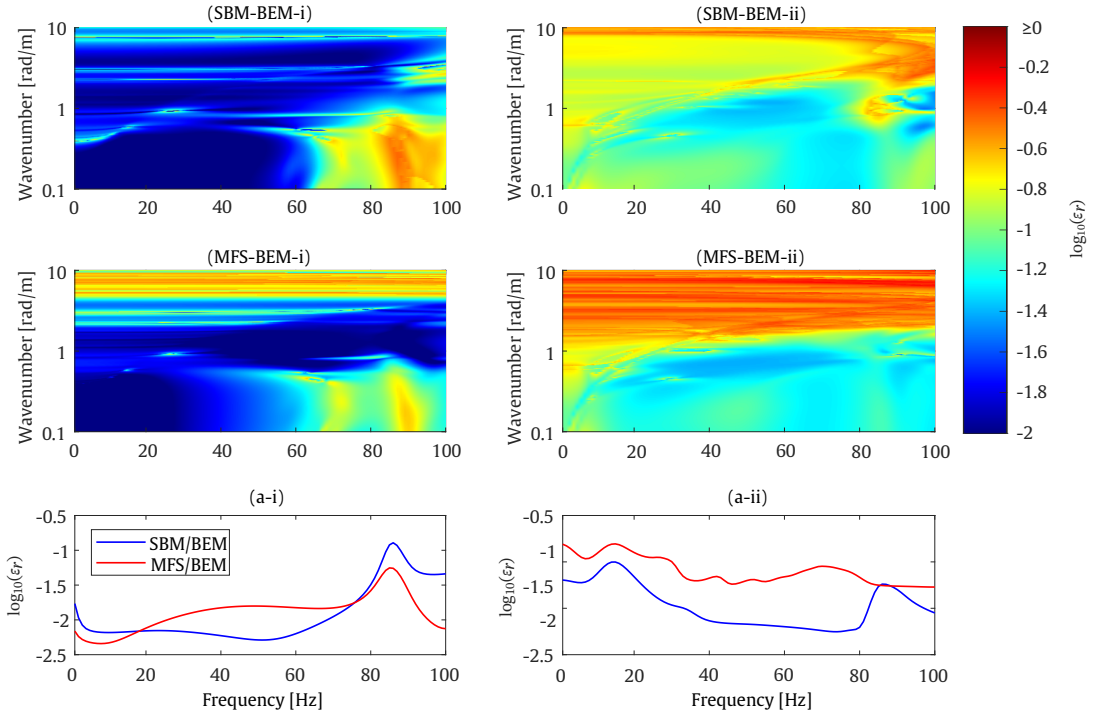

FIGURE 4.10: Relative error of the displacement Green's functions (i) and traction Green's functions (ii) on the boundary considering 10 NpW. Plots denoted by (a-i) and (a-ii) represent the relative error in terms of receptances and traction transfer functions, respectively. SBM/BEM refers to the relative error when the selected method is the 2.5D FEM-SBM and the reference is the 2.5D FEM-BEM approach and MFS/BEM refers to the relative error when the selected method is the 2.5D FEM-MFS and the reference is the 2.5D FEM-BEM one.

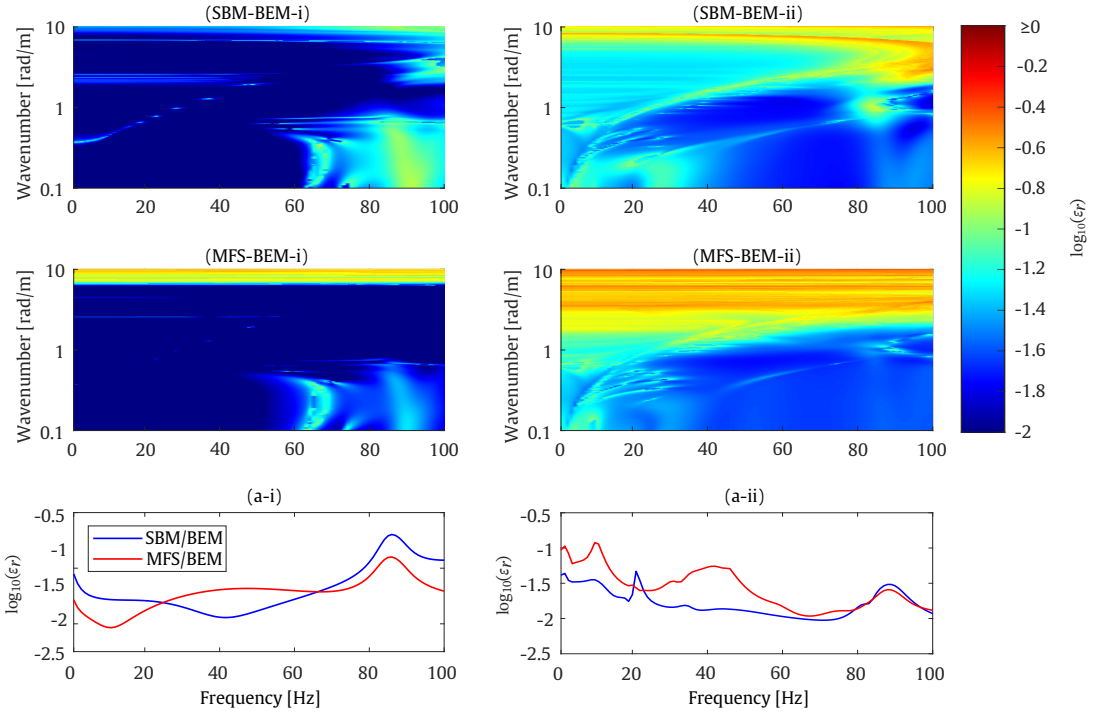

FIGURE 4.11: Relative error of the displacement Green's functions (i) and traction Green's functions (ii) on the boundary considering 24 NpW. Plots denoted by (a-i) and (a-ii) represent the relative error in terms of receptances and traction transfer functions, respectively. SBM/BEM refers to the relative error when the selected method is the 2.5D FEM-SBM and the reference is the 2.5D FEM-BEM approach and MFS/BEM refers to the relative error when the selected method is the 2.5D FEM-MFS and the reference is the 2.5D FEM-BEM one.

4.2.4 Investigation of the computational efficiency of the method

In this section, the proposed 2.5D FEM-SBM method is compared to the 2.5D FEM-BEM and 2.5D FEM-MFS approaches in terms of computational efficiency. The comparison is performed in the framework of the thin cylindrical shell case study presented in Section 4.2.1. All three methodologies have been implemented in MATLAB and have been executed using a single core of a high-performance cluster with 2 GHz Intel® Xeon® Gold 6138 CPU (with 40 cores). The computational time of each one of these methods is evaluated for two different case scenarios. In the first case, the soil responses are computed in a single field point, for a specific frequency, for 1024 wavenumber values and considering different values for the number of NpW: 6, 10, 17 and 24. In the second case, the soil responses are

computed for one frequency, 1024 wavenumber samples, 24 NpW and considering different values for the number of field points: from 5 to 200. The computational time spent in both defined cases is shown in terms of the percentage with respect to the computational time of the 2.5D FEM-BEM.

The results obtained in the first case are indicated in Table. 4.1. It can be observed that the computational time spent by the 2.5D FEM-MFS and the 2.5D FEM-SBM approaches are averagely 61.5% and 77% of the computational time spent by the 2.5D FEM-BEM method.

The computational times obtained in the second case are presented in Table. 4.2. In this case, by increasing the number of field points points from 5 to 200, the computational time of the 2.5D FEM-MFS and 2.5D FEM-SBM approaches with respect to the the computational time of the 2.5D FEM-BEM method decrease significantly. This result shows the clear benefit that the use of 2.5D FEM-MFS or 2.5D FEM-SBM approaches has when the response of a large number of evaluation points is required.

From the results presented in Tables 4.1 and 4.2, it can be concluded that the 2.5D FEM-MFS and the 2.5D FEM-SBM approaches can be much more efficient than the 2.5D FEM-BEM approach in many practical scenarios. The comparison also shows that the 2.5D FEM-SBM approach is slightly slower than the 2.5D FEM-MFS approach. This extra computational time spent by the 2.5D FEM-SBM approach comes from the evaluation of the OIF terms.

Number of NpW	6	10	17	24
Time: 2.5D FEM-MFS [%]	63	60	63	60
Time: 2.5D FEM-SBM [%]	78	77	76	77

TABLE 4.1: Computational time in percentage of the two methods for different number of NpW.

Number of field points	5	25	60	100	160	200
Time: 2.5D FEM-MFS [%]	64	47	32	24	17	15
Time: 2.5D FEM-SBM [%]	81	61	41	31	22	19

TABLE 4.2: Computational time in percentage of the two methods for different number of field points.

4.3 Application to the assessment of railway-induced ground-borne vibrations

4.3.1 Model description

The numerical implementation and accuracy of the proposed 2.5D FEM-SBM have been fully addressed in the previous sections. The aim of this section is to present an application example of the 2.5D FEM-SBM approach to the assessment of tunnel-soil transfer functions required for railway-induced ground-borne vibration assessment. With the purpose of depicting the potentialities of the proposed method, two examples of underground railway tunnels are presented: a circular tunnel and a cut-and-cover tunnel. For the circular tunnel case, a tunnel with an external radius of 3 m and a wall thickness of 0.3 m embedded in a layered half-space is considered. The system is illustrated in Fig. 4.12a. The centre of the tunnel is located at a depth of 9 meters from the ground surface and the structure is excited by two harmonic point loads symmetrically applied on the tunnel invert and separated 1.5 meters. The response of the soil has been calculated at two different evaluation points (identified as A and B), one located on the ground surface and the other within the soil. For the cut-and-cover tunnel case, a tunnel with a length and width of 6 m, embedded in a layered half-space is presented. The geometry of the system is shown in Fig. 4.12b. The centre of the tunnel is located at a depth of 5 meters from the ground surface and the structure is excited by two harmonic point loads symmetrically applied on the tunnel invert and separated 1.5 meters. The response of the soil has been obtained at three different evaluation points (identified as A, B and C), two located on the ground surface and the other within the soil. As before, in these examples it is assumed that the evaluation points and the applied point loads are all always in the same cross-section. The geometry of both cases and the locations of the considered evaluation points are also presented in Fig. 4.12. The mechanical properties of the tunnel lining and the soil are presented in Table. 4.3, where the only difference between both cases is the thickness of the first soil layer. The FEM mesh, the position of the collocation/source points and the position of the two forces associated with the circular and cut-and-cover railway tunnels are specified in Figs. 4.13 and 4.14, respectively. Since the frequency range of interest for railway-induced vibration problems is 1-80 Hz [86], the application of the proposed method is evaluated up

to 100 Hz. For the circular tunnel case, two FEM meshes have been created to deal with this problem, having 6 and 8 NpW (considering a maximum frequency of 100 Hz, as mentioned) along the boundary. For the cut-and-cover example, only a FEM mesh with 10 NpW along the boundary is considered.

Type	E [MPa]	ρ [kg/m^3]	ν	Thickness [m]	Damping
Tunnel	31000	2500	0.2	0.3	0.001
Soil layer 1	50	1900	0.3	4 / 3	0.05
				Figs. (4.12a / 4.12b)	
Soil layer 2	180	1980	0.3	9	0.05
Soil layer 3	400	2050	0.3	∞	0.05

TABLE 4.3: Mechanical parameters of the tunnel and the layered soil.

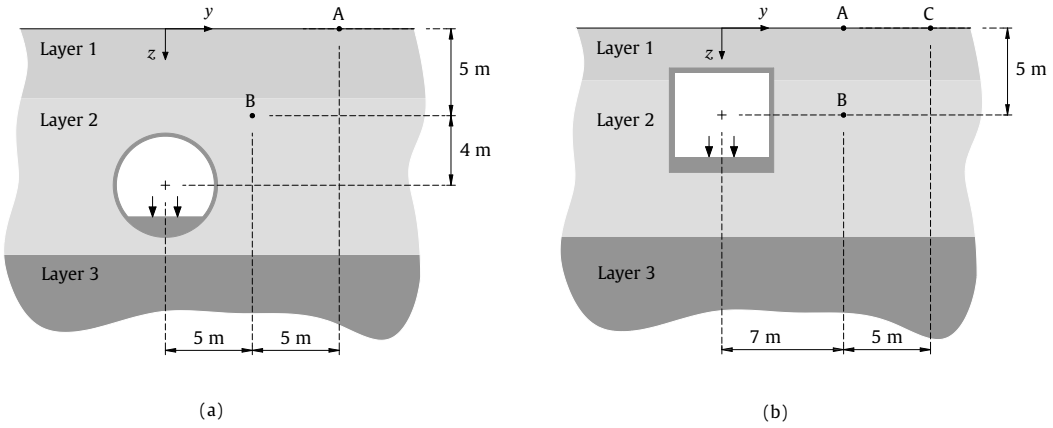

FIGURE 4.12: Geometry of the problem: Circular tunnel (a), Cut-and-cover tunnel (b). The position of the forces and the position of the receivers are also presented.

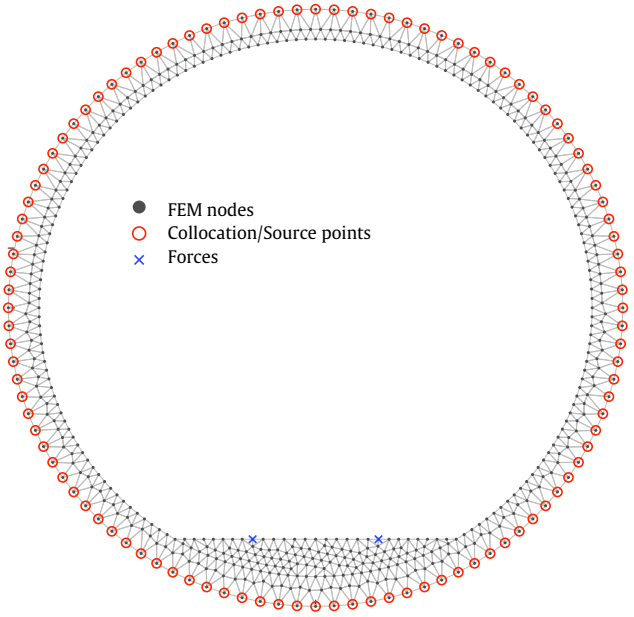

FIGURE 4.13: FEM mesh for 6 NpW along the boundary. The FEM nodes, the collocation/source points and the position of the applied forces used in the case study are also included.

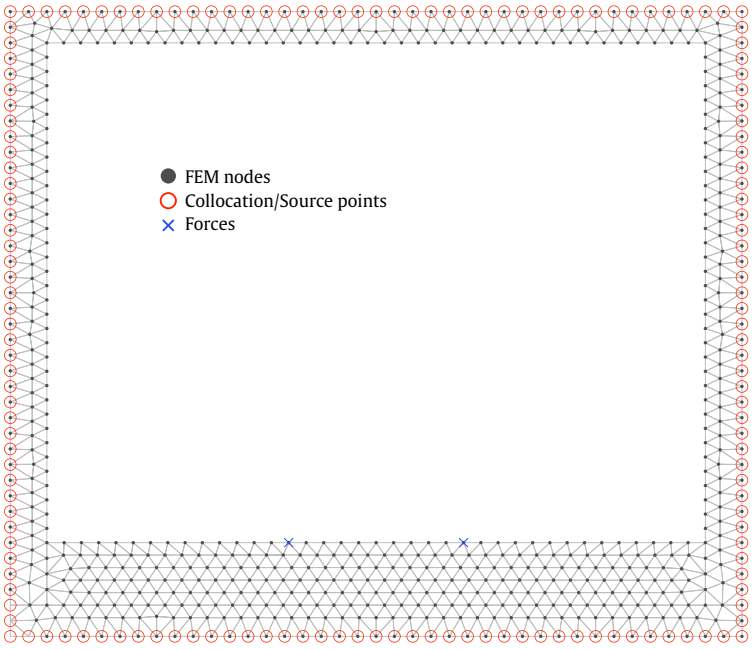

FIGURE 4.14: FEM mesh for 10 NpW along the boundary. The FEM nodes, the collocation/source points and the position of the applied forces used in the case study are also included.

4.3.2 Results

In this section, the response of the tunnel-soil models previously described is presented. For the circular tunnel example, the results are presented in terms of response at the evaluation points A and B (Fig. 4.12a) for each one of the three numerical methods compared in previous sections: 2.5D FEM-SBM, 2.5D FEM-MFS and 2.5D FEM-BEM. For the 2.5D FEM-BEM, a mesh with 6 NpW along the boundary has been used. For 2.5D FEM-SBM and 2.5D FEM-MFS, both 6 and 8 NpW meshes (referred to as 6NpW and 8NpW, respectively) are considered. For the cut-and-cover tunnel example, the response obtained with the proposed approach is compared to the one obtained using the 2.5D FEM-BEM approach at evaluation points A, B and C (Fig. 4.12b) and considering 10 NpW along the boundary. The longitudinal wavenumber has been sampled using a logarithmic sampling from 0 to 100 rad/m with 129 points. In the computations using the 2.5D FEM-BEM, two Gaussian points have been used in this case. The layered soil Green's functions are computed using the EDT toolbox [84], considering for the wavenumber associated with the y direction a logarithmic sampling in a range from 10^{-7} rad/m and 10^{3} rad/m with 2048 samples. Convergence tests showed that the number of samples was sufficient to obtain accurate results. In what follows, the soil displacement response caused by the action of the two unit point loads is referred to as receptance.

Fig. 4.15 shows the receptance at the evaluation points A and B and for y and z components.

Based on the results shown in Fig. 4.15, a generally good agreement is observed between the responses obtained with the proposed approach and those obtained using the other two methods for the case of 6 NpW. Comparing the results obtained with the 2.5D FEM-SBM with 6 NpW and 8 NpW at the maximum frequency, an adequate convergence of the method is observed. Results start to differ just at 60 Hz, which is consistent with the fact that, above this frequency, the number of NpW is going below 10 for the 6 NpW case. Regarding 2.5D FEM-MFS, the method shows larger discrepancies between 6 NpW and 8 NpW cases at large frequencies with respect to the 2.5D FEM-SBM. Comparing the results between the 2.5D FEM-SBM and the 2.5D FEM-BEM, both with 6 NpW, discrepancies up to 0.8 dB can be observed. These small discrepancies assure very accurate predictions of the railway-induced ground-borne vibrations.

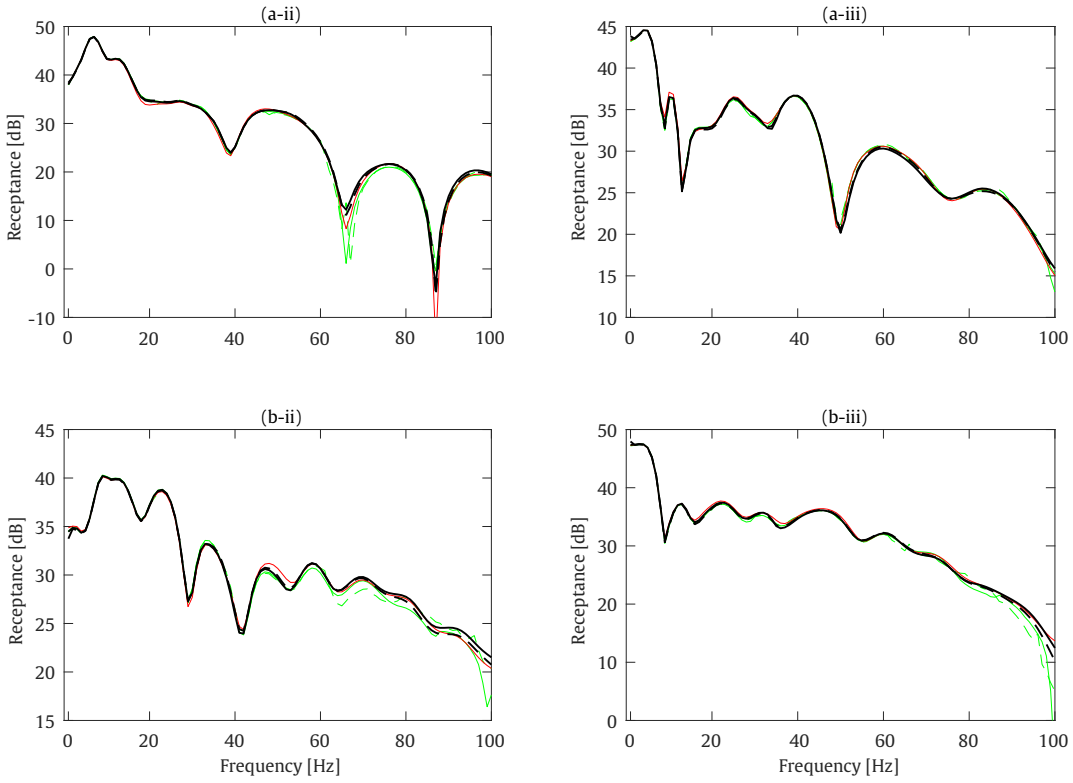

FIGURE 4.15: Receptances at points A (a) and B (b) for y (ii) and z (iii) directions. Methods: 2.5D FEM-BEM 6NpW (solid red line), 2.5D FEM-SBM 6NpW (solid black line), 2.5D FEM-MFS 6NpW (solid green line), 2.5D FEM-SBM 8NpW (dashed black line) and 2.5D FEM-MFS 8NpW (dashed green line).

Fig. 4.16 presents the receptance at the evaluation points A, B and C and for y and z components. As in the circular tunnel case, a very good agreement is observed between the response computed by the proposed method and the one obtained using the 2.5D FEM-BEM approach. This agreement is obtained for all the range of frequencies of interest, indicating that the use of 10 NpW in the computation is a suitable choice. Some small discrepancies (up to 1.8 dB) are only observed around 55 Hz and for some of the receptances in the y direction. The larger discrepancies in comparison with the circular railway tunnel example are due to the higher complexity of the current geometry. In the other field points and directions, differences up to 1 dB are observed between the considered methods. The mentioned discrepancies are acceptable for railway-induced ground-borne vibration problems.

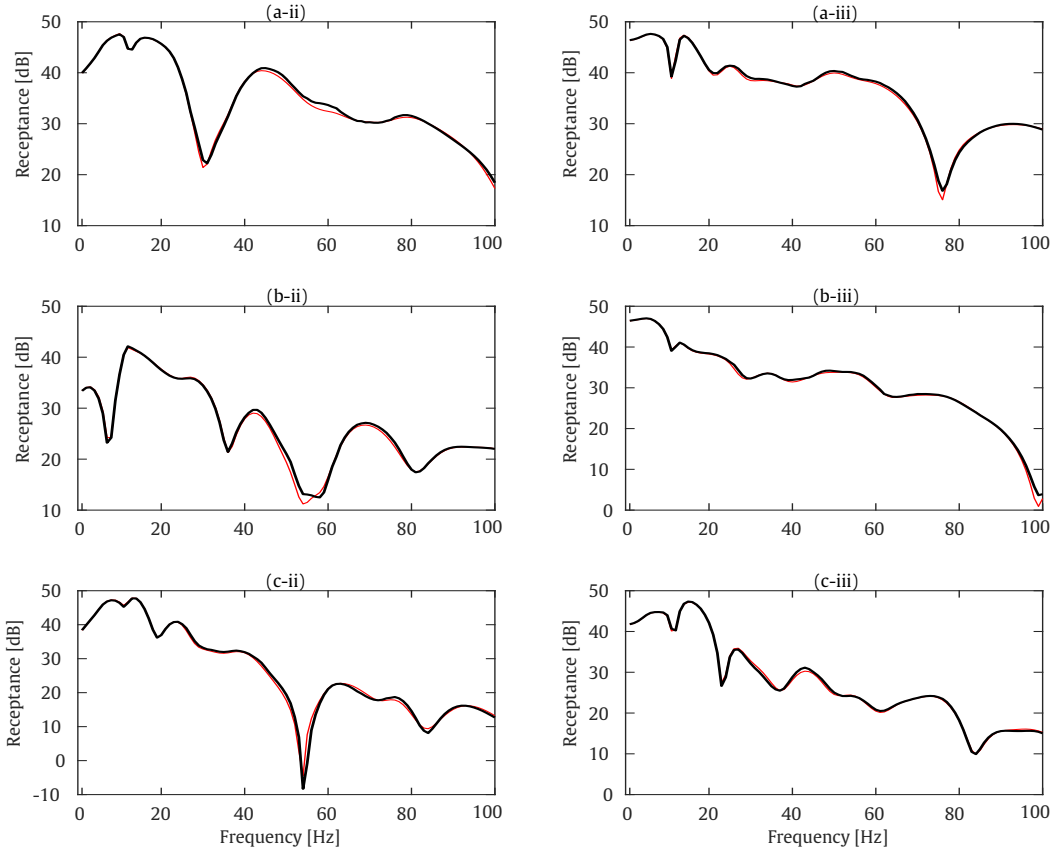

FIGURE 4.16: Receptances at points A (a), B (b) and C (c) for y (ii) and z (iii) directions. Methods: 2.5D FEM-BEM (solid red line) and 2.5D FEM-SBM (solid black line),

4.4 Conclusions

In this chapter, a novel numerical methodology to deal with longitudinally invariant SSI problems is proposed. This approach works in the wavenumber-frequency domain and models the structure with the FEM and the soil with the SBM. This new approach has been compared with two previously well-established approaches: the 2.5D FEM-BEM [23] and 2.5D FEM-MFS [52]. In general, the results show that the novel approach provides higher accuracy than 2.5D FEM-MFS with almost similar computational time. With respect to the 2.5D FEM-BEM, similar accuracy is reached with larger computational efficiency. The particular merits of the proposed approach are listed below:

- The approach combines the benefits of the FEM and the SBM, providing

the capability for dealing with detailed structures (FEM) and the efficient treatment of the wave propagation in the soil (SBM).

- The method is studied in the framework of simple (a thin cylindrical shell) and more complex (a star-like beam structure) smooth geometries of the soil-structure interface, showing that the proposed method not only is practical for structures with geometrically simple boundaries but also it has reasonable accuracy in cases where the interface is more intricate.

- The convergence analysis carried out has pointed out that the proposed method has an acceptable performance when compared to the other presented approaches at low frequencies while at high frequencies more than 10 NpW are required to achieve an acceptable level of accuracy.

- Comparing with the 2.5D FEM-BEM methodology, the computational efficiency of the novel 2.5D FEM-SBM is a great advantage of the method, while exhibiting a similar accuracy considering the same number of NpW. Moreover, using SBM strongly simplifies the formulation and implementation of the method.

- Comparing with the 2.5D FEM-MFS approach, 2.5D FEM-SBM is more robust since no virtual boundary is required. This is of special importance for problems with complex geometries for the SSI boundary. The overlapping between collocation and source points also allows the method to couple a structure just on the soil surface and keep using half-space Green's functions, a capability that the 2.5D FEM-MFS does not have. This can be used to deal with the SSI of several structures such as at-grade railway tracks and roads.

- Two examples of application for the novel method in underground railway-induced vibration assessment has been presented for a realistic scenario, showing the adequacy of the method for dealing with these kinds of problems.

To conclude, the 2.5D FEM-SBM is found to be an adequate prediction tool for the SSI problems since it inherits some of the key advantages of the BEM and of the MFS while keeping the versatility presented by the FEM.

This chapter has shown that the SBM is a suitable alternative for modelling the propagation of elastic waves in a soil. However, the presented results have shown

that, despite being much more computationally efficient than the BEM, the method is less efficient than the MFS, as the later does not require to determine the OIFs associated with the considered boundary conditions. In contrast, it has also been discussed that the SBM is much more robust than the MFS, because it does not require to define a virtual boundary, a definition that can be very challenging for cases with complicated geometries. Both results suggest that if a methodology was capable of combining the key features of SBM with those of MFS, it would be an even better alternative for the type of problems that have been addressed in this chapter. This will be the objective of the next chapter, in which the SBM and the MFS are combined to develop a hybrid SBM-MFS methodology that will inherit the computational efficiency of the MFS and also the accuracy and robustness of the SBM.

Chapter 5

A 2.5D hybrid SBM-MFS methodology to deal with elastic wave propagation problems

In this chapter, a novel 2.5D hybrid SBM-MFS approach in the frequency domain to simulate elastic wave propagation through a soil medium is presented. The methodology is mainly developed to address radiation or scattering problems involving complex boundary geometries of the structure, being the complex parts of shape modelled with the SBM and the smooth parts with the MFS. The method is studied in the framework of three case studies: a circular shape, a partially circular shape and a square geometry, all embedded in a homogeneous full-space. These three examples are selected to assess the accuracy and robustness of the proposed hybrid method. Once it is properly used, the method is found to be inheriting the accuracy of the MFS while keeping the robustness associated with the SBM on dealing with the more complex geometries. Three features can be mentioned as the main advantages of the proposed method with respect to the SBM or the MFS. Firstly, for problems with complex geometries involving edges, the hybrid method is more accurate than the MFS. Secondly, the computational efficiency of the proposed approach overcomes the one developed by the SBM. Accordingly, the new method is significantly faster than the BEM. Lastly, the hybrid approach naturally mitigates the effect of fictitious eigenfrequencies, a feature that neither the SBM nor the BEM posses.

This chapter is organised as follows. In Section 5.1, the proposed formulation of

the novel 2.5D SBM-MFS method is presented in detail. Section 5.2 presents an assessment of the accuracy of the methods in the context of the three examples previously mentioned. For the sake of presenting a detailed assessment of the proposed method, the response of the soil in each example is compared in terms of accuracy and robustness to the results obtained by the 2.5D MFS, the 2.5D SBM and the 2.5D BEM. Generally, two types of virtual sources distributions are considered and assessed in all the examples: regular, following an auxiliar boundary with the same shape of the physical one, and random, distributed all along the cavity space. To ensure the validity of the proposed method for the whole frequency range of interest, a comparison is also carried out in terms of frequency spectra. Afterwards, in Section 5.3, the computational efficiency of the hybrid method is assessed and then compared to the ones of the alternative methods considered, (2.5D MFS and the 2.5D SBM) in the context of the first calculation example. Finally, the effect of the fictitious eigenfrequencies on the accuracy of the presented methods is discussed in Section 5.4.

5.1 Numerical method formulation

The proposed 2.5D hybrid SBM-MFS methodology is an approach designed to deal with elastic wave propagation problems, when the boundary of the structure involved is (or it might be considered to be) longitudinally invariant. The methodology is useful for the structures that involve both complicated and smooth geometries, where the complex parts of the shape are modelled with the SBM and the smooth parts are addressed with the MFS. As before, the system is assumed to be invariant in the x direction. A general description of the proposed methodology is illustrated in Fig. 5.1. The figure shows a distribution example of the MFS and SBM virtual sources in the proposed methodology. The methodology considers two sets of virtual sources. The first set is distributed within the physical boundary (Γ), while the other virtual sources are located outside the domain Ω (inside the cavity space). In the following, the formulation of this novel approach is outlined in detail. In the same manner as in previous chapters, the bar notation is used to denote that a variable is defined in the wavenumber domain and capital notation is used for frequency domain variables. Thus, the dynamic Green's functions are represented with capital-bar notation and static Green's functions are represented just with uppercase letters.

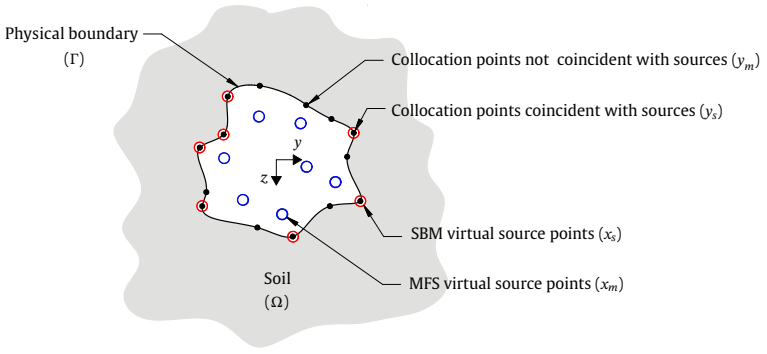

FIGURE 5.1: General description of the proposed hybrid methodology. Collocation points are denoted by black solid circles and the virtual sources associated with MFS and SBM are denoted by blue and red circles, respectively.

Based on radial basis function interpolation, the displacement and traction fields in the soil can be approximated throughout the domain using the following linear

combination of the fundamental solution of the governing equations:

$$\bar{\boldsymbol{U}}(\boldsymbol{y}) = \sum_{n=1}^{N_M} \bar{\mathbf{H}}(\boldsymbol{y}, \boldsymbol{x}_M^n)\bar{\boldsymbol{S}}_{M,n} + \sum_{n=1}^{N_S} \bar{\mathbf{H}}(\boldsymbol{y}, \boldsymbol{x}_S^n)\bar{\boldsymbol{S}}_{S,n}, \tag{5.1a}$$

$$\bar{\boldsymbol{T}}(\boldsymbol{y}) = \sum_{n=1}^{N_M} \bar{\mathbf{H}}^{\tau}(\boldsymbol{y}, \boldsymbol{x}_M^n)\bar{\boldsymbol{S}}_{M,n} + \sum_{n=1}^{N_S} \bar{\mathbf{H}}^{\tau}(\boldsymbol{y}, \boldsymbol{x}_S^n)\bar{\boldsymbol{S}}_{S,n}, \tag{5.1b}$$

where the terms $\bar{\mathbf{H}}(\boldsymbol{y}, \boldsymbol{x}_{M/S}^n)$ and $\bar{\mathbf{H}}^{\tau}(\boldsymbol{y}, \boldsymbol{x}_{M/S}^n)$ represent the displacement and traction Green's functions of the soil considering a point load applied at $\boldsymbol{x}_{M/S}^n$ and an arbitrary field point at y. The terms $\bar{\boldsymbol{S}}_{M,n}$ and $\bar{\boldsymbol{S}}_{S,n}$ represent vectors that collect the three components of the strength of the nth virtual source associated with the SBM and MFS sources, respectively, and $\bar{\boldsymbol{U}}(\boldsymbol{y})$ and $\bar{\boldsymbol{T}}(\boldsymbol{y})$ are the displacements and tractions of the soil at the arbitrary field point. The number of MFS and SBM sources points are denoted by N_M and N_S, respectively, being $N = N_M + N_S$ the total amount of sources. Also, it should be noted that the terms $\boldsymbol{x}_M^n$ and $\boldsymbol{x}_S^n$ are the location of the nth source point associated with the MFS and SBM, respectively. To avoid the singularities that arise when Eqs. (5.1a) and (5.1b) are employed to evaluate the solution on collocation points geometrically coincident with virtual sources, the equations can be rewritten as follows [19, 54]

$$\begin{aligned}\bar{\boldsymbol{U}}(\boldsymbol{y}_S^m) = &\sum_{n=1}^{N_M} \bar{\mathbf{H}}(\boldsymbol{y}_S^m, \boldsymbol{x}_M^n)\bar{\boldsymbol{S}}_{M,n} + \sum_{n=1, n\neq m}^{N_S} \bar{\mathbf{H}}(\boldsymbol{y}_S^m, \boldsymbol{x}_S^n)\bar{\boldsymbol{S}}_{S,n} \\ &+ \bar{\mathbf{H}}_{mm}\bar{\boldsymbol{S}}_{S,m}, \text{for } m = 1, 2, ..., N\end{aligned} \tag{5.2a}$$

$$\begin{aligned}\bar{\boldsymbol{T}}(\boldsymbol{y}_S^m) = &\sum_{n=1}^{N_M} \bar{\mathbf{H}}^{\tau}(\boldsymbol{y}_S^m, \boldsymbol{x}_M^n)\bar{\boldsymbol{S}}_{M,n} + \sum_{n=1, n\neq m}^{N_S} \bar{\mathbf{H}}^{\tau}(\boldsymbol{y}_S^m, \boldsymbol{x}_S^n)\bar{\boldsymbol{S}}_{S,n} \\ &+ \bar{\mathbf{H}}_{mm}^{\tau}\bar{\boldsymbol{S}}_{S,m}, \text{for } m = 1, 2, ..., N\end{aligned} \tag{5.2b}$$

where $\bar{\mathbf{H}}_{mm}$ and $\bar{\mathbf{H}}_{mm}^{\tau}$ are, as in Chapter 4, the SBM origin (or source) intensity factors (OIFs) and where $\boldsymbol{y}_S^m$ is the location of the mth collocation point associated with the SBM formulation.

In this work, it is assumed that the OIFs associated with the hybrid SBM-MFS formulation are equal to the ones that are obtained by formulating the problem using the SBM. Therefore, these OIFs can be computed from a formulation of the problem that does not consider MFS sources, i.e. where all the collocation points

are coincident with virtual sources. Therefore, referring to this total set of collocation points simply as $\{\boldsymbol{y}^1,\ \ldots,\ \boldsymbol{y}^N\} = \{\boldsymbol{y}_S^1,\ \ldots,\ \boldsymbol{y}_S^{N_S}\} \cup \{\boldsymbol{y}_M^1,\ \ldots,\ \boldsymbol{y}_M^{N_M}\}$, the expression that defines the OIF associated with the Neumann boundary condition of the hybrid SBM-MFS formulation at the mth collocation point is given by

$$\bar{\mathbf{H}}_{mm}^{\tau} = \frac{1}{L_m}\left[\mathbf{I} + \mathbf{A}_m - \sum_{n=1, n\neq m}^{N} L_n \mathbf{H}^{\tau}(\boldsymbol{y}^n, \boldsymbol{y}_S^m)\right], \tag{5.3}$$

where

$$\mathbf{A}_m \approx \int_{\Gamma_m} \left[\mathbf{H}^{\tau}(\boldsymbol{y}^m, \boldsymbol{y}) + \mathbf{H}^{\tau}(\boldsymbol{y}, \boldsymbol{y}^m)\right] \mathrm{d}\Gamma_m(\boldsymbol{y}), \tag{5.4}$$

being Γ_m the segment of the boundary with length L_m on which the mth collocation point is located. The detailed derivation of the previous expression has been presented in Chapter 4. In the numerical calculations of $\mathbf{A}_m$, Γ_m is approximated by the following union of two straight segments $\Gamma_\mathrm{m} \approx [(\boldsymbol{y}^{m-1} + \boldsymbol{y}^m)/2, \boldsymbol{y}^m] \cup [\boldsymbol{y}^m, (\boldsymbol{y}^m + \boldsymbol{y}^{m+1})/2]$.

As it was mentioned in Chapter 4, the OIFs associated with the Dirichlet boundary condition $\bar{\mathbf{H}}_{mm}$, can be directly calculated as an average value of the fundamental solution over Γ_m [54]. As before, the real boundary is approximated by two straight segments.

In contrast with what happened for the SBM collocation points, the responses on the MFS points are simply given by Eqs. (5.5a) and (5.5b), since no singularity arises in the required Green's functions.

$$\bar{\boldsymbol{U}}(\boldsymbol{y}_M^m) = \sum_{n=1}^{N_M} \bar{\mathbf{H}}(\boldsymbol{y}_M^m, \boldsymbol{x}_M^n)\bar{\boldsymbol{S}}_{M,n} + \sum_{n=1}^{N_S} \bar{\mathbf{H}}(\boldsymbol{y}_M^m, \boldsymbol{x}_S^n)\bar{\boldsymbol{S}}_{S,n}, \quad \text{for } m = 1, 2, ..., N \tag{5.5a}$$

$$\bar{\boldsymbol{T}}(\boldsymbol{y}_M^m) = \sum_{n=1}^{N_M} \bar{\mathbf{H}}^{\tau}(\boldsymbol{y}_M^m, \boldsymbol{x}_M^n)\bar{\boldsymbol{S}}_{M,n} + \sum_{n=1}^{N_S} \bar{\mathbf{H}}^{\tau}(\boldsymbol{y}_M^m, \boldsymbol{x}_S^n)\bar{\boldsymbol{S}}_{S,n}, \quad \text{for } m = 1, 2, ..., N \tag{5.5b}$$

The source strengths resulting of a prescribed boundary condition can be determined arranging the previous expressions in the form of Eq. (4.17) and solving

the resulting system of equations.

Once the source strengths are computed, the displacement and traction response at an arbitrary field point in the soil can be computed by means of Eqs. (5.1a) and (5.1b).

5.2 Assessment of the hybrid method

In this section, the assessment of the accuracy and robustness of the proposed method is conducted in the framework of three examples. The first example deals with a circular cylindrical cavity, the second example considers a partially circular shape, and the last one presents the results for a square geometry. The methods are compared with other numerical strategies and the comparison is performed in terms of an error analysis with respect to a reference solution to evaluate the accuracy of the method, and in terms of the conditioning of the system of equations employed to determine the source strengths, to study its robustness. Furthermore, the frequency spectrum is also presented for all examples, in order to assess the performance of the method in a broad frequency range. As mentioned previously, the 2.5D BEM, the 2.5D MFS and the 2.5D SBM approaches are applied together with the 2.5D hybrid SBM-MFS method to carry out a thorough comparison. For the application of the 2.5D SBM, the same methodology used in the previous chapter in where sources located at the locations of all collocation points is also employed here. The hybrid SBM-MFS and MFS approaches are analysed, in contrast, for two distinct configurations of the MFS virtual sources: regular, following an interior auxiliar boundary with the same shape of the physical one, and random, distributed all along the cavity space, while the SBM sources are located with different distributions depending on the problem. The error analysis is performed by computing the root mean square error (RMSE), which is calculated as

$$\text{RMSE} = \frac{\sqrt{\dfrac{1}{3N_E}\displaystyle\sum_{j=1}^{N_E}\left|\sum_{i=1}^{3}U_f^{ij}-\sum_{i=1}^{3}U_{fr}^{ij}\right|^2}}{\sqrt{\dfrac{1}{3N_E}\displaystyle\sum_{j=1}^{N_E}\left|\sum_{i=1}^{3}U_{fr}^{ij}\right|^2}}, \tag{5.6}$$

where i is the index associated with the Cartesian coordinates (x, y and z), j is the index associated with the evaluation points, and N_E refers to the total number of evaluation points considered. Moreover, U_f^{ij} and U_{fr}^{ij} represent the receptances in the frequency domain on the evaluation points obtained by the selected method and by the reference method, respectively, at the field point j and in the direction i. The procedure to compute the receptances is presented in Section 3.2.

In contrast to the previous chapter, the exact geometrical data from the curve equation of the boundary is considered for the determination of influence lengths to be used in the computation of OIFs and also to obtain the normal vectors. However, it is found that for the considered cases in this chapter, the accuracy of the 2.5D SBM and the hybrid approaches will not change considerably by considering the node-based approximation instead of the exact geometry of the boundary.

In this chapter, the RMSE analysis is performed based on integrals computed numerically with a total of 513 sampling points consisting of $k_x = 0$ and a logarithmically spaced vector of wavenumbers ranging from 10^{-3} to 10^2 rad/m. More details on this regard can be found in Section 3.2. The considered material properties of the soil can be found in Table. 3.1.

5.2.1 Example 1: Circular shape cavity

This example provides a thorough comparative study of the considered approaches in the context of the radiation problem caused by a load acting on a cylindrical cavity. For this case, the reference for the determination of the error is the semi-analytical solution of a cylindrical cavity in a homogeneous elastic medium presented in [27]. The particular system considered is a cylindrical cavity with a unit radius excited by a vertical harmonic load applied to the bottom of the

cavity. The RMSE is calculated at two different sets of test points (each set consists of 100 evaluation points), both distributed on circles centred at the cylinder axis and with radii 2 m and 20 m, representing near-field and far-field positions, respectively. The RMSE trends are shown against NpW, ranging from 3 to 21, considering the mentioned soil properties and maximum frequencies of 80 Hz and 250 Hz.

5.2.1.1 Regular distribution of MFS source points

Prior to the comparison of the proposed approach with the other numerical methods, various distributions for the MFS sources are studied. For all cases, the virtual sources are distributed uniformly in a concentric circle of radius r_s and, afterwards, the hybrid and MFS approaches are assessed for different values of this radius. The adopted distributions for the case of $r_s = 0.75$ m are shown in Fig. 5.2. On the one hand, the distribution of the source points associated with the full MFS method is shown in Fig. 5.2a. On the other hand, two different configurations are assumed for the hybrid method, illustrated in Fig. 5.2b and 5.2c, and named as one-in-between (OIB), and half-half (HH) configurations, respectively. In OIB configuration, the neighbouring points of each SBM source point are collocation points without a coincident source at them. In HH configuration, all SBM sources are located consecutively along the boundary in its upper half side. In both arrangements of the hybrid approach, 50% of the virtual sources are SBM sources and the remaining 50% are MFS sources.

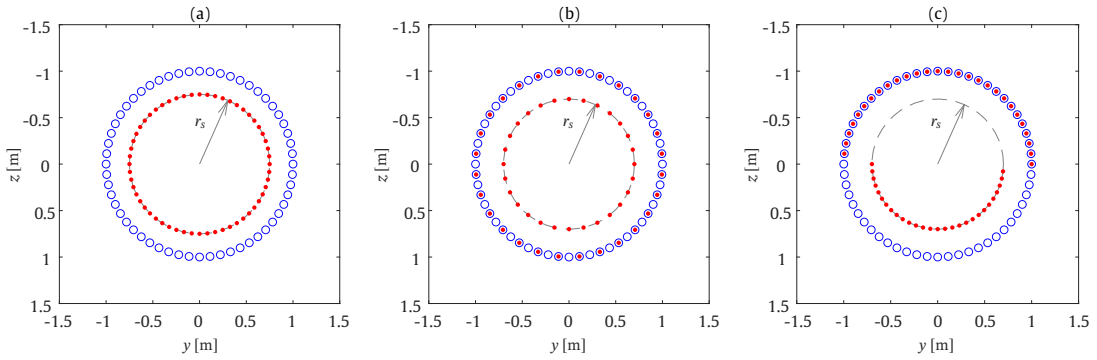

FIGURE 5.2: Distributions of the collocation points (blue) and virtual sources (red) for the circular shape case, adopting a regular distribution approach for the full MFS method (a) and the OIB (b) and HH (c) configurations for the hybrid approach.

The RMSE of the MFS and hybrid (OIB configuration) methods for different values of the r_s is shown in Fig. 5.3. The HH configuration for the hybrid approach is not presented since it is found to present a similar behaviour to the OIB configuration. The RMSE of the full SBM method is also presented for comparison purposes. As shown in this figure, the hybrid method behaves more consistently than the MFS, even though it can not reach the high accuracy levels of the full MFS method at particular radii. As it can be seen, both hybrid and MFS approaches present large errors at very small or very large radii. This finding is consistent with the previous investigations in the field [14, 90]. Moreover, the hybrid method presents the same level of accuracy in a wide range of radii, reaching a RMSE value slightly smaller than the one associated with the full SBM method. The results of this analysis are used to select an optimal r_s for the hybrid and MFS methods that will be used all along the calculations for regular distribution of MFS sources in the circular shape cavity case. Corresponding optimal distances depending on the method and the frequency are used.

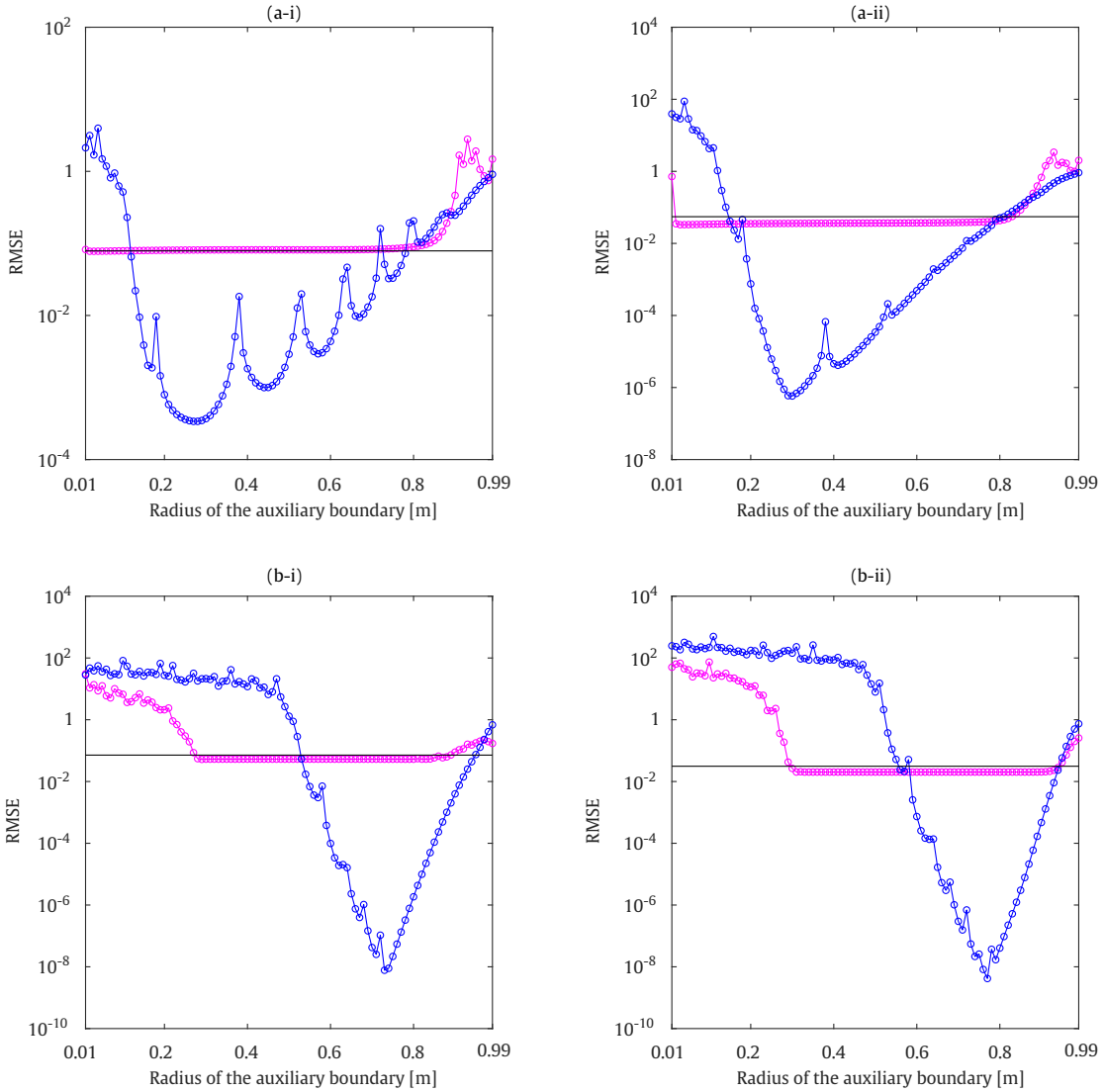

FIGURE 5.3: The RMSE of the studied methods against the position of the virtual sources, considering 10 NpW and frequencies of 80 Hz (a) and 250 Hz (b). The field points are located at a radius of 2 m (i) and 20 m (ii). Methods: 2.5D MFS (blue line), hybrid method with OIB configuration (purple line) and 2.5D SBM (black line).

The accuracy of the hybrid method is compared with the considered alternative approaches in terms of the RMSE. Fig. 5.4 shows the RMSE at two chosen frequencies (80 Hz and 250 Hz) versus NpW. For the hybrid and MFS approaches, the previously determined optimal r_s has been employed in the calculations. Based on the results shown in Fig. 5.4, the 2.5D MFS is the most accurate solution among all methods, as expected for such a smooth geometry [91]. In this figure, the RMSE values below 10^{-3} are not shown to highlight the differences between the other numerical methods. Comparing the results obtained by the 2.5D SBM

and the 2.5D BEM with the 2.5D SBM-MFS, it is found that the hybrid method with OIB configuration presents a higher numerical accuracy than the 2.5D SBM and 2.5D BEM, specially at far-field responses. Also, it demonstrates a similar error decay rate that SBM and BEM approaches. In contrast, as depicted, the accuracy of the hybrid approach with HH configuration is less stable, although is generally better than the one associated with the 2.5D BEM.

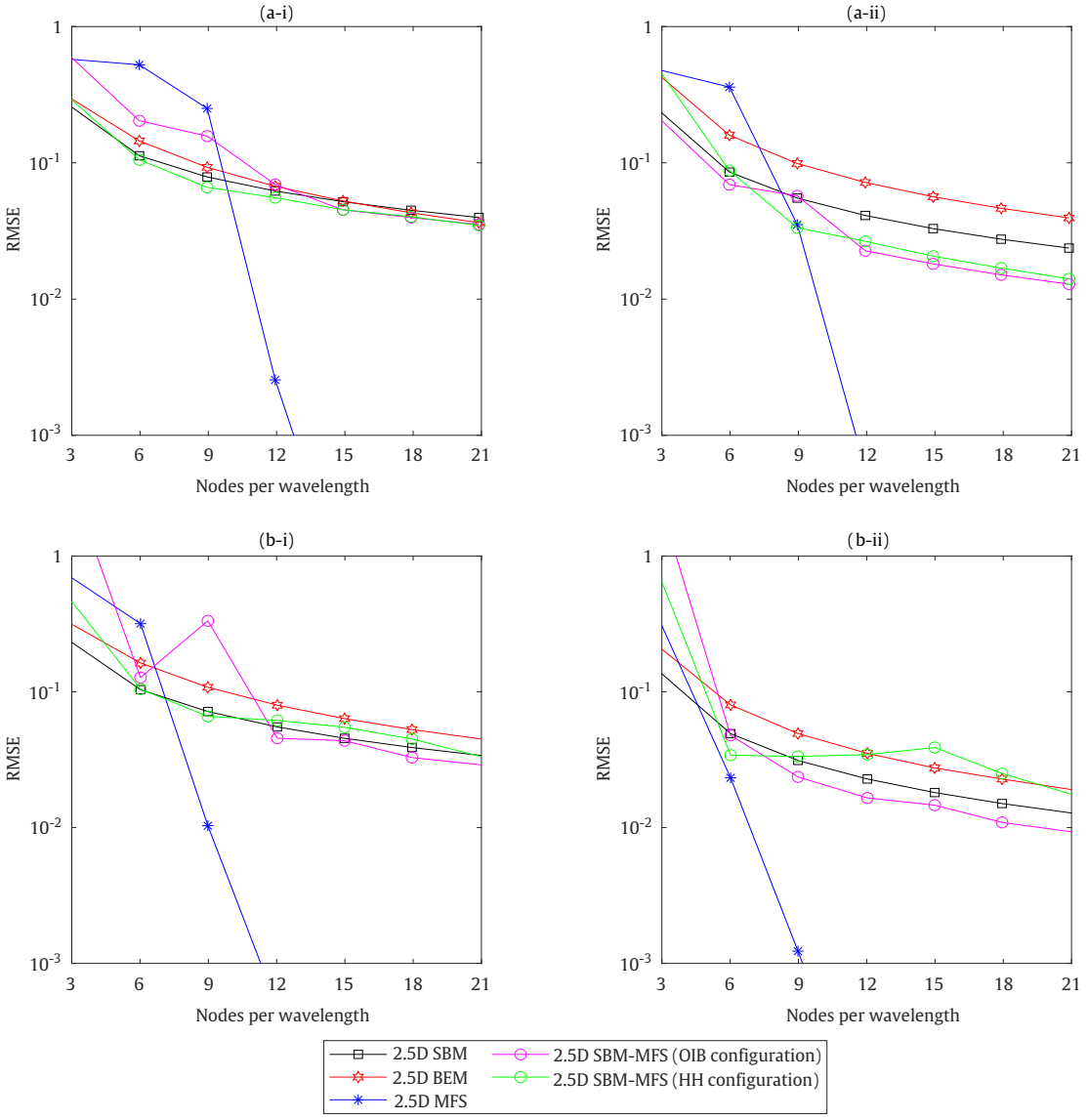

FIGURE 5.4: RMSE for different numerical strategies, considering regular distribution of the MFS sources for the case of a circular shape cavity. Two sets of evaluation points at radii of 2 m (i) and 20 m (ii) are considered. Calculation frequencies: 80 Hz (a) and 250 Hz (b).

Previous results were useful to evaluate the global performance of the method at

two specific frequencies. However, it is also interesting to check the performance of the method along the frequency. In this context, the frequency response functions delivered by the hybrid method are compared against the ones provided by the semi-analytical solution of the cylindrical cavity [27]. The comparison is conducted in terms of receptances and TTF. Three evaluation points in the soil are settled: points A ($x = 0$ m; $y = 2$ m; $z = 2$ m), B ($x = 0$ m; $y = 5$ m; $z = 2$ m) and C ($x = 0$ m; $y = 8$ m; $z = -4$ m). In these cases, the number of collocation points are constant along the frequency range to ensure 10 NpW at 250 Hz. As shown in Figs. 5.5 and 5.6, very good agreement can be seen between the semi-analytical solution of the cylindrical cavity and the proposed approach along the frequency range of interest. Also, these figures give a more visual representation of the errors delivered by the new methodology: despite the 2.5D MFS is clearly more accurate than the other methods, these figures highlight the fact that they are still highly accurate.

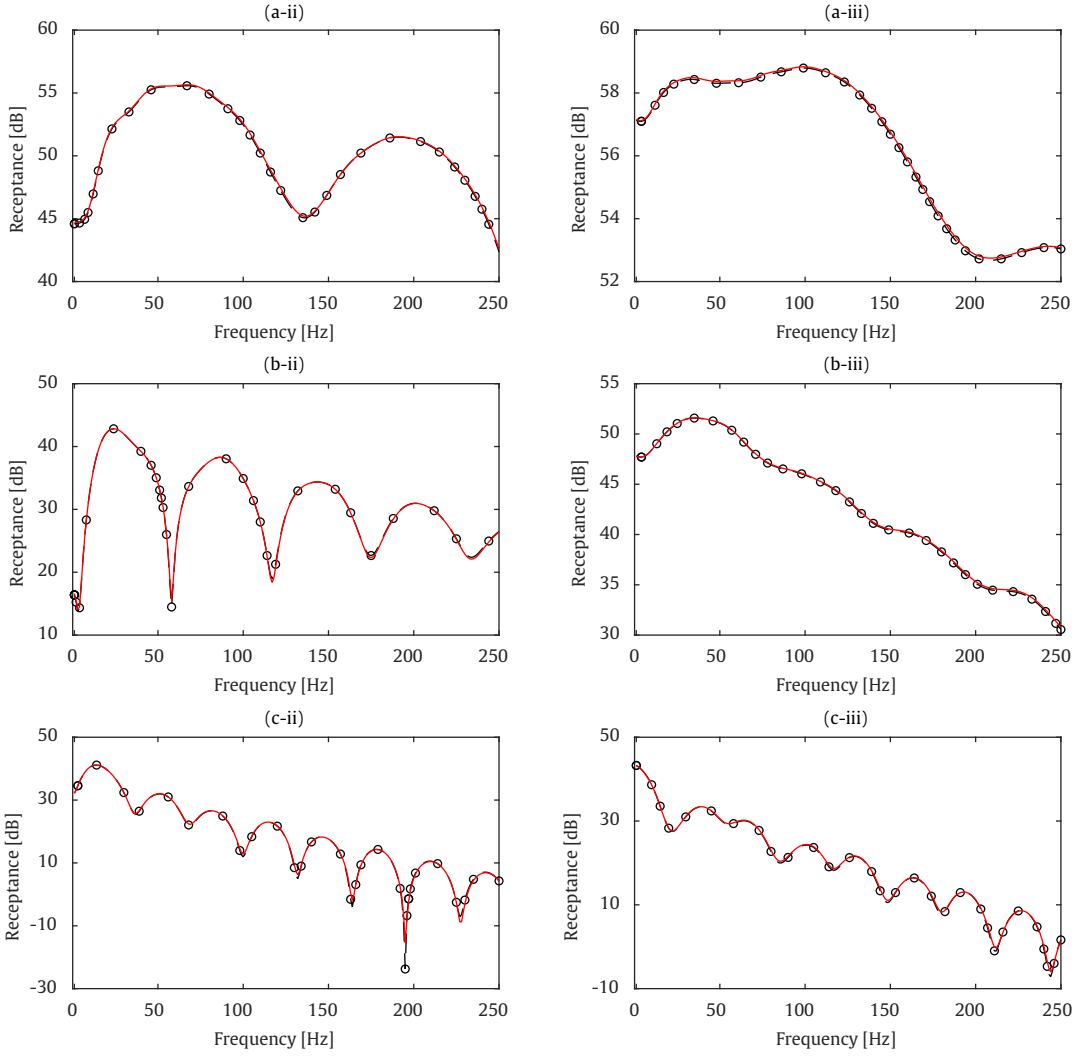

FIGURE 5.5: Receptances for the circular shape case at the field points A (a), B (b) and C (c) for y (ii) and z (iii) directions. Methods: semi-analytical solution of the cylindrical cavity (solid red line) and hybrid method (dashed black line with circular markers).

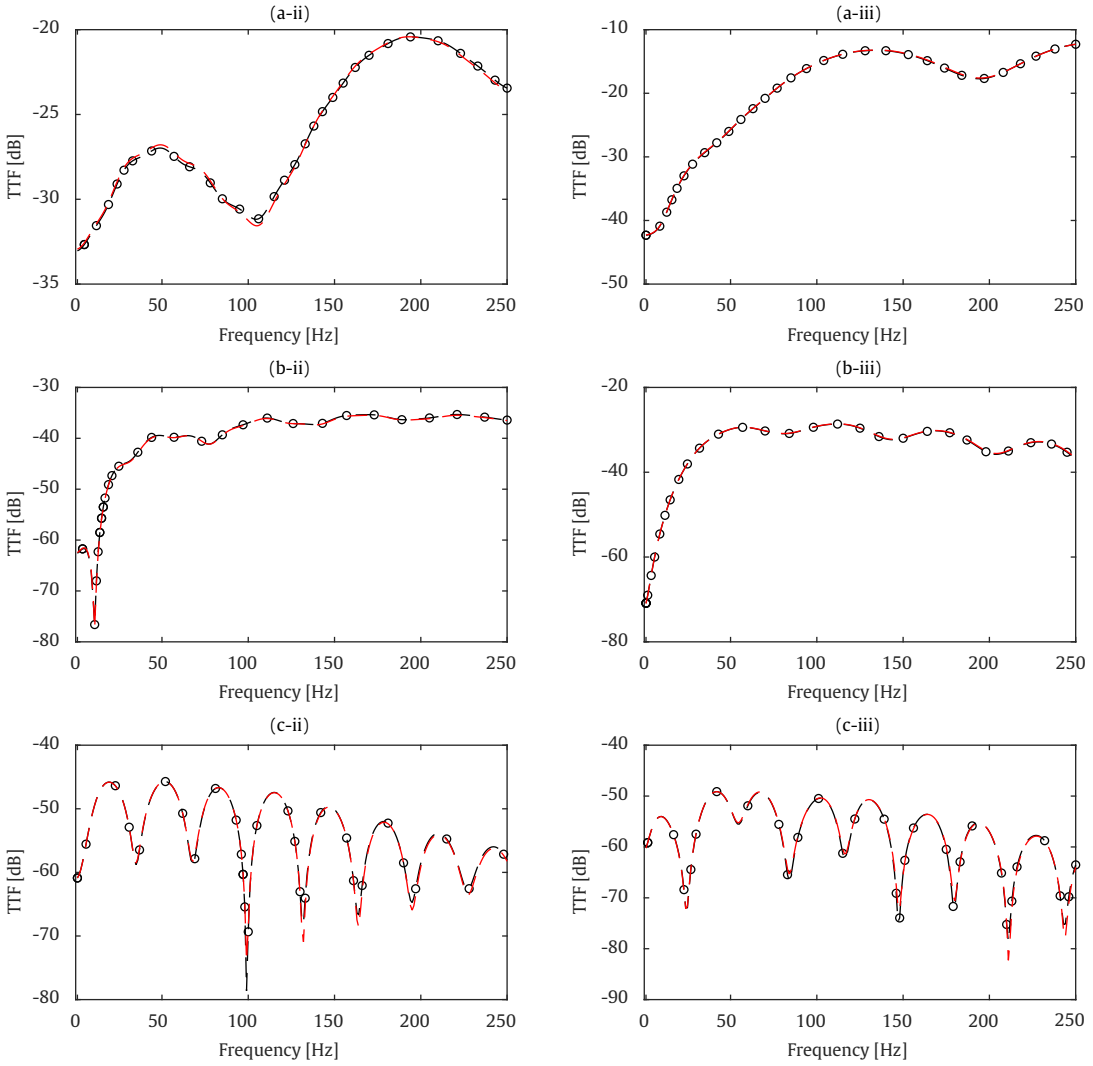

FIGURE 5.6: Traction transfer functions for the circular shape case at the field points A (a), B (b) and C (c) for y (ii) and z (iii) directions. Methods: semi-analytical solution of the cylindrical cavity (solid red line) and hybrid method (dashed black line with circular markers).

5.2.1.2 Random distribution of MFS source points

In order to assess the robustness of the proposed method, the RMSE obtained by the hybrid approach, considering different random distributions of the MFS sources, is compared with those obtained by the alternative methods. Fig. 5.7a illustrates the distribution of collocation points and, more importantly, sources location for one of the multiple random source distribution cases for the 2.5D MFS. Similarly, Fig. 5.7b indicates a random realisation of source points arrangement for the hybrid method. Similar to the regular distribution of source points, these

random distributions for the hybrid method consider 50% of the sources to be MFS sources, being the remaining 50% of SBM nature. To limit the proximity between MFS sources and also between MFS sources and collocation points, two restrictions are assumed. These restrictions are calculated based on the RMSE analysis presented in Fig. 5.3. Firstly, a minimum distance of 0.1 m is assigned between the virtual sources and the physical boundary for all cases. Secondly, a minimum allowed distance between source points is defined. At 80 Hz, a minimum gap of 0.02 m is defined between MFS sources for both methods, while, the minimum permitted values for the case of 250 Hz are 0.05 m and 0.08 m for the hybrid and MFS approaches, respectively. In this work the distribution is generated using an iterative procedure where each new source is randomly located inside the boundary taking into account the source-boundary constraint and assuming a uniform probability distribution. Once defined, the source-source constraint is assessed for the new source location and, if the condition is not satisfied, the source is discarded. The procedure is repeated until the desired number of sources are generated.

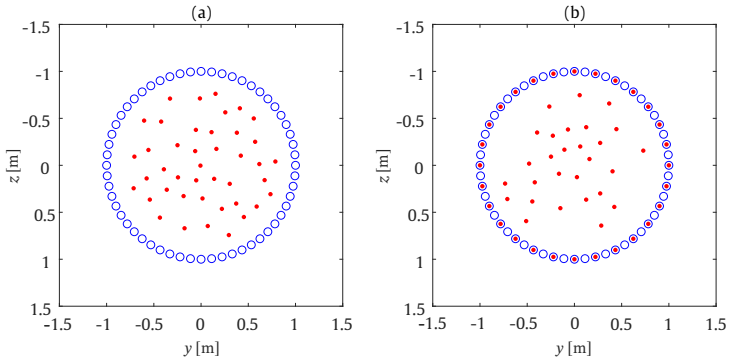

FIGURE 5.7: Examples of distributions of the collocation points (blue) and virtual sources (red) for the circular shape case, adopting a random distribution approach for the placement of MFS sources. Methods: full MFS approach (a) and hybrid approach (b).

The robustness of the hybrid and full MFS approaches are quantified at two different frequencies by comparing the RMSE obtained assuming a random distribution of the MFS sources with those delivered by the 2.5D SBM and 2.5D BEM. The RMSE analysis is carried out for 100 distinct realisations of random sources distributions. The underlying idea of this particular comparison is to study how much dependent to the source distributions the methods are. Fig. 5.8 illustrates the results of this comparative study in where, for this specific geometry, the 2.5D

MFS presents, generally, more accurate and stable results than the hybrid method. Moreover, the hybrid method presents a similar mean RMSE to the 2.5D SBM in all cases. The analysis carried out in this section illustrates that the full MFS is the most accurate method for a circular boundary and that the hybrid method does not provide a significant improvement when compared with the SBM approach. However, next sections show that the benefits of the hybrid approach arise when a geometrically complex boundary is considered.

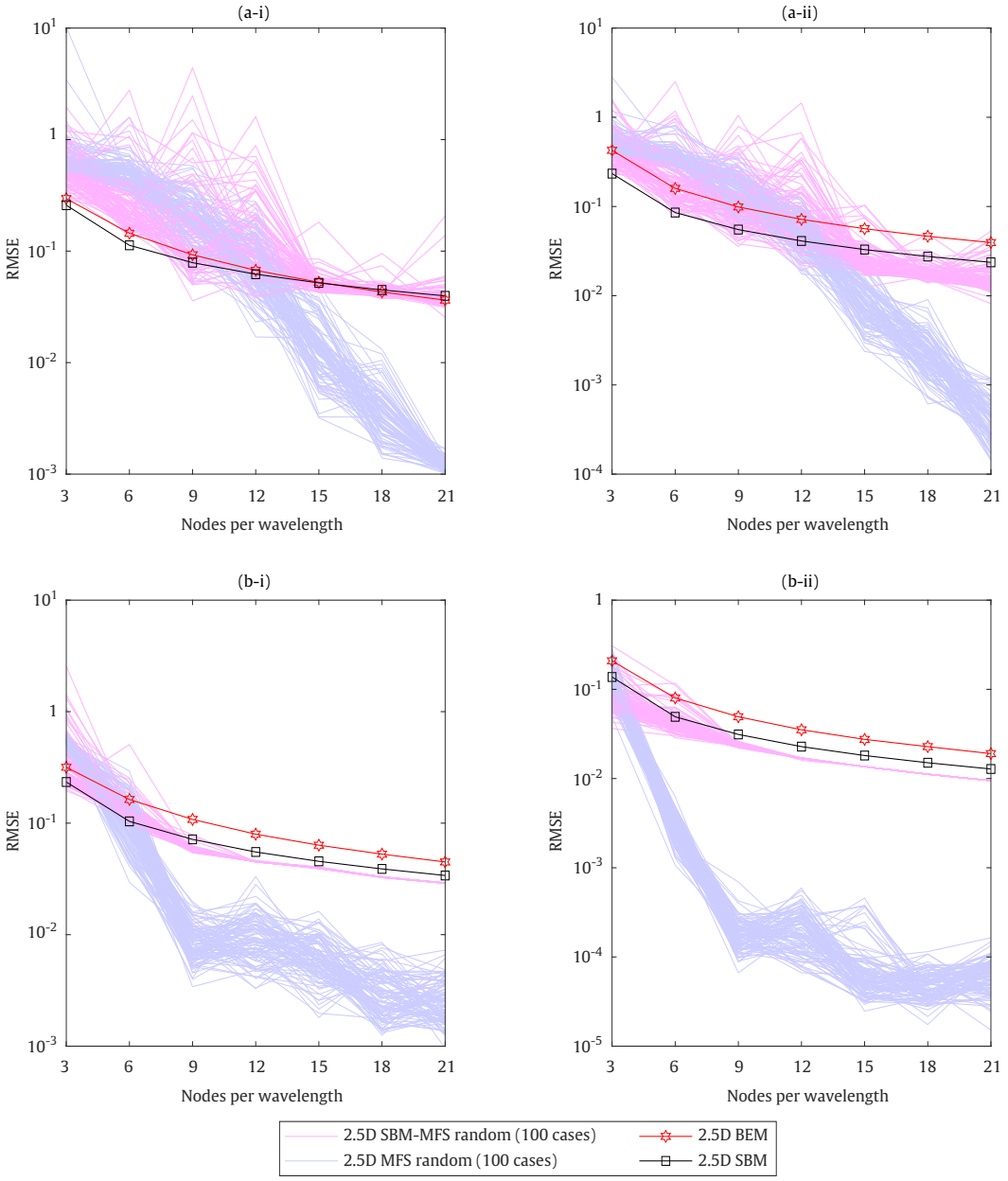

FIGURE 5.8: RMSE for different numerical strategies when considering random distributions of the MFS sources for the case of a circular shape cavity. Two sets of evaluation points at radii of 2 m (i) and 20 m (ii) are considered. Calculation frequencies: 80 Hz (a) and 250 Hz (b).

5.2.1.3 Condition number

In order to analyse the accuracy of the considered numerical methods, the concept of condition number is defined in this chapter. The condition number of a function measures how much the output value of the function is sensitive to small

perturbations in the input data [92]. To be specific, the 2-norm condition number associated with the linear systems of equations appearing in Eq. (4.17) is considered to show the sensitiveness of the solution of the system, which is the source strengths, for a small change in the input boundary condition. In this context, the condition number can be defined as the ratio between the largest and smallest singular value of the inverted matrix of the system in this work [93]. This indicator is important to be studied since a high condition number of $\bar{\mathbf{H}}^{\tau}$ would mean that a correct solution of the system is more difficult to be accurately determined. In this analysis, the system of equations is named as ill-conditioned if the condition number exceeds 10^{16}. The analysis of the condition number is presented for two wavenumbers (0.1 and 1 rad/m) and two frequencies (80 Hz and 250 Hz). To evaluate the asymptotic behaviour of the condition number, the NpW considered in this section are considerably larger than those required for any practical computation. Fig. 5.9 illustrates the condition number obtained by the 2.5D SBM, the 2.5D MFS and the hybrid approaches. It should be noted that the OIB configuration is used for the hybrid approach for the case of regular distribution of source points. The trend associated with the 2.5D SBM indicates that this method is very well-conditioned or in other words, the condition number of the matrix $\bar{\mathbf{H}}^{\tau}$ that defines the coefficients of the system of equations required to determine the source strengths for a Neumann boundary condition is not sensitive to the number of NpW. The comparison between the 2.5D MFS and the hybrid method for the regular distribution of MFS source points shows that the 2.5D MFS has ill-conditioned system of equation for values above 95 NpW and 23 NpW for the frequencies of 80 Hz and 250 Hz, respectively, while the hybrid method presents an ill-conditioned system of equation for values above 190 NpW and 47 NpW for the frequencies of 80 Hz and 250 Hz, respectively. For the random distributions of sources points, average condition numbers are considered for both full MFS and hybrid methods. This assumption for all condition number calculation based on random source distributions presented in this chapter. The comparison between the 2.5D MFS and the hybrid method with random distribution of MFS sources demonstrates that they present ill-conditioned system of equation for values above 47 NpW and 23 NpW for the frequencies of 80 Hz and 250 Hz, respectively. Thus, it can be concluded that the hybrid approach produces generally more conditioned systems of equations for the determination of the required source strengths.

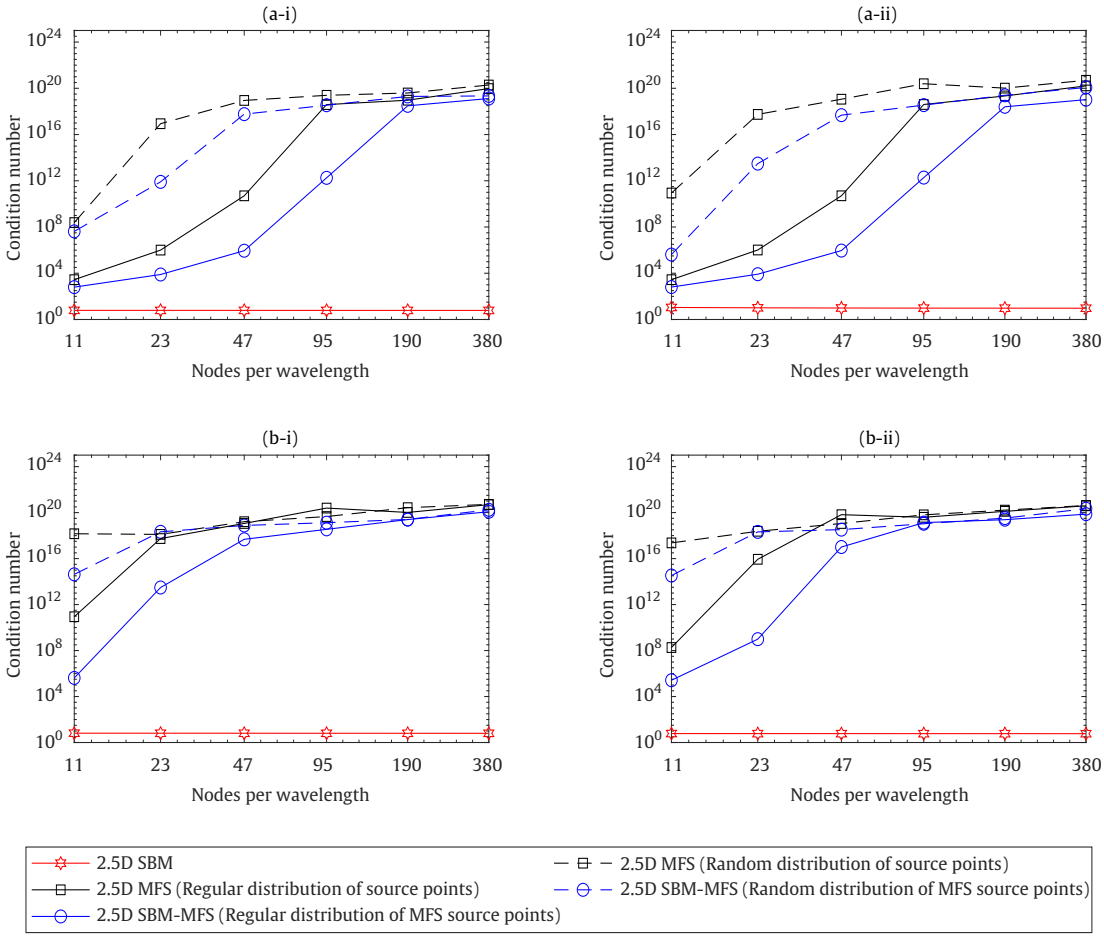

FIGURE 5.9: Condition number with respect to the discretisation density for the 2.5D MFS, the 2.5D SBM, and the hybrid methods in the circular boundary shape case at frequencies of 80 Hz (a) and 250 Hz (b) and for wavenumbers of 0.1 rad/m (i) and 1 rad/m (ii).

5.2.2 Example 2: Partially circular

In the previous section, it was shown that the hybrid method does not provide any particular improvement for the case of a circular cavity in comparison with the other considered methods. In fact, it was found that the full 2.5D MFS is the most accurate approach for that specific geometry. In order to present the benefits provided by the hybrid method, more complex geometries are considered in examples 2 and 3. The second example is presented in this section, where a circular boundary with a flat is adopted. This geometry has been called partially circular shape along the section. Since the considered problem does not have a known analytical solution, the 2.5D FEM-BEM approach with a highly refined

mesh is taken as the reference in the error analysis. The radius of the circular segment of the geometry is taken to be 3 m, and the length of the lower straight segment has been set to 5 m. The system is excited by two vertical harmonic loads, both applied to the bottom of the geometry, as shown in Fig. 5.10a. The mesh employed for the reference case is presented in Fig. 5.10b, where the soil material is assigned to both FEM and BEM to properly represent the studied system. The reference case uses the 2.5D FEM to model the local surrounding soil to the cavity in order to accurately model the geometry of the cavity. Particularly refined FEM mesh is adopted in the two corners for this purpose. Moreover, BEM mesh in the reference solution adopts 40 NpW for a frequency of 80 Hz, the maximum frequency of interest settle in the this example. As in example 1, RMSE is used to assess the accuracy of the different methods studied. It is again computed at two sets of test points, with 100 points each one, both homogeneously distributed on circles centred at the cylinder axis and with radii 5 m and 20 m, representing near-field and far-field positions, respectively.

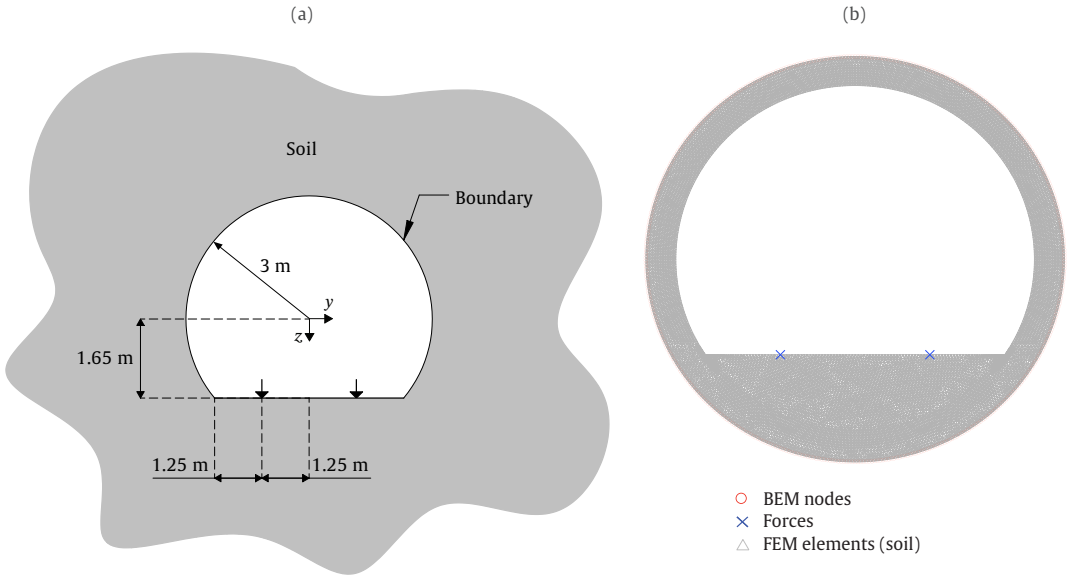

FIGURE 5.10: The geometry and loading pattern of the problem (a) and the mesh considered in the 2.5D FEM-BEM reference solution (b).

5.2.2.1 Regular distribution of MFS source points

In this section, the accuracy of the hybrid and MFS approaches when the MFS source points are distributed in a regular pattern is compared with the 2.5D SBM and the 2.5D BEM approaches. In this example, it is supposed that the fictitious

boundary uses a scaled partially circular shape corresponding to the physical geometry, as shown in Fig. 5.11a. Previous works has shown that the MFS requires of large amounts of collocation points to provide accurate results for complicated geometries [94], In contrast, the SBM is an appropriate approach to deal with complex geometries with sharp edges [18]. Having this in mind, the hybrid method uses the SBM to deal with these complex parts of boundary while the MFS is used for the remaining smooth sections. In the present example, thus, the circular section of the geometry (referred as the smooth segment in this example) is handled with the MFS and the SBM is used to deal with the lower straight segment of shape including the two corners (referred as the complex segment in this example). As a consequence of this distribution, 65% of the virtual sources are the MFS sources and 35% of the sources are the SBM source points. This ratio is kept constant for all the calculations presented for this example. The optimal position of the MFS virtual sources is chosen based on RMSE analysis similar to the one presented for the previous example.

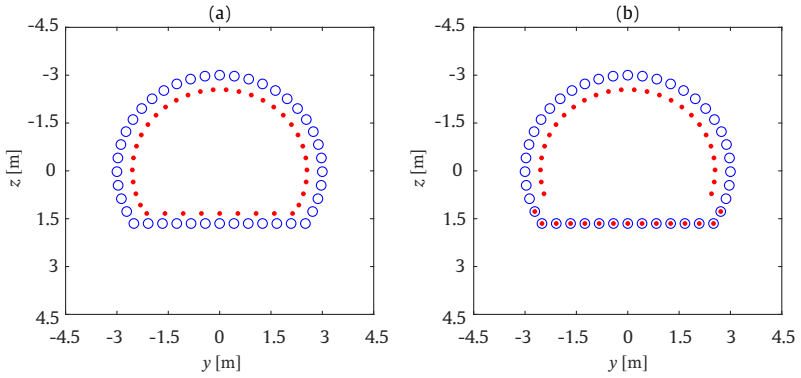

FIGURE 5.11: The collocation points (blue) and virtual sources (red) for the partially circular shape case, adopting a regular distribution approach, for the full MFS (a) and hybrid (b) methods.

Fig. 5.12, shows a comparative of the RMSE for all considered approaches in the context of the present example. In contrast to example 1, the 2.5D MFS presents the largest errors and a fluctuating behaviour, when compared with the other methods. That is due to higher complexity of the considered geometry. In general, the hybrid approach demonstrates the most accurate results at 80 Hz among all methods, while SBM is the most precise method at 20 Hz. The performance of the hybrid method versus the amount of NpW is stable and smooth in all cases, similar to the 2.5D BEM and 2.5D SBM approaches. When comparing these methods, it is

important to notice that the hybrid method is more computationally efficient than the full SBM due to the reduction of OIF required to be computed. Furthermore, the capability of the MFS to have less sources than collocation points is also a potential benefit of the hybrid method with respect to the SBM not discussed in the present thesis.

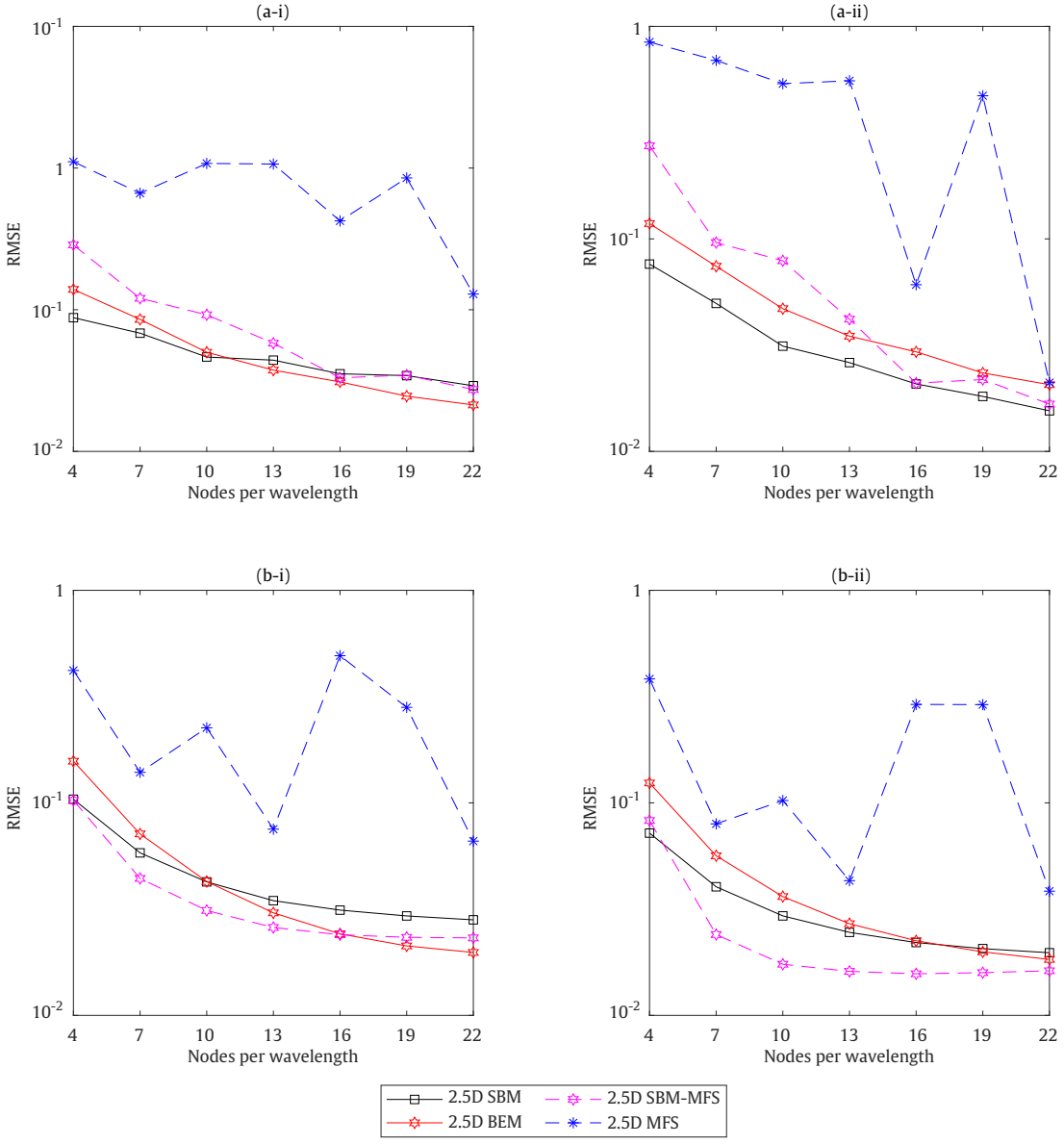

FIGURE 5.12: RMSE for different numerical strategies, considering regular distribution of the MFS sources for the case of a partially circular shape. Two sets of evaluation points at radii of 5 m (i) and 20 m (ii) are considered. Calculation frequencies: 20 Hz (a) and 80 Hz (b).

In order to assess the accuracy of the proposed approach for a frequency range of

interest, a comparison is conducted between the receptances and TTF obtained by the hybrid approach and those of 2.5D FEM-MFS approach. The 2.5D FEM-MFS is used here instead of the 2.5D FEM-BEM since it provides good accuracy and also an easier evaluation procedure for the tractions. The mesh illustrated in Fig. 5.10b also is used for the 2.5D FEM-MFS calculations. Three evaluation points in the soil are considered: points A ($x = 0$ m; $y = 4$ m; $z = -4$ m), B ($x = 0$ m; $y = 8$ m; $z = -3$ m) and C ($x = 0$ m; $y = 12$ m, $z = 6$ m). In these cases, a minimum of 10 NpW and 40 NpW are considered for the hybrid method and the 2.5D FEM-MFS, respectively, for the range of frequencies of interest, considering a maximum frequency of 100 Hz. From the results shown in Figs. 5.13 and 5.14, it can be interpreted that the proposed method is a good prediction model for the considered geometry. This accuracy is consistent with the RMSE values presented in Fig. 5.12 which is 3% for 10 NpW.

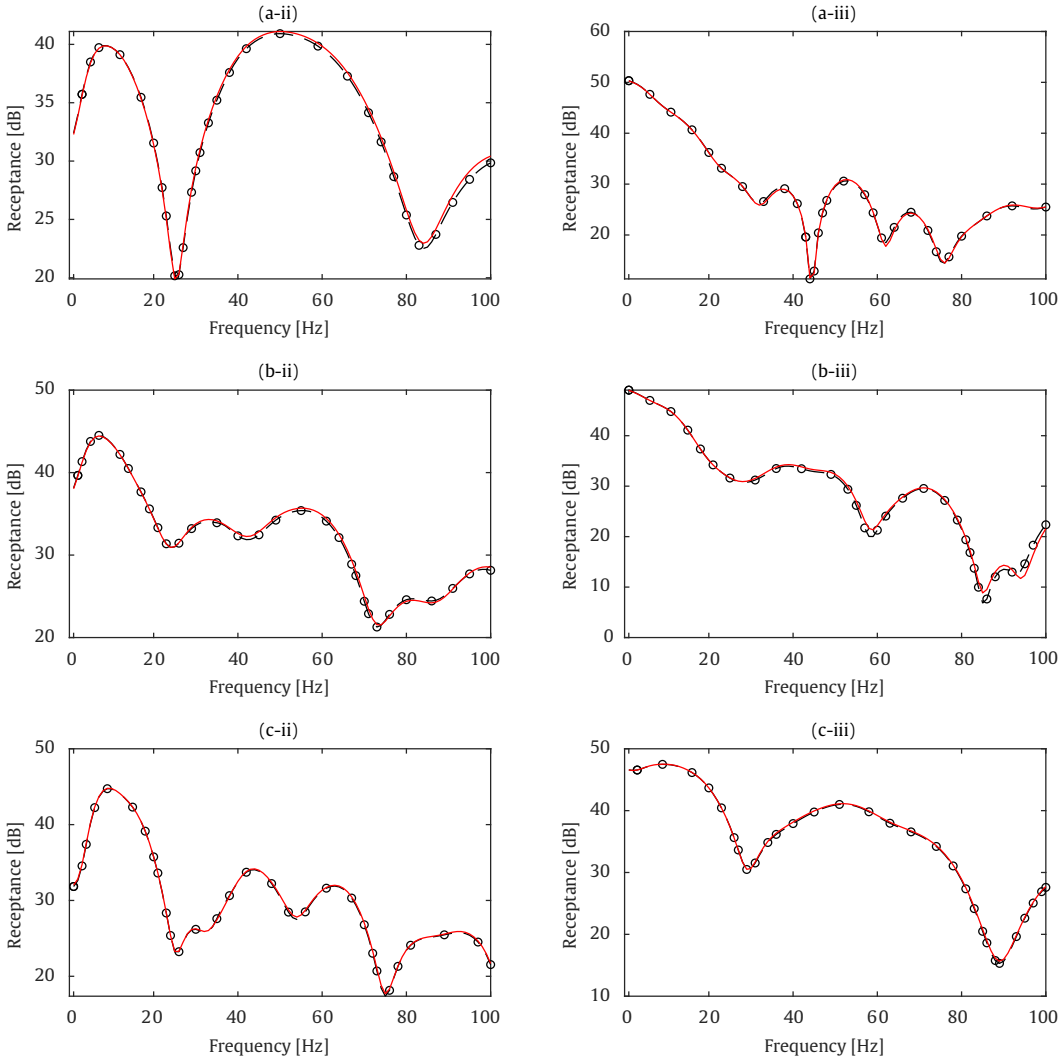

FIGURE 5.13: Receptances for the partially circular shape case at the field points A (a), B (b) and C (c) for y (ii) and z (iii) directions. Methods: 2.5D FEM–MFS (solid red line) and hybrid method (dashed black line with circular markers).

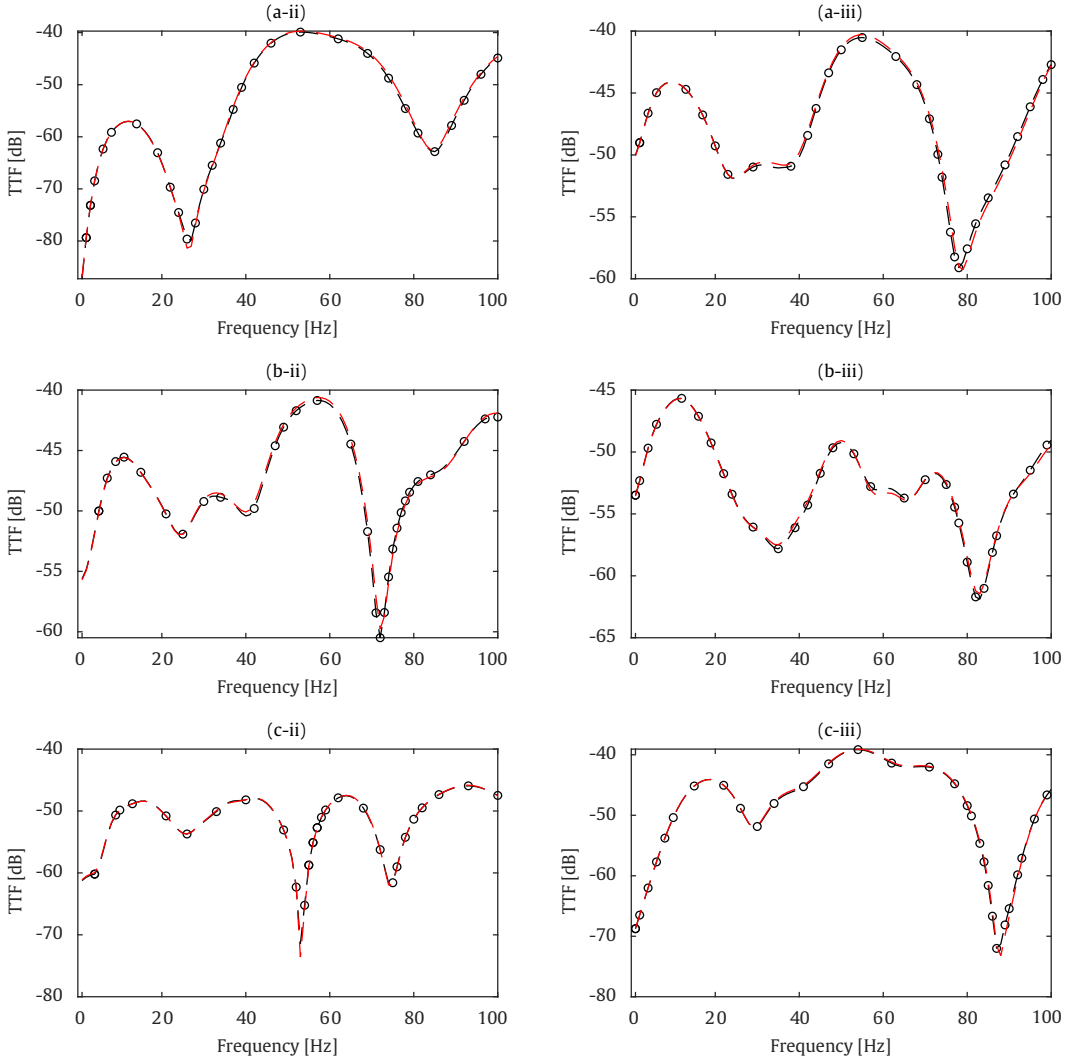

FIGURE 5.14: Traction transfer functions for the partially circular shape case at the field points A (a), B (b) and C (c) for y (ii) and z (iii) directions. Methods: 2.5D FEM–MFS (solid red line) and hybrid method (dashed black line with circular markers).

5.2.2.2 Random distribution of MFS source points

The robustness of the hybrid and 2.5D MFS approaches is again assessed by considering random distributions of MFS sources. Figs. 5.15a and 5.15b illustrate the distribution for one of the randomisation of the MFS sources for the 2.5D MFS and the hybrid methods, respectively. The applied restrictions of this case are corresponding to the ones considered in Section 5.2.1.2. Similar to the case of regular distribution of MFS source points, 65% of the sources are MFS sources and the remaining 35% are of SBM nature.

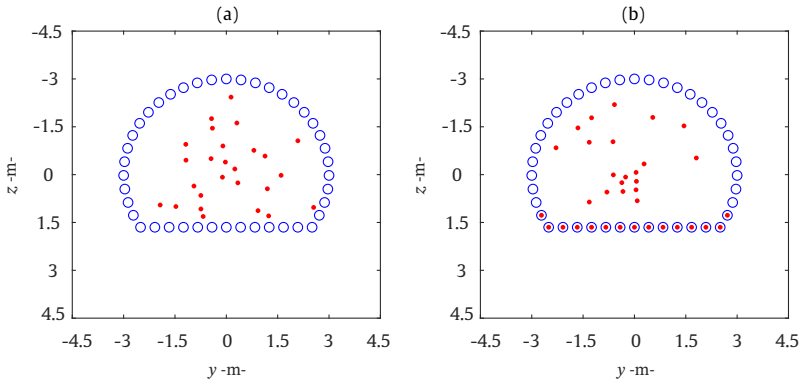

FIGURE 5.15: Examples of distributions of the collocation points (blue) and virtual sources (red) for the partially circular shape case, adopting a random distribution approach for the placement of MFS sources. Methods: full MFS approach (a) and hybrid approach (b).

The RMSE plot associated with the random distribution of the MFS sources is illustrated in Fig. 5.16. Similar to example 1, RMSE analysis is conducted for 100 distinct realisations of random sources distributions. As shown, at 20 Hz the RMSE of the hybrid approach is lower than the one of 2.5D MFS, and it follows the RMSE trend of the 2.5D SBM and the 2.5D BEM with slightly lower accuracy. At 80 Hz, there is a larger difference between the RMSE of the hybrid and the 2.5D MFS. However, this large difference also is observed between the hybrid approach and two other methods (2.5D SBM and 2.5D BEM). The results obtained for this example indicate that the hybrid method can properly deal with the present geometry, showing acceptable levels of accuracy even for random placement of the MFS sources, clearly surpassing the capabilities of the full MFS approach in this regard.

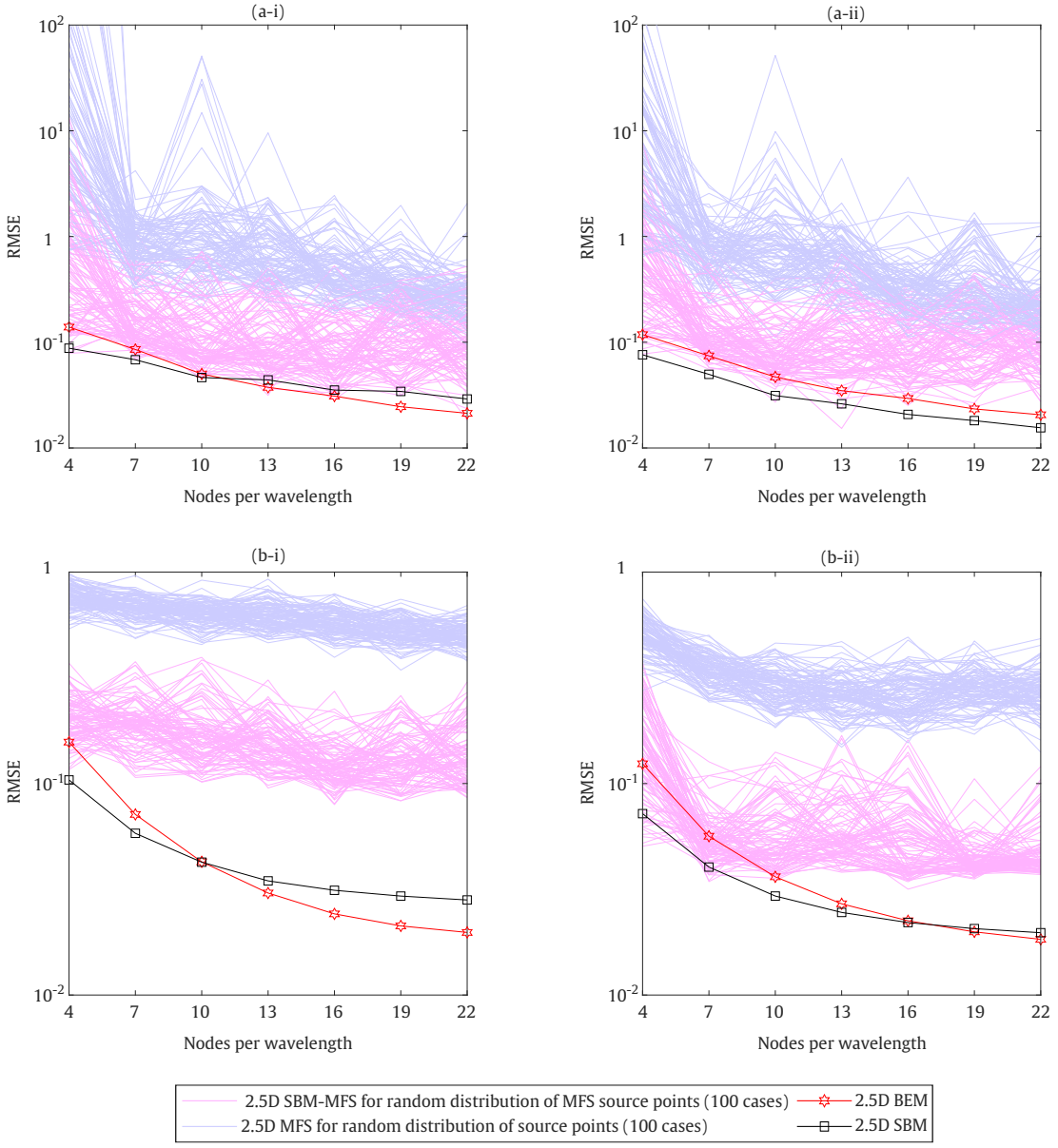

FIGURE 5.16: RMSE for different numerical strategies when considering random distribution of the MFS sources for the case of a partially circular shape. Two sets of evaluation points at radii of 5 m (i) and 20 m (ii) are considered. Calculation frequencies: 20 Hz (a) and 80 Hz (b).

5.2.2.3 Condition number

The conditioning of the system of equation associated with the 2.5D SBM, the 2.5D MFS and the hybrid approaches for the present example is studied in this section. The condition number is calculated for both regular and random distribution of the MFS sources and the results are presented for two wavenumbers (0.1 rad/m

and 1 rad/m) and two frequencies (20 Hz and 80 Hz) in Fig. 5.17. The condition number obtained for the 2.5D SBM shows that, as in example 1, the system of equation is very well-conditioned in this method. The comparison between the 2.5D MFS and the hybrid method for the regular distribution of MFS sources shows that 2.5D MFS suffers from an ill-conditioned system of equation for values above 95 NpW and 47 NpW, at frequencies of 20 Hz and 80 Hz, respectively, while the hybrid method presents an ill-conditioned system of equations for values above 380 NpW and 95 NpW, at frequencies of 20 Hz and 80 Hz, respectively. For the random distribution of the MFS sources, it is observed that the 2.5D MFS presents an ill-conditioned system of equation for values above 47 NpW and 23 NpW, at frequencies of 20 Hz and 80 Hz, respectively. The system of equations delivered by the hybrid approach becomes ill-conditioned for values of NpW above 95 and 47, at frequencies of 20 Hz and 80 Hz, respectively. These results are aligned with the previous findings associated to this example.

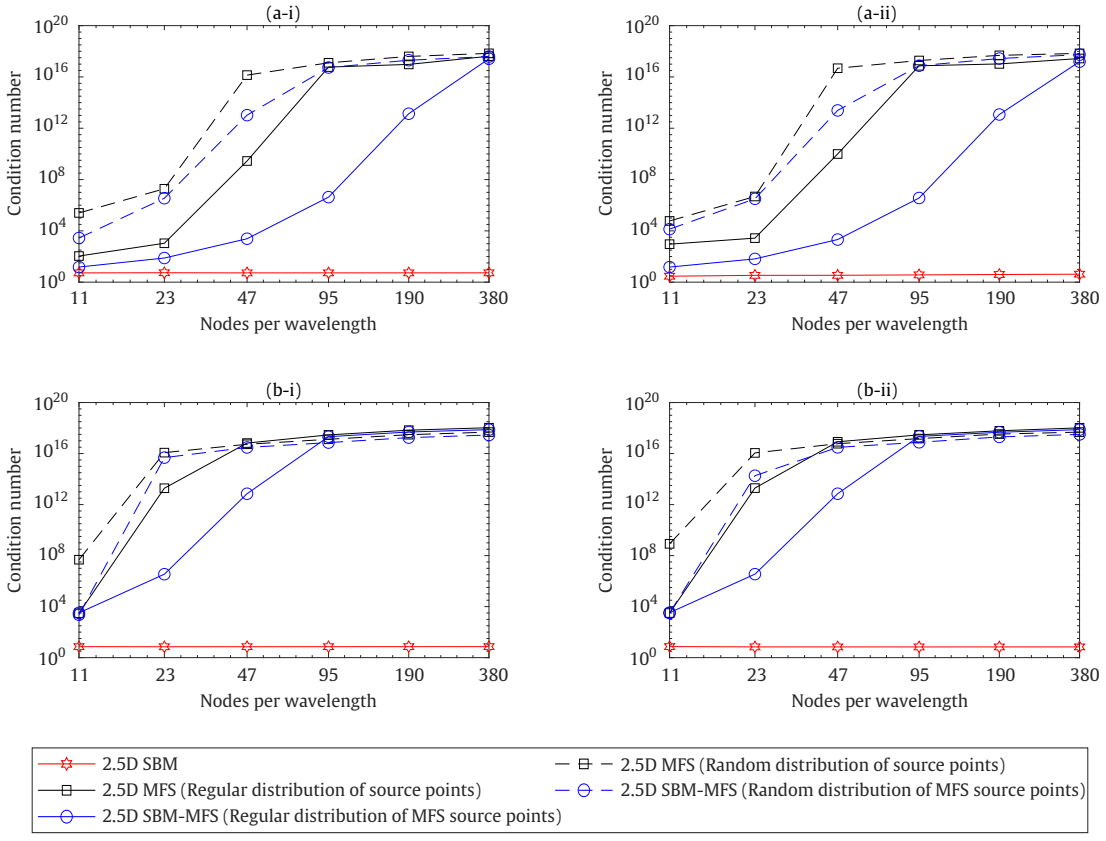

FIGURE 5.17: Condition number with respect to the discretisation density for the 2.5D MFS, the 2.5D SBM, and the hybrid methods in the partially circular shape case at frequencies of 20 Hz (a) and 80 Hz (b) and for wavenumbers of 0.1 rad/m (i) and 1 rad/m (ii).

5.2.3 Example 3: Square shape

As illustrated in Fig. 5.18, a square shape is selected for this example. The length of each side of the square is equal to 6 m, as shown in Fig. 5.18a. The system is excited by a vertical unit load applied at the bottom of the cavity. Since there is no known analytical solution for this geometry, the 2.5D FEM-BEM is taken as the reference method. The FEM mesh and the boundary nodes are indicated in Fig. 5.18b. The RMSE is computed at two distinct sets of test points, both distributed on circles centred at the centre of the tunnel and with radii 7 m and 20 m, representing near-field and far-field positions, respectively. For both sets, the evaluation points are distributed uniformly on the circle perimeter. Two frequencies are chosen for the present RMSE analysis: 20 Hz and 80 Hz. In all the calculations carried out for this example, 30% of the virtual sources are SBM sources and the remaining 70% are MFS sources.

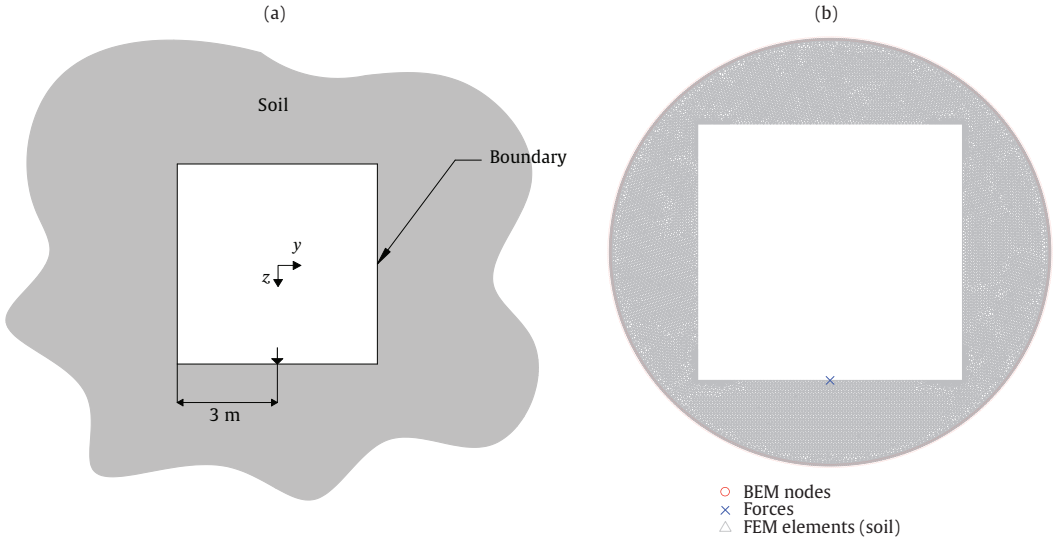

FIGURE 5.18: The geometry and loading pattern of the problem (a) and the mesh considered in the 2.5D FEM-BEM reference solution (b).

5.2.3.1 Regular distribution of MFS source points

For the distribution of the virtual sources in the hybrid approach, the SBM virtual sources are located at the edges of the square, while the MFS source points are employed for the smooth part of the geometry. Also, it is found that placing SBM virtual source at the position of the applied force can boost the accuracy of the

proposed approach. The distributions of the sources associated with full MFS and hybrid methods are shown in Figs. 5.19a and 5.19b, respectively.

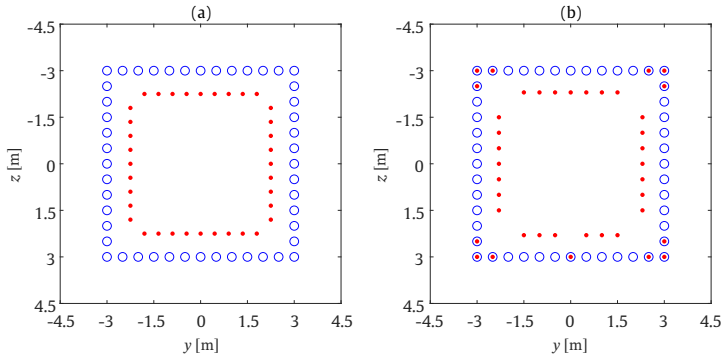

FIGURE 5.19: The collocation points (blue) and virtual sources (red) for the square shape case, adopting a regular distribution approach, for the full MFS (a) and hybrid (b) methods.

In this framework, resulting RMSE for all the methods considered in this case study is shown in Fig. 5.20, the SBM method is the most accurate approach for a frequency of 20 Hz, while SBM and hybrid approaches are the most accurate methods at 80 Hz and from 5 to 15 NpW. Also, it should be noted that, as expected, the MFS does not presents accurate results in any of the cases. Generally, the performance of the proposed hybrid approach in terms of accuracy and stability of the results is almost as good as the ones presented by the SBM approach. Again, to highlight the benefits of the hybrid approach, it is important to mention the previously mentioned potentialities of it in terms of computational performance with respect to full SBM modelling, thanks to the reduction of SBM sources and even total sources.

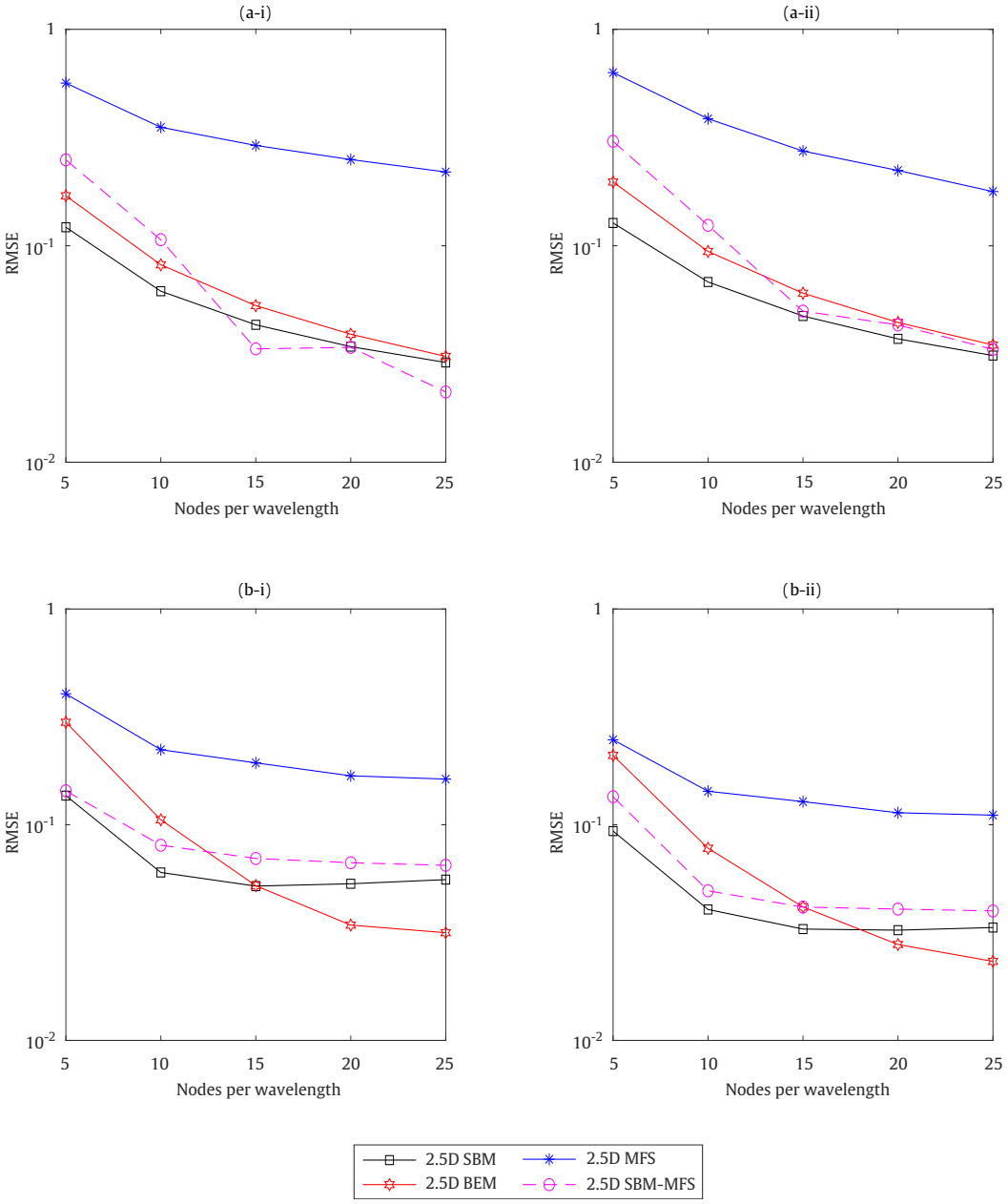

FIGURE 5.20: RMSE for different numerical strategies, considering regular distribution of the MFS sources for the case of a square shape. Two sets of evaluation points at radii of 7 m (i) and 20 m (ii) are considered. Calculation frequencies: 20 Hz (a) and 80 Hz (b).

Similar to example 2, the proposed approach is compared with the 2.5D FEM-MFS for frequencies ranging from 0 to 100 Hz. The mesh used to compute the 2.5D FEM-MFS model is shown in Fig. 5.18b. The receptances and TTF are computed at three defined evaluation points: point A ($x = 0$ m; $y = 6$ m; $z = -6$ m), B ($x = 0$ m; $y = 12$ m; $z = -3$ m) and C ($x = 0$ m; $y = 18$ m; $z = 6$

m). The number of collocation points are constant along the frequency range to ensure 10 NpW and 40 NpW for the hybrid and the 2.5D FEM-MFS methods, respectively, at 100 Hz. From the responses presented in Figs. 5.21 and 5.22, it can be observed that there is a good agreement between the hybrid method and the 2.5D FEM-MFS approach. The largest discrepancies are found at the highest frequencies, which is consistent with the NpW chosen.

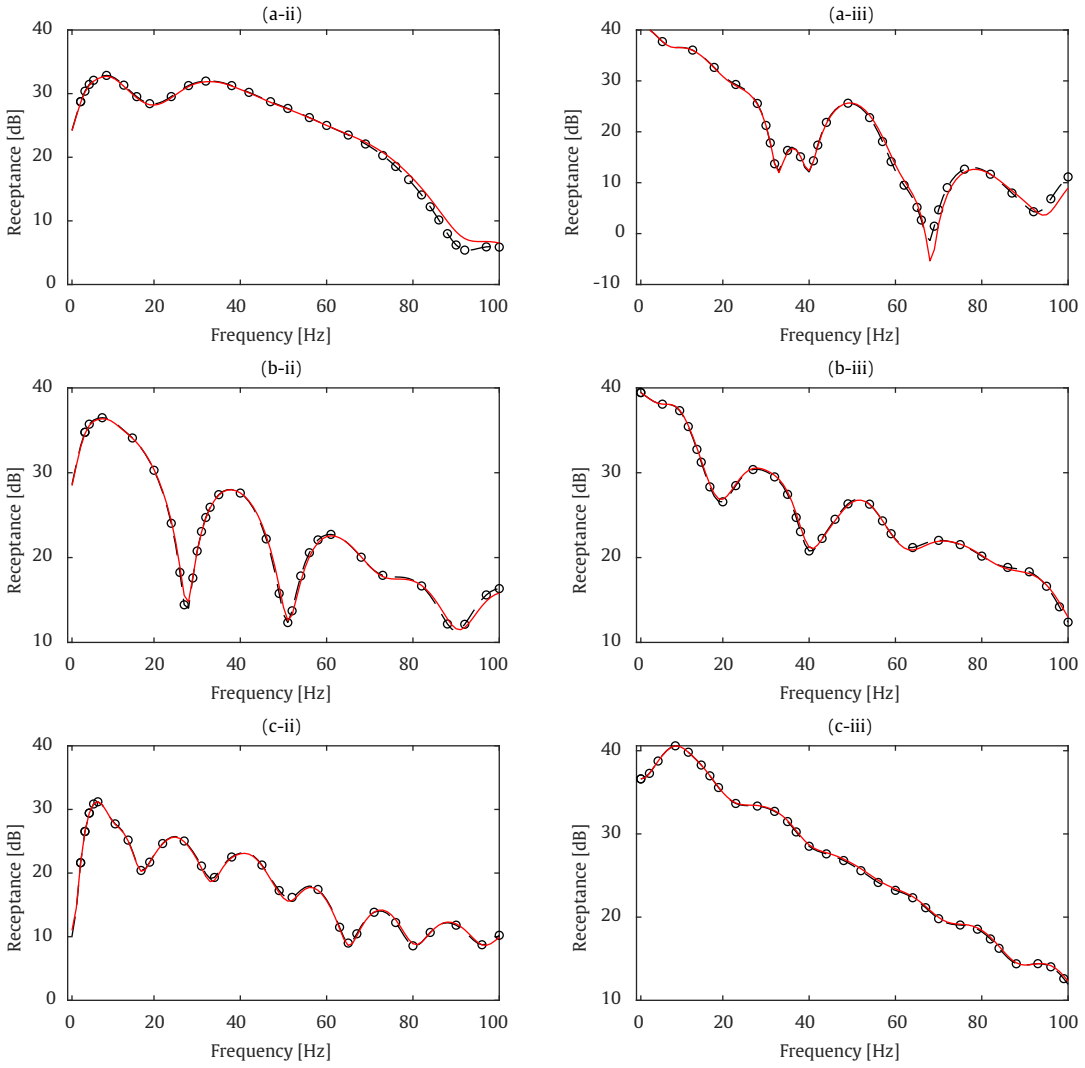

FIGURE 5.21: Receptances for the square shape case at the field points A (a), B (b) and C (c) for y (ii) and z (iii) directions. Methods: 2.5D FEM–MFS (solid red line) and hybrid method (dashed black line with circular markers).

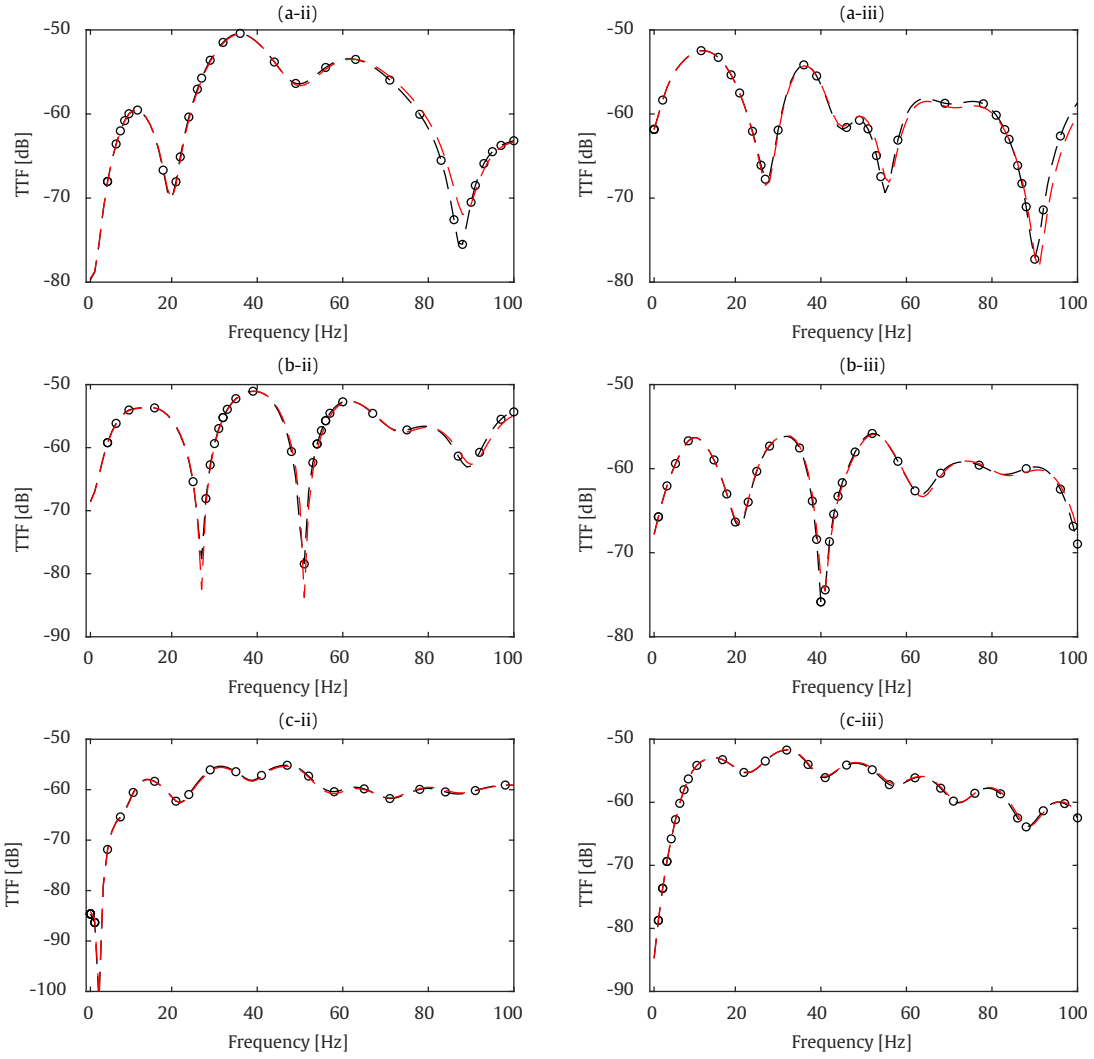

FIGURE 5.22: Traction transfer functions for the square shape case at the field points A (a), B (b) and C (c) for y (ii) and z (iii) directions. Methods: 2.5D FEM–MFS (solid red line) and hybrid method (dashed black line with circular markers).

5.2.3.2 Random distribution of MFS source points

The robustness of the hybrid and 2.5D MFS methods is also evaluated for this example by considering random distributions of MFS sources. Figs. 5.23a and 5.23b show the distribution for one of the randomisation of the MFS sources for the 2.5D MFS and the hybrid methods, respectively. The restrictions to distribute the random MFS sources are similar to the ones presented in Section 5.2.1.2. In the hybrid approach, the position of the SBM sources is the one used in the case of the regular distribution of source points and the MFS sources are distributed

randomly. Similar to the regular distribution of source points, 70% of the sources are MFS sources and the remaining 30% are of SBM nature.

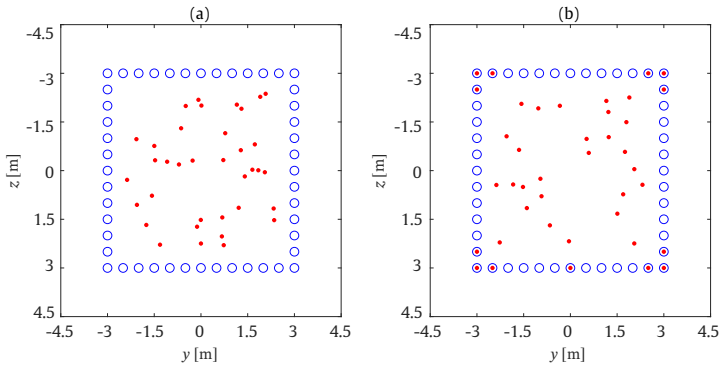

FIGURE 5.23: Examples of distributions of the collocation points (blue) and virtual sources (red) for the square shape case, adopting a random distribution approach for the placement of MFS sources. Methods: full MFS approach (a) and hybrid approach (b).

The RMSE analysis of cases associated with the random distribution of the MFS sources is illustrated in Fig. 5.24. Similar to examples 1 and 2, RMSE analysis is carried out for 100 distinct realisations of random sources distributions. Results show that, in the same manner as demonstrated in example 2, the hybrid method is consistently providing better results than the 2.5D full MFS approach. This result is more clear at 80 Hz than at 20 Hz. However, the hybrid method is less accurate than the 2.5D SBM and the 2.5D BEM for any NpW. It is important to mention that considerable improvement in the performance of the method in comparison with the 2.5D MFS has been achieved by employing only 30% of the SBM sources, an important point to demonstrate the computational benefits of the proposed approach.

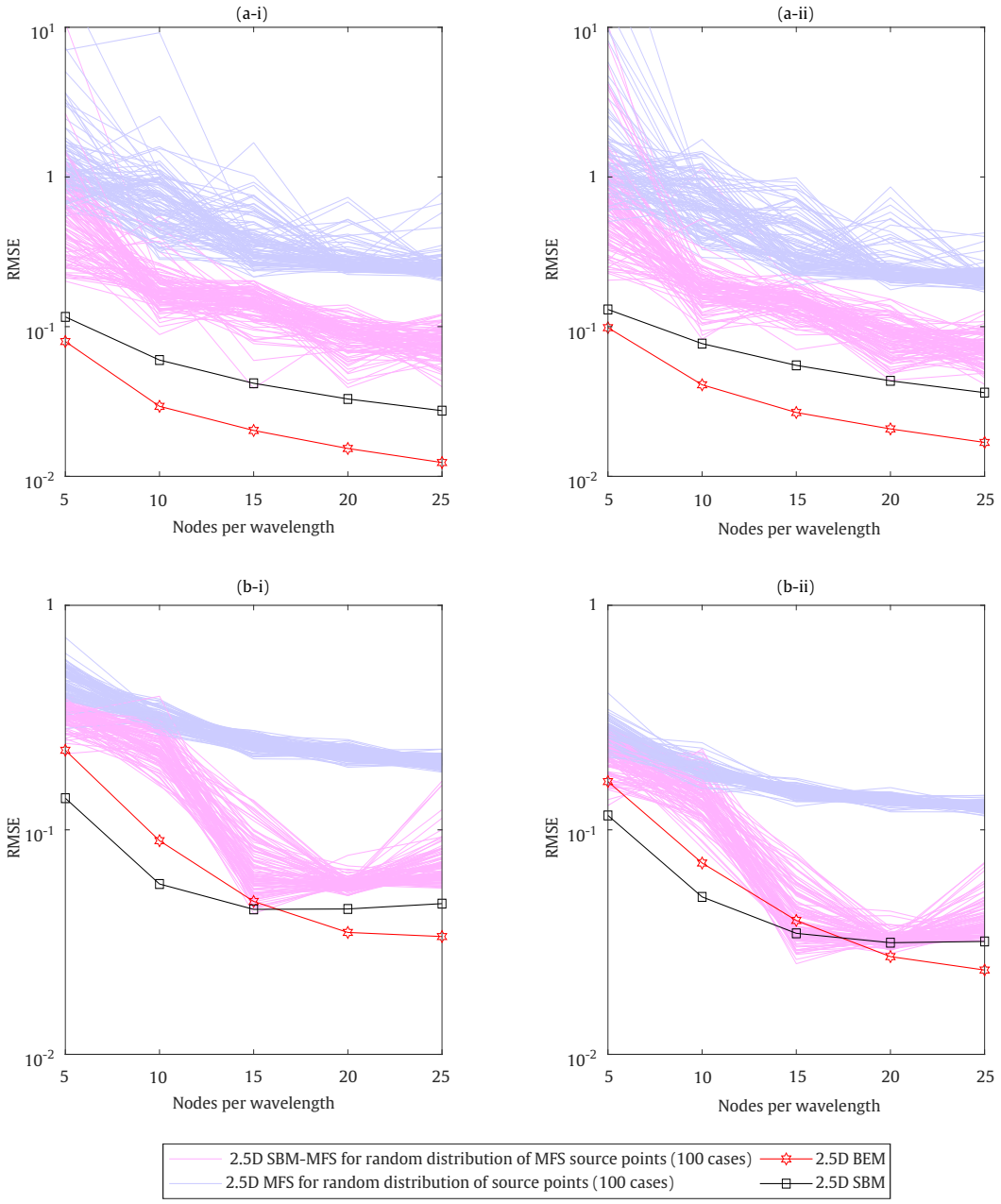

FIGURE 5.24: RMSE for different numerical strategies, considering random distribution of the MFS sources for the case of a square shape. Two sets of evaluation points at radii of 7 m (i) and 20 m (ii) are considered. Calculation frequencies: 20 Hz (a) and 80 Hz (b).

5.2.3.3 Condition number

Similar to previous examples, the condition numbers of the 2.5D SBM, 2.5D MFS and the hybrid approaches are also assessed for a square shape. The considered calculation frequencies, wavenumbers and methodologies used for this example

are the same as those used in example 2. Fig. 5.25 shows the condition number obtained by the three meshless methods. As expected, and similar to previous examples, the condition number for the 2.5D SBM is not sensitive to the number of NpW. For regular distribution of the MFS sources, the 2.5D MFS suffers from the ill-conditioned system of equations for NpW above 95 and 23, at frequencies of 20 Hz and 80 Hz, respectively, while the hybrid method presents an ill-conditioned system of equations for NpW above 380 and 95, at frequencies of 20 Hz and 80 Hz, respectively. For random distribution of MFS sources, the hybrid method is well-conditioned for the considered range of NpW, while the 2.5D MFS has an ill-conditioned system of equations for NpW above 95 and 23, at frequencies of 20 Hz and 80 Hz, respectively.

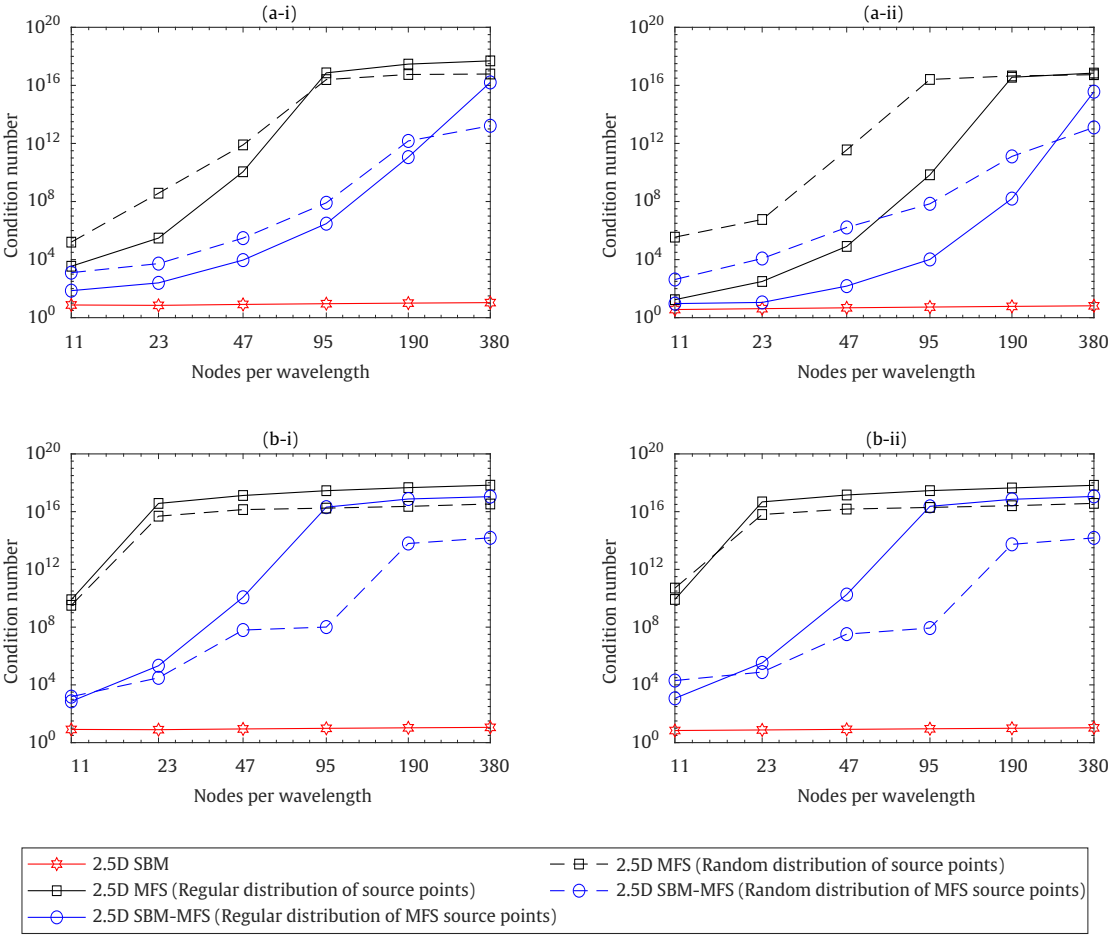

FIGURE 5.25: Condition number with respect to the discretisation density for the 2.5D MFS, the 2.5D SBM, and the hybrid methods in the square shape case at frequencies of 20 Hz (a) and 80 Hz (b) and for wavenumbers of 0.1 rad/m (i) and 1 rad/m (ii).

5.3 Computational efficiency of the method

In this section, the proposed 2.5D MFS, 2.5D SBM-MFS and 2.5D SBM approaches are compared in terms of computational efficiency. It is known that the meshless methods are significantly more efficient than mesh-based numerical strategies such as the 2.5D BEM. Thus, the comparison is only made between the meshless methods previously mentioned. The comparison is performed in the framework of the case study presented in Section 5.2.1.1 and for the evaluation of the receptances at a discrete frequency and for 513 discrete values of the wavenumbers and for 100 field points distributed on a circle centred at the cylinder axis and with radius of 2 m. All three methodologies have been implemented in MATLAB and have been executed using a single core of a high-performance cluster with 2 GHz Intel® Xeon® Gold 6138 CPU (with 40 cores). The computational cost of the three methods is evaluated at a frequency of 250 Hz, considering different values of NpW ranging from 3 to 21. The computational times spent in the previously defined calculations for the 2.5D MFS and 2.5D hybrid SBM-MFS methods are shown in Table. 5.1 in terms of the percentage with respect to the computational cost of the 2.5D SBM.

As shown in Table. 5.1, the 2.5D MFS and the 2.5D SBM-MFS models are more efficient than the 2.5D SBM, where the relative computational cost of the 2.5D MFS and the hybrid methods with respect to the one of the 2.5D SBM are averagely 68% and 81%, respectively. It should be noted that the computational costs presented in this section are calculated for the case of a prescribed Neumann boundary condition, for which, as stated in Eq. (5.3), the determination of the OIFs requires to compute the 2D static traction Green's functions which can be computed just once for all wavenumber and frequency discrete values at which the response is desired to be computed. On the contrary, for the case of Dirichlet boundary conditions, the computational efficiency of the hybrid method with respect to 2.5D SBM is higher, since the OIFs are frequency and wavenumber dependent in this case.

NpW	3	6	9	12	15	18	21
Computational time (2.5D MFS) [%]	70	64	77	57	73	65	72
Computational time (2.5D SBM-MFS) [%]	80	75	88	73	88	87	79

TABLE 5.1: Computational time spent by calculating the receptances of 100 field points using the 2.5D MFS and hybrid methods in percentage with respect to the computational cost of the 2.5D SBM method, considering different NpW.

5.4 Influence of the fictitious eigenfrequencies

The boundary integral equation formulations for exterior problems suffer of loss of solution uniqueness at frequencies close to the eigenvalues of the corresponding interior problem [95], which are called fictitious eigenfrequencies. In this section, the effect of the fictitious eigenfrequencies on the results obtained by the numerical methods considered in this chapter is assessed. To enable detecting those frequencies that are close to the eigenvalues of the corresponding interior problem, no damping is considered for all calculations presented in this section. For 2.5D problems, a set of fictitious eigenfrequencies exist at each wavenumber, resulting in a set of curves in the wavenumber-frequency domain, called dispersion curves. In this regard, the calculation are performed in the framework of the system presented in example 1 and considering 10 NpW at 500 Hz. Hybrid method with the optimal OIB distribution of source points is employed. The RMSE is computed using a alternative version of Eq. (5.6) that considers displacement Green's functions instead of receptance. A total of 100 evaluation points uniformly distributed on circles centred at the cylinder axis and with radius 2 m are considered for the calculations. The colour map plots shown in Fig. 5.26 show the results of the RMSE analysis of the presented 2.5D approaches, considering the semi-analytical solution of a cylindrical cavity as a reference solution. As expected and shown in Fig. 5.4, the 2.5D MFS show high levels of accuracy all along the wavenumber-frequency spectrum [41]. Conversely, the 2.5D BEM and the 2.5D SBM demonstrate a poor accuracy in the areas of influence of fictitious dispersion curves. In the results associated to the newly proposed approach, however, it can be seen that this pattern is clearly attenuated, which is consistent with the fact the MFS, since its sources are placed in the interior domain, naturally overcomes the problems associated with the fictitious eigenfrequencies.

In order to highlight the effect of the fictitious eigenfrequencies, the RMSE calculated using the original Eq. (5.6) (i.e. using receptances) and just considering one evaluation point at $x = 0$, $y = 0$ and $z = -2$ m is presented for a frequency range from 0 to 500 Hz. Results are shown in Fig. 5.27 for the hybrid and full SBM approaches. In accordance of what is shown in Fig. 5.26, the fictitious eigenfrequencies turn the error to be a noisy signal. It can be seen that both methods exhibit similar accuracy at low frequencies, a range where the fictitious eigenfrequencies are not affecting. In contrast, the accuracy of the 2.5D SBM approach drops considerably above 60 Hz which is consistent with the results presented in Fig. 5.26, where the first problems of fictitious eigenfrequencies appear around 60 Hz.

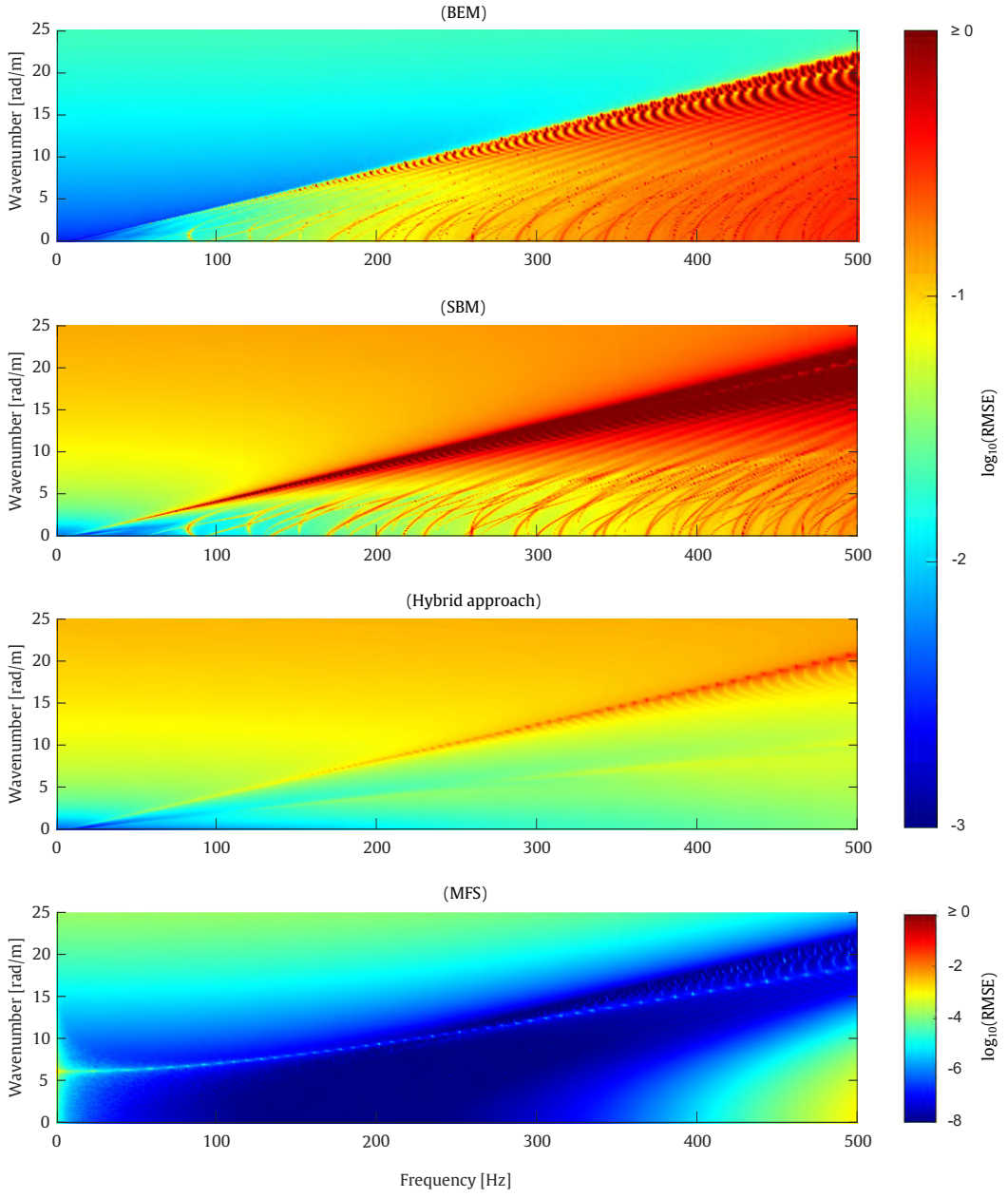

FIGURE 5.26: The comparison of the RMSE of the displacement Green's functions of the considered methods in the wavenumber-frequency domain.

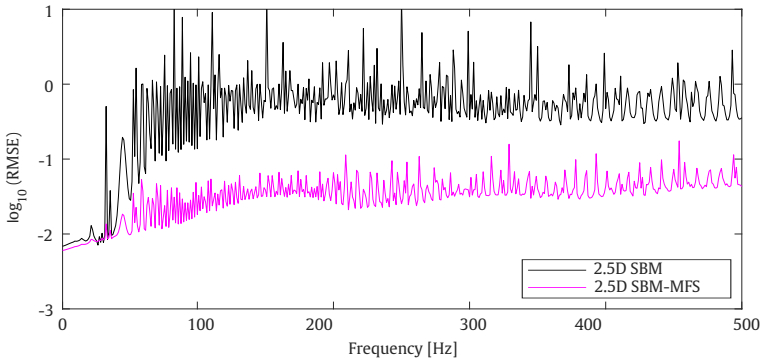

FIGURE 5.27: Errors delivered by the 2.5D SBM and hybrid approach in the calculation of the receptances for the case 1 scenario.

5.5 Conclusions

This chapter has proposed a novel hybrid methodology to simulate wave propagation problems in elastodynamics. In this method, the 2.5D MFS is used to deal with smooth sections of the boundary, while the complex segments are modelled through the 2.5D SBM method. The performance of the new method is compared to other numerical modelling techniques in the framework of three examples, increasing the complexity of the geometry step by step: circular shape, partially circular shape and square geometry. The following conclusions can be drawn from the numerical analyses presented in this chapter:

- For the circular shape of the boundary, the 2.5D MFS is the most accurate method when compared to all other approaches. This is a well-established finding for smooth boundary geometries that can be read in other research works on the topic [91, 96]. Among the compared approaches, the hybrid method presents the most accurate results at the far field. In contrast, as depicted, the accuracy of the hybrid approach is higher than the 2.5D BEM and similar to the 2.5D SBM at near field evaluation points. The accuracy of the hybrid approach in both configurations of the MFS sources (regular and random) is almost the same, while the accuracy of the 2.5D MFS for random distribution of MFS sources case is less than those ones of the regular distribution of MFS sources, which shows the instability of the 2.5D MFS approach.

- The hybrid method is a more robust approach than the 2.5D MFS, since it presents acceptable accuracy when the MFS sources are randomly distributed, a behaviour not seen in the 2.5D MFS, which is clearly unstable assuming this kind of distributions.

- For partially circular geometry, the 2.5D MFS presents the largest errors and a fluctuating behaviour due to the added complexity of the geometry. For the random distribution of MFS sources, the hybrid method shows a great improvement in the RMSE in compare with the MFS. However, its accuracy does not reach to the level of the ones obtained by the 2.5D BEM and the 2.5D SBM methods.

- For square shape, the accuracy of the hybrid method is higher than the one of the 2.5D MFS, while it is approximately the same as the 2.5D BEM and the 2.5D SBM. The inaccurate results obtained by the 2.5D MFS indicate that it is not a suitable approach for the considered geometry. For random distribution of the MFS sources, the difference between the RMSE of the 2.5D MFS and the hybrid method is considerable in all cases. However, its accuracy does not reach the ones of the 2.5D SBM.

- The condition number of the 2.5D SBM method is not sensitive to the number of NpW in all examples which means its system of equation is very well-conditioned. On the contrary, the 2.5D MFS suffers from an ill-conditioned system of equation when a large number of collocation points (or NpW) is considered. The hybrid method shows a remarkable improvement in the condition number comparing with the 2.5D MFS. This improvement can be observed in both types of MFS sources distribution (random and regular distribution of MFS source points).

- The hybrid method is more computationally efficient than the 2.5D SBM since fewer singular terms exist in the hybrid approach, resulting less computational time to compute the OIFs. It is shown that for the circular geometry, where 50% of the virtual sources are selected to be MFS sources and 50% are considered to be the SBM sources, the computational efficiency of the hybrid method is approaching the one of 2.5D MFS. The 2.5D MFS and the 2.5D SBM-MFS models are more efficient than the 2.5D SBM, where the computational cost of the 2.5D MFS and the hybrid method are averagely 68% and 81% of the 2.5D SBM, respectively.

- The fictitious eigenfrequencies negatively influences the accuracy of the 2.5D BEM and 2.5D SBM approaches, while the effects over hybrid approach are insignificant.
- Analogous to the 2.5D SBM and the 2.5D MFS, the implementation procedure of the proposed method is simpler than the ones of integration-based approaches, such as BEM.

To conclude with a general remark, the 2.5D hybrid SBM–MFS methodology is found to be an adequate prediction tool for wave propagation in elastodynamic problems when a method with computational efficiency and, at the same time, and robust of the method are desired.

In this chapter, the hybrid method was simply employed to model the radiation or scattering problems of a cavity in the soil. In the next chapter, it is discussed how to adapt this method to deal with full SSI problems, using this hybrid method to also model the structure.

Chapter 6

A 2.5D hybrid SBM-MFS methodology for soil-structure interaction problems

The previously explained novel 2.5D hybrid SBM-MFS methodology has been further developed to deal with soil-structure interaction problems. In this chapter, the formulation of this new method is outlined, together with a verification study and two application examples. In contrast with the methodologies presented in chapters 3 and 4, the FEM method is no longer used to model the structure in the proposed novel method, which results in a fully meshless approach. The method uses the 2.5D MFS and/or the 2.D hybrid SBM-MFS methods to model the structure and the wave propagation in the soil. Due to the benefits of the meshless methods with respect to the mesh-based (or partially based) approaches, the proposed 2.5D hybrid SBM-MFS method exhibits three main advantages. Firstly, the 2.5D hybrid SBM-MFS is not subjected to any mesh and only requires distributions of collocation points in physical boundaries and/or interfaces of the problem as well as virtual forces on physical and/or auxiliary boundaries to operate. Secondly, this approach is simpler to be implemented. Lastly, the method is in many cases more computationally efficient and lower memory storage is required for analysis due to the dramatic reduction of degrees of freedom involved.

This chapter is organised as follows. In Section 6.1, the formulation of the proposed 2.5D hybrid methodology is presented in detail. In this context, the numerical formulation to model the structure and the elastic wave propagation problem are

presented. Then, in the same section, the coupling strategy between the soil and the structure models is explained. Section 6.2 presents a verification of the novel methodology by comparing its results with the PiP solution considering cylindrical thin shell embedded in a full-space model of the soil. Afterwards, in Section 6.3, the applicability of the proposed method is assessed for the railway soil-tunnel interaction problems in the framework of two examples: a circular railway tunnel (Section 6.3.1) and a cut-and-cover tunnel (Section 6.3.2), both embedded in a soil modelled as a full-space.

6.1 Numerical method formulation

As the name indicates, SSI problems involves at least two distinct domains: the structure and the soil. In previous chapters, the structure was modelled using the FEM due to the geometrical flexibility of the method. The present novel method proposes, in contrast, to use also the 2.5D SBM-MFS developed in the previous chapter to model the structure too. In should be noted, however, that due to the boundary nature of the method, it is only valid for homogeneous structures, which is normally the case of a railway tunnel, for example. A general overview of the system to be modelled with the new approach is presented in Fig. 6.1, where the structure is denoted by Ω_1 and the surrounding medium by Ω_2. Moreover, the boundary interface between the soil and structure is referred by Γ_1 while the interior boundary of the structure, which will not be considered for completely solid structures, is also presented.

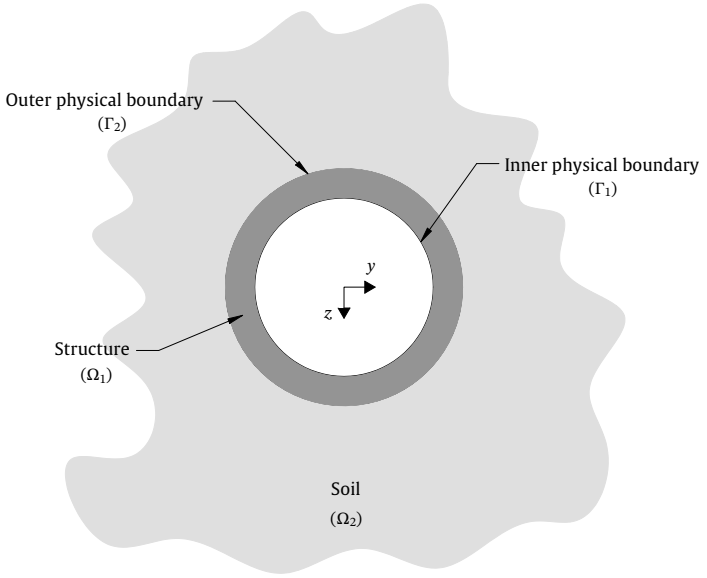

FIGURE 6.1: General description of the proposed 2.5D coupled SBM-MFS methodology.

Fig. 6.2 illustrates the uncoupled soil-structure methodology proposed in the present chapter. As shown in this figure, the methodology consists of two general steps. As indicated in Fig. 6.2a, first of all, the resulted displacements and the tractions at the soil-structure interface (Γ_2) due to the excitation of a structure Ω_1 embedded inside the medium Ω_2 are calculated, using two sets of virtual sources (S_1 and S_2) that comply with the boundary conditions evaluated in the collocation points. The

coupling between the two sub-systems is done by compatibility of displacements and tractions on the boundary (Γ_2). In the second step, as shown in Fig. 6.2b, the desired displacement and traction fields on the soil are computed using a set of virtual sources (S_3) and the collocation points in the second sub-domain (Ω_2). It should be noted that for each domain of the problem, the method to be employed can be decided based on the smoothness of the geometry. Thus, for the smooth geometries (such as circles and ellipses), the 2.5D MFS can be a proper choice and for the more complex geometries (such as a rectangle), the hybrid method can be selected. The detailed formulations for the structure and its coupling with the soil are explained in the following. In the same manner, as in previous chapters, the bar notation is used to represent that a variable is defined in the wavenumber domain, and capital notation is employed for frequency domain variables. Therefore, the dynamic Green's functions are denoted with capital-bar notation and static Green's functions are denoted just with capital notation.

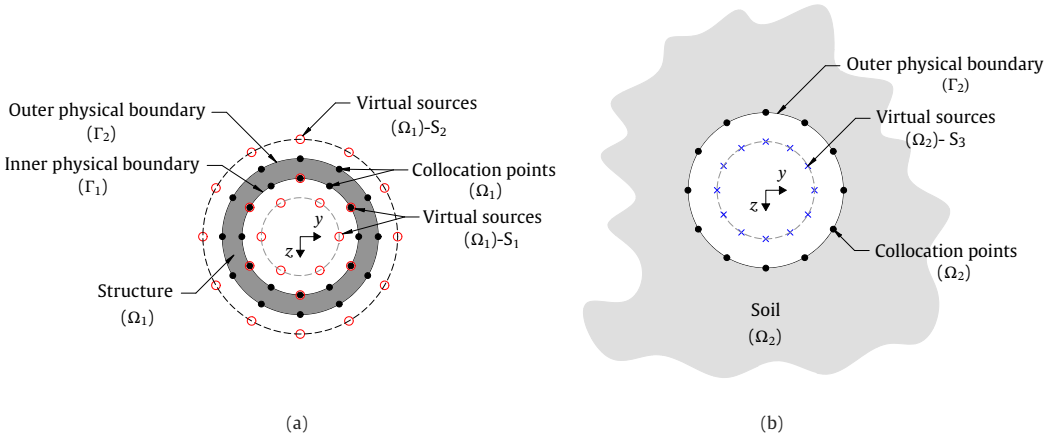

FIGURE 6.2: General description of the proposed 2.5D hybrid SBM-MFS methodology. The problem descriptions are associated with the model of the structure (a), the soil (b).

Prior to developing the formulations of the proposed method, the sets of collocations points and virtual source points associated with the considered soil-structure system are firstly introduced. The set of collocation points associated with the two boundaries of the considered system are defined as

$$\left\{\boldsymbol{y}_1^1, \cdots, \boldsymbol{y}_1^{N_1}\right\} = \left\{\boldsymbol{y}_{S,1}^1, \cdots, \boldsymbol{y}_{S,1}^{N_{1,S}}\right\} \cup \left\{\boldsymbol{y}_{M,1}^1, \cdots, \boldsymbol{y}_{M,1}^{N_{1,M}}\right\} \subset \Gamma_1, \tag{6.1}$$

$$\left\{\boldsymbol{y}_2^1,\cdots,\boldsymbol{y}_2^{N_2}\right\}=\left\{\boldsymbol{y}_{S,2}^1,\cdots,\boldsymbol{y}_{S,2}^{N_{2,S}}\right\}\cup\left\{\boldsymbol{y}_{M,2}^1,\cdots,\boldsymbol{y}_{M,2}^{N_{2,M}}\right\}\subset\mathit{\Gamma}_2, \tag{6.2}$$

where $\boldsymbol{y}_1^m$ and $\boldsymbol{y}_2^m$ are the positions of collocation points located on the inner and outer boundaries, respectively, and where N_1 and N_2 denote the total number of collocation points considered on these boundaries. As in the previous chapter, the subscript/superscript M is used for the collocation points that are not coincident with virtual sources (MFS sources), while the subscript/superscript S is used for the collocation points coincident with the virtual sources (SBM sources). Thus, the terms $\boldsymbol{y}_{S,1}^m$ and $\boldsymbol{y}_{M,1}^m$ represent the mth collocation points coincident and not coincident with virtual source points, respectively, all located on the inner boundary. The terms $\boldsymbol{y}_{S,2}^m$ and $\boldsymbol{y}_{M,2}^m$ can be defined correspondingly, being these ones located on the outer boundary.

The position and strengths of the virtual sources associated to the inner boundary of the structure are

$$\left\{\boldsymbol{x}_1^1,\cdots,\boldsymbol{x}_1^{N_1}\right\}=\left\{\boldsymbol{x}_{S,1}^1,\cdots,\boldsymbol{x}_{S,1}^{N_{1,S}}\right\}\cup\left\{\boldsymbol{x}_{M,1}^1,\cdots,\boldsymbol{x}_{M,1}^{N_{1,M}}\right\}\subset\mathit{\Gamma}_1, \tag{6.3a}$$

$$\bar{\boldsymbol{S}}^{(1)}=\left\{\bar{\boldsymbol{S}}_1^{(1)},\cdots,\bar{\boldsymbol{S}}_{N_1}^{(1)}\right\}=\left\{\bar{\boldsymbol{S}}_{S,1}^{(1)},\cdots,\bar{\boldsymbol{S}}_{S,N_{1,S}}^{(1)}\right\}\cup\left\{\bar{\boldsymbol{S}}_{M,1}^{(1)},\cdots,\bar{\boldsymbol{S}}_{M,N_{1,M}}^{(1)}\right\}, \tag{6.3b}$$

where the terms $\boldsymbol{x}_{S,1}^m$ and $\boldsymbol{x}_{M,1}^m$ represent the location of the mth SBM and MFS virtual sources, respectively, and the terms $\boldsymbol{S}_{S,1}^m$ and $\boldsymbol{S}_{M,1}^m$ denote their corresponding source strengths.

Equivalent definitions are used for the virtual sources associated to the outer boundary of the structure

$$\left\{\boldsymbol{x}_{21}^1,\cdots,\boldsymbol{x}_{21}^{N_2}\right\}=\left\{\boldsymbol{x}_{S,21}^1,\cdots,\boldsymbol{x}_{S,21}^{N_{21,S}}\right\}\cup\left\{\boldsymbol{x}_{M,21}^1,\cdots,\boldsymbol{x}_{M,21}^{N_{21,M}}\right\}\subset(\mathit{\Gamma}_2,\mathit{\Omega}_1), \tag{6.4a}$$

$$\bar{\boldsymbol{S}}^{(21)}=\left\{\bar{\boldsymbol{S}}_1^{(21)},\cdots,\bar{\boldsymbol{S}}_{N_2}^{(21)}\right\}=\left\{\bar{\boldsymbol{S}}_{S,1}^{(21)},\cdots,\bar{\boldsymbol{S}}_{S,N_{21,S}}^{(21)}\right\}\cup\left\{\bar{\boldsymbol{S}}_{M,1}^{(21)},\cdots,\bar{\boldsymbol{S}}_{M,N_{21,M}}^{(21)}\right\}, \tag{6.4b}$$

where the subscripts/superscripts (21) are used to express that the sources are associated to the interface Γ_2, when the domain Ω_1 is considered.

In a similar way, the virtual sources associated to the inner boundary of the soil are

$$\left\{\boldsymbol{x}_{22}^{1},\cdots,\boldsymbol{x}_{22}^{N_2}\right\}=\left\{\boldsymbol{x}_{S,22}^{1},\cdots,\boldsymbol{x}_{S,22}^{N_{22,S}}\right\}\cup\left\{\boldsymbol{x}_{M,22}^{1},\cdots,\boldsymbol{x}_{M,22}^{N_{22,M}}\right\}\subset(\mathit{\Gamma}_2,\mathit{\Omega}_2), \tag{6.5a}$$

$$\bar{\boldsymbol{S}}^{(22)}=\left\{\bar{\boldsymbol{S}}_{1}^{(22)},\cdots,\bar{\boldsymbol{S}}_{N_2}^{(22)}\right\}=\left\{\bar{\boldsymbol{S}}_{S,1}^{(22)},\cdots,\bar{\boldsymbol{S}}_{S,N_{22,S}}^{(22)}\right\}\cup\left\{\bar{\boldsymbol{S}}_{M,1}^{(22)},\cdots,\bar{\boldsymbol{S}}_{M,N_{22,M}}^{(22)}\right\}, \tag{6.5b}$$

where the subscripts/superscripts (22) refers to the same interface as in the previous case (Γ_2), but when the domain Ω_2 is considered.

In the presented formulation the wavefield within Ω_1 is expressed as the one generated by the two sets of virtual sources presented in Eqs. (6.3) and (6.4) [97]. Therefore, the displacement and traction fields within this domain can be expressed as

$$\begin{aligned}\bar{\boldsymbol{U}}(\boldsymbol{y})=&\sum_{n=1}^{N_{1,S}}\bar{\mathbf{H}}(\boldsymbol{y},\boldsymbol{x}_{S,1}^{n})\bar{\boldsymbol{S}}_{S,n}^{(1)}+\sum_{n=1}^{N_{1,M}}\bar{\mathbf{H}}(\boldsymbol{y},\boldsymbol{x}_{M,1}^{n})\bar{\boldsymbol{S}}_{M,n}^{(1)}\\&+\sum_{n=1}^{N_{21,S}}\bar{\mathbf{H}}(\boldsymbol{y},\boldsymbol{x}_{S,21}^{n})\bar{\boldsymbol{S}}_{S,n}^{(21)}+\sum_{n=1}^{N_{21,M}}\bar{\mathbf{H}}(\boldsymbol{y},\boldsymbol{x}_{M,21}^{n})\bar{\boldsymbol{S}}_{M,n}^{(21)},\end{aligned} \tag{6.6}$$

$$\begin{aligned}\bar{\boldsymbol{T}}(\boldsymbol{y})=&\sum_{n=1}^{N_{1,S}}\bar{\mathbf{H}}^{\tau}(\boldsymbol{y},\boldsymbol{x}_{S,1}^{n})\bar{\boldsymbol{S}}_{S,n}^{(1)}+\sum_{n=1}^{N_{1,M}}\bar{\mathbf{H}}^{\tau}(\boldsymbol{y},\boldsymbol{x}_{M,1}^{n})\bar{\boldsymbol{S}}_{M,n}^{(1)}\\&+\sum_{n=1}^{N_{21,S}}\bar{\mathbf{H}}^{\tau}(\boldsymbol{y},\boldsymbol{x}_{S,21}^{n})\bar{\boldsymbol{S}}_{S,n}^{(21)}+\sum_{n=1}^{N_{21,M}}\bar{\mathbf{H}}^{\tau}(\boldsymbol{y},\boldsymbol{x}_{M,21}^{n})\bar{\boldsymbol{S}}_{M,n}^{(21)},\end{aligned} \tag{6.7}$$

where $\bar{\boldsymbol{U}}(\boldsymbol{y})$ and $\bar{\boldsymbol{T}}(\boldsymbol{y})$ are the displacements and tractions of the structure, respectively, at an arbitrary field point $\boldsymbol{y}$ caused by the sets of virtual sources. As in previous chapters, $\bar{\mathbf{H}}(y,x)$ and $\bar{\mathbf{H}}^{\tau}(y,x)$ are the displacement and traction dynamic Green's functions at $\boldsymbol{y}$, due to a load applied at $\boldsymbol{x}$.

On the other hand, the wavefield within Ω_2 is defined as the one generated by the set of virtual sources presented in Eq. (6.5). The displacement and traction fields within this domain are given by

$$\bar{\boldsymbol{U}}(\boldsymbol{y})=\sum_{n=1}^{N_{22,S}}\bar{\mathbf{H}}(\boldsymbol{y},\boldsymbol{x}_{S,22}^{n})\bar{\boldsymbol{S}}_{S,n}^{(22)}+\sum_{n=1}^{N_{22,M}}\bar{\mathbf{H}}(\boldsymbol{y},\boldsymbol{x}_{M,22}^{n})\bar{\boldsymbol{S}}_{M,n}^{(22)}, \tag{6.8}$$

$$\bar{\boldsymbol{T}}(\boldsymbol{y}) = \sum_{n=1}^{N_{22,S}} \bar{\mathbf{H}}^{\tau}(\boldsymbol{y}, \boldsymbol{x}_{S,22}^{n}) \bar{\boldsymbol{S}}_{S,n}^{(22)} + \sum_{n=1}^{N_{22,M}} \bar{\mathbf{H}}^{\tau}(\boldsymbol{y}, \boldsymbol{x}_{M,22}^{n}) \bar{\boldsymbol{S}}_{M,n}^{(22)}, \tag{6.9}$$

where in this case, $\bar{\mathbf{H}}$ and $\bar{\mathbf{H}}^{\tau}$ are the displacement and traction dynamic Green's functions associated with the soil.

The singularities that arise when the response of a collocation point geometrically coincident with a virtual source is considered are avoided using, as in previous chapters, OIFs. Therefore, when the collocation point $\boldsymbol{y} = \boldsymbol{y}_{S,1}^{m}$ is considered, Eqs. (6.6) and (6.7) become [19, 54]

$$\begin{aligned} \bar{\boldsymbol{U}}(\boldsymbol{y}_{S,1}^{m}) = & \sum_{n=1, n\neq m}^{N_{1,S}} \bar{\mathbf{H}}(\boldsymbol{y}_{S,1}^{m}, \boldsymbol{x}_{S,1}^{n}) \bar{\boldsymbol{S}}_{S,n}^{(1)} + \sum_{n=1}^{N_{1,M}} \bar{\mathbf{H}}(\boldsymbol{y}_{S,1}^{m}, \boldsymbol{x}_{M,1}^{n}) \bar{\boldsymbol{S}}_{M,n}^{(1)} + \bar{\mathbf{H}}_{mm}^{(1)} \bar{\boldsymbol{S}}_{S,m}^{(1)} \\ & + \sum_{n=1}^{N_{21,S}} \bar{\mathbf{H}}(\boldsymbol{y}_{S,1}^{m}, \boldsymbol{x}_{S,21}^{n}) \bar{\boldsymbol{S}}_{S,n}^{(21)} + \sum_{n=1}^{N_{21,M}} \bar{\mathbf{H}}(\boldsymbol{y}_{S,1}^{m}, \boldsymbol{x}_{M,21}^{n}) \bar{\boldsymbol{S}}_{M,n}^{(21)}, \end{aligned} \tag{6.10}$$

$$\begin{aligned} \bar{\boldsymbol{T}}(\boldsymbol{y}_{S,1}^{m}) = & \sum_{n=1, n\neq m}^{N_{1,S}} \bar{\mathbf{H}}^{\tau}(\boldsymbol{y}_{S,1}^{m}, \boldsymbol{x}_{S,1}^{n}) \bar{\boldsymbol{S}}_{S,n}^{(1)} + \sum_{n=1}^{N_{1,M}} \bar{\mathbf{H}}^{\tau}(\boldsymbol{y}_{S,1}^{m}, \boldsymbol{x}_{M,1}^{n}) \bar{\boldsymbol{S}}_{M,n}^{(1)} + \bar{\mathbf{H}}_{mm}^{\tau(1)} \bar{\boldsymbol{S}}_{S,m}^{(1)} \\ & + \sum_{n=1}^{N_{21,S}} \bar{\mathbf{H}}^{\tau}(\boldsymbol{y}_{S,1}^{m}, \boldsymbol{x}_{S,21}^{n}) \bar{\boldsymbol{S}}_{S,n}^{(21)} + \sum_{n=1}^{N_{21,M}} \bar{\mathbf{H}}^{\tau}(\boldsymbol{y}_{S,1}^{m}, \boldsymbol{x}_{M,21}^{n}) \bar{\boldsymbol{S}}_{M,n}^{(21)}, \end{aligned} \tag{6.11}$$

where $\bar{\mathbf{H}}_{mm}^{(i)}$ and $\bar{\mathbf{H}}_{mm}^{\tau(i)}$ are, respectively, the displacement and traction OIFs associated to the source strength $\bar{\boldsymbol{S}}_{S,m}^{(i)}$.

Similarly, when $\boldsymbol{y} = \boldsymbol{y}_{S,2}^{m}$, Eqs. (6.6) and (6.7) become

$$\begin{aligned} \bar{\boldsymbol{U}}^{\Omega_1}(\boldsymbol{y}_{S,2}^{m}) = & \sum_{n=1}^{N_{1,S}} \bar{\mathbf{H}}(\boldsymbol{y}_{S,2}^{m}, \boldsymbol{x}_{S,1}^{n}) \bar{\boldsymbol{S}}_{S,n}^{(1)} + \sum_{n=1}^{N_{1,M}} \bar{\mathbf{H}}(\boldsymbol{y}_{S,2}^{m}, \boldsymbol{x}_{M,1}^{n}) \bar{\boldsymbol{S}}_{M,n}^{(1)} \\ & + \sum_{n=1, n\neq m}^{N_{21,S}} \bar{\mathbf{H}}(\boldsymbol{y}_{S,2}^{m}, \boldsymbol{x}_{S,21}^{n}) \bar{\boldsymbol{S}}_{S,n}^{(21)} + \sum_{n=1}^{N_{21,M}} \bar{\mathbf{H}}(\boldsymbol{y}_{S,2}^{m}, \boldsymbol{x}_{M,21}^{n}) \bar{\boldsymbol{S}}_{M,n}^{(21)} \\ & + \bar{\mathbf{H}}_{mm}^{(21)} \bar{\boldsymbol{S}}_{S,m}^{(21)}, \end{aligned} \tag{6.12}$$

$$\begin{aligned}\bar{\boldsymbol{T}}^{\Omega_1}(\boldsymbol{y}_{S,2}^m) = &\sum_{n=1}^{N_{1,S}} \bar{\mathbf{H}}^{\tau}(\boldsymbol{y}_{S,2}^m, \boldsymbol{x}_{S,1}^n)\bar{\boldsymbol{S}}_{S,n}^{(1)} + \sum_{n=1}^{N_{1,M}} \bar{\mathbf{H}}^{\tau}(\boldsymbol{y}_{S,2}^m, \boldsymbol{x}_{M,1}^n)\bar{\boldsymbol{S}}_{M,n}^{(1)} \\ &+ \sum_{n=1,n\neq m}^{N_{21,S}} \bar{\mathbf{H}}^{\tau}(\boldsymbol{y}_{S,2}^m, \boldsymbol{x}_{S,21}^n)\bar{\boldsymbol{S}}_{S,n}^{(21)} + \sum_{n=1}^{N_{21,M}} \bar{\mathbf{H}}^{\tau}(\boldsymbol{y}_{S,2}^m, \boldsymbol{x}_{M,21}^n)\bar{\boldsymbol{S}}_{M,n}^{(21)} \\ &+ \bar{\mathbf{H}}_{mm}^{\tau(21)}\bar{\boldsymbol{S}}_{S,m}^{(21)},\end{aligned} \tag{6.13}$$

where the superscript Ω_1 has been added to express that the resulting displacements and tractions are associated to the structure subsystem.

The same strategy is considered for collocation points geometrically coincident with virtual sources in the soil subsystem. In this regard, when $\boldsymbol{y} = \boldsymbol{y}_{S,2}^m$, Eqs. (6.8) and (6.9) become

$$\begin{aligned}\bar{\boldsymbol{U}}^{\Omega_2}(\boldsymbol{y}_{S,2}^m) = &\sum_{n=1,n\neq m}^{N_{22,S}} \bar{\mathbf{H}}(\boldsymbol{y}_{S,2}^m, \boldsymbol{x}_{S,22}^n)\bar{\boldsymbol{S}}_{S,n}^{(22)} + \sum_{n=1}^{N_{22,M}} \bar{\mathbf{H}}(\boldsymbol{y}_{S,2}^m, \boldsymbol{x}_{M,22}^n)\bar{\boldsymbol{S}}_{M,n}^{(22)} \\ &+ \bar{\mathbf{H}}_{mm}^{(22)}\bar{\boldsymbol{S}}_{S,m}^{(22)},\end{aligned} \tag{6.14}$$

$$\begin{aligned}\bar{\boldsymbol{T}}^{\Omega_2}(\boldsymbol{y}_{S,2}^m) = &\sum_{n=1,n\neq m}^{N_{22,S}} \bar{\mathbf{H}}^{\tau}(\boldsymbol{y}_{S,2}^m, \boldsymbol{x}_{S,22}^n)\bar{\boldsymbol{S}}_{S,n}^{(22)} + \sum_{n=1}^{N_{22,M}} \bar{\mathbf{H}}^{\tau}(\boldsymbol{y}_{S,2}^m, \boldsymbol{x}_{M,22}^n)\bar{\boldsymbol{S}}_{M,n}^{(22)} \\ &+ \bar{\mathbf{H}}_{mm}^{\tau(22)}\bar{\boldsymbol{S}}_{S,m}^{(22)},\end{aligned} \tag{6.15}$$

where the superscript Ω_2 states that the resulting displacements and tractions are associated to the soil subsystem.

As in previous chapters, the OIFs associated with Neumann boundary conditions ($\bar{\mathbf{H}}_{mm}^{\tau}$) are obtained by applying a substracting and adding-back technique to the corresponding singular equation. The resulting expression is

$$\begin{aligned}\bar{\mathbf{H}}_{mm}^{\tau} = &\frac{1}{L_m}\left[\kappa\mathbf{I} + \int_{\Gamma_m}\left[\mathbf{H}^{\tau}(\boldsymbol{y}^m, \boldsymbol{y}) + \mathbf{H}^{\tau}(\boldsymbol{y}, \boldsymbol{y}^m)\right]\mathrm{d}\Gamma_m(\boldsymbol{x})\right. \\ &\left. - \sum_{n=1,n\neq m}^{N} L_n\mathbf{H}^{\tau}(\boldsymbol{y}^n, \boldsymbol{y}_S^m)\right],\end{aligned} \tag{6.16}$$

where $\mathbf{H}^{\tau}(\boldsymbol{y}^n, \boldsymbol{y}_S^m)$ is the elastostatic traction Green's functions of the plane strain case associated to the exterior domain problem, Γ_{m} is the segment of the boundary with length L_m on which the mth collocation point coincident with a virtual source

is located, $\mathbf{I}$ is the identity matrix and term κ is defined as

$$\kappa = \begin{cases} 1, & \text{for exterior problems,} \\ 0, & \text{for interior problems.} \end{cases} \tag{6.17}$$

It should be noted that the OIFs appearing in Eqs. (6.10) and (6.11) are associated with the exterior problem and the structure domain, the OIFs in Eqs. (6.14) and (6.15) are associated with the exterior problem and the soil domain, and the ones in Eqs. (6.12) and (6.13) correspond to the interior problem and the structure domain.

The procedure to overcome the singularities for Dirichlet boundary conditions ($\bar{\mathbf{H}}_{mm}$) is the same one that has been used in previous chapters, which consisted on averaging the value of the fundamental solution over Γ_m. Additional details can be found in Chapter 4 (Section 4.1.1) and Chapter 5 (Section 5.1).

Regarding the response of collocations points not coincident with any virtual source point, it should be noted that in these cases no singularity arises. Therefore, Eqs. (6.6)-(6.9) can be directly employed to obtain the responses of interest.

When the responses at all the collocation points (geometrically coincident and not coincident with virtual sources) associated to the inner and outer boundary of the structure are considered, the resulting system of equations can be expressed as the following matrix equation

$$\begin{Bmatrix} \bar{\boldsymbol{U}}_{b_1} \\ \bar{\boldsymbol{U}}_{b_2}^{\Omega_1} \end{Bmatrix} = \begin{bmatrix} \bar{\mathbf{H}}_{b_1 b_1} & \bar{\mathbf{H}}_{b_1 b_2} \\ \bar{\mathbf{H}}_{b_2 b_1} & \bar{\mathbf{H}}_{b_2 b_2}^{\Omega_1} \end{bmatrix} \begin{Bmatrix} \bar{\boldsymbol{S}}^{(1)} \\ \bar{\boldsymbol{S}}^{(21)} \end{Bmatrix}, \tag{6.18}$$

where $\bar{\boldsymbol{U}}_{b_1}$ and $\bar{\boldsymbol{U}}_{b_2}^{\Omega_1}$ represent vectors that collect the displacements at all the collocation points defined on the inner and outer boundaries of the structure, respectively, and where $\bar{\mathbf{H}}_{b_i b_j}$ is a matrix that contains the displacement Green's functions associated to the collocation points defined on boundary b_i due to the set of virtual sources associated to the boundary b_j (note that all sources are considered but only the SBM sources will actually be located on the boundary).

When the responses at all the collocation points associated to the inner boundary of the soil are considered, the resulting set of equations can be expressed as

$$\bar{\boldsymbol{U}}_{b_2}^{\Omega_2} = \bar{\mathbf{H}}_{b_2 b_2}^{\Omega_2} \bar{\boldsymbol{S}}^{(22)}, \tag{6.19}$$

being $\bar{\boldsymbol{U}}_{b2}^{\Omega_2}$ a vector that collects the displacements at all the collocation points on the soil boundary.

Equivalent matrix equations can be obtained when the tractions at all the collocation points defined on each boundary are considered. For the structure subsystem the resulting expression is

$$\begin{Bmatrix} \bar{\boldsymbol{T}}_{b_1} \\ \bar{\boldsymbol{T}}_{b_2}^{\Omega_1} \end{Bmatrix} = \begin{bmatrix} \bar{\mathbf{H}}_{b_1 b_1}^{\tau} & \bar{\mathbf{H}}_{b_1 b_2}^{\tau} \\ \bar{\mathbf{H}}_{b_2 b_1}^{\tau} & \bar{\mathbf{H}}_{b_2 b_2}^{\tau,\Omega_1} \end{bmatrix} \begin{Bmatrix} \bar{\boldsymbol{S}}^{(1)} \\ \bar{\boldsymbol{S}}^{(21)} \end{Bmatrix}, \tag{6.20}$$

where $\bar{\mathbf{H}}_{b_i b_j}^{\tau}$ contains the traction Green's functions associated to the collocation points on b_i due to the virtual sources associated to b_j. Furthermore, the matrix equation associated to the soil tractions is

$$\bar{\boldsymbol{T}}_{b_2}^{\Omega_2} = \bar{\mathbf{H}}_{b_2 b_2}^{\tau \Omega_2} \bar{\boldsymbol{S}}^{(22)}, \tag{6.21}$$

where $\bar{\boldsymbol{T}}_{b_2}^{\Omega_2}$ is a vector that collects the tractions at all the collocation points on the soil boundary.

The coupling between both subsystems is performed by considering continuity of displacement and force equilibrium at the soil-structure interface Γ_2. These boundary conditions can be expressed as

$$\begin{cases} \bar{\boldsymbol{U}}_{b_2}^{\Omega_1} = \bar{\boldsymbol{U}}_{b_2}^{\Omega_2} = \bar{\boldsymbol{U}}_{b_2}, & \text{(6.22a)} \\ \bar{\boldsymbol{T}}_{b_2}^{\Omega_1} = -\bar{\boldsymbol{T}}_{b_2}^{\Omega_2}. & \text{(6.22b)} \end{cases}$$

Considering the displacement compatibility condition, Eqs. (6.18) and (6.19) become

$$\begin{Bmatrix} \bar{\boldsymbol{U}}_{b_1} \\ 0 \end{Bmatrix} = \begin{bmatrix} \bar{\mathbf{H}}_{b_1 b_1} & \bar{\mathbf{H}}_{b_1 b_2} & \\ \bar{\mathbf{H}}_{b_2 b_1} & \bar{\mathbf{H}}_{b_2 b_2}^{\Omega_1} & -\bar{\mathbf{H}}_{b_2 b_2}^{\Omega_2} \end{bmatrix} \begin{Bmatrix} \bar{\boldsymbol{S}}^{(1)} \\ \bar{\boldsymbol{S}}^{(21)} \\ \bar{\boldsymbol{S}}^{(22)} \end{Bmatrix}. \tag{6.23}$$

Additionally, considering the force equilibrium condition, Eqs. (6.20) and (6.21) become

$$\begin{Bmatrix} \bar{\boldsymbol{T}}_{b_1} \\ 0 \end{Bmatrix} = \begin{bmatrix} \bar{\mathbf{H}}^{\tau}_{b_1 b_1} & \bar{\mathbf{H}}^{\tau}_{b_1 b_2} & \\ \bar{\mathbf{H}}^{\tau}_{b_2 b_1} & \bar{\mathbf{H}}^{\tau,\Omega_1}_{b_2 b_2} & \bar{\mathbf{H}}^{\tau,\Omega_2}_{b_2 b_2} \end{bmatrix} \begin{Bmatrix} \bar{\boldsymbol{S}}^{(1)} \\ \bar{\boldsymbol{S}}^{(21)} \\ \bar{\boldsymbol{S}}^{(22)} \end{Bmatrix}. \tag{6.24}$$

For the type of SSI problems proposed in this thesis, the results of interest are always displacements caused by a known excitation. Thus, the type of boundary condition that is considered is that the tractions on the interior boundary of the structure are known, but that the displacements on this boundary are not. Therefore, the second equation in Eq (6.23) and Eq. (6.24) can be combined to obtain

$$\begin{Bmatrix} \bar{\boldsymbol{T}}_{b_1} \\ 0 \\ 0 \end{Bmatrix} = \begin{bmatrix} \bar{\mathbf{H}}^{\tau}_{b_1 b_1} & \bar{\mathbf{H}}^{\tau}_{b_1 b_2} & \\ \bar{\mathbf{H}}_{b_2 b_1} & \bar{\mathbf{H}}^{\Omega_1}_{b_2 b_2} & -\bar{\mathbf{H}}^{\Omega_2}_{b_2 b_2} \\ \bar{\mathbf{H}}^{\tau}_{b_2 b_1} & \bar{\mathbf{H}}^{\tau,\Omega_1}_{b_2 b_2} & \bar{\mathbf{H}}^{\tau,\Omega_2}_{b_2 b_2} \end{bmatrix} \begin{Bmatrix} \bar{\boldsymbol{S}}^{(1)} \\ \bar{\boldsymbol{S}}^{(21)} \\ \bar{\boldsymbol{S}}^{(22)} \end{Bmatrix}. \tag{6.25}$$

The third equation in Eq. (6.25) allows to express $\bar{\boldsymbol{S}}^{(22)}$ in terms of the other virtual source strengths as

$$\bar{\boldsymbol{S}}^{(22)} = \left(\bar{\mathbf{H}}^{\Omega_2}_{b_2 b_2}\right)^{-1} \left(\bar{\mathbf{H}}_{b_2 b_1} \bar{\boldsymbol{S}}^{(1)} + \bar{\mathbf{H}}^{\Omega_1}_{b_2 b_2} \bar{\boldsymbol{S}}^{(21)}\right). \tag{6.26}$$

Then, substituting Eq. (6.26) into the third equation in Eq. (6.25), the following relation between $\bar{\boldsymbol{S}}^{(1)}$ and $\bar{\boldsymbol{S}}^{(21)}$ can be obtained

$$\bar{\mathbf{H}}^{\tau}_{b_2 b_1} \bar{\boldsymbol{S}}^{(1)} + \bar{\mathbf{H}}^{\tau,\Omega_1}_{b_2 b_2} \bar{\boldsymbol{S}}^{(21)} + \bar{\mathbf{H}}^{\tau,\Omega_2}_{b_2 b_2} \left(\bar{\mathbf{H}}^{\Omega_2}_{b_2 b_2}\right)^{-1} \left(\bar{\mathbf{H}}_{b_2 b_1} \bar{\boldsymbol{S}}^{(1)} + \bar{\mathbf{H}}^{\Omega_1}_{b_2 b_2} \bar{\boldsymbol{S}}^{(21)}\right) = 0. \tag{6.27}$$

Combining the terms related to each source strength, Eq. (6.27) becomes

$$\left[\bar{\mathbf{H}}^{\tau,\Omega_2}_{b_2 b_2} \left(\bar{\mathbf{H}}^{\Omega_2}_{b_2 b_2}\right)^{-1} \bar{\mathbf{H}}_{b_2 b_1} + \bar{\mathbf{H}}^{\tau}_{b_2 b_1}\right] \bar{\boldsymbol{S}}^{(1)} + \left[\bar{\mathbf{H}}^{\tau,\Omega_2}_{b_2 b_2} \left(\bar{\mathbf{H}}^{\Omega_2}_{b_2 b_2}\right)^{-1} \bar{\mathbf{H}}^{\Omega_1}_{b_2 b_2} + \bar{\mathbf{H}}^{\tau,\Omega_1}_{b_2 b_2}\right] \bar{\boldsymbol{S}}^{(21)} = 0, \tag{6.28}$$

which allows to express $\bar{\boldsymbol{S}}^{(21)}$ as

$$\bar{\boldsymbol{S}}^{(21)} = -\boldsymbol{B}^{-1} \boldsymbol{A} \bar{\boldsymbol{S}}^{(1)}, \tag{6.29}$$

where the terms $\boldsymbol{A}$ and $\boldsymbol{B}$ are formulated as

$$\boldsymbol{A} = \bar{\mathbf{H}}^{\tau,\Omega_2}_{b_2b_2} \left(\bar{\mathbf{H}}^{\Omega_2}_{b_2b_2}\right)^{-1} \bar{\mathbf{H}}_{b_2b_1} + \bar{\mathbf{H}}^{\tau}_{b_2b_1}, \tag{6.30}$$

$$\boldsymbol{B} = \bar{\mathbf{H}}^{\tau,\Omega_2}_{b_2b_2} \left(\bar{\mathbf{H}}^{\Omega_2}_{b_2b_2}\right)^{-1} \bar{\mathbf{H}}^{\Omega_1}_{b_2b_2} + \bar{\mathbf{H}}^{\tau,\Omega_1}_{b_2b_2}. \tag{6.31}$$

Finally, substituting Eq. (6.29) into the first equation of Eq. (6.25), the following relation between $\bar{\boldsymbol{S}}^{(1)}$ and the known boundary tractions is obtained

$$\bar{\boldsymbol{T}}_{b_1} = \bar{\mathbf{H}}^{\tau}_{b_1b_2}\bar{\boldsymbol{S}}^{(1)} - \bar{\mathbf{H}}^{\tau}_{b_1b_2}\boldsymbol{B}^{-1}\boldsymbol{A}\bar{\boldsymbol{S}}^{(1)}. \tag{6.32}$$

Therefore, the strengths of the first set of virtual sources is given by

$$\bar{\boldsymbol{S}}^{(1)} = \left[\bar{\mathbf{H}}^{\tau}_{b_1b_2} - \bar{\mathbf{H}}^{\tau}_{b_1b_2}\boldsymbol{B}^{-1}\boldsymbol{A}\right]^{-1}\bar{\boldsymbol{T}}_{b_1}. \tag{6.33}$$

Once $\bar{\boldsymbol{S}}^{(1)}$ has been determined, the strengths of the second set of virtual sources is obtained using Eq. (6.29). With the second set known, the remaining set of strengths is obtained from Eq. (6.26). Finally, once all the source strengths have been computed, the displacement and traction responses at any arbitrary field point on the soil or the structure can be computed by means of Eqs. (6.6)-(6.9).

6.2 Verification of the methodology

The accuracy of the proposed hybrid methodology is exhibited in this section for the case presented in Fig. 6.3a. As illustrated, the structure of this case consists of a cylindrical thin shell embedded in a full-space model of the soil. In this case, a harmonic vertical point load is applied on the bottom of the shell and at $x = 0$. The external radius of the thin shell is 1 m and its thickness is 0.1 m. Although the MFS can be used for all sets three sets of virtual forces due to the smoothness of the two boundaries involved, the hybrid method is used to deal with the inner boundary while the MFS is used for the two sets of forces associated with the outer boundary with the aim of demonstrating its capability of the proposed methodology. The analysis is carried out for 10 NpW, considering a maximum frequency of 250 Hz and the soil characteristics presented in Table. 3.1. The soil response has been calculated at three different locations, identified as points A

($x = 0$ m; $y = 2$ m; $z = -2$ m), B ($x = 0$ m; $y = 4$ m; $z = -1$ m) and C ($x = 0$ m; $y = 8$ m; $z = 2$ m).

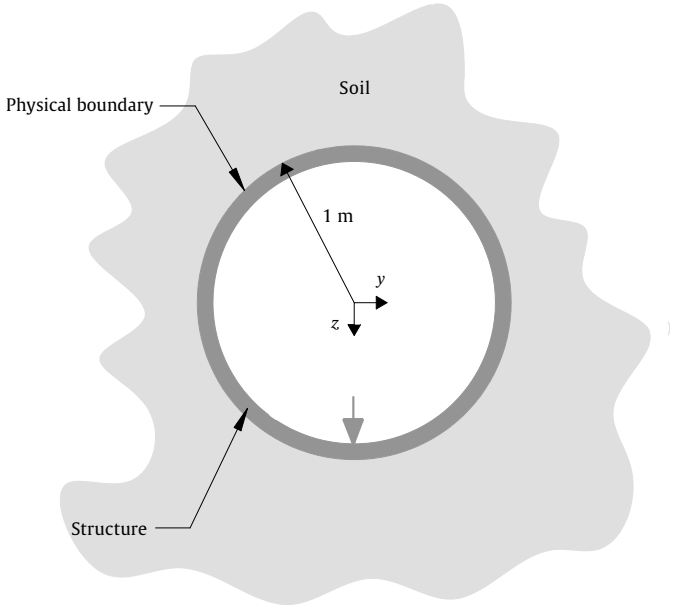

FIGURE 6.3: The geometry of the cylindrical thin shell. The position of the load is represented with a large grey arrow.

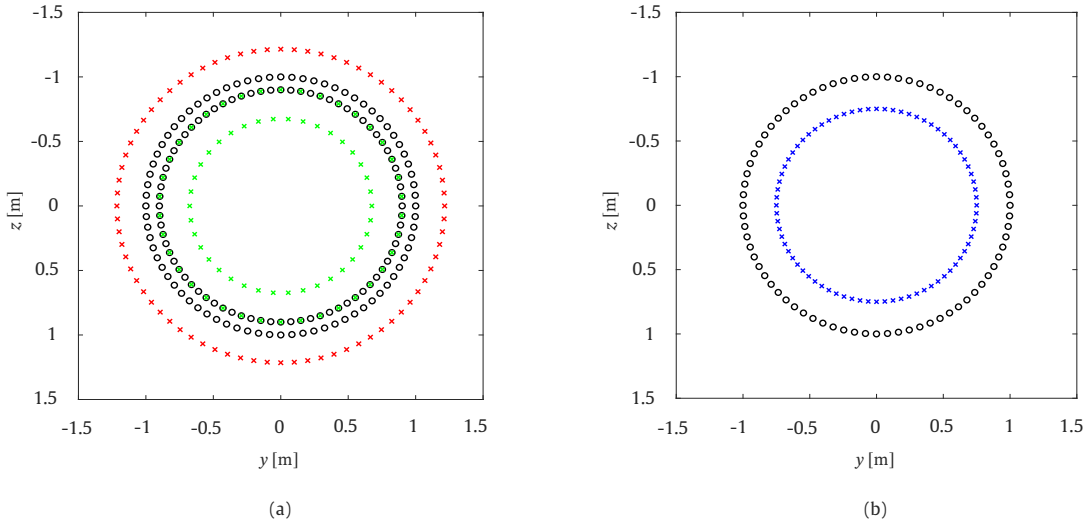

FIGURE 6.4: The distribution of the collocation (black circles) and source points (red and blue crosses) for the circular thin shell, representing tunnel (a) and the soil (b).

The results obtained using the proposed hybrid methodology are compared with those obtained using the PiP model [27]. To assess the accuracy of the presented

approach, the results are firstly presented in terms of the root mean square errors (RMSE) associated to the receptances and to the traction transfer functions (TTF), taking the response of the PiP model as the reference solution. These RMSE have been computed using Eq. (5.6), and the receptances and TTFs of each case have been calculated using Eqs. (3.6)-(3.8). The number of ring modes considered for the calculation of the PiP solution has been set to 30 and the considered wavenumber samplings can be found in Section 5.2.

Fig. 6.5 presents the RMSE obtained for each field point in y and z directions. As can be observed, the RMSE of the proposed method is below 1% at all considered evaluation points for most of the range of frequencies of interest, confirming the accuracy of the proposed approach.

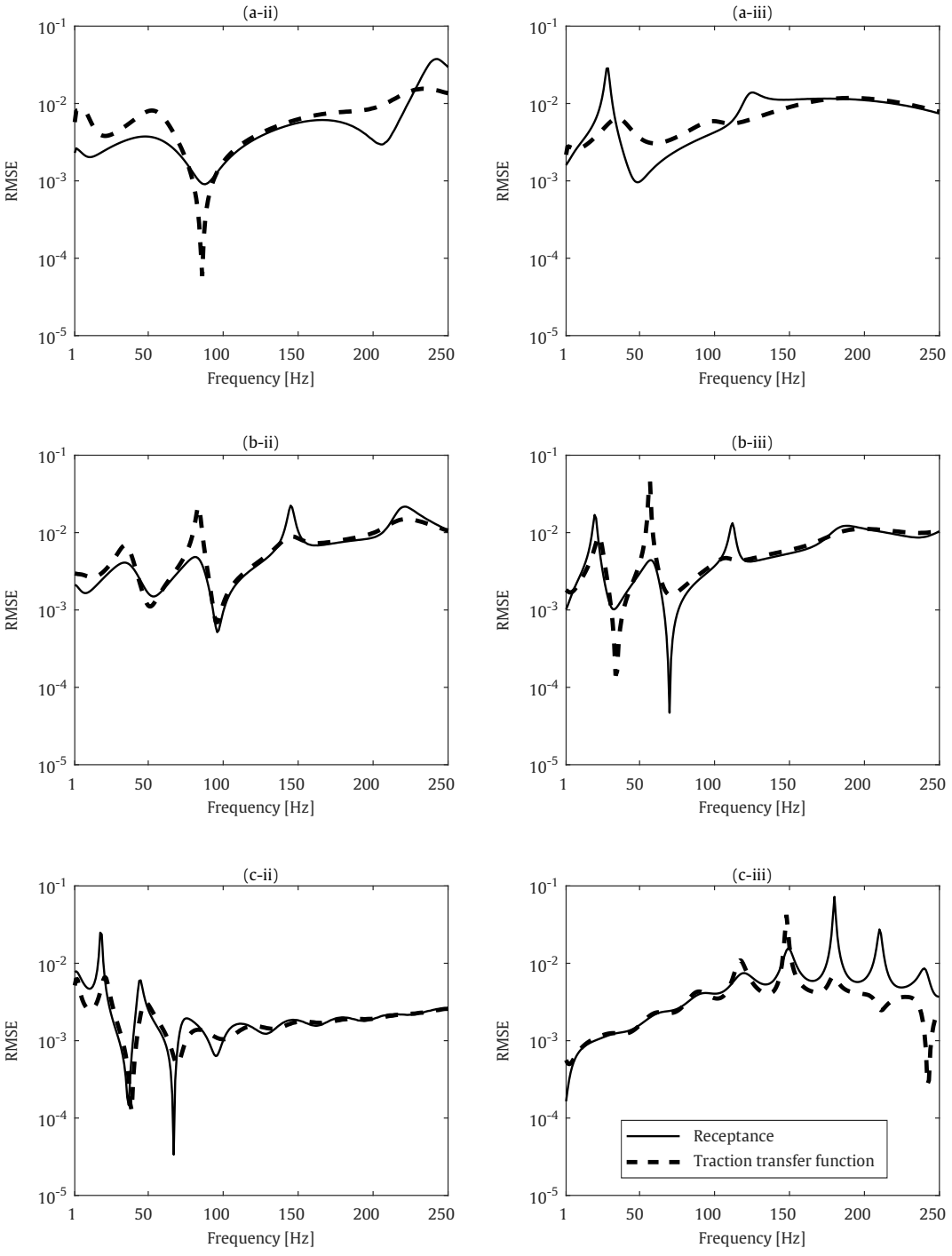

FIGURE 6.5: RMSE at field points A (a), B (b) and C (c) for y (ii) and z (iii) directions.

To confirm the accuracy of the method, the comparison between the hybrid method and PiP solution has also been performed with a direct comparison of the receptances and TTFs results obtained by both methods for each one of the field points considered. These comparisons are presented in Fig. 6.6 (receptances) and

Fig. 6.7 (TTF). The results show that, as indicated by the previous RMSE results, there is a very good agreement between both methods for the whole range of frequencies considered.

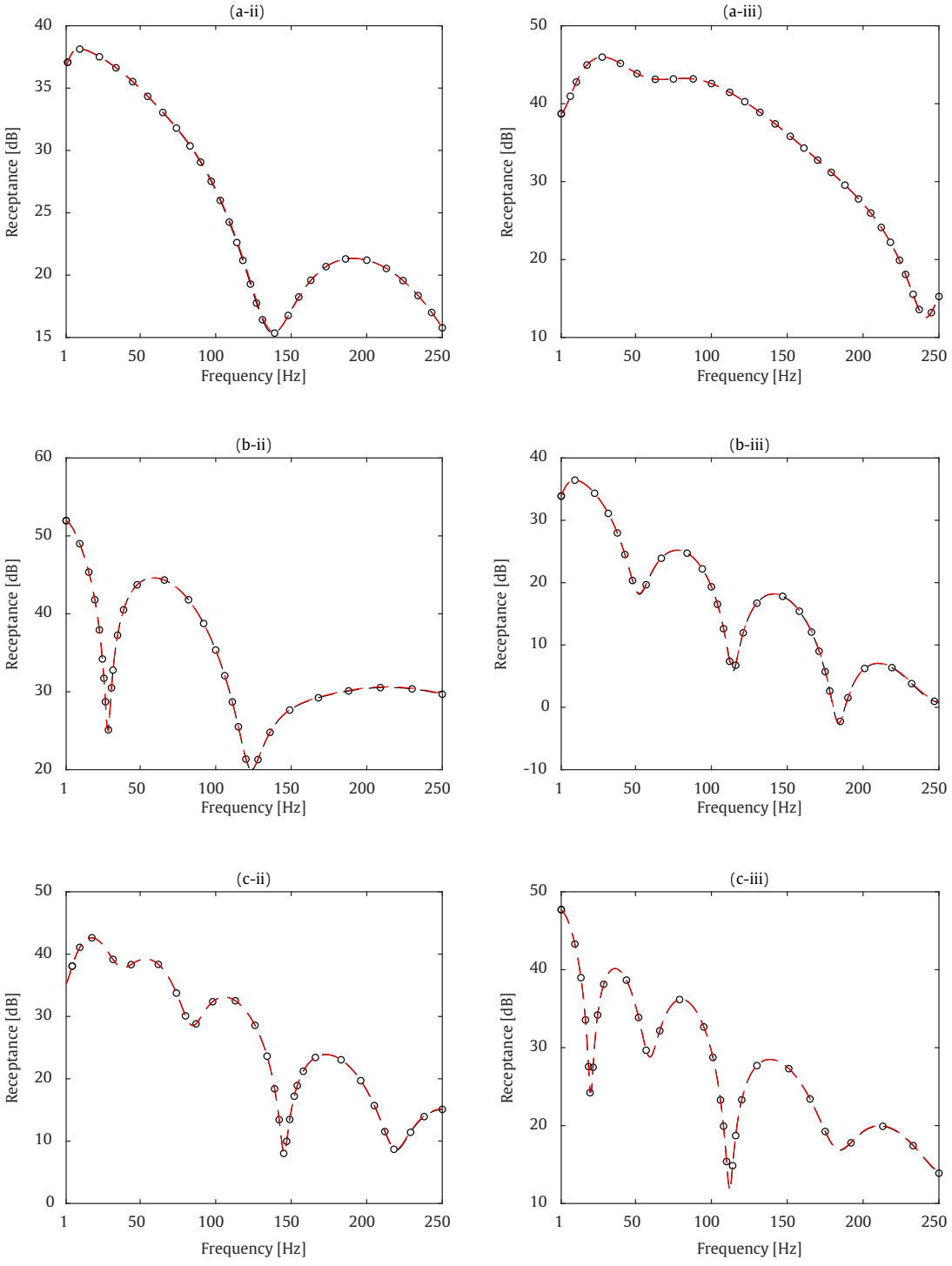

FIGURE 6.6: Receptances at field points A (a), B (b) and C (c) for y (ii) and z (iii) directions. Methods: Pipe-in-Pipe (dashed red line) and hybrid method (dashed black line with circle markers).

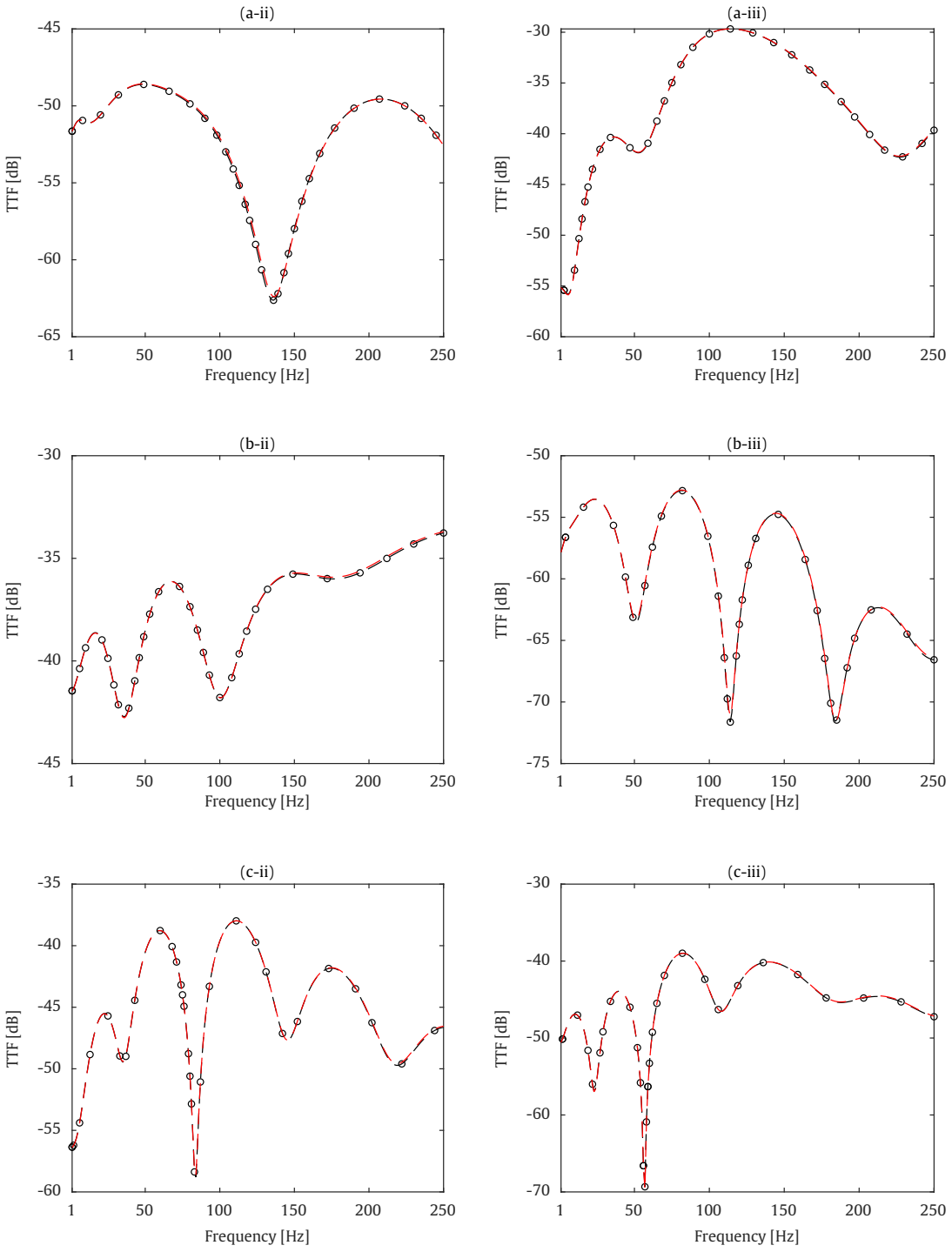

FIGURE 6.7: Traction transfer functions at field points A (a), B (b) and C (c) for y (ii), and z (iii) directions. Methods: Pipe-in-Pipe (dashed red line) and hybrid method (dashed black line with circle markers).

6.3 Assessment of railway soil-tunnel interaction

This section presents two application examples of the proposed hybrid SBM-MFS multi-domain approach for railway-induced ground-borne vibration assessment. More precisely, the aim is to assess the accuracy of the method in the calculation of soil receptances at different field points for two types of railway tunnel structures: a circular tunnel with a slab and a cut-and-cover tunnel, both embedded in an homogeneous full-space soil. The mechanical properties of the tunnel lining and of the soil are the ones that were presented in Table. 3.1. Since the considered examples do not have a known analytical solution, the 2.5D FEM-BEM approach with a highly refined mesh is taken as the reference solution. In both examples the receptances have been computed for a frequency range between 1 Hz and 100 Hz, containing the range that is usually considered for railway-induced vibration problems [86]. The number of collocation points and boundary nodes used for the calculations have been defined imposing the requirement of having at least 10 NpW for an excitation frequency of 100 Hz.

6.3.1 Example 1: circular railway tunnel

In this example a circular tunnel with an internal radius of 3 m and a wall thickness of 0.3 m embedded in a homogeneous full-space soil is considered. The tunnel is excited by two harmonic point loads symmetrically applied on the tunnel invert, separated 1.435 meters and located at a cross-section $x = 0$. The geometry of the system and the position of the applied forces are illustrated in Fig. 6.8, and the distribution of the collocation and sources points associated with the tunnel and soil models are shown in Figs. 6.9a and 6.9b, respectively. As the inner boundary of the structure consists of smooth and non-smooth parts, the hybrid SBM-MFS method is used to represent it. Therefore, the set of virtual sources $\bar{\boldsymbol{S}}^{(1)}$ combines SBM and MFS sources. In contrast, the remaining two sets of virtual sources ($\bar{\boldsymbol{S}}^{(21)}$ and $\bar{\boldsymbol{S}}^{(22)}$) contain only MFS sources, as they are adequate to represent the outer boundary of the structure (and inner boundary of the soil), which is smooth. The sets of virtual sources corresponding to each boundary have been presented in Fig. 6.9 using green, red and blue crosses.

The results obtained with the multi-domain hybrid method are compared with the ones obtained using a 2.5D FEM-BEM approach. The comparison is performed by

considering the receptance of the soil at three different evaluation points (identified as A ($x = 0$ m; $y = 4$ m; $z = 4$ m), B ($x = 0$ m; $y = 8$ m; $z = 2$ m) and C ($x = 0$ m; $y = 12$ m; $z = -2$ m)). The mesh considered for the FEM-BEM model of the structure is illustrated in Fig. 6.10.

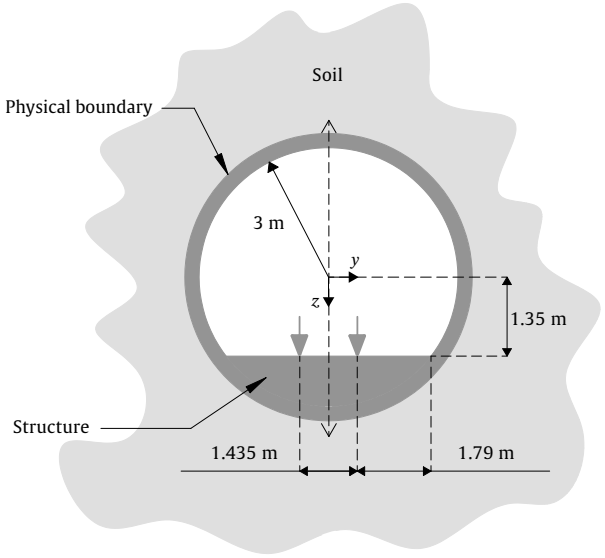

FIGURE 6.8: The geometry of the circular railway tunnel. The position of two equal loads are represented with large grey arrow.

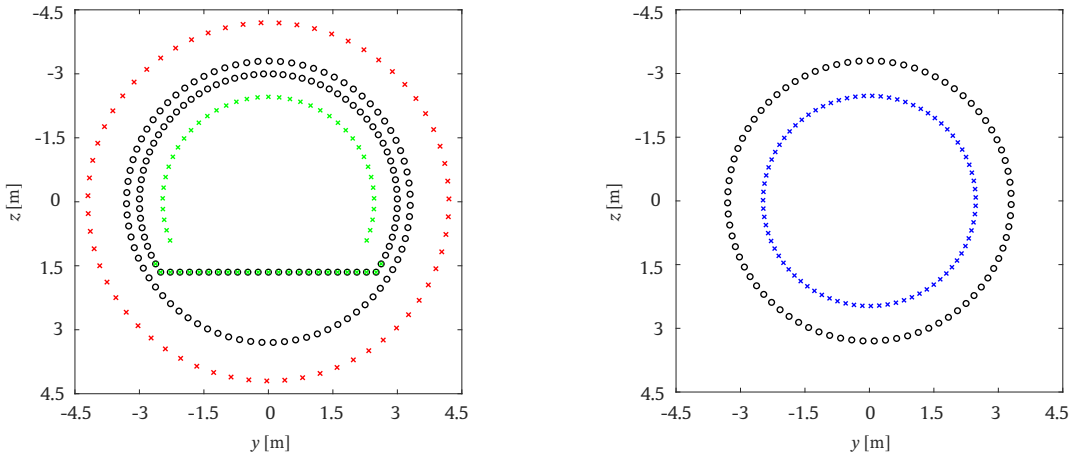

FIGURE 6.9: The distribution of the collocation (black circles) and source points (red and blue crosses) for the circular railway tunnel geometry, representing tunnel (a) and the soil (b).

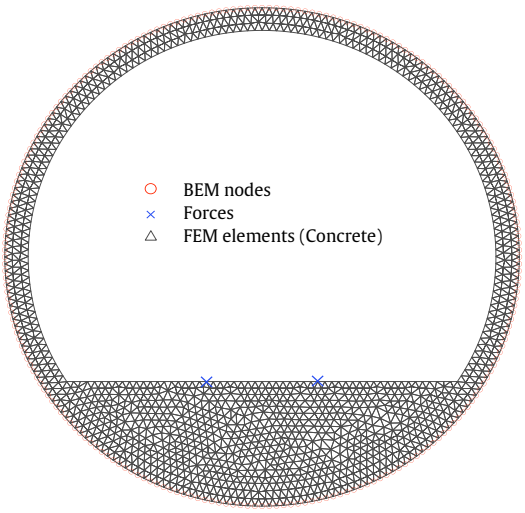

FIGURE 6.10: The FEM elements, the BEM points and the position of the applied forces used in the reference case (2.5D FEM-BEM).

Fig. 6.11 compares the receptances obtained by both methods for the range of frequencies of interest. Despite that the results show large discrepancies between the approaches at 69 Hz (point B, y direction) and at 73 Hz (points C, z direction), these discrepancies are found at troughs of the response curves. In all the other cases, an acceptable agreement has been obtained for all the evaluation points considered, where up to 2 dB differences are observed between the approaches. These results suggest that the approach proposed in this chapter, which is totally based on meshless methods and it is much simpler to implement than the 2.5D FEM-BEM approach, can be used to obtain responses with an accuracy that can be acceptable for many engineering applications.

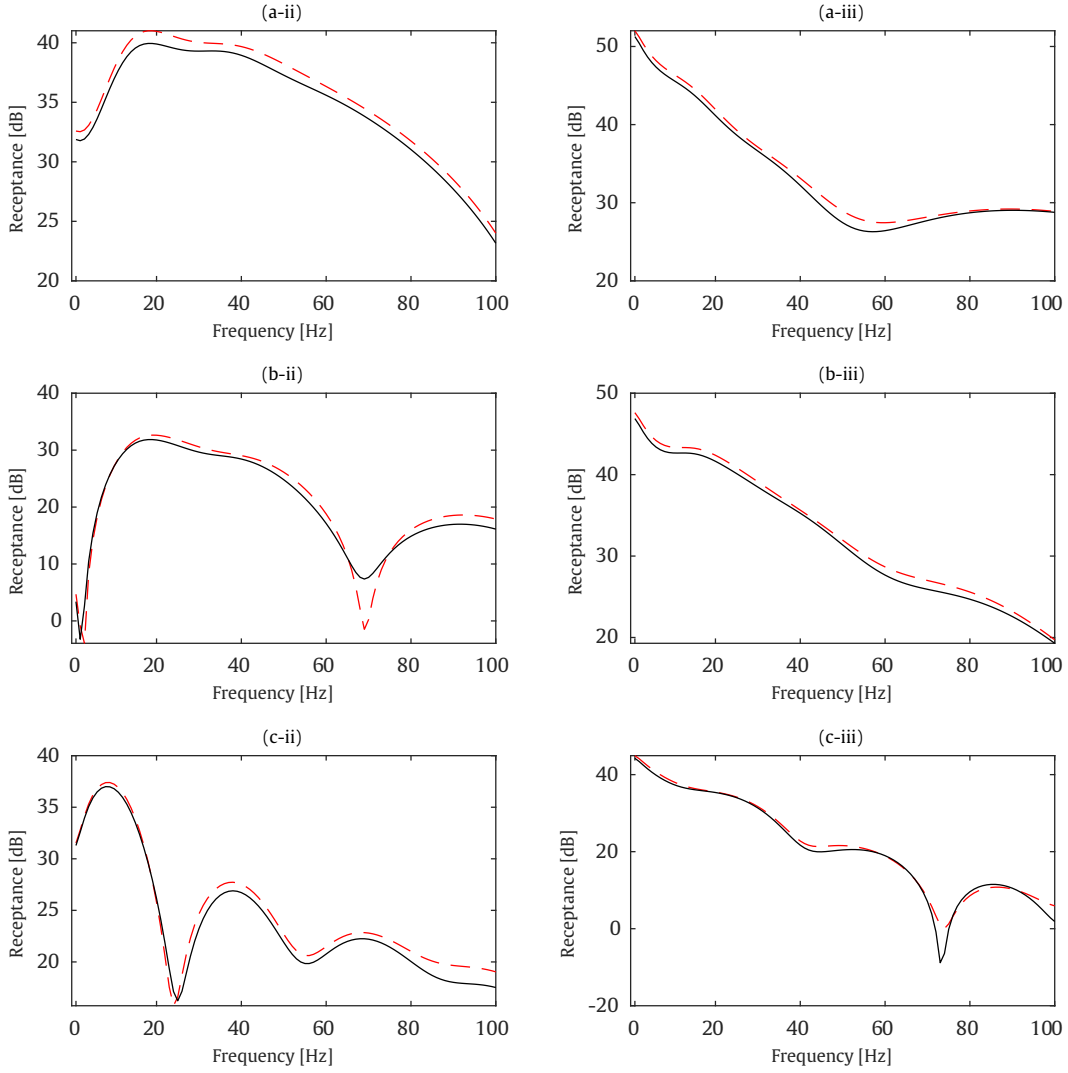

FIGURE 6.11: Receptances at the field points A (a), B (b) and C (c) for y (ii) and z (iii) directions for the circular tunnel case. Methods: 2.5D FEM–BEM (dashed red line), hybrid method (solid black line).

6.3.2 Example 2: cut-and-cover tunnel

The second example considers a cut-and-cover tunnel with a side length of 6 m and a wall thickness of 0.3 m, embedded in a homogeneous full-space soil. As in the previous example, the tunnel is excited by two harmonic point loads symmetrically applied on the tunnel invert and separated 1.435 meters. The geometry of the system and the position of the applied forces are illustrated in Fig. 6.12a, and the distribution of the collocation and sources points related to the tunnel and soil models are presented, respectively, in Figs. 6.13a and 6.13b. In this case both

(inner and outer) boundaries consist of smooth and non-smooth parts, and the hybrid SBM-MFS method has been used to represent them. Therefore, all sets of virtual sources consist of both MFS and SBM sources.

As in the previous example, the soil receptances obtained by the hybrid approach are compared with the ones obtained using a 2.5D FEM-BEM approach. The evaluation points used for this comparison are A ($x = 0$ m; $y = 5$ m; $z = 5$ m), B ($x = 0$ m; $y = 9$ m; $z = 4$ m) and C ($x = 0$ m; $y = 14$ m; $z = -2$ m), and the mesh considered in the FEM-BEM model of the structure is shown in Fig. 6.14.

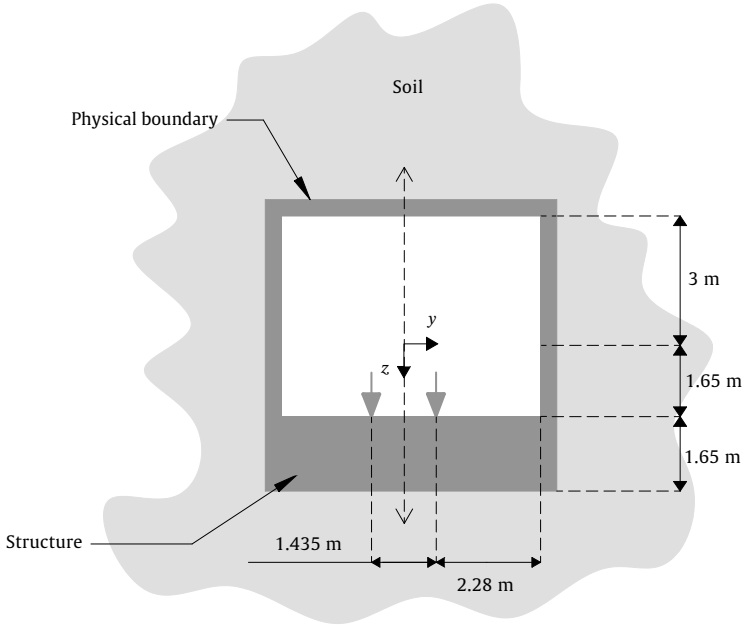

FIGURE 6.12: The geometry of the cut-and-cover railway tunnel. The position of two equal loads are represented with large grey arrow.

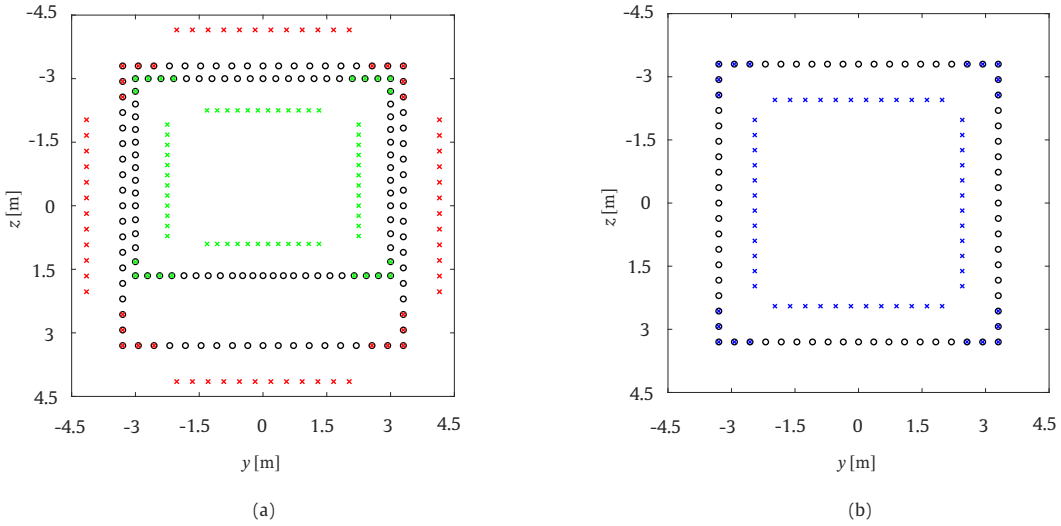

FIGURE 6.13: The distribution of the collocation (black circles) and source points (red and blue crosses) for the cut-and-cover railway tunnel geometry, representing tunnel (a) and the soil (b).

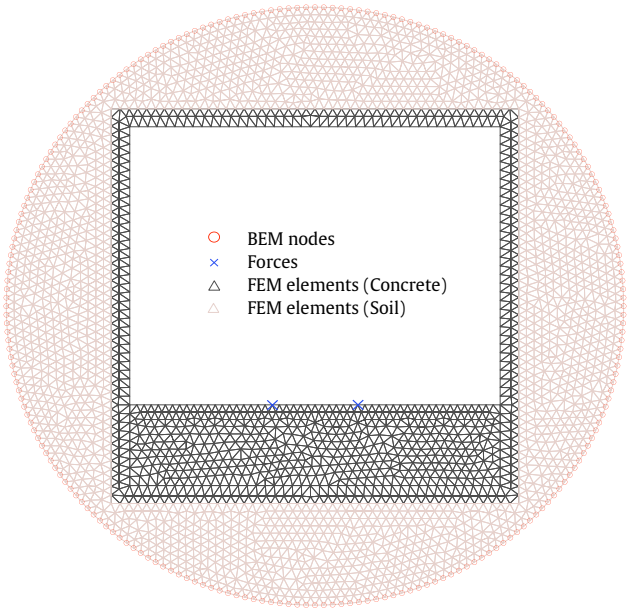

FIGURE 6.14: The FEM elements, the BEM points and the position of the applied forces used in the reference case (2.5D FEM-BEM).

Fig. 6.15 compares the receptances obtained by the two methods for this second calculation example. As before, the results show a good agreement between both methods, where discrepancies below 2 dB can be seen between both approaches, indicating that, due to its accuracy, efficiency and implementation simplicity, the

novel meshless approach can be a very interesting alternative to mesh-based methods for many engineering problems.

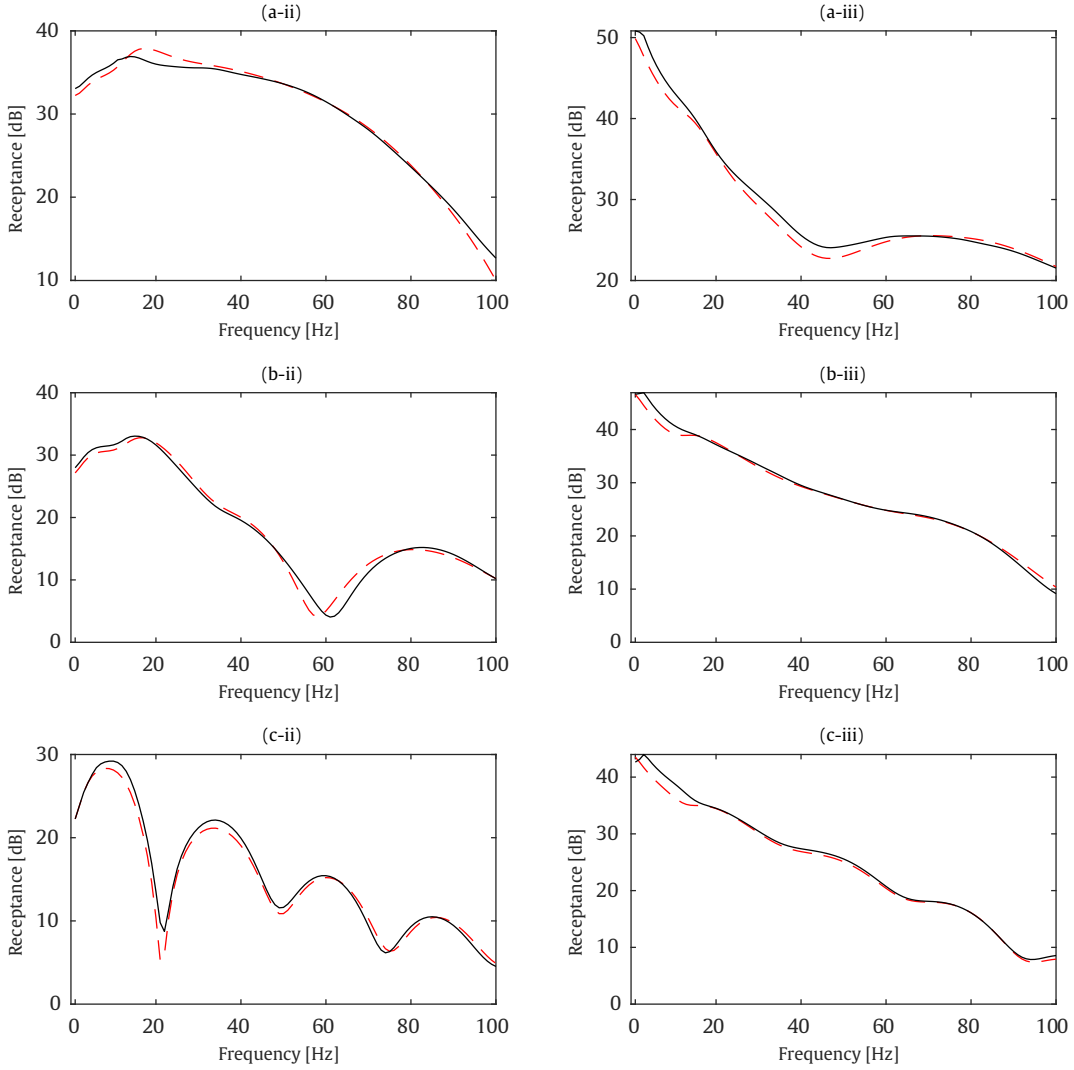

FIGURE 6.15: Receptances at the field points A (a), B (b) and C (c) for y (ii) and z (iii) directions for the cut-and-cover case. Methods: 2.5D FEM–BEM (dashed red line), hybrid method (solid black line).

6.4 Conclusions

This chapter has extended the hybrid SBM-MFS methodology presented in Chapter 5 to the case where, both, an embedded structure and its surrounding soil are modelled using it, obtaining a fully meshless approach to deal with longitudinally invariant SSI problems. This new approach has been validated in the context of a simple example consisting in a thin cylindrical shell embedded in a full-space

medium. The application of the methodology to the assessment of railway induced vibrations has been considered in the framework of two examples: a circular tunnel and a cut-and-cover tunnels, both embedded in a full-space soil. The particular merits of the proposed approach are listed below:

- The approach combines the benefits of the SBM and the MFS, being capable of dealing with detailed structures and of computing the wave propagation in the soil efficiently.
- The calculation examples considered in this chapter shows that the proposed method is not only practical for structures with geometrically simple boundaries but it can also be considered in those cases containing intricate interfaces.
- The proposed method is fully based on meshless approaches and, therefore, it usually requires less modelling time than the one needed by mesh-based approaches such as FEM-BEM. Moreover, the method can be computationally more efficient than mesh-based approaches, specially if the considered structure requires to use a mesh with a large number of elements.
- The implementation procedure is simpler than the ones usually required by mesh-based approaches, such as 2.5D FEM-BEM, 2.5D FEM-MFS and 2.5D FEM-SBM.
- The presented examples for railway applications indicate that the method is adequate for assessing the vibration impact of these structures.

To conclude, the 2.5D hybrid SBM-MFS method is found to be an adequate prediction tool for the SSI problems since it is fully meshless, computationally efficient and easy to be implemented.

Chapter 7

Conclusions and future work

In this chapter, the summary of the main findings of the thesis is presented. Moreover, various recommendations for further research on the topic are proposed.

7.1 Thesis conclusions

The development of new meshless methodologies to deal with longitudinally invariant SSI problems has been pursued throughout this thesis. To this end, a 2.5D FEM-BEM-MFS methodology has been firstly developed to deal with longitudinally invariant SSI problems. The method uses a 2.5D FEM-BEM approach to model the structure and the surrounding soil and, afterwards, considers a 2.5D MFS approach to model the wave propagation in the soil. In order to address the drawbacks of the 2.5D FEM-BEM-MFS method related to the computational efficiency and the location of the virtual sources, a novel 2.5D FEM-SBM methodology has been developed and introduced. This method also uses the FEM to model the structure and, in contrast, it employs the SBM to model the soil. The previous soil modelling strategy has been improved by considering a novel hybrid methodology that employs the 2.5D MFS approach to deal with smooth sections of the boundary, while the complex segments are accounted through the 2.5D SBM method. Finally, the previous hybrid SBM-MFS approach has been extended to model both the structure and wave propagation in the soil, resulting in a fully meshless methodology capable of dealing with longitudinally invariant SSI problems.

In order to compare the considered methods along this thesis, Table 7.1 is presented. As shown, the 2.5D FEM-BEM, the 2.5D FEM-MFS and the three methodologies developed in this thesis are compared in terms of computational efficiency, accuracy (considering cases with circular or complex geometry), condition number, implementation procedure, formulation simplicity and capability to solve the effects of fictitious eigenfrequencies. The comparison carried out in this table is qualitative, although is based on the calculation examples presented through this work. In the table, one asterisk represents the lowest performance and four asterisks denotes the highest one.

Methods	Computational efficiency	Accuracy (circular/complex geo.)	Condition number	Implementation procedure	Formulation simplicity	Deals with fictitious eigenfrequencies
2.5D FEM-BEM	*	***/***	****	*	*	×
2.5D FEM-BEM-MFS	**	****/*	**	*	*	×
2.5D FEM-MFS	***	****/*	*	***	***	✓
2.5D FEM-SBM	***	***/***	****	**	**	×
2.5D SBM-MFS	****	***/***	***	****	****	✓

TABLE 7.1: Qualitative comparison of various methods considered along this thesis.

Based on the studies provided, the following conclusions can be drawn from this thesis.

Computational efficiency

In terms of computational efficiency, for the calculation examples, the 2.5D FEM-BEM-MFS method is more efficient than the 2.5D FEM-BEM approach, when a large number of evaluation points is considered. For the half-space calculation examples, the presented results confirm the improvement of the 2.5D FEM-BEM-MFS methodology in terms of computational time, although the improvement is not as large as in full-space problems. Comparing the 2.5D FEM-SBM approach with the 2.5D FEM-BEM methodology, the computational efficiency of the novel 2.5D FEM-SBM is a great merit of the method, while providing a similar accuracy to the 2.5D FEM-BEM. However, the 2.5D FEM-MFS is computationally more efficient than the 2.5D FEM-SBM, due to the extra calculation task of OIFs. The hybrid method is more computationally efficient than the 2.5D SBM since fewer singular terms exist in the 2.5D coupled SBM-MFS which means less computational time is needed to compute the OIFs. The fully meshless 2.5D hybrid

SBM-MFS can also be more efficient than the mesh-based methods, such as 2.5D FEM-BEM, 2.5D FEM-MFS and the 2.5D FEM-SBM approaches, in those cases where a dense FEM mesh is required to model the structure.

Accuracy

The study on the 2.5D FEM-BEM-MFS method indicates that the use of the proposed control technique in Chapter 3 allows to obtain very accurate results. The investigation on the 2.5D FEM-SBM approach in the framework of smooth and complex geometries of the soil-structure interface shows that the proposed method not only is practical for structures with geometrically simple boundaries but it has also a reasonable accuracy in cases where this interface is more intricate. In contrast to the 2.5D FEM-SBM method, the accuracy of the results obtained by the 2.5D FEM-MFS approach is very sensitive to the location of the virtual sources. The 2.5D SBM-MFS method as a fully meshless approach presented by this thesis shows an acceptable level of accuracy for the modelling of the tunnel-soil interaction problems.

The comparison between the proposed methods for modelling the wave propagation in the soil illustrates that for the completely smooth geometries, the 2.5D MFS is the most accurate method of the considered approaches. However, the hybrid method results are less sensitive to the position of the virtual sources than the 2.5D MFS ones. When more complicated geometries are considered, the hybrid method provides more accuracy than the 2.5D MFS and, for most cases, the smallest discrepancies are the ones obtained using the 2.5D SBM approach. From the studies conducted on the use of a random distribution of the virtual sources it is observed that the hybrid method provides acceptable level of accuracy even in the cases where the MFS sources points are not distributed on a particular auxiliar boundary.

Condition number

For the calculation examples presented in this thesis has been observed that the system of equation of the 2.5D SBM approach is well-conditioned. On the contrary, the 2.5D MFS suffers from an ill-conditioned system of equation when a large

number of collocation points (or NpW) is considered. The hybrid method presents a remarkable improvement in the condition number when compared to the 2.5D MFS.

Fictitious eigenfrequencies

The investigation on the effect of the fictitious eigenfrequencies has been shown that the responses calculated by the 2.5D BEM and 2.5D SBM are affected by this phenomena. This is an issue induced by the non-uniqueness problem of the systems of equations resulting from the application of those approaches close to the dispersion curves of the corresponding interior problem, a well-reported drawback of direct boundary integral methods. The SBM, although it cannot be called a direct boundary integral method as the BEM, places the sources in the boundary, which could result in a system of equations that can not distinguish whether the problem in hands is interior or exterior. In contrast, the MFS uses source outside the domain to model the system, providing a mathematical clarification about the exterior/interior problem ambiguity. Thus, MFS and hybrid approaches effectively deal with the issue of fictitious eigenfrequencies.

Implementation procedure

The implementation of the BEM in practical algorithms for the modelling of wave propagation problems is a complex task, due to the inner complexity of the method associated to the mixture between boundary integral equations and finite element discretisation concepts. Also, its computer memory needs require of experienced programmers to reach efficient algorithms. Thus, FEM-BEM-based approaches are the most difficult to be implemented from all the studied methods. On the contrary, a much simpler implementation procedure are required by the 2.5D FEM-MFS numerical strategy as the soil response is obtained using a meshless approach. A slightly more complicated case is the one of the 2.5D FEM-SBM as, despite considering also a meshless approach for modelling the soil, it requires to compute the corresponding OIFs. An even simpler implementation is the one that it is required by the hybrid SBM-MFS method, which, as a fully meshless approach, does not require to discretise the structure in finite elements. This method overcomes the

other mesh-based models (such as 2.5D FEM-BEM, 2.5D FEM-MFS and 2.5D FEM-SBM) in terms of simplicity in the algorithm implementation effort.

7.2 Recommendations and future work

The research work described in this thesis was focused on the development of efficient meshless methods to deal with SSI problems. To this end, four methodologies were developed and assessed for several numerical examples. All the proposed methodologies in this work have shown the potentiality to deal with longitudinally invariant SSI problems. Although it has been considered that the main objectives of thesis are accomplished, the developed investigations have raised additional questions that may be interesting to address in the future, in order to develop more accurate and efficient numerical approaches to deal with such problems. In the following, some of the open issues on the present topic that deserve further research are listed.

- One of the approaches to improve the computational efficiency of the meshless methods is reducing the number of virtual sources. From calculation examples conducted in this thesis, it was found that in the problems with complicated geometries, the MFS and hybrid approaches provide accurate results if the number of collocation points is larger than the number of virtual sources. The recommendation is to study the reasons of the mentioned issue in detail.

- In the analysis carried out in Chapter 5 regarding the random distribution of the MFS sources, it was observed that the responses obtained by the 2.5D MFS and the hybrid methods are inaccurate in a few randomisation cases chosen by the programming code. It is recommended to perform a deeper investigation on the uncertainty of the random distribution of the virtual sources in the 2.5D MFS and hybrid methods, applying more efforts to study the restrictions on the positioning of the sources to ensure accurate responses.

- In Chapter 6, the formulation of the 2.5D SBM-MFS approach is presented only for a single inclusion in a medium (Chapter 6). The potential extension of this methodology to account for multiple layers of material is a very interesting topic for the future.

- The problems induced by the fictitious eigenfrequencies have been briefly studied in this thesis, where it has been shown that the fictitious eigenfrequencies affects the responses of the 2.5D SBM. In this context, to assess about the mitigation strategies to be used in the 2.5D SBM formulations for dealing with the problems arising from the fictitious eigenfrequencies in elastodynamics is suggested. In this context, the application of the Burton-Miller approach [98, 99] to the 2.5D SBM could be of great interest to mitigate the negative effects of the fictitious eigenfrequencies.

- All the calculation examples considered in this work were presented for radiation problems. It would be interesting to study if the benefits presented in radiation problems in terms of accuracy, robustness and computational efficiency, can also be observed in the scattering problems.

References

[1] E. Kausel, Early history of soil-structure interaction, Soil Dynamics and Earthquake Engineering 30 (2010) 822–832.

[2] V. A. Baranov, On the calculation of excited vibrations of an embedded foundation (in Russian), Voprosy Dynamiki Prochnocti 14 (1967) 195–209.

[3] M. Novak, Dynamic stiffness and damping of piles, Canadian Geotechnical Journal 11 (1974) 574–598.

[4] G. Lombaert, G. Degrande, S. François, D. J. Thompson, Ground-Borne Vibration due to Railway Traffic: A Review of Excitation Mechanisms, Prediction Methods and Mitigation Measures, in: Noise and Vibration Mitigation for Rail Transportation Systems. Notes on Numerical Fluid Mechanics and Multidisciplinary Design, Springer, Berlin, Heidelberg, 2015, pp. 253–287.

[5] A. Amorosi, D. Boldini, A. di Lernia, Dynamic soil-structure interaction: A three-dimensional numerical approach and its application to the Lotung case study, Computers and Geotechnics 90 (2017) 34–54.

[6] X. Sheng, C. J. Jones, D. J. Thompson, Modelling ground vibration from railways using wavenumber finite- and boundary-element methods, Proceedings of the Royal Society A: Mathematical, Physical and Engineering Sciences 461 (2005) 2043–2070.

[7] P. Lopes, P. Alves Costa, R. Calçada, A. Silva Cardoso, P. A. Costa, R. Calçada, A. S. Cardoso, Influence of soil stiffness on building vibrations due to railway traffic in tunnels: Numerical study, Computers and Geotechnics 61 (2014) 277–291.

[8] B. Bogosel, The method of fundamental solutions applied to boundary eigenvalue problems, Journal of Computational and Applied Mathematics 306 (2016) 265–285.

[9] G. Khatiashvili, G. Silagadze, On a numerical solution of twodimensional problems of elasticity for anisotropic medium by the method of fundamental solutions, Reports of Enlarged Session of the Seminar of I. Vekua Institute of Applied Mathematics 14 (1999).

[10] A. Poullikkas, A. Karageorghis, G. Georgiou, The method of fundamental solutions in Three-dimensional Elastostatics, Lecture Notes in Computer Science (including subseries Lecture Notes in Artificial Intelligence and Lecture Notes in Bioinformatics) 2328 (2002) 747–755.

[11] L. Godinho, A. Tadeu, P. Amado Mendes, Wave propagation around thin structures using the MFS, Computers, Materials and Continua 5 (2007) 117–127.

[12] W. Chen, J. Lin, C. S. Chen, The method of fundamental solutions for solving exterior axisymmetric helmholtz problems with high wave-number, Advances in Applied Mathematics and Mechanics 5 (2013) 477–493.

[13] L. P. Zhang, Z. C. Li, H. T. Huang, Y. Wei, The modified method of fundamental solutions for exterior problems of the Helmholtz equation; spurious eigenvalues and their removals, Applied Numerical Mathematics 145 (2019) 236–260.

[14] H. Liravi, R. Arcos, D. Ghangale, B. Noori, J. Romeu, A 2.5D coupled FEM-BEM-MFS methodology for longitudinally invariant soil-structure interaction problems, Computers and Geotechnics 132 (2021) 104009.

[15] Z. J. Fu, W. Chen, Y. Gu, Burton-Miller-type singular boundary method for acoustic radiation and scattering, Journal of Sound and Vibration 333 (2014) 3776–3793.

[16] Z.-J. Fu, W. Chen, J. Lin, A. H.-D. Cheng, Singular Boundary Method for Various Exterior Wave Applications, International Journal of Computational Methods 12 (2014) 1550011.

[17] L. Sun, X. Wei, B. Chen, A meshless singular boundary method for elastic wave propagation in 2D partially saturated poroelastic media, Engineering Analysis with Boundary Elements 113 (2020) 82–98.

[18] X. Wei, W. Luo, 2.5D singular boundary method for acoustic wave propagation, Applied Mathematics Letters 112 (2021) 106760.

[19] H. Liravi, R. Arcos, A. Clot, K. F. Conto, J. Romeu, A 2.5D coupled FEM–SBM methodology for soil–structure dynamic interaction problems, Engineering Structures 250 (2022) 113371.

[20] V. Kumar, M. Kumar, M. Kumar, A. Priyadarshee, Dynamic analysis of ssi effects on underground structures, in: T. G. Sitharam, S. Kolathayar, R. Jakka (Eds.), Earthquakes and Structures, Springer Singapore, Singapore, 2022, pp. 1–20.

[21] L. Andersen, C. Jones, Coupled boundary and finite element analysis of vibration from railway tunnels—a comparison of two- and three-dimensional models, Journal of Sound and Vibration 293 (2006) 611–625.

[22] P. Galvín, S. François, M. Schevenels, E. Bongini, G. Degrande, G. Lombaert, A 2.5D coupled FE-BE model for the prediction of railway induced vibrations, Soil Dynamics and Earthquake Engineering 30 (2010) 1500–1512.

[23] S. François, M. Schevenels, P. Galvín, G. Lombaert, G. Degrande, A 2.5D coupled FE–BE methodology for the dynamic interaction between longitudinally invariant structures and a layered halfspace, Computer Methods in Applied Mechanics and Engineering 199 (2010) 1536–1548.

[24] Q. Jin, D. J. Thompson, D. E. J. Lurcock, M. G. R. Toward, E. Ntotsios, A 2.5D finite element and boundary element model for the ground vibration from trains in tunnels and validation using measurement data, Journal of Sound and Vibration 422 (2018) 373–389.

[25] G. Lombaert, G. Degrande, D. Clouteau, Numerical modelling of free field traffic-induced vibrations, Soil Dynamics and Earthquake Engineering 19 (2000) 473–488.

[26] Z. Ozdemir, P. Coulier, M. A. Lak, S. François, G. Lombaert, G. Degrande, Numerical evaluation of the dynamic response of pipelines to vibrations induced by the operation of a pavement breaker, Soil Dynamics and Earthquake Engineering 44 (2013) 153–167.

[27] J. A. Forrest, H. E. M. Hunt, A three-dimensional tunnel model for calculation of train-induced ground vibration, Journal of Sound and Vibration 294 (2006) 678–705.

[28] J. A. Forrest, H. E. M. Hunt, Ground vibration generated by trains in underground tunnels, Journal of Sound and Vibration 294 (2006) 706–736.

[29] M. Hussein, S. François, M. Schevenels, H. Hunt, J. Talbot, G. Degrande, The fictitious force method for efficient calculation of vibration from a tunnel embedded in a multi-layered half-space, Journal of Sound and Vibration 333 (2014) 6996–7018.

[30] C. He, S. Zhou, H. Di, P. Guo, J. Xiao, Analytical method for calculation of ground vibration from a tunnel embedded in a multi-layered half-space, Computers and Geotechnics 99 (2018) 149–164.

[31] R. N. Hwang, J. Lysmer, Response of buried structures to traveling waves, International Journal of Rock Mechanics and Mining Sciences & Geomechanics Abstracts 18 (1981) 73.

[32] Y. B. Yang, H. H. Hung, A 2.5D finite/infinite element approach for modelling visco-elastic bodies subjected to moving loads, International Journal for Numerical Methods in Engineering 51 (2001) 1317–1336.

[33] L. Gavrić, Finite element computation of dispersion properties of thin-walled waveguides, Journal of Sound and Vibration 173 (1994) 113–124.

[34] L. Gavrić, Computation of propagative waves in free rail using a finite element technique, Journal of Sound and Vibration 185 (1995) 531–543.

[35] X. Sheng, C. J. Jones, D. J. Thompson, Modelling ground vibration from railways using wavenumber finite- and boundary-element methods, Proceedings of the Royal Society A: Mathematical, Physical and Engineering Sciences 461 (2005) 2043–2070.

[36] J. M. De Oliveira Barbosa, E. Kausel, Á. Azevedo, R. Calçada, Formulation of the boundary element method in the wavenumber-frequency domain based on the thin layer method, Computers and Structures 161 (2015) 1–16.

[37] P. Lopes, P. A. Costa, M. Ferraz, R. Calçada, A. S. Cardoso, Numerical modeling of vibrations induced by railway traffic in tunnels: From the source to the nearby buildings, Soil Dynamics and Earthquake Engineering 61-62 (2014) 269–285.

[38] S. Gupta, G. Degrande, Modelling of continuous and discontinuous floating slab tracks in a tunnel using a periodic approach, Journal of Sound and Vibration 329 (2010) 1101–1125.

[39] S. Gupta, M. F. M. Hussein, G. Degrande, H. E. M. Hunt, D. Clouteau, A comparison of two numerical models for the prediction of vibrations from underground railway traffic, Soil Dynamics and Earthquake Engineering 27 (2007) 608–624.

[40] D. J. Shippy, P. S. Kondapalli, G. Fairweather, Analysis of acoustic scattering in fluids and solids by the method of fundamental solutions, Mathematical and Computer Modelling 14 (1990) 74–79.

[41] P. S. Kondapalli, D. J. Shippy, G. Fairweather, Analysis of acoustic scattering in fluids and solids by the method of fundamental solutions, Journal of the Acoustical Society of America 91 (1992) 1844–1854.

[42] A. Karageorghis, The Method of Fundamental Solutions for the Calculation of the Eigenvalues of the Helmholtz Equation, Applied Mathematics Letters 14 (2001) 837–842.

[43] P. S. Kondapalli, Time-harmonic solutions in acoustics and elastodynamics by the method of fundamental solutions, Ph.D. thesis, University of Kentucky, 1991.

[44] C. J. Alves, On the choice of source points in the method of fundamental solutions, Engineering Analysis with Boundary Elements 33 (2009) 1348–1361.

[45] Y. Sun, L. Marin, An invariant method of fundamental solutions for two-dimensional isotropic linear elasticity, International Journal of Solids and Structures 117 (2017) 191–207.

[46] C. S. Chen, A. Karageorghis, Y. Li, On choosing the location of the sources in the MFS, Numerical Algorithms 72 (2016) 107–130.

[47] K. Y. Wong, L. Ling, Optimality of the method of fundamental solutions, Engineering Analysis with Boundary Elements 35 (2011) 42–46.

[48] Y. Hon, T. Wei, The method of fundamental solution for solving multidimensional inverse heat conduction problems, CMES - Computer Modeling in Engineering and Sciences 7 (2005) 119–132.

[49] A. Neumaier, Solving ill-conditioned and singular linear systems: a tutorial on regularization, Society for Industrial and Applied Mathematics 40 (1998) 636–666.

[50] L. Wang, Z. Wang, Z. Qian, A meshfree method for inverse wave propagation using collocation and radial basis functions, Computer Methods in Applied Mechanics and Engineering 322 (2017) 311–350.

[51] L. Godinho, P. Amado-Mendes, A. Pereira, D. Soares, A coupled MFS-FEM model for 2-D dynamic soil-structure interaction in the frequency domain, Computers and Structures 129 (2013) 74–85.

[52] P. Amado-Mendes, P. Alves Costa, L. M. Godinho, P. Lopes, 2.5D MFS-FEM model for the prediction of vibrations due to underground railway traffic, Engineering Structures 104 (2015) 141–154.

[53] L. Godinho, P. Amado-Mendes, A. Tadeu, Meshless analysis of soil-structure interaction using an MFS-MLPG coupled approach, Engineering Analysis with Boundary Elements 55 (2015) 80–92.

[54] Y. Gu, W. Chen, Z. J. Fu, B. Zhang, The singular boundary method: Mathematical background and application in orthotropic elastic problems, Engineering Analysis with Boundary Elements 44 (2014) 152–160.

[55] X. Wei, W. Chen, L. Sun, B. Chen, A simple accurate formula evaluating origin intensity factor in singular boundary method for two-dimensional potential problems with Dirichlet boundary, Engineering Analysis with Boundary Elements 58 (2015) 151–165.

[56] W. Chen, Z.-J. Fu, X. Wei, Potential Problems by Singular Boundary Method, Computer Modeling in Engineering and Sciences (2009).

[57] W. Chen, F. Z. Wang, A method of fundamental solutions without fictitious boundary, Engineering Analysis with Boundary Elements 34 (2010) 530–532.

[58] W. Chen, Y. Gu, An Improved Formulation of Singular Boundary Method, Advances in Applied Mathematics and Mechanics 4 (2012) 543–558.

[59] J. Lin, W. Chen, C. S. Chen, Numerical treatment of acoustic problems with boundary singularities by the singular boundary method, Journal of Sound and Vibration 333 (2014) 3177–3188.

[60] W. Chen, Y. Gu, Recent Advances on Singular Boundary Method, Joint International Workshop for Trefftz method 4 (2011) 543–558.

[61] L. Sun, W. Chen, A. H. Cheng, Singular boundary method for 2D dynamic poroelastic problems, Wave Motion 61 (2016) 40–62.

[62] G. Pang, W. Chen, Symmetric singular boundary method for potential problems with mixed boundary conditions, Engineering Analysis with Boundary Elements 56 (2015) 49–56.

[63] Z. Fu, W. Chen, P. Wen, C. Zhang, Singular boundary method for wave propagation analysis in periodic structures, Journal of Sound and Vibration 425 (2018) 170–188.

[64] Z. Fu, Q. Xi, Y. Li, H. Huang, T. Rabczuk, Hybrid FEM–SBM solver for structural vibration induced underwater acoustic radiation in shallow marine environment, Computer Methods in Applied Mechanics and Engineering 369 (2020) 113236.

[65] J. Fakhraei, R. Arcos, T. Pàmies, J. Romeu, 2.5D singular boundary method for exterior acoustic radiation and scattering problems, Engineering Analysis with Boundary Elements (2022).

[66] W. Li, B. Wu, A fast direct singular boundary method for three-dimensional potential problems, Engineering Analysis with Boundary Elements 139 (2022) 132–136.

[67] F. Wang, Z. Chen, P. W. Li, C. M. Fan, Localized singular boundary method for solving Laplace and Helmholtz equations in arbitrary 2D domains, Engineering Analysis with Boundary Elements 129 (2021) 82–92.

[68] J. Lin, L. Qiu, F. Wang, Localized singular boundary method for the simulation of large-scale problems of elliptic operators in complex geometries, Computers and Mathematics with Applications 105 (2022) 94–106.

[69] D. L. Young, K. H. Chen, C. W. Lee, Novel meshless method for solving the potential problems with arbitrary domain, Journal of Computational Physics 209 (2005) 290–321.

[70] L. Liu, Single layer regularized meshless method for three dimensional exterior acoustic problem, Engineering Analysis with Boundary Elements 77 (2017) 138–144.

[71] Y. J. Liu, A new boundary meshfree method with distributed sources, Engineering Analysis with Boundary Elements 34 (2010) 914–919.

[72] S. Kim, An improved boundary distributed source method for two-dimensional Laplace equations, Engineering Analysis with Boundary Elements 37 (2013) 997–1003.

[73] J. T. Chen, M. H. Chang, K. H. Chen, S. R. Lin, The boundary collocation method with meshless concept for acoustic eigenanalysis of two-dimensional cavities using radial basis function, Journal of Sound and Vibration 257 (2002) 667–711.

[74] W. Chen, Y. C. Hon, Numerical investigation on convergence of boundary knot method in the analysis of homogeneous helmholtz, modified helmholtz, and convection-diffusion problems, Computer Methods in Applied Mechanics and Engineering 192 (2003) 1859–1875.

[75] F. Wang, Y. Gu, W. Qu, C. Zhang, Localized boundary knot method and its application to large-scale acoustic problems, Computer Methods in Applied Mechanics and Engineering 361 (2020).

[76] D. L. Young, K. H. Chen, C. W. Lee, Singular meshless method using double layer potentials for exterior acoustics, The Journal of the Acoustical Society of America 119 (2006) 96–107.

[77] M. Dehghan, R. Salehi, A meshless local Petrov-Galerkin method for the time-dependent Maxwell equations, Journal of Computational and Applied Mathematics 268 (2014) 93–110.

[78] A. Tadeu, P. Stanak, J. Sladek, V. Sladek, Coupled bem-mlpg acoustic analysis for non-homogeneous media, Engineering Analysis with Boundary Elements 44 (2014) 161–169.

[79] Y. Miao, Y. Wang, Y. H. Wang, A meshless hybrid boundary-node method for helmholtz problems, Engineering Analysis with Boundary Elements 33 (2009) 120–127.

[80] Q. Wang, P. Kim, W. Qu, A hybrid localized meshless method for the solution of transient groundwater flow in two dimensions, Mathematics 10 (2022) 515.

[81] D. Ghangale, R. Arcos, A. Clot, J. Cayero, J. Romeu, A methodology based on 2.5D FEM-BEM for the evaluation of the vibration energy flow radiated by underground railway infrastructures, Tunnelling and Underground Space Technology 101 (2020) 103392.

[82] A. Tadeu, J. António, L. Godinho, Green's function for two-and-a-half dimensional elastodynamic problems in a half-space, Computational Mechanics 27 (2001) 484–491.

[83] D. Ghangale, A. Colaço, P. Alves Costa, R. Arcos, A methodology based on structural FEM-BEM and acoustic BEM models in 2.5D for the prediction of re-radiated noise in railway-induced ground-borne vibration problems, Journal of Vibration and Acoustics 141 (2019) 1–14.

[84] M. Schevenels, S. François, G. Degrande, EDT: An ElastoDynamics Toolbox for MATLAB, Computers and Geosciences 35 (2009) 1752–1754.

[85] B. Noori, R. Arcos, A. Clot, J. Romeu, A method based on 3D stiffness matrices in Cartesian coordinates for computation of 2.5D elastodynamic Green's functions of layered half-spaces, Soil Dynamics and Earthquake Engineering 114 (2018) 154–158.

[86] International Organization for Standardization, ISO 14837-1. Mechanical vibration. Ground-borne noise and vibration arising from rail systems. Part 1: General Guidance, 2005.

[87] E. Kausel, J. M. Roësset, Stiffness matrices for layered soils, Bulletin of the Seismological Society of America 71 (1981) 1743–1761.

[88] Y. Gu, W. Chen, J. Zhang, Investigation on near-boundary solutions by singular boundary method, Engineering Analysis with Boundary Elements 36 (2012) 1173–1182.

[89] Z. J. Fu, W. Chen, J. T. Chen, W. Z. Qu, Singular boundary method: Three regularization approaches and exterior wave applications, CMES - Computer Modeling in Engineering and Sciences 99 (2014) 417–443.

[90] A. Tadeu, J. António, L. Godinho, Defining an accurate MFS solution for 2.5D acoustic and elastic wave propagation, Engineering Analysis with Boundary Elements 33 (2009) 1383–1395.

[91] J. Li, W. Chen, Z. Fu, L. Sun, Explicit empirical formula evaluating original intensity factors of singular boundary method for potential and Helmholtz problems, Engineering Analysis with Boundary Elements 73 (2016) 161–169.

[92] T. Poggio, G. Kur, A. Banburski, Double descent in the condition number, arXiv:1912.06190 (2019) 1–6.

[93] S. N. Atluri, W. Chen, Z. Fu, X. Wei, Potential problems by singular boundary method satisfying moment condition, CMES 54 (2009) 65–85.

[94] N. K. Dezfouli, M. R. Hematiyan, M. Mohammadi, A modification of the method of fundamental solutions for solving 2D problems with concave and complicated domains, Engineering Analysis with Boundary Elements 123 (2021) 168–181.

[95] M. Bonnet, Boundary integral equation methods for solids and fluids, John Wiley and Sons, Chichester, United Kingdom (1995).

[96] Z. Razafizana, Z. J. Fu, Singular boundary method for water wave problems, Ocean Engineering 96 (2015) 330–337.

[97] A. Tadeu, J. António, L. Godinho, Defining an accurate MFS solution for 2.5D acoustic and elastic wave propagation, Engineering Analysis with Boundary Elements 33 (2009) 1383–1395.

[98] J. Li, W. Chen, Q. Qin, A modified dual-level fast multipole boundary element method based on the Burton–Miller formulation for large-scale three-dimensional sound field analysis, Computer Methods in Applied Mechanics and Engineering 340 (2018) 121–146.

[99] L. Chen, X. Li, A Burton-Miller boundary element-free method for Helmholtz problems, Applied Mathematical Modelling 83 (2020) 386–399.